STEEL CORROSION IN COASTAL RC STRUCTURES UNDER COUPLED EFFECTS OF CHLORIDE INGRESS AND ELEVATED ENVIRONMENTAL TEMPERATURES

CHANDRA SEKHAR DAS

PhD

The Hong Kong Polytechnic University

2025

The Hong Kong Polytechnic University

Department of Civil and Environmental Engineering

Steel Corrosion in Coastal RC Structures Under Coupled Effects of Chloride Ingress and Elevated Environmental Temperatures

DAS Chandra Sekhar

A thesis submitted in partial fulfillment of the requirements for the degree of Doctor of Philosophy

April 2025

CERTIFICATE OF ORIGINALITY

I hereby declare that this thesis is my own work and that, to the best of my knowledge and belief, it reproduces no material previously published or written, nor material that has been accepted for the award of any other degree or diploma, except where due acknowledgement has been made in the text.

_____ (Signed)

Chandra Sekhar Das (Name of student)

ABSTRACT

Reinforcement corrosion is a primary contributor to the early-age deterioration of coastal reinforced concrete (RC) structures, leading to significant economic costs on a global scale. As a key climatic parameter, temperature affects the corrosion risk of structures. Based on the geographic locations and the influence of urban heat islands, structures experience daily, seasonal, and annual fluctuations in temperatures. The global temperatures are also forecasted to rise by 4.4°C compared to current average temperatures by 2100 due to climate change, influencing service temperatures. Thus, accurately assessing corrosion initiation under various service conditions needs to consider these time-dependent temperature variations and their effect on the physical, chemical and electrochemical properties of corrosion. However, the temperature has traditionally been considered to influence the physical nature of chloride transport through concrete pores based on the Arrhenius equation, with less focus directed towards other interactions. This simplistic assumption has been the basis for service life prediction models considering chloride-induced corrosion initiation in RC structures, which may lead to an inaccurate assessment of the service life of RC structures against corrosion.

This thesis involves experimental works to elucidate the interactions during chloride ingress through the concrete pore network up to the steel surface, leading to the breakdown of the passive film and corrosion initiation for different service temperatures. Based on the findings from these studies, an improved numerical framework has been developed that incorporates temperature-dependent chloride transport rate, chloride binding, and chloride threshold value in the modelling of steel corrosion initiation in coastal RC structures.

The passivation and depassivation (i.e., corrosion initiation) of steel bars were first analysed in a simulated concrete environment maintained at three different temperatures of 25 ˚C, 35 ˚C and 45 ˚C through combined electrochemical and steel surface characterisation techniques.

Findings reveal that exposure of the reinforcing steel to pore solutions at elevated temperatures of 35 ˚C and 45 ˚C accelerated the formation of Fe(III) oxides compared to 25 ˚C, resulting in a higher Fe(III)/Fe(II) ratio and nobler stable potential values. However, the overall metal oxide content was lower, reducing the passive film's protective ability. Additionally, the passive film formed on the steel surface had more defects. Consequently, corrosion initiated at a significantly lower chloride concentration when chlorides were introduced into the pore solution. Interestingly, the passivity breakdown was triggered for nearly the same pore solution resistivity value, even when exposed to the three different temperatures.

To understand the contents of free chlorides in cement pore solution that pose a corrosion risk to steel reinforcement in uncarbonated conditions, chloride binding by cement hydration products at 25 ℃ and 45 ℃ was subsequently explored at different chloride concentrations. The main purpose was to (a) quantify the physically and chemically bound chlorides, (b) relate the physically bound chlorides to the structure and composition of C-(A)-S-H, and (c) assess the implications of elevated temperatures on steel corrosion risk. Results reveal that when exposed to low chloride concentration (0.5M), akin to seawater conditions, total chloride binding remained unchanged for OPC and increased for lower content of fly ash addition with increased temperature. However, it decreased significantly for binders with a high fly ash content and silica fume addition despite increased chemical chloride binding. At higher chloride concentrations (3M), total chloride binding increased for all the mixes with increasing temperatures. A hypothesis was then proposed to explain these trends in chloride binding with exposure temperatures.

The long-term corrosion performance (20 months) of steel reinforcement was also monitored in different mortars prepared with fly ash and silica fume when exposed to chloride solutions at two environmental temperatures of 25 ℃ and 45 ℃. The aim was (a) to quantify temperature-dependent chloride threshold values, (b) to assess any benefits of adding siliceous

SCM contents in these extreme conditions, and (c) to characterize the evolution of mortar properties. It was observed that incorporating SCMs marginally offset the adverse effect of elevated temperatures on corrosion initiation time due to enhanced pore refinement in mortars. Analysis of mortars around the steel-mortar interface revealed that the chloride threshold value for corrosion initiation was significantly reduced when the samples were exposed to chlorides at elevated temperatures, supporting the findings from the simulated concrete pore solution study. The chloride threshold value increased with fly ash but reduced drastically when silica fume was added to the mix. Elevated temperature also modified the corrosion morphology and the products formed on the steel surface due to chloride attack.

Finally, considering future climate projections, a multi-physics modelling framework was developed that integrates mass transport, electrochemical reactions, and material damage to simulate the corrosion processes in RC structures. The experimentally validated parameters, such as temperature-dependent chloride transport rates, binding capacities, and threshold values, were included to enhance its fidelity. The model was used to predict the corrosion initiation time for reinforced mortar mix, and the framework was then applied to assess the corrosion risk of representative RC structures in Hong Kong under various projected climate scenarios. The results showed that while higher temperatures accelerated chloride transport, increased chloride binding partially suppressed this effect, resulting in only a slight reduction in corrosion initiation time for a temperature rise of 5 °C. Thus, the different climate projections had minimal impact on tidal exposure zones, as corrosion was primarily due to chlorides. The effect was more complicated for atmospheric zones due to the interaction between the deeper carbonation front and chlorides.

An improved understanding of corrosion in RC structures under different service conditions will enable the development of accurate life cycle models to forecast maintenance needs for coastal infrastructures and ensure efficient carbon management during their service life.

PUBLICATIONS ARISING FROM THE THESIS

The thesis is submitted for the Degree of Philosophy at The Hong Kong Polytechnic University. The work was carried out during the years 2020 to 2025 in the Department of Civil and Environmental Engineering.

Journal papers related to the thesis:

Das, C. S., Zheng, H., & Dai, J. G. (2025). A review of chloride-induced steel corrosion in coastal reinforced concrete structures: Influence of micro-climate. Ocean Engineering, 325, 120794.

Das, C. S., Ahmad, R. M., Zhao, X. L., & Dai, J. G. Influences of temperatures on the physical and chemical chloride binding of calcium silicate hydrate and Friedel salt at different chloride concentrations. Construction and Building Materials, 476, 141303.

Das, C. S., Zheng, H., & Dai, J. G. (2025). Influences of elevated temperature on the passivation and depassivation properties of reinforcing steel in a concrete environment. Cement and Concrete Composites, 106164.

Das, C. S., Ahmad, R. M., Zhao, X. L., & Dai, J. G. Unveiling long-term corrosion behavior of reinforcement in mortars with SCMs in chloride environment at elevated temperatures (To be submitted)

Das, C. S., Zhang, P., Zhao, X. L., Dai, J. G., & Ahmad, R. M. Corrosion risk of reinforced concrete structures against combined chloride ingress and carbonation under future climate projections (To be submitted)

Other publications during PhD study:

Das, C. S., Zheng, H., Zhao, X. L., & Dai, J. G. (2023). Corrosion inhibition of steel reinforcements in seawater sea sand concrete by alkali-activated slag based coatings. Construction and Building Materials, 394, 132210.

Ahmad, R. M, **Das, C. S.**, Khan, M. & Dai, J.G. (2023), Development of low-carbon alkali-activated materials solely activated by flue gas residues (FGR) waste from incineration plants. Journal of Cleaner Production, 397, Article 136597

Zhang, P., Dai, J. G., **Das, C. S.**, & Zheng, J. J. (2023). A fully coupled meso-scale electro-chemo-mechanical phase field method for corrosion-induced fracture in concrete. International Journal of Solids and Structures, 267, 112165.

Yang, N., **Das, C. S.**, Xue, X., Li, W., & Dai, J. G. (2022). Geopolymer coating modified with reduced graphene oxide for improving steel corrosion resistance. Construction and Building Materials, 342, 127942.

Conference papers/abstracts:

Das, C. S., Zheng, H., & Dai, J. G., Influence of elevated environmental temperatures on passivation and corrosion risk of steel reinforcement. 16th International Congress on the Chemistry of Cement ICCC 2023, Bangkok, Thailand

Das, C. S., Zhao, X. L., & Dai, J. G. Temperature-dependent chloride binding ability of fly ash and silica fume modified ordinary Portland cement. 10th International Conference on CONcrete under SEvere Conditions – Environment and Loading 2024, Chennai, India

Das, C. S., Zhao, X. L., & Dai, J. G. Corrosion risk in coastal RC structures by combined chloride ingress and carbonation. International conference on Decarbonising the Building Industry, DBI 2024, Melbourne, Australia

ACKNOWLEDGEMENTS

During the last ten years of my journey through Civil Engineering, I have received immense care, support and encouragement from many individuals. All those learnings have made me who I am today, and I dedicate my thesis to each of you.

First and foremost, I would like to express my heartfelt gratitude to my supervisors, Prof. Jian-Guo Dai and Prof. Xiao-Lin Zhao, for introducing me to the fascinating topic of steel corrosion. I could complete my thesis because of their constant support and guidance throughout my PhD journey. Studying under their supervision is a great honour, and I will forever cherish this experience. Then, I would like to thank Dr. Haibing and Dr. Riaz, who were always available for insightful discussions and words of encouragement. I also acknowledge the support of my group members, who trained me for many experiments and Dhanada sir, who introduced me to the practical application side of my research area.

Second, I would like to thank my supervisors during my undergraduate years, Dr Tanish Dey, Prof. Rishi Gupta and Prof Sonalisa Ray, who introduced me to research and encouraged me to pursue higher degrees.

I am grateful to The Hong Kong Polytechnic University for providing me with the opportunity to pursue a PhD degree and for providing all research support. Thanks to Ms Dorothy Chan, Mr John Chan, Ms Emily Fung, Mr Jonathan, Mr Lam, Dr. Hardy and Ms Kwan of the laboratories, who were always kind and supportive of the experimental works.

Then, I would like to thank all my colleagues and friends who were always there to support me with research discussions and give me directions about life. I would like to acknowledge many incredible people in my life, starting from my childhood friend Subhasis and school friends Aseem and Minakshi, who have been by my side for nearly 15 years now. I am also thankful to the people I met at ISM Dhanbad, including Arijit, Chinmaya, Sumit, Gunjan, Vaishnav,

Bhoi sir, Panda sir, Himanshu sir and other people from Kalinga Society and Civil Engineering department who supported me immensely during my undergrad years. I learned a lot from each one of you. I am grateful to the small Indian community at PolyU (Parth bhai, Sushil bhai, Sashi bhai, Seema di, Teja bhai, and Bharati), all of whom supported me during my years in HK. I also want to acknowledge Super Serious Tutors (Partha, Mehrnaz, Caroline, Qinyu, Daniyar and Mohana) for creating a relaxing and ranting space after working hours. All the late-night drinks and travel plans gave me the energy to endure difficult times. Thanks to Emma for all the philosophical discussions. I am also thankful to all the folks at the campus, restaurants and back at the student hall, who ensured my daily life went smoothly. I also want to acknowledge people who were a brief part of my life but gave me a lot of learning.

As always, I have to close this chapter by acknowledging the contribution from everyone back at home. I am indebted to my parents and two sisters for everything in my life. Thank you for giving me all the valuable lessons since I was a child and asking me to trust God when I doubted myself. I am grateful to the ISKCON temple in Hong Kong, which has always been my safe space whenever I have felt confused. Finally, I am grateful for this PhD journey, which brought me closer to spirituality and reinforced my beliefs in God. Jai Jagannath.

TABLE OF CONTENTS

CERTIFICATE OF ORIGINALITY ..... **I**

ABSTRACT ..... **I**

PUBLICATIONS ARISING FROM THE THESIS ..... **IV**

ACKNOWLEDGEMENTS ..... **VI**

TABLE OF CONTENTS ..... **VIII**

LIST OF FIGURES ..... **XIV**

LIST OF TABLES ..... **XXI**

CHAPTER 1

INTRODUCTION **1**

1.1 General Background on Corrosion **1**

1.2 Research Motivation **3**

1.3 Research Objectives **5**

1.4 Thesis Overview **6**

CHAPTER 2

LITERATURE REVIEW **8**

2.1 Introduction **8**

2.2 Critical micro-climate factors in different exposure zones **10**

2.3 Effects of micro-climatic factors on chloride transport **13**

2.3.1 Effect of wind **13**

2.3.2 Effect of periodic drying and wetting **14**

2.3.3 Effect of rainfall 18

2.3.4 Effect of surrounding temperature 18

2.3.5 Effect of carbon dioxide ingress 23

2.4 Effect of micro-climatic factors on chloride threshold 29

2.4.1 Effect of carbon dioxide ingress 29

2.4.2 Effect of relative humidity and periodic wetting and drying 33

2.4.3 Effect of temperature 37

2.5 Discussion and future perspectives 39

2.5.1 Chloride transport 40

2.5.2 Chloride threshold 42

2.6 Overall Summary 45

CHAPTER 3

STEEL CORROSION BEHAVIOUR IN SIMULATED CONCRETE ENVIRONMENT 48

3.1 Introduction 48

3.2 Experimental Program 50

3.2.1 Material preparation and exposure scheme 50

3.2.2 Electrochemical measurements 51

3.2.3 Composition and morphology of passive film 53

3.3 Results 54

3.3.1 Electrochemical analyses of passivation behaviour 54

3.3.2 Passive film composition.....65

3.3.3 Passive film morphology.....70

3.3.4 Depassivation and chloride threshold value.....71

3.4 Discussion.....76

3.5 Overall Summary.....77

CHAPTER 4

CHLORIDE BINDING BY CEMENT HYDRATION PRODUCTS.....80

4.1 Introduction.....80

4.2 Experimental Program.....84

4.2.1 Raw materials.....84

4.2.2 Preparation of paste samples.....84

4.2.3 Free water content of the rehydrated cement powders.....86

4.2.4 Chloride exposure.....87

4.2.5 Analysis after chloride exposure.....87

4.3 Results.....90

4.3.1 Chloride binding Isotherms.....90

4.3.2 Hydration phases changes of binders under chloride exposure.....92

4.3.3 Thermogravimetric/Differential thermogravimetric analysis.....94

4.3.4 Physically bound chlorides on C-A-S-H.....99

4.3.5 Effect of temperature and chlorides on the structure of C-S-H and C-(A)-S-H.101

4.3.6 Relation between C-A-S-H gel composition and physical chloride binding.....105

4.3.7 Ionic composition of binder pore solution 107

4.3.8 Discussions 108

4.4 Overall Summary 113

CHAPTER 5

CHLORIDE THRESHOLD VALUE AND STEEL CORROSION SUSCEPTIBILITY IN DIFFERENT MORTARS 115

5.1 Introduction 115

5.2 Experimental Program 117

5.2.1 Material preparation 117

5.2.2 Electrochemical measurements 119

5.2.3 Corrosion morphology and rust characterization 120

5.2.4 Chloride contents at the steel surface 120

5.2.5 Characterization of mortar properties 121

5.3 Results 122

5.3.1 Open circuit potential of steel bars 122

5.3.2 Electrochemical Impedance Spectroscopy (EIS) analyses 123

5.3.3 Chloride threshold value for corrosion initiation 133

5.3.4 Corrosion Morphology 136

5.3.5 Rust characterization 137

5.3.6 Characterization of mortar properties 139

5.4 Overall Summary 143

CHAPTER 6

SERVICE LIFE MODELING AGAINST CORROSION CONSIDERING DIFFERENT CLIMATE PROJECTION SCENARIOS 145

6.1 Introduction 145

6.2 Methodology 148

6.2.1 Evaluation of concrete properties 148

6.2.2 Mass transport 149

6.2.3 Corrosion propagation model 155

6.2.4 Time to first crack formation 158

6.3 Model Verification 159

6.3.1 Chloride transport model 159

6.3.2 Corrosion model considering varying climate conditions 161

6.4 Results and Discussions 162

6.4.1 Influence of temperature on chloride transport rate through concrete 162

6.4.2 Corrosion initiation prediction of 35FA8SF mortars from Chapter 5 163

6.4.3 Geometry of the structural model 164

6.4.4 Sensitivity of the model to temperature rise 165

6.4.5 Service life modeling considering different climate projections 168

6.5 Overall Summary 180

CHAPTER 7

CONCLUSIONS AND RECOMMENDATIONS 182

7.1 Conclusions.....182

7.2 Recommendations.....185

REFERENCES.....187

Appendix 1.....222

Appendix 2.....230

LIST OF FIGURES

Figure 1.1. Annual publications relevant to corrosion in concrete structures and climate change in recent years at Web of Science…… 04

Figure 1.2. Framework of the dissertation…….. 07

Figure 2.1. Schematic of different exposure zones in a coastal RC structure and the critical micro-climate factors affecting chloride transport and chloride threshold in each zone……12

Figure 2.2. Peak chloride concentration and convection depth in concretes subjected to different wet/dry periods observed in (a) data obtained from (Cao et al., 2022) and (b) data obtained from (Lu et al., 2015)…….17

Figure 2.3. Bound chloride contents in equilibrium with 1M free chloride concentration at different temperatures (data obtained from (Dousti & Shekarchi, 2015); (Panesar & Chidiac, 2011); (Zibara, 2001))……...20

Figure 2.4. Activation energy of concrete mixes obtained from the diffusion coefficient of chlorides of concretes at different temperatures when immersed in chloride solutions (data obtained from (Al-Sodani, 2022; Al-Sodani et al., 2021; Dousti et al., 2013; Nguyen et al., 2009; Yuan et al., 2008))……..22

Figure 2.5. Effect of prior carbonation on chloride diffusion coefficients through different concrete mixes (data obtained from (Holthuizen et al., 2018; Jin et al., 2018; Li et al., 2018; J. Liu et al., 2016; J. Liu et al., 2017; Malheiro et al., 2020; Wang et al., 2017; Xie et al., 2019))……...24

Figure 2.6. Schematic of the effect of carbonation on chloride-contaminated concrete showing (i) reduction of OH^- concentration in the carbonated zone, (ii) decomposition of Friedel salt which increases the free chloride concentration, (iii) deeper penetration of free chlorides and

shift of peak chloride concentration inside and (iv) reaction between carbonate ions or bicarbonate ions (produced from dissolution of CO_2) with calcium hydroxide to form calcium carbonate which precipitates in concrete pores…….29

Figure 2.7. Degradation effect due to carbonation on (a) passive film formed on steel in simulated pore solution (data obtained from Liu et al., 2016c) and (b) corrosion initiation time in mortars (data obtained from Shi et al., 2020)……31

Figure 2.8 Schematic diagram for anodic polarization curves under the effect of chloride ingress and carbonation showing (i) reduction of pitting potential with increasing chloride concentrations in concrete pore solution and (ii) breakdown of passivity and transformation of steel from passive to active state due to carbonation (Bertolini et al., 2013)……32

Figure 2.9. Schematic diagram for the accessibility of oxygen to the steel surface when reinforced concrete is subjected to four cases of exposure in periodic wetting and drying cycles of salt water and the corresponding changes in corrosion current density controlled by electrolyte resistance and oxygen reduction resistance (Raupach, 1996c)…….35

Figure 2.10. Schematic diagram for cathodic polarization curves, which shows (i) increasing corrosion current density due to greater availability of oxygen at steel surface and (ii) negligible electrochemical reaction in the absence of oxygen (Bertolini et al., 2013)…….37

Figure 2.11. Schematic diagram showing the main micro-climate factors that affect (i) the nature and transport rate of chlorides through concrete and (ii) chloride threshold value required for steel corrosion initiation……..41

Figure 3.1. Test setup for electrochemical measurements at different temperatures……53

Figure 3.2. Current vs. Potential curves from cyclic voltammetry tests at (a) 25 ˚C, (b) 35 ˚C, (c) 45 ˚C and (d) comparison of plots on the 5th scan……56

Figure 3.3. EIS response of steel at (a) 12 hours, (b) 7 days and (c) 14 days expressed in terms of (1) Nyquist plot and (2) Bode plot…….59

Figure 3.4. Equivalent electrical circuit (EEC) for the proposed study……60

Figure 3.5. Variation of steel (a) passive film resistance and capacitance and (b) charge transfer resistance and double layer capacitance with immersion time at different temperatures……..62

Figure 3.6. Evolution of open circuit potential (OCP) of steel at different temperatures……..64

Figure 3.7. Mott Schottky curves of steel after 14 days of passivation at different temperatures…….65

Figure 3.8. High-resolution XPS spectra of Fe 2p at different depths after 14 days of passivation at different temperatures……68

Figure 3.9. XPS fitting data to obtain the (a) atomic ratio of iron, (b) atomic ratio of oxygen, (c) ratio of iron oxides formed and (d) ratio of Fe^{2+}/Fe^{3+} at different depths after 14 days of passivation……70

Figure 3.10. Surface morphology of passive film formed after 14 days of immersion……72

Figure 3.11. Nyquist response plots of steel after different contents of chloride addition at different temperatures……...73

Figure 3.12. Evolution of (a) solution resistance (Rsol) and (b) polarization resistance (Rp) with different chloride additions for steel samples exposed to different temperatures……75

Figure 3.13. Evolution of OCP with chloride addition for steels at different temperatures….76

Figure 3.14. Schematic of the developed passive film and corrosion initiation at different exposure temperatures……..78

Figure 4.1. Schematic of sample preparation for chloride binding experiment……87

Figure 4.2. Chloride binding isotherms for the four mixes at (a) 25 ℃ and (b) 45 ℃……..92

Figure 4.3. pH of leachates after exposure to chlorides at (a) 25 ℃ and (b) 45 ℃……...93

Figure 4.4. XRD patterns for samples (a) OPC, (b) 15FA, (c) 35FA and (d) 35FA8SF post chloride

exposure……... 94

Figure 4.5. DTG plots of paste samples (a) OPC, (b) 15FA, (c) 35FA and (d) 35FA8SF after chloride exposure……..97

Figure 4.6. Portlandite content in paste samples obtained from DTG curves……..98

Figure 4.7. Variations of chemically bound chloride by Friedel salt in samples exposed to different chloride concentrations and temperatures…….…….99

Figure 4.8. Effect of temperature on physical chloride binding for different chloride exposures……....101

Figure 4.9. FTIR spectra of paste samples (a) OPC, (b) 15FA, (c) 35FA and (d) 35FA8SF exposed to chlorides at different temperatures……..…..103

Figure 4.10. Average EDS point ratios (20 random points) of binder residue to find the relation between (a) Cl/Si vs Ca/Si and (b) Cl/(Si+Al) vs Al/(Si+Al)…….106

Figure 4.11. Aluminium and calcium ion concentration in pore solution……..107

Figure 4.12. Chloride distribution in different phases at different chloride exposure concentrations and temperatures…….……110

Figure 4.13. Schematic figure of chloride bound by AFm phase and C-S-H surface at different temperature exposures and chloride concentrations……..…….….113

Figure 4.14. Impact of temperature on Cl/OH ratio in different binders…….114

Figure. 5.1. Test setup for exposure to chlorides at different temperatures……...120

Figure 5.2. Variation in open circuit potential values during the exposure period for steel embedded in (a) OPC, (b) 15FA, (c) 35FA and (d) 35FA8SF binders at 25 ℃ and 45 ℃….124

Figure 5.3. EIS response of steel bar cured in different binder systems expressed in terms of (a) Nyquist plot, (b) Bode impedance plot and (c) Bode phase angle plot…….125

Figure 5.4. Equivalent electrical circuit (EEC) for the proposed study……....126

Figure 5.5. Variation of (a) mortar resistance, (b) passive film properties and (c) charge transfer behaviour of passive film during curing conditions……...127

Figure 5.6. Evolution of EIS spectrum during chloride exposure in the format of (1) Nyquist plot, (2) Bode impedance plot and (3) Bode phase angle plot for steel samples embedded in (a) OPC, (b) 15FA, (c) 35FA and (d) 35FA8SF binders at 25 ℃ and 45 ℃……130

Figure 5.7. Evolution of polarization resistance, Rp, during chloride exposure for samples exposed to chlorides at (a) 25 ℃ and (b) 45 ℃ …….131

Figure 5.8. Chloride threshold value of steel embedded in different mortars expressed in terms of (a) Total chloride content and (b) Free chloride content…….134

Figure 5.9. Ratio of [Cl-]/[OH-] at the steel mortar interface after corrosion initiation……137

Figure 5.10. Corrosion attack on steel reinforcement embedded in different mortars……...138

Figure 5.11. Raman mapping of corroded areas of steel embedded in 35FA mortars and exposed to chlorides at 25 ℃ and 45 ℃……..139

Figure 5.12. Compressive strength of mortars at 28 days and 90 days of curing……..141

Figure 5.13. Pore structure characterization of (a) 15FA and (b) 35FA8SF samples after exposure to chloride solutions until the embedded steel started to corrode……143

Figure 5.14. TG/DTG curves of the outermost 3 mm of the (a) 15FA and (b) 35FA samples after exposure to chloride solutions until the embedded steel started to corrode…….144

Figure 6.1. Influence of temperature on chloride binding isotherm for 35FA8SF mix after chloride exposure for 8 weeks at exposure temperatures of 25 ℃ and 45 ℃…….155

Figure 6.2. Flowchart of the proposed numerical model for service life analysis…….160

Figure 6.3. Comparison of experimental data and data from the numerical model for chloride distribution inside concrete after (a) 60 days and (b) 90 days immersion in chloride solution of concentration 165 g/l and effect of accelerated carbonation (5%) for (c) 30 days and (d) 60 days on chloride redistribution in concretes specimens post 90 days chloride exposure……....161

Figure 6.4. Comparison of experimental data and data from the numerical model for (a) internal relative humidity at the steel surface and (b) corrosion current density for 2-D reinforced beam considering time-varying temperature and humidity exposure conditions...162

Figure 6.5. Influence of temperature on chloride diffusion coefficients mix obtained through NT Build 392 method at 28 and 56 days of curing of 35FA8SF concrete mix……..163

Figure 6.6. (a) Calculated chloride contents at the surface of steel bar for 35FA8SF samples exposed to chlorides at 25 ℃ and 45 ℃ through numerical modelling and (b) comparison of time for corrosion initiation between modelling and experiment ……..164

Figure 6.7. Geometries of the RC beams exposed to combined chloride ingress and carbonation from three sides for a cover depth of (a) 50 mm and (b) 75 mm…….166

Figure 6.8. Prediction of free chloride distribution at the surface of (a, b) corner rebar, (c) central rebar for different orientations and (d) corrosion initiation time using the three different corrosion models for three different constant temperatures (i.e., 25 ℃, 27 ℃ and 30 ℃)…169

Figure 6.9. Prediction of (a) annual temperature variations considering different climate projections, (b) seasonal temperature variations, (c) daily temperature variations, (d) annual CO_2 concentrations for different projections and (e) seasonal variations in atmospheric relative humidity……..…172

Figure 6.10. Prediction of (a-c) carbonation degrees and (d-f) chloride profiles at different concrete depths for 10, 20 and 30 years of service period, maximum free chloride contents at the surface of (g) central rebar and (h) corner rebar in tidal exposure zone……173

Figure 6.11. Total corrosion current for (a, b) corner rebar and (c) central rebar with different orientations, (d) mass loss in steel for corner rebar in the most severe orientation and time for cracking for tidal exposure……..175

Figure 6.12. Prediction of (a-c) carbonation degrees and (d-f) free chloride profiles at different concrete depths for 10, 30 and 50 years of service period, maximum free chloride contents at the surface of (g) central rebar and (h) corner rebar in tidal exposure zone with 75 mm cover……...……176

Figure 6.13. Prediction of (a-c) carbonation degrees and (d-f) free chloride profiles at different concrete depths for 20, 40 and 60 years of service period, maximum free chloride contents at the surface of (g) central rebar and (h) corner rebar in atmospheric exposure zone……178

Figure 6.14. Total corrosion current for (a, b) corner rebar and (c) central rebar with different orientations, (d) mass loss in steel for corner rebar in the most severe orientation and time for cracking……..179

LIST OF TABLES

Table 3.1. Calculated donor densities (N_D) of steel at different exposure temperatures……..66

Table 4.1. Summary of temperature effect on chloride binding in different binders……83

Table 4.2. Oxide composition of raw materials from XRF……..85

Table 4.3. Mix proportions of control and blended cement pastes……85

Table 4.4. Water contents in rehydrated cement powders(%)….……87

Table 5.1. Weight ratios of raw materials for the preparation of mortar samples……..119

Table 5.2. Oxide composition of raw materials obtained through XRF…….119

Table 5.3. Fitting data from EIS analysis of samples after different exposure days……..133

Table 5.4. pH of the mortar pore solution after 28 days……..141

Table 6.1. Mass transport and electrochemical parameters used for modelling…….166

Table 6.2. Environmental exposure parameters…….171

CHAPTER 1

INTRODUCTION

1.1 General Background on Corrosion

Reinforced concrete (RC) is the predominant composite material utilized globally in infrastructure projects, offering the dual advantages of steel's high tensile strength and concrete's compressive strength. Given the critical social, economic, and strategic roles of infrastructure, it is essential to ensure these structures remain durable and structurally sound over extended periods. However, one of the most significant challenges faced by these structures in coastal regions is the corrosion of the embedded steel reinforcement. Steel corrosion in concrete is a complex phenomenon that can severely compromise the structural integrity and safety of buildings, bridges, and other infrastructures (P. Zhang et al., 2023b; Zhu et al., 2018; Zhu et al., 2017).

Concrete typically provides a highly alkaline environment that forms a thin passive film on the steel reinforcement and protects it from corrosion. This development of passive film (i.e., passivation) is a spontaneous electrochemical process involving the simultaneous oxidation of Fe metal to higher oxidation states and oxygen reduction. The passivation rate is highest at an early age after casting. With the growth and thickening of the passive film, the anodic reaction rate decreases, and the passive film achieves a steady thickness nearly two weeks after casting (Poursaee and Hansson, 2007).

However, this protective film on steel reinforcement can be disrupted by various factors, including the ingress of chlorides from deicing salts or seawater, carbonation due to atmospheric CO_2, and inadequate construction practices (M. Liu et al., 2017; Yang et al., 2022; Zheng, Dai, Li, et al., 2018). Aggressive ions, such as chlorides and atmospheric CO_2, get

transported through the concrete's interconnected pore network or cracks due to loadings. The transport of these ions involves combined physical transport and chemical reactions with the cement hydration products. For example, a significant part of the chlorides ingressing inside concrete gets bound to the cement hydration products (e.g., hydrated calcium aluminate phases (AFm) and calcium silicate hydrates (C-(A)-S-H)) and reduces corrosion risk. However, the ability of these hydration products to immobilize chlorides decreases in the presence of CO_2. The moisture content within reinforced concrete structures varies over time, influencing how these ions move through the concrete. In fully saturated concrete, chloride ions primarily enter the concrete through diffusion, which follows Fick's law, while CO_2 ingress is limited. This fully saturated state is typical for undersea concrete, whereas most structures experience partial saturation during their lifespan. In such cases, the ingress of chloride ions occurs through diffusion via fully saturated pores and through capillary suction via unsaturated pores. The unsaturated pores also provide a pathway for the atmospheric CO_2 to flow through the concrete cover and ultimately reach the steel surface.

When there is a breakdown of the protective passive film (either localised or uniform), the steel undergoes corrosion, forming rust products. This rust occupies a greater volume than the original steel, causing internal stresses, cracking, and spalling of the concrete cover (Avadh et al., 2021; Behera et al., 2016). Due to the local heterogeneities, potential gradients are created on the steel surface, causing electrons to flow from anodic to cathodic sites, which leads to the formation of corrosion products at the anodic sites. This process reduces the cross-sectional area of the steel, diminishing its load-carrying capacity and leading to spalling under severe deterioration. The resulting structural degradation poses significant safety risks and economic burdens due to the need for repairs and maintenance.

1.2 Research Motivation

A report by NACE in 2013 highlighted the significant cost of corrosion, which is about 3.4% of global GDP (US$2.5 trillion). These costs arise not only from direct expenditures on repairs and maintenance but also from indirect costs associated with service disruptions, reduced asset lifespan, and potential liability claims. For example, the deterioration of critical infrastructure can lead to traffic delays, increased transportation costs, and even catastrophic failures that endanger public safety. Accurately estimating the service life of structures enables the implementation of proactive maintenance strategies and optimal resource allocation, which can significantly reduce lifecycle costs and net carbon emissions. By employing advanced modelling techniques and understanding the climatic factors influencing corrosion, engineers can predict the performance of reinforced concrete structures over time. This foresight is essential for developing effective rehabilitation strategies and ensuring that infrastructure investments yield maximum returns.

Therefore, many research studies have been conducted in the last half-century to accurately predict the time for corrosion initiation and subsequent cracking of concrete cover in RC structures under various service conditions. The RC structures are exposed to different micro-climate parameters such as temperature, carbon dioxide concentration, wetting and drying exposures, rainfall, wind and humidity during their service, which are unique to the structure's location. These micro-climates are also marked by annual, seasonal, and daily fluctuations, as well as the impacts of climate change. Urbanization has also led to the development of urban heat islands, trapping heat due to the dense nature of structures and ultimately increasing the local temperature. Thus, the effect of micro-climates and their projected changes needs to be accounted for in the service life models. Figure 1.1 shows the number of annual publications on corrosion in RC structures and climate change, which indicates the increasing emphasis on understanding how climate change will affect corrosion risk in RC structures.

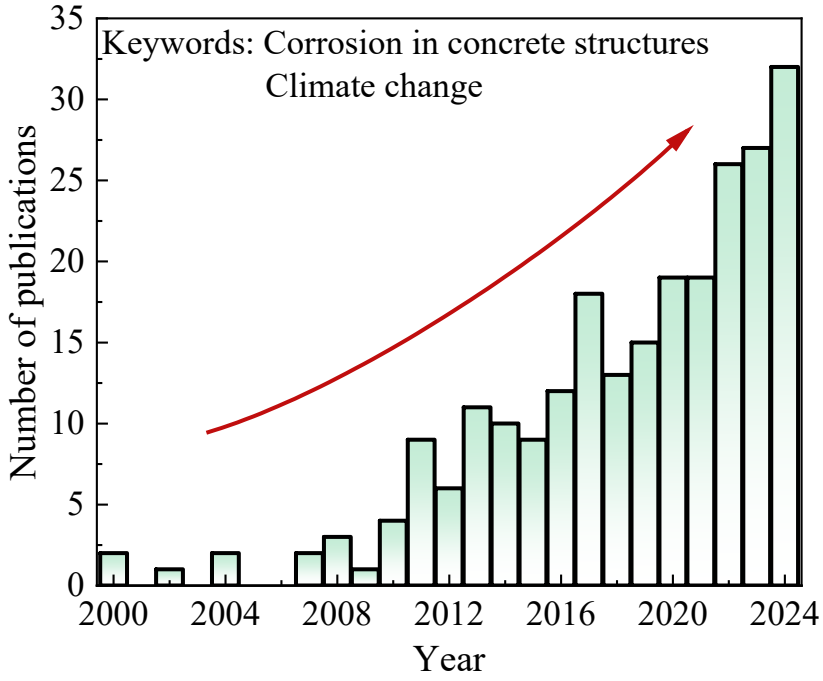

Figure 1.1. Annual publications relevant to corrosion in concrete structures and climate change in recent years (Source: Web of Science).

Among the different micro-climate factors influencing corrosion, temperature shows the most extreme variations in terms of amplitude and frequency. However, the role of external environmental temperature is rarely considered in reinforcement corrosion studies, with most of the experiments being conducted under controlled laboratory conditions (typically 20-25 °C). The limited studies considering the role of temperature in the corrosion initiation process have been achieved through chloride diffusion experiments, which have shown that the rate of chloride transport through the pores increases with temperature rise due to enhanced ionic mobility. Subsequently, the temperature-dependent chloride diffusion coefficient is used in long-term service life modelling against chloride-induced corrosion, considering future climate projections (Guo et al., 2020; Stewart et al., 2011; G. Zhang et al., 2021). This assumption for service life modelling of RC structures can represent an overly simplistic approach that disregards the complexity of the corrosion process, as summarised in Section 1.1. In this situation, there is a need to develop a more accurate service life prediction model for coastal

RC structures, taking into account the effect of daily, seasonal and annual variations of environmental temperatures on the entire physio-chemical process of reinforcement corrosion under the impact of climate change.

1.3 Research Objectives

In this thesis, a comprehensive experimental and numerical program has been carried out to develop accurate service life models for predicting steel corrosion and deterioration in coastal RC structures, considering the role of environmental temperature. The main objectives associated with the thesis are:

(1) To obtain a comprehensive understanding of the role of micro-climate on chloride-induced corrosion in RC structures.

(2) To understand the passivation and depassivation behavior of steel reinforcement in a simulated concrete environment using electrochemical and surface characterization techniques.

(3) To investigate the mechanism influencing the physical and chemically bound chlorides in hydrated cement pastes modified with supplementary cementitious materials (SCMs) such as fly ash and silica fume.

(4) To evaluate the long-term corrosion behaviour of steel in some commonly used mortar mixes due to their exposure to chlorides at elevated temperatures and the chloride threshold value for corrosion initiation.

(5) To investigate the chloride transport rate through concrete under an accelerated setup and develop a Finite element analysis model that incorporates the temperature-dependent chloride transport rate, chloride binding and chloride threshold value as parameters and estimates the time to corrosion initiation for different climate change scenarios.

1.4 Thesis Overview

The thesis consists of several chapters, and the overall structure of the thesis is shown in Figure 1.2. Chapter 1 briefly introduces the steel reinforcement corrosion in RC structures, research motivations and objectives. Chapter 2 provides an extensive review of how chloride ingress and the chloride threshold value in coastal RC structures are affected by the prevailing micro-climates at the location. Based on the review, understanding the role of temperature was considered the main focus of the dissertation. Chapter 3 focuses on the characterization of thin protective passive film formed on steel surfaces in simulated concrete pore solutions at different temperatures and its influence on corrosion initiation in the presence of chlorides. Chapter 4 focuses on the influence of temperature on chloride binding behaviour by hydrated cement pastes, which has a significant role in extending the structure's service life against chloride attack. Based on the understanding from Chapters 3 and 4, the steel bars are embedded in some mortar specimens in Chapter 5 to assess the overall impact of elevated temperature on corrosion susceptibility and chloride contents required for depassivation over a long-term study of 20 months. Chapter 6 focuses on assessing the chloride transport rate at different temperatures in typical concrete used in marine construction in Hong Kong. It utilizes parameters from Chapters 4 and 5 to predict the long-term corrosion initiation time and first crack formation, taking into account climate projections up to 2100 by the IPCC. Finally, Chapter 7 presents the overall conclusions summarized from the previous chapters.

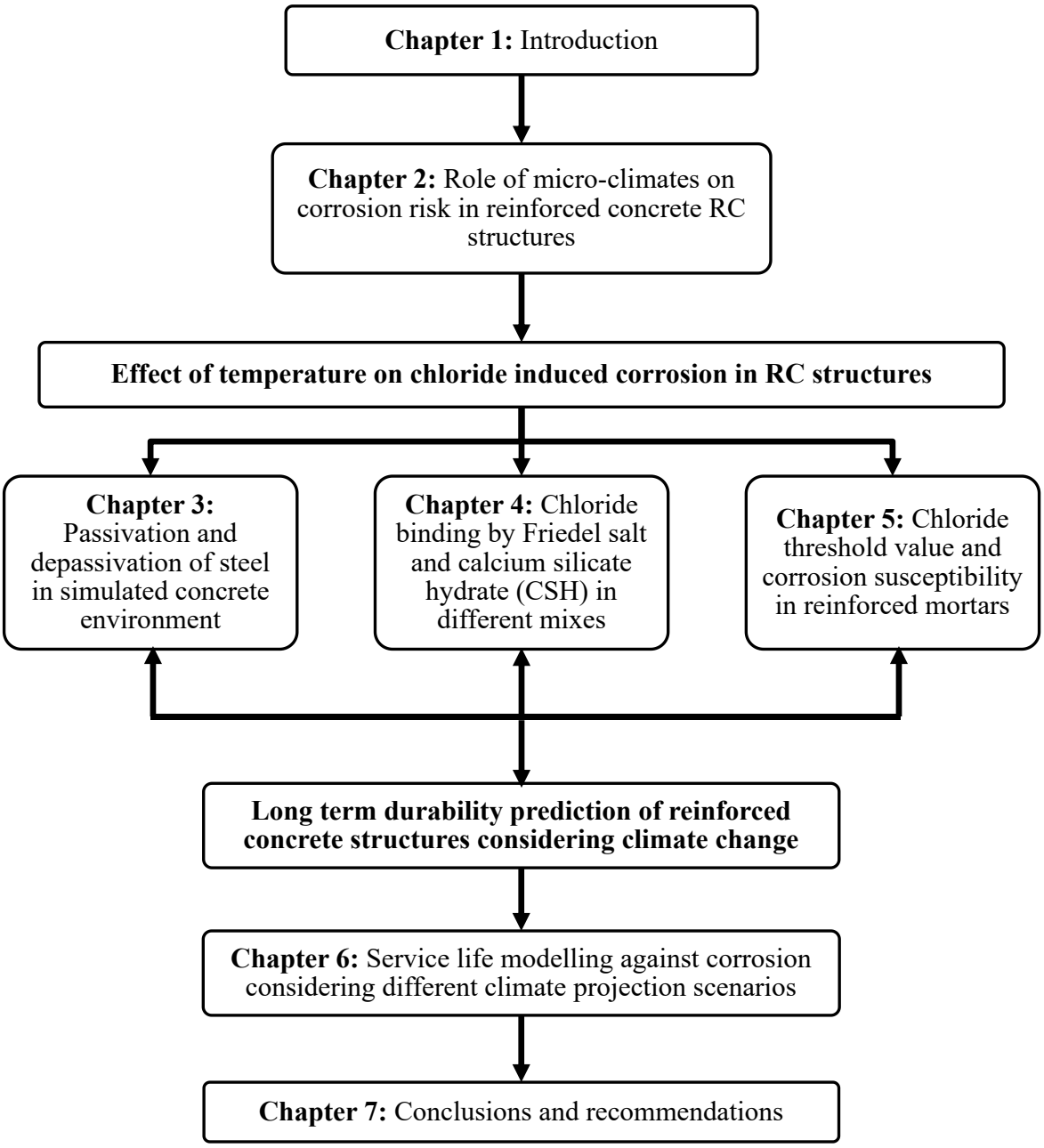

Figure 1.2. Framework of the dissertation.

CHAPTER 2

LITERATURE REVIEW

2.1 Introduction

The primary cause of early-age deterioration in coastal reinforced concrete (RC) structures is reinforcement corrosion, which is triggered by the accumulation of chloride ions at the steel surface beyond a certain threshold (Angst et al., 2009; Ann & Song, 2007; Cao et al., 2019). Even in cases where carbonation proceeds simultaneously with chloride ingress, previous studies indicate that, in coastal areas, carbonation is slower than chloride transport (Kuosa et al., 2014; J.-z. Liu et al., 2016; Qiu, 2020; Yoon, 2007), making chlorides the leading factor behind corrosion. This is due to the ability of chlorides to partially clog the concrete pores and retain moisture, leading to increased pore relative humidity (Malheiro et al., 2021). However, the progress of the carbonation front changes the chloride distribution in concrete. Gradually, as chlorides accumulate at the steel surface, they cause the breakdown of the passive film and depassivation of the steel. Due to a thick concrete cover, chlorides take several years to reach the steel surface and start corrosion. The time to depassivation is known as the corrosion initiation time and is crucial in assessing the structure's long-term serviceability against corrosion.

Structures in different regions are constantly exposed to the natural climate, which varies globally across diverse climate zones characterized by factors such as humidity, temperature, and salt concentrations in the oceans. These climate zones often have sub-classifications that further define the specific characteristics of a region's climate, marked by annual, seasonal, and daily fluctuations. Even in the same area, the structure's orientation and local modification brought by construction and rapid development create urban heat islands and alter wind patterns, leading to distinct micro-climate conditions for different structural elements. It has

been observed that micro-climate conditions tend to cause a great degree of variation in chloride distribution even for the same structure (Costa & Appleton, 1999) and also corrosion current density (El Hassan et al., 2010; Jaśniok & Jaśniok, 2015), leading to varying levels of corrosion severity by chlorides.

Many studies have shown that these distinct micro-climate conditions can significantly impact the long-term corrosion-induced damage caused by chlorides. For instance, during an inspection of 879 RC piles for the Hornibrook Bridge in Australia, extensive damage was found on the underside of bridge slabs, while the piles remained in good condition after 75 years of service (Melchers et al., 2017). A similar situation occurred at a cooling tower in a thermal power station, which experienced severe deterioration in specific areas just three years into its 25-year design service life (Segura et al., 2016). Analysis revealed that the southeastern side of the structure, facing the sea, experienced accelerated corrosion initiation due to wetting and drying cycles. In a structure in Brazil, locations subjected to wetting and drying cycles of salt water suffered severe damage, with chloride contents about 3-8 times those of locations without such cycles (Medeiros et al., 2013). Another case involved a chimney structure located in the Mediterranean region that had to undergo several cycles of repairs during 47 years of service due to the synergistic effect of chloride contents exceeding the threshold value at steel reinforcement and carbonation of concrete cover (Carsana et al., 2022).

While the cause of variations in chloride distribution and corrosion damage in concrete has been attributed to the micro-climate effect in many literature, the existing reviews have mainly focused on the evaluation of the durability of different concrete mixes, testing methodologies and protection methods in marine environments (Song et al., 2008); (Angst et al., 2009); (Shi et al., 2012); (Shafikhani & Chidiac, 2019; Zhang & Zhang, 2014); (Yi et al., 2020); (Liang et al., 2021). The current ways to assess corrosion risk due to chlorides in RC structures at laboratories rely on simplistic exposure schemes such as wet-dry cycles, sustained

submergence in a salt solution, salt spray, accelerated carbonation, and chloride electromigration to simulate the conditions encountered in practice, which fails to accurately capture the role of each micro-climate parameter (Andrade et al., 2002; Lindvall, 2007). This becomes particularly relevant in light of the ongoing unprecedented climate change, which may lead to more uncertain events in the future.

Therefore, this research aims to provide an overview of how different micro-climates influence corrosion initiation in reinforcing steel due to chlorides. The corrosion initiation time has been presented to depend on the rate of chloride transport in concrete cover and the chloride threshold. First, we evaluate the critical micro-climate factors in different exposure zones. Then, we discuss the influence of critical micro-climate factors on chloride transport and chloride threshold. This is followed by identifying the limitations of current work and directions for future research. Finally, the review ends with an overall summary of the findings. The outcome of this review would shed light on some coupled interactions that have not yet been well understood and enable the selection of a suitable concrete mix to achieve maximum long-term serviceability against chloride-induced corrosion. It is worth noting that this study only considers the service environments of RC structures where corrosion risk due to chlorides is more than carbonation.

2.2 Critical micro-climate factors in different exposure zones

The chlorides accumulate on the surface of the RC structure either when they are in direct contact with seawater (as in port and offshore structures) or due to the winds carrying airborne chlorides (as for coastal buildings and bridges). Generally, the field data have shown that higher chloride deposits on a concrete surface increase its corrosion susceptibility (Meira et al., 2010; G ROCHA Meira et al., 2007). For example, Meira et al. (Meira et al., 2010) found that when the chloride deposition rate increased from 120 mg/m^2.day to 500 mg/m^2.day, the structure's

service life due to corrosion was shortened by about 30-60%. This surface chloride deposition rate varies by the structure's location (e.g., its height above sea level and distance from sea) such that as the structure location moves away from the sea, the chloride deposition drops significantly in the first 200 meters, followed by a gradual decrease after that. Based on the risk of corrosion by chlorides, RC structures are classified into different exposure zones: submerged zone, tidal zone, splash zone, and atmospheric zone.

The submerged zone represents the structures or a part of the structure that remains below sea level year-round. The chloride penetrates the concrete cover by diffusion due to the concentration gradient. However, the corrosion rate in this case is limited by the dissolved oxygen in seawater. Thus, the corrosion rate is generally low (Page, 1975). Only in some underwater tubular structures, such as tunnels, severe chloride-induced corrosion occurs by macrocell formation in zones with different aerations and can be quite severe (Pergola et al., 2013). The primary degradation mechanism for the concrete submerged inside seawater is a combined chemical attack by sulphate ions and other salts, and physical weathering (Yi et al., 2020); (Santhanam & Otieno, 2016). Thus, the relevant micro-climate parameters in submerged zones affecting chloride transport are the salinity of seawater (i.e., salt concentration) and concentrations of other aggressive ions, which can cause degradation in concrete.

The atmospheric zone refers to any part of a structure that is aerated throughout the year, including coastal reinforced structures located within a few kilometres from the shore. In this zone, chlorides from seawater can reach the structure in the form of airborne chlorides carried by winds. Due to the fully aerated condition, there is easy access for gases such as oxygen and carbon dioxide to the steel surface. The degree of pore saturation, which affects the chloride and gas transport rate, is primarily influenced by micro-climate factors such as temperature, relative humidity and rainfall characteristics in atmospheric zones.

The tidal and splash zones comprise any part of a structure that undergoes wetting and drying cycles and are sometimes grouped (Yi et al., 2020). The tidal zone encompasses the area between high and low tide levels of seawater, while the splash zone refers to the parts above the tidal zone that are exposed to marine splashes. Due to their relatively higher elevation, the splash zone experiences longer drying periods than the tidal zone. The drying and wetting periods are also influenced by local micro-climate factors such as temperature, humidity, wind speed, and direction, which ultimately affect the nature of chloride transport and the accessibility of gases into the concrete pores for tidal and splash zones.

The dominating climatic factors influencing chloride transport when exposed to different conditions can be illustrated as shown in Figure 2.1.

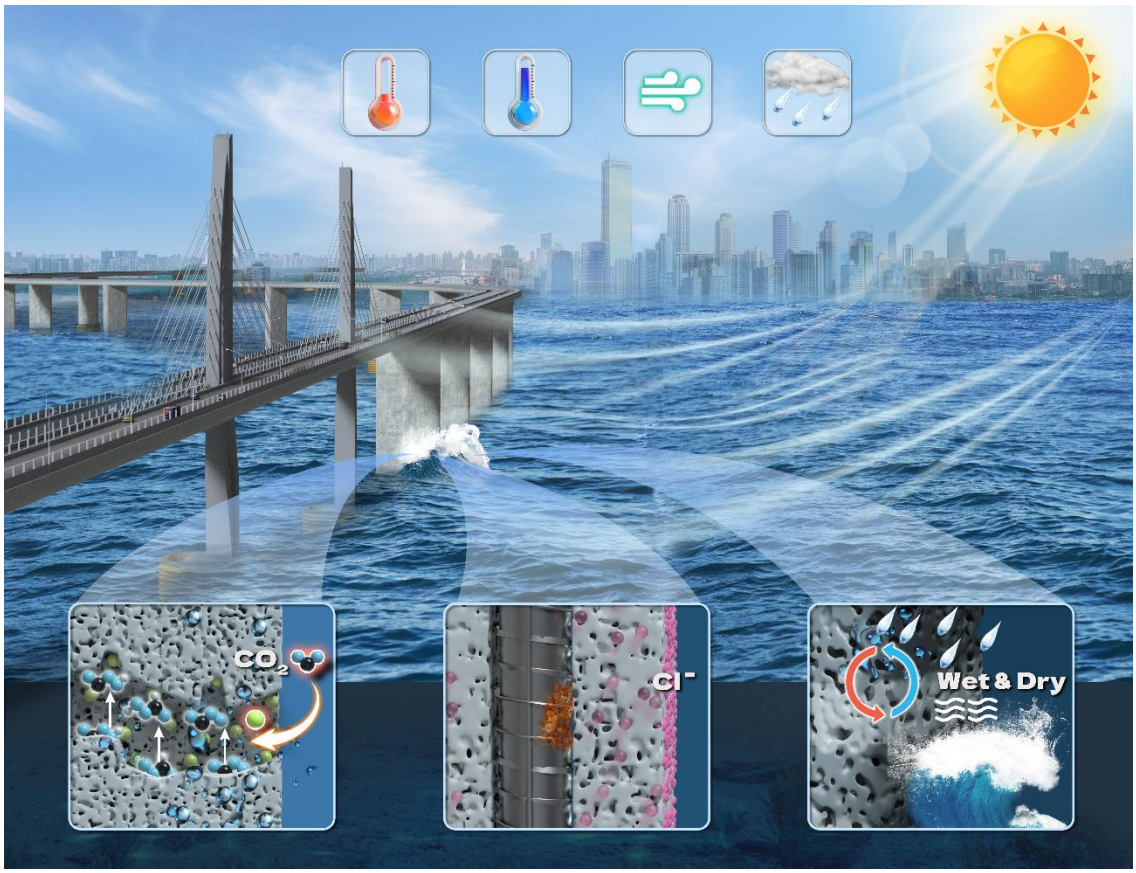

Figure 2.1. Schematic of different exposure zones in a coastal RC structure and the critical micro-climate factors affecting chloride transport and chloride threshold in each zone.

Once chlorides reach the steel surface, the transition from passive to active state depends on the chloride threshold and varies with the nature of aggressive ions and the concrete's internal environment. The internal concrete environment, such as moisture content in the pores, chemical composition of the pore solution and oxygen availability at the steel surface, are altered by micro-climatic factors such as exposed temperature, carbonation and relative humidity of the region or periods of drying and wetting seawater cycles (Andrade et al., 2002; P. Zhang et al., 2023a). These ultimately affect the chloride threshold value. Thus, the interaction between micro-climatic factors and the chloride threshold value is more indirect than the chloride transport process.

2.3 Effects of micro-climatic factors on chloride transport

2.3.1 Effect of wind

Winds primarily act as carriers for chloride ions from seawater to coastal structures in the atmospheric zone. The oceanic winds are rich in marine aerosols, comprising particles of sizes ranging from 0.1 to 400 μm. Among these particles, it has been observed that marine aerosol particles of size > 10 μm have the highest corrosivity impact (Ambler & Bain, 1955). However, with an increase in particle size, the tendency of the particles to settle down (sediment) increases. In such situations, the ability of the wind to transport particles over large distances plays a key role in promoting corrosion. One key point observed is that a certain threshold wind speed exists beyond which the salt concentration increases steeply. This speed has been identified to vary between 3 m/s and 7.1 m/s in different studies (Gibson Rocha Meira et al., 2007; Meira et al., 2008; Meira et al., 2006; Morcillo et al., 2000)., and the reason has been attributed to the increased number of salt particles and increased percentage of larger-sized particles at higher wind speeds.

An exponential growth function has been used to draw the relationship between salt concentration (D) and wind speed with time (t) (Gibson Rocha Meira et al., 2007), as represented by Equation 2.1.

$$D = D_1 + ae^{b(\frac{3t_3}{t})} \quad (2.1)$$

where, a and b are constants influenced by location and local climatic conditions, D_1 is the chloride deposition by wind speeds less than 3 m/s, t_3 is the time length when wind speed was more than 3 m/s.

However, a previous study has pointed out that chloride deposition may hold more relevance to wind power, defined by the product of wind speed and the residence time (Feliu et al., 1999). For example, a high-intensity wind speed for a longer duration can significantly increase salt deposition. This is particularly evident during storms, which deposit large quantities of salt despite impacting for a few hours.

In addition to influencing surface chloride deposits, the winds influence chloride penetration in wet-dry cycles. A study performed in coastal regions of Northeast Brazil (de Medeiros-Junior et al., 2015) concluded that winds promoted faster drying of concrete surfaces for sidewalls subjected to cyclic wetting and drying. This moisture reduction in concrete created an imbalance that slowed the chloride penetration.

2.3.2 Effect of periodic drying and wetting

For offshore and port structures, the moisture condition in the concrete is significantly influenced by the wet-dry cycles due to marine splashes (Medeiros et al., 2013). Several laboratory studies and field exposure results have demonstrated that the wet-dry periodic cycles in marine splash zones accelerate the chloride migration and change the chloride profile distribution in the concrete (Arya et al., 2014; Cai et al., 2020; H. Jin et al., 2022; Ju et al.,

2021; Tongning et al., 2020; Ye et al., 2016; Zuquan et al., 2018). This causes the peak chloride concentration value to be obtained at a certain depth inside the concrete. This depth is termed as convection zone and mainly originates due to the coupling effect of convection and diffusion in the concrete surface layer.

When concrete subjected to marine splashes undergoes a drying period after wetting, water loss starts from the evaporation front (exposed surface of concrete) and proceeds inwards. Thus, depending on the drying period's length and the concrete's quality, only a certain depth of the concrete will undergo moisture loss (i.e., a decrease in the saturation degree) during the drying stage (Hong & Hooton, 1999). Typically, these depths range between 0-15 mm (Lu et al., 2015; Wu et al., 2023; Yun Zhang et al., 2023) and are formed due to the slower drying rate of concrete than its wetting (Spragg et al., 2011). Thus, these shallow concrete depths will have a high concentration of chlorides, which are later transported into the concrete depths in the subsequent wetting stage. Depending on the length of the drying period and degree of saturation in the near-surface regions, the chloride transport through this layer in the following wetting stages can be by capillary action or diffusion.

The time for the development of this convection zone is dependent on durations of wet and dry cycles. For example, the convection zone is only formed after a prolonged exposure period in concretes subjected to short dry/wet cyclic exposures but is more evident at a short exposure duration in concretes exposed to longer dry/wet cycles (Cao et al., 2022; Gang et al., 2015; Jin et al., 2023) (Figure 2.2 (a)). This is because, in small dry/wet cycle exposure, concrete remains nearly saturated, thus leading to slower diffusion-based transport almost uniformly throughout the concrete. However, in the case of extended dry/wet cycles, the capillary action of chloride transport plays a dominating role in the near-surface concrete, followed by diffusion-based transport at greater depths. An increase in the number of wetting and drying cycles also increases the convection depth and the peak chloride concentration in the concrete (Cao et al.,

2022; Chen et al., 2023). This is attributed to the moisture changes in the concrete until a greater depth and subsequent higher chloride ingress under capillary action. Notably, the capillary-based absorption also varies with the chloride content in concrete (Xie et al., 2023). For example, at low chloride levels, water absorption is promoted due to the hygroscopic effect of salts. However, at higher chloride levels, the blockage of some of the pores by chlorides reduces water uptake.

The influence of concrete mix proportions on convection depth and peak chloride content is rather unclear from available studies. There seems to be a consensus that increasing porosity in concrete increases the convection depth and peak chloride, which is observed in samples with different w/b ratios where high w/b results in greater convection depth (Chang et al., 2017; Yun Zhang et al., 2023). However, the addition of SCMs has contradicting effects in available studies. Cao et al. (Cao et al., 2022) observed that adding FA and GGBS reduced peak chloride contents but had a negligible impact on convection depth. These results align with the trend in the study by Zhang et al. (Yun Zhang et al., 2023), who exposed 14 sample groups to natural and simulated environments and predicted the randomness of convection depth. Their study found that the random distribution in convection depth for short-term studies followed the same trend as natural long-term exposures. Moradllo et al. (Moradllo et al., 2018) observed that increasing silica fume dosage from 5% to 12.5% in concrete reduced the convection depth. On the contrary, experimental results from Lu et al. (Lu et al., 2015) demonstrated that increasing FA contents negatively affected concrete durability by increasing peak chloride contents and the convection depth (Figure 2.2 (b)). The detailed experimental conditions for studies by Cao et al. (Cao et al., 2022) and Lu et al. (Lu et al., 2015) are provided in Table 1 of Appendix 1.

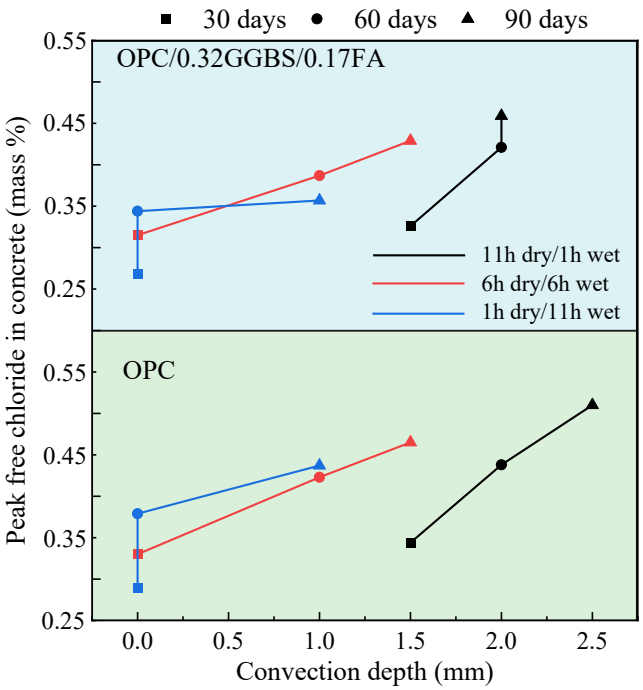

(a)

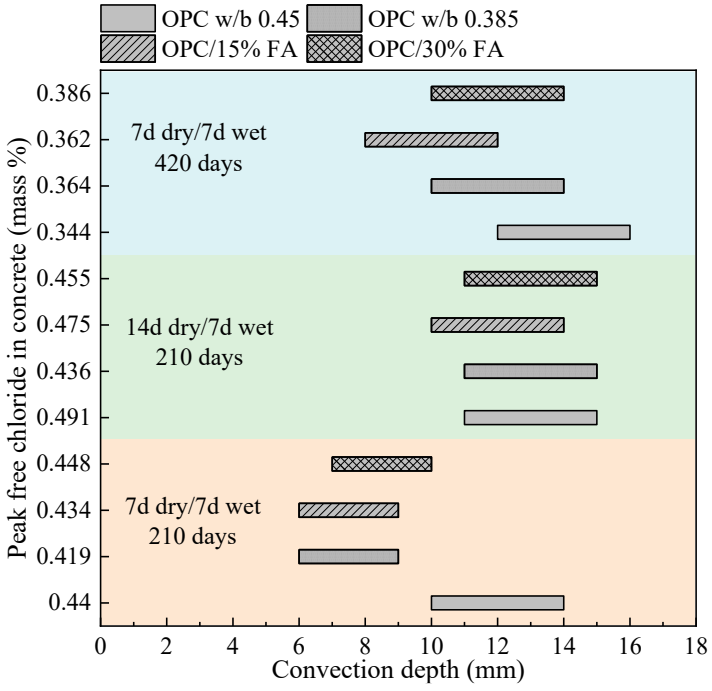

(b)

Figure 2.2. Peak chloride concentration and convection depth in concretes subjected to different wet/dry periods observed in (a) data obtained from (Cao et al., 2022) and (b) data obtained from (Lu et al., 2015).

2.3.3 Effect of rainfall

While the moisture states of concrete in splash and tidal zones are governed by wetting and drying cycles, the RC structure in a coastal atmospheric zone is primarily influenced by the relative humidity and rainfall distribution (Andrade et al., 1999; Liu et al., 2018; P. Liu et al., 2016; Medeiros-Junior, 2018). The exposure of unsheltered chloride-contaminated concrete structures (i.e., with airborne chloride deposits) has two effects: the rainwater washes off some chloride ions from the surface, and there is some rainwater absorption by concrete.

For completely saturated concrete, chloride transport from the surface to the inside of concrete occurs primarily by diffusion. Hence, the surface chloride content only decreases slightly for a shorter exposure. With the increase in exposure time, a convective zone is usually formed due to the higher erosion of chlorides from the concrete surface, as observed in marine splash zones. In contrast, for the unsaturated chloride-contaminated concrete exposed to rainwater, a convection zone and a decrease in surface chloride concentration occur even at a shorter exposure. This can be attributed to more rainwater absorption and chloride transport by capillary action.

For the same rainfall duration, this difference between surface and peak chloride concentration also increases with the increase in rainfall intensity, attributed to the higher kinetic energy of rain and subsequent damage to the surface (Jin et al., 2021). It has been reported that degradation due to high rainfall intensity also reduces the chloride binding capacity of concrete. This is a consequence of the deterioration of concrete pores and the subsequent release of chloride ions from Friedel's salt (Jin et al., 2021).

2.3.4 Effect of surrounding temperature

Generally, an RC structure is subjected to different temperatures due to daily and seasonal variations. The effect of service temperature on chloride transport can be explained in terms of

1) the chemical interaction between chloride ions and concrete; and 2) the transport rate of chlorides through concrete.

Chemical interaction between chloride ions and concrete

A significant part of the chlorides entering the concrete gets bound to the hydration products (i.e., undergoes chloride binding) and does not pose a corrosion risk in non-carbonated concrete (Florea & Brouwers, 2012). Thus, a greater chloride binding capacity of binders is usually preferred as it slows down the net chloride ingress (Li & Shao, 2014). It has been observed that when concretes are exposed to chlorides at different temperatures, there is an increase in free chloride as the temperature is increased in plain and blended Portland cement (Dousti & Shekarchi, 2015; Hussain, 1993; Maslehuddin et al., 1997; Panesar & Chidiac, 2011; Tran et al., 2021; Xu et al., 2016). However, some studies have pointed out that variation of chloride binding at different temperatures does not follow the same trend at different chloride concentrations (Ogirigbo & Black, 2017; Zibara, 2001). For example, the chloride binding reduces with temperature rise at lower chloride concentrations of 1 M or less. At high chloride concentrations, i.e., 3M, the chloride binding increases with increasing temperature. The variation arises due to different mechanisms controlling the binding at different temperatures. However, there seems to be no general consistency in both results and the mechanism governing chloride binding at different temperatures. Another important phenomenon is that the mix proportions also seem to affect the chloride binding changes at different temperatures. This could be observed in the bound chloride contents observed in equilibrium with 1 M free chlorides, as shown in Figure 2.3. However, the trend is not quite clear. It must also be noted that among the three studies compared ((Dousti & Shekarchi, 2015; Panesar & Chidiac, 2011)), even for the same mix of OPC, the observed chloride binding ability varies significantly in the study by Dousti and Shekarchi (Dousti & Shekarchi, 2015). This could be primarily linked to the higher curing age of 56 days in one study (Dousti & Shekarchi, 2015) compared to 28 days

in the other two studies (Panesar & Chidiac, 2011); (Zibara, 2001). The detailed experimental conditions are given in Table 2 of the Appendix 1.

In addition to chlorides, seawater contains a large concentration of sulphate ions, which penetrate the concrete along with chloride ions. It has been observed that the presence of sulphate ions reduces the amount of chloride that gets bound to the hydration products. This is attributed to the preferential reaction of the sulphate over chloride ions with tricalcium aluminate (C_3A) to form calcium sulphoaluminate hydrate compounds (Dehwah et al., 2003; Maslehuddin et al., 1997). Thus, the presence of high chloride and sulphate ions in the pore solution of binders at elevated temperatures can pose serious corrosion issues to the reinforcement.

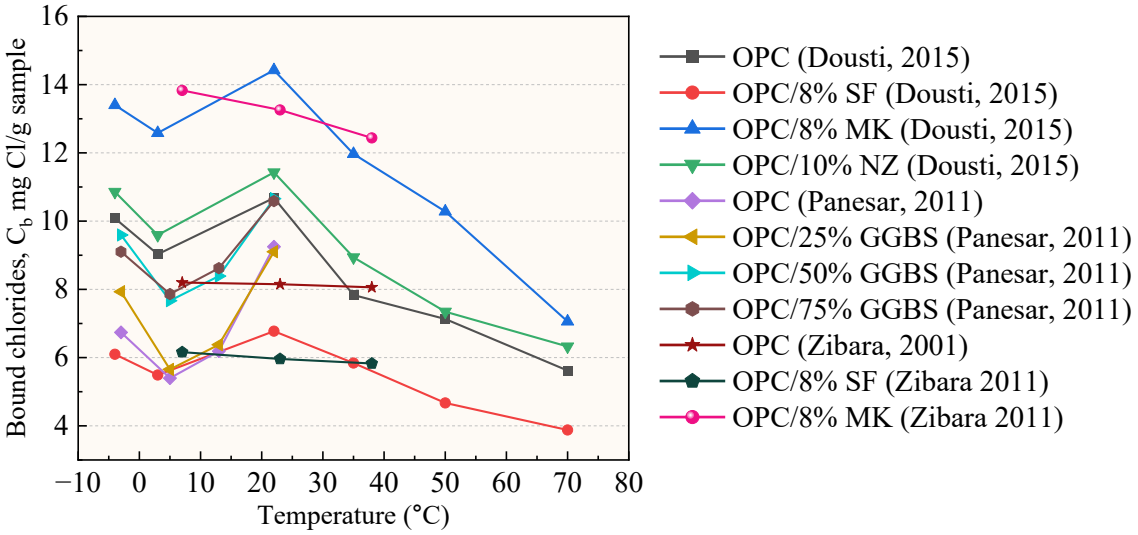

Figure 2.3. Bound chloride contents in equilibrium with 1M free chloride concentration at different temperatures (data obtained from (Dousti & Shekarchi, 2015); (Panesar & Chidiac, 2011); (Zibara, 2001))

Effect on chloride ion transport rate

In addition to affecting the chloride binding ability of concrete, the surrounding temperature also influences the mobility of chloride ions through the pores in concrete. Studies investigating

the temperature effect on chloride transport have used constant temperature (Care, 2008; Dousti et al., 2013; Yuan et al., 2008) or temperature gradient (Isteita & Xi, 2017) under natural diffusion and electric migration tests. All the investigations observed a higher chloride permeability and higher penetration depth with temperature rise. The primary reason attributed to the increased permeability was increased porosity and macroscopic crack network formed in concrete after exposure to even temperatures as low as 45 ˚C (Care, 2008). The chloride permeability is usually measured in terms of diffusion coefficients and can be measured using the Arrhenius equation to account for different temperatures (Equation 2.2).

$$D_2 = D_1 e^{\frac{E_a}{R}(\frac{1}{T_1} - \frac{1}{T_2})} \qquad (2.2)$$

Where D_1 and D_2 represent the diffusion coefficients at temperatures T_1 and T_2, respectively; E_a is the activation energy for chloride transport in the concrete, and R is the gas constant. Thus, increased activation energy results in greater susceptibility of concrete to chloride permeability at higher temperatures. The activation energies of different concrete mixes have been provided in Figure 2.4. The detailed experimental methodology is provided in Table 3 of the Appendix 1. It can be observed that the activation energy of concretes with the same mix proportions also varies with the exposure duration, e.g., with longer immersion periods, the activation energy increases. Additionally, it can also be observed that for concretes using different water/binder ratios, the activation energy changes significantly once the water-to-binder ratio exceeds 0.5 due to the availability of largely unconstrained capillaries (Yuan et al., 2008). This is a cause for greater temperature susceptibility of concrete with high water-to-binder ratios (Page et al., 1981; Yuan et al., 2008). In some cases, high-temperature exposure has also been reported to increase the surface chloride concentrations in concretes (Samson & Marchand, 2007).

However, the adverse effect of temperature on chloride permeability has been observed to reduce in concretes containing different supplementary cementitious materials (SCMs). One of the reasons for this effect is the decreased activation energy of concrete with the addition of SCMs (Dousti et al., 2013; Nguyen et al., 2009). Dhir (Dhir et al., 1993) pointed out that high-temperature exposure also leads to a greater pozzolanic effect of SCMs such as fly ash (FA) and results in concrete densification, compensating for increased ionic diffusion. However, this beneficial effect of FA was prominent for higher cement replacement by FA in the mixing of concrete.

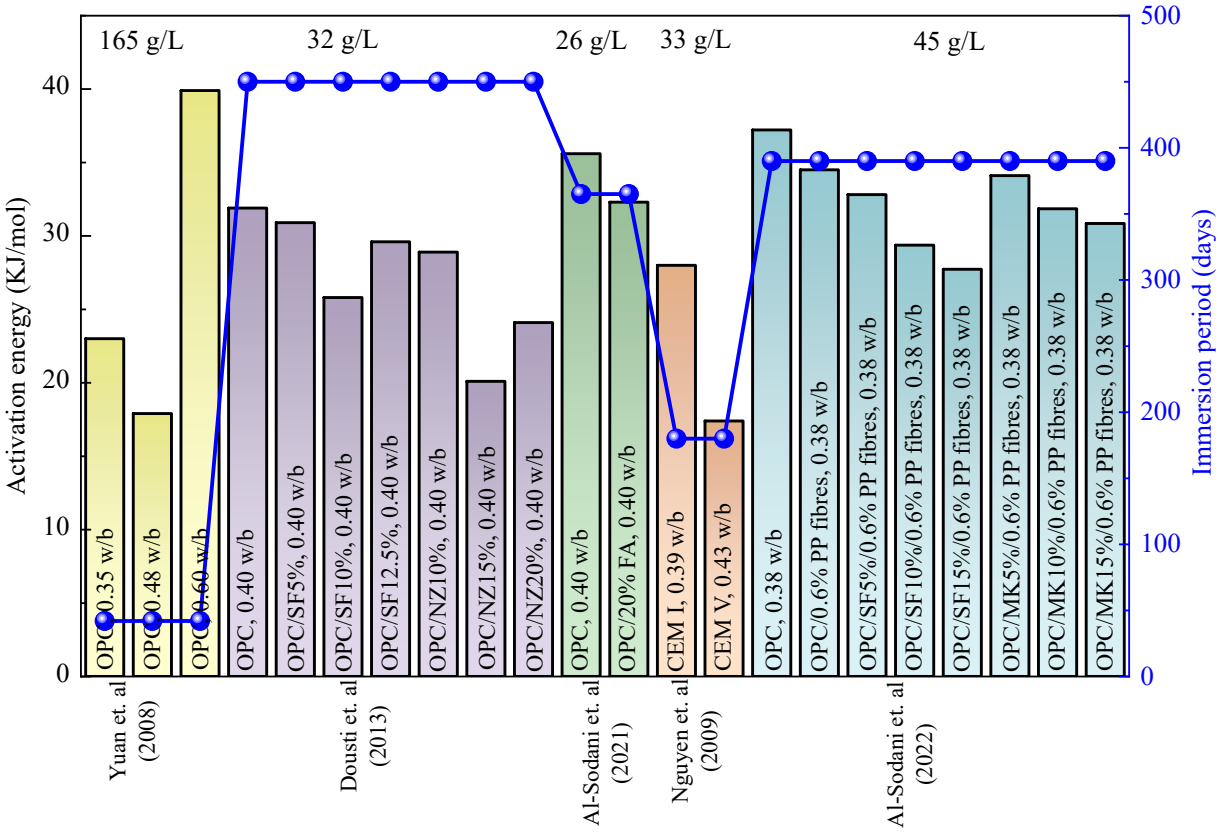

Figure 2.4. Activation energy of concrete mixes obtained from the diffusion coefficient of chlorides of concretes at different temperatures when immersed in chloride solutions (data obtained from (Al-Sodani, 2022; Al-Sodani et al., 2021; Dousti et al., 2013; Nguyen et al., 2009; Yuan et al., 2008))*

**SF (Silica fume), NZ (Natural zeolite), FA (fly ash), MK (Metakaolin), PP(Polypropylene fibres), OPC(ordinary Portland cement), w/b (water to binder ratio)*

2.3.5 Effect of carbon dioxide ingress

Carbon dioxide (CO_2) from the atmosphere slowly diffuses into porous concrete during its service life and reacts with concrete's alkaline constituents in a moist environment. This reaction is called carbonation and leads to a drop in the alkalinity of the pore solution. This drop in pH results in the release of chloride ions bound to the different hydration products, thereby increasing the concentration of free chlorides (i.e., increasing the corrosion risk). In addition to releasing the bound chlorides, the interaction between CO_2 and cement hydration products also changes the concrete pore structure. However, it has been identified that both these effects (i.e., the release of bound chlorides and changes in concrete pore structure) are dependent on the extent of carbonation and the nature of cement hydration products (von Greve-Dierfeld et al., 2020).

Attempts to study the synergistic effects of carbonation on chloride transport properties have generally employed two experimental sequences:

a) Carbonation followed by chloride attack

b) Chloride attack followed by carbonation

Carbonation followed by chloride exposure

This scenario represents the chloride transport process through the carbonated top surface layer of the concrete cover of RC structures. The progress of the carbonation front induces changes in pore structure (Ngala & Page, 1997) and near-surface microcracking (Wang et al., 2017). This significantly changes the chloride diffusivity in all the concrete types. A detailed figure highlighting the effect of carbonation on chloride diffusion rate, as observed in previous

literature studies, is presented in Figure 2.5. The detailed experimental conditions are listed in Table 4 of Appendix 1. It can be observed that there is a wide variation concerning the influence of carbonation on chloride diffusion coefficient brought about broadly by the difference in concrete properties and carbonation exposure scheme (Holthuizen et al., 2018; Jin et al., 2018; Li et al., 2018; J. Liu et al., 2016; J. Liu et al., 2017; Malheiro et al., 2020; Wang et al., 2017; Xie et al., 2019)).

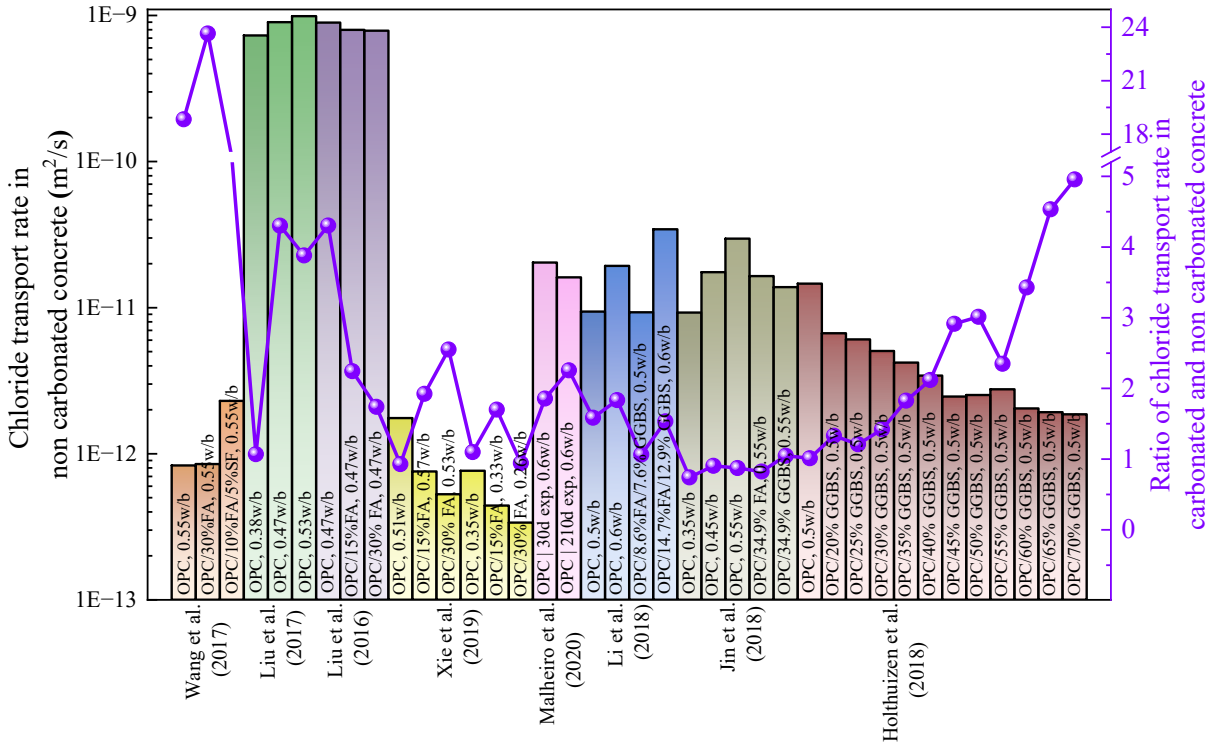

Figure 2.5. Effect of prior carbonation on chloride diffusion coefficients through different concrete mixes (data obtained from (Holthuizen et al., 2018; Jin et al., 2018; Li et al., 2018; J. Liu et al., 2016; J. Liu et al., 2017; Malheiro et al., 2020; Wang et al., 2017; Xie et al., 2019)).

Once CO_2 penetrates the concrete, it reacts with different hydration products such as calcium hydroxide (CH) and calcium silicate hydrate (C-(A)-S-H) and unhydrated constituents (C_3S and C_2S). CH most readily reacts with CO_2 to form calcium carbonate among the different cement hydrates. The volume of calcium carbonate formed by the carbonation of CH is higher

than that of the reactant, which decreases concrete porosity. After destabilizing all the accessible CH, calcium silicate hydrate (C-(A)-S-H) carbonation starts, accompanied by several other hydrates. The carbonation of C-(A)-S-H involves a complex decalcification – polymerization reaction with the formation of silica gel and the release of some water. Studies have pointed out that the properties of C-(A)-S-H (i.e., Ca/Si ratio and water content) determine whether its carbonation will have a net positive or negative volume change. For Portland cement pastes, the C-(A)-S-H gel generally comprises a Ca/Si ratio between 1.5 and 1.9 with a jennite-like structure (Lothenbach et al., 2011). However, adding silica-rich SCMs as a partial replacement for OPC leads to the formation of tobermorite-like structured C-(A)-S-H gels with a lower Ca/Si ratio and more defects. It has been observed that the most significant shrinkage due to carbonation happens in these lower Ca/Si characterized C-(A)-S-H hydrates (Ca/Si less than 1.2), which increase the porosity of the concerned paste after carbonation (Chen et al., 2006; Justnes et al., 2020; von Greve-Dierfeld et al., 2020). The replacement levels of SCMs that trigger this transition vary significantly with the CaO content of the SCMs and can be identified using thermodynamic modelling (Lothenbach et al., 2011). It has been observed that the transition of C-(A)-S-H from a high Ca/Si ratio to a low Ca/Si generally takes place with the addition of about 15% SF or 20% FA, or 65% GGBS. However, this transition threshold changes with concrete's age and composition due to the variations in anhydrous and hydrated phase contents (Saillio et al., 2019). Thus, the CaO content of SCMs and the mixing amount significantly affect the chloride diffusion behaviour of concrete after carbonation (Saillio et al., 2021; von Greve-Dierfeld et al., 2020).

Studies on the effect of GGBS have reported a fairly consistent trend with higher GGBS replacement leading to a higher diffusion ratio (ratio of chloride rate in carbonated and non-carbonated concrete) in all cases, and this is attributed to the increased carbonation depth (Holthuizen et al., 2018; Jin et al., 2018). However, studies investigating FA-modified concrete

have reported contrasting results. Xie et al. (Xie et al., 2019) observed that when cement was replaced up to 30% by weight of FA, there was always an increase in diffusion ratio, with a lower diffusion ratio observed in concretes prepared with a lower w/b ratio. However, Liu et al. (J. Liu et al., 2016) and Jin et al. (Jin et al., 2018) observed a decrease in diffusion ratio on increasing FA content, aligning with the pore structure analysis by Wu and Ye (Wu & Ye, 2017).

An increased water/binder ratio in OPC has been attributed to increasing cement hydration, increasing the available CaO for reaction with CO_2 (Jin et al., 2018; Xie et al., 2019) and the subsequent densification (i.e., decreased porosity). This can lead to a more remarkable decrease in the chloride diffusion coefficient of OPC concretes after carbonation. However, these results have been contradicted by observations from Liu et al. (J. Liu et al., 2017) and Wang et al. (Wang et al., 2017), where the chloride diffusion coefficient increased after carbonation when the w/b ratio employed was 0.47 or higher. Wang et al. (Wang et al., 2017) attributed this to the development of shrinkage cracks in C-(A)-S-H when subjected to accelerated carbonation.

In addition to concrete mix properties, the nature of the CO_2 exposure scheme also affects its chloride diffusivity. Increased exposure to CO_2 increases the amount of CO_2 that can react with the hydration products and features a deeper penetration into the concrete. This may amplify the effect of carbonation on the chloride diffusion coefficient, as observed previously (Malheiro et al., 2020). However, it has been observed that the extent of interaction decreases with the exposure time, with the most significant decalcification of cement hydrates taking place in the first month of exposure to CO_2 (Wang et al., 2017).

In addition to modifying the chloride diffusivity, the new products formed by the carbonation process reduce the ability of the matrix to bind chlorides. Generally, for chloride ingress from an external source, the chlorides can bind physically to C-(A)-S-H gels due to their large surface area or get chemically bound to form Friedel's salt through their reaction with

aluminate-ferrite-monosubstituted phases (AFm). This chloride binding ability greatly depends on the alumina content of the binder. Hence, the chloride binding increases with the addition of SCMs like metakaolin, GGBS and FA but decreases with SF (Thomas et al., 2012). In the case of carbonation, these AFm phases react with carbonate ions to form monocarboaluminate (Mc) phases, thus reducing the availability of AFm to bind the incoming chlorides chemically (Balonis et al., 2010; Chang, 2017). It is worth noting that some previous research works have shown that in the presence of high chloride ions, the carbonate ions can be replaced by chloride ions to form Friedel's salt. However, the extent of this reaction is minimal. Thus, the ability of carbonated binders to bind ingressed chlorides at a later stage is very low (Saillio et al., 2014).

Chloride exposure followed by carbonation:

This scenario represents the progress of the carbonation front into the inner layers of the concrete cover of the RC structure. Since carbonation is a slow process that may take years to progress, it can be assumed that a considerable amount of chlorides might have already been ingressed into the structure and are bound to the hydration products. A schematic diagram demonstrating the effect of carbonation on chloride-contaminated concrete has been provided in Figure 2.6. The main consequence of carbonation in concretes containing chlorides is a decrease in the pH of the pore solution and subsequent release of chlorides bound to the hydration products. Geng et al. (Geng et al., 2016) found that the release of chlorides is facilitated by the decomposition of both C-(A)-S-H and Friedel salt, which are responsible for the physical and chemical chloride binding, respectively.

In experiments that investigated the effect of carbonation on chloride-contaminated concrete, there was significant chloride redistribution with deeper chloride penetration, a decrease in surface chloride content and a slight inward shift in peak chloride front (Chang et al., 2018; Dousti & Khaksar, 2023; Geng et al., 2016; Wang et al., 2017; Ye et al., 2016). A few reasons

that were pointed out for this phenomenon are (1) diffusion of free chlorides because of the concentration gradient; (2) maintaining a charge balance after a decrease in OH^-; (3) subsequent inward movement of water generated through carbonation, carrying free chlorides. Further, it was observed that chloride contamination also reduced the carbonation depth compared to regular concrete due to pore refinement (Kuosa et al., 2014; J. Liu et al., 2017). This was linked to the higher moisture content in the pores due to the hygroscopic nature of chloride salts (Malheiro et al., 2021). When evaluating this effect on concretes with different water/binder ratios, it was observed that the reduced carbonation front in chloride-contaminated concrete was more prominent in concretes with lower water/binder ratios. In addition to high moisture content, another reason pointed out was the ability of chlorides to block some of the concrete pores and thus reduce CO_2 penetration (B. Li et al., 2024).

While carbonation has been observed to have a generally detrimental effect on chloride binding, one study by Zheng et al. (Zheng et al., 2021) found that at low w/b ratios, mild carbonation led to increased chloride binding. The hypothesis was that the carbonate deposits formed as a result of the reaction blocked some of the concrete pores, trapping the free and adsorbed chlorides and inhibiting their mobility.

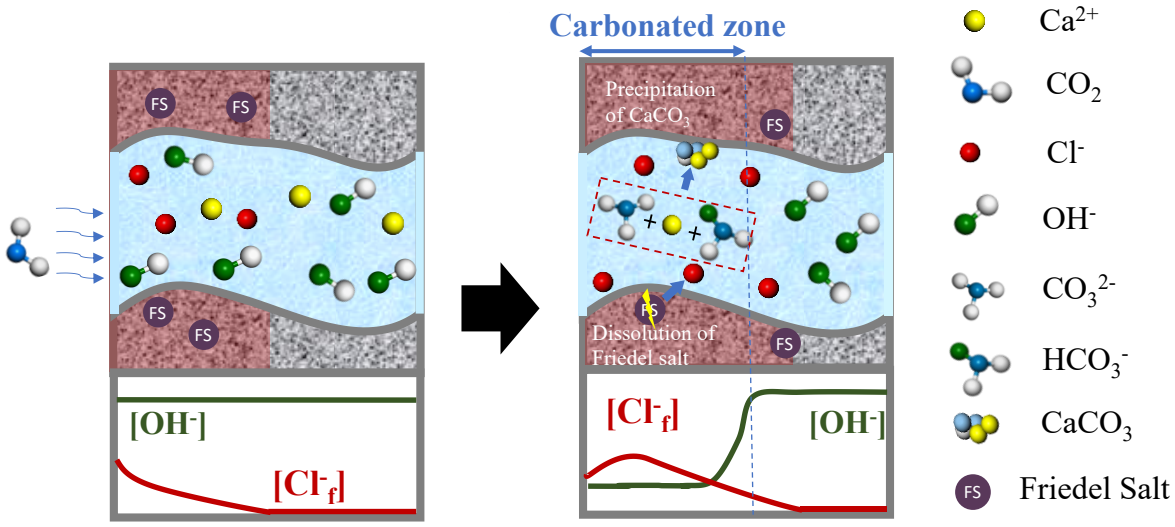

Figure 2.6. Schematic of the effect of carbonation on chloride-contaminated concrete

showing (a) reduction of OH^- concentration in the carbonated zone, (b) decomposition of Friedel salt which increases the free chloride concentration, (c) deeper penetration of free chlorides and shift of peak chloride concentration inside and (d) reaction between carbonate ions or bicarbonate ions (produced from dissolution of CO_2) with calcium hydroxide to form calcium carbonate which precipitates in concrete pores

2.4 Effect of micro-climatic factors on chloride threshold

2.4.1 Effect of carbon dioxide ingress

A thin iron oxide film (passive film) is formed in an alkaline solution because of the reaction between metal and hydroxyl ions (Guzman et al., 1979). This phenomenon is called passivation, and the passive film grows to a steady thickness in nearly two weeks after casting (Poursaee & Hansson, 2007). As the chloride front goes inside the concrete, it leads to the leaching of alkalis. This progressively increases the $[Cl^-]/[OH^-]$ at the steel surface and, with sufficient oxygen availability, leads to depassivation and an active corrosion state of the reinforcement (Melchers, 2020; Melchers & Chaves, 2020). Hence, the initial concentration of hydroxyl ions (i.e., pH of the solution) significantly affects steel's passivation and chloride threshold value. The influence of pH on the Tafel polarization plots has been extensively studied by Liu et al. (Liu et al., 2021) and validated using Mixed Potential Model (MPM). For a deaerated solution, an increase in pH reduces the water reduction rate (responsible for the cathodic half-cell reaction), leading to a lower current density. An increase in pH ($pH > 12.5$) also decreases the time required for steel passivation (Li et al., 2017) and affects the final steady potential. In addition to affecting the passive film properties and its protectiveness, even a minor decrease in pH reduces the chloride threshold value (R. Liu et al., 2016; Liu et al., 2014). This highlights the importance of pH on corrosion initiation.

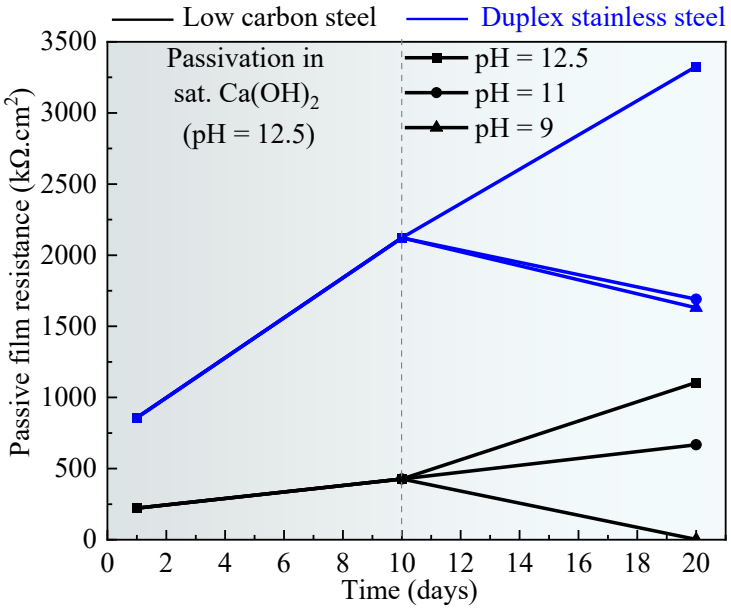

(a)

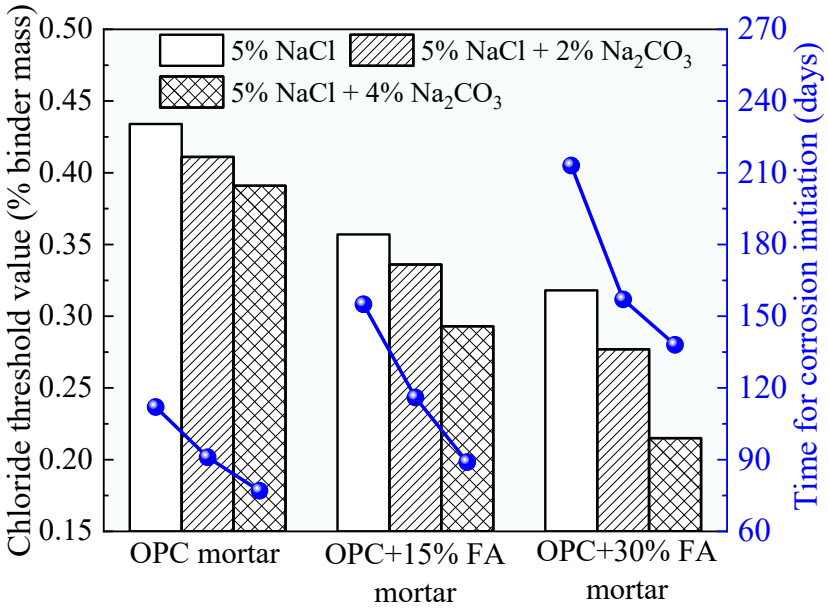

(b)

Figure 2.7. Degradation effect due to carbonation on (a) passive film formed on steel in simulated pore solution (data obtained from Liu et al., 2016c) and (b) corrosion initiation time in mortars (data obtained from Shi et al., 2020).

Generally, the pH of the concrete's pore solution can vary significantly with the diffusion of CO_2. Several studies have added different concentrations of bicarbonate/carbonate ions to the pore solution to simulate the above situation (R. Liu et al., 2016; Shi et al., 2020). In all the studies, it has been reported that the introduction of carbonate ions leads to a drop in passive film resistance (refer to Figure 2.7 (a)) such that, in very low pH systems (pH ~9), the steel corrosion can initiate even without chloride ions (Huet et al., 2005; Shi et al., 2020). Additionally, in such cases, it has been observed that passivation is relatively slower in the alkaline solution, along with a higher passive current density, denoting a porous passive film formation. The risk of pitting corrosion is also higher (Figueira et al., 2017; M. Liu et al., 2017). However, the effect is highly dependent on the steel type. The sharp drop in pH of the concrete pore solution at severe carbonation changes the $[Cl^-]/[OH^-]$ significantly in the pore solution, increasing the corrosion susceptibility against chloride ions (De Weerdt et al., 2019; Hay & Celik, 2024; R. Liu et al., 2016). This can be observed in Figure 2.7 (b), with two different fly ash contents under combined chloride and carbonate ion penetration. With the addition of fly ash, the drop in chloride threshold value is more drastic, which aligns with the observations in Section 3. In fact, for severely carbonated concretes, adding fly ash has negligible benefit in delaying corrosion initiation time. Thus, based on the observations, the effect of pH and chloride ions on the anodic polarization curves of steel reinforcement can be represented as shown in Figure 2.8 (Wang et al., 2016).

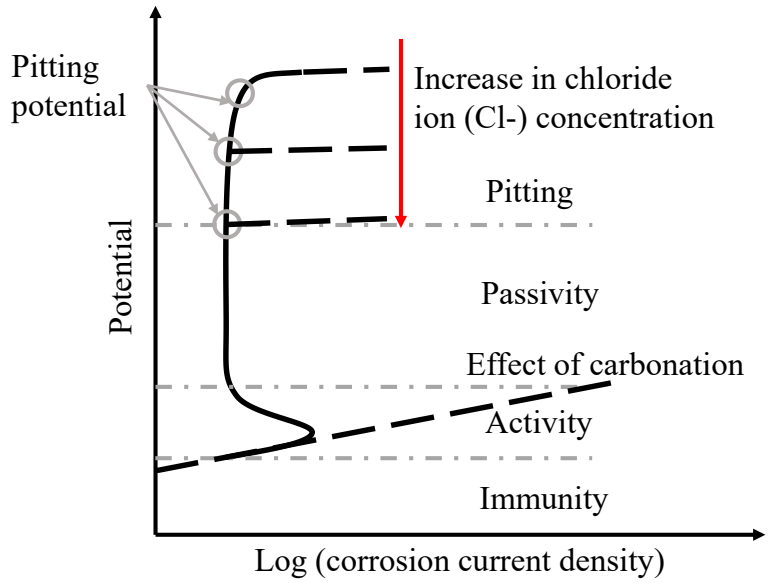

Figure 2.8 Schematic diagram for anodic polarization curves under the effect of chloride ingress and carbonation showing (i) reduction of pitting potential with increasing chloride concentrations in concrete pore solution and (ii) breakdown of passivity and transformation of steel from passive to active state due to carbonation (Bertolini et al., 2013)

The ingress of carbon dioxide into concrete and the subsequent carbonation reactions also alter the pore structure, as explained in Section 2.3.5. This affects concrete resistance, primarily facilitating electron transfer between the anode and cathode. While this effect is negligible in microcell corrosion, it is significant for macrocell corrosion, where the cathode and anodic regions are separated. The number of studies on this aspect is very limited. Revert et al. (Revert et al., 2019) investigated the effect of carbonation on macrocell corrosion current density for OPC and concretes with cement replacements of 18% and 30% by FA. They observed that the concrete resistance increased with fly ash addition for non-carbonated cases. When carbonated, the concretes with FA showed similar bulk resistance to OPC and a higher macrocell corrosion current density. Chen and Su (Chen & Su, 2023) extended this study to consider other SCMs like GGBS and SF. They observed increased macrocell current density irrespective of any SCM

additions, suggesting that macrocell corrosion risk is highly intensified in SCM-modified concrete due to carbonation.

2.4.2 Effect of relative humidity and periodic wetting and drying

The moisture changes in concrete brought about by relative humidity in the atmosphere and periodic drying and wetting have two impacts: one is electrolytic resistance, responsible for electron transfer between anodic and cathodic sites, and the other is cathodic polarization resistance, which controls oxygen reduction at cathodic sites. When the concrete is completely dry, a lack of electrolyte for the electrochemical reaction inhibits corrosion. When the concrete is fully submerged in water such that oxygen diffusion is restricted, the high cathodic polarization resistance is the controlling factor (Liu & Weyers, 1998).

For RC structures or some of its parts exposed to the atmosphere and well aerated, the internal humidity of concrete (i.e., moisture content) varies with the relative humidity of the atmosphere. A 12-month exposure study observed that the fluctuations in concrete internal humidity were less than atmospheric humidity, with the fluctuations being more significant in summer than in winter, suggesting that temperature also plays an important role (Lu et al., 2017). Even the concrete composition seemed to affect the magnitude of changes in internal humidity. For example, the change was more significant for concretes with more than 30% FA contents and was attributed to the larger pores, allowing easier moisture exchange. It has been observed that the presence of chlorides in concrete can also increase the moisture content in concrete due to their hygroscopic effect (Bai et al., 2021). This is because the NaCl crystals get easily electrolysed to Na+ and Cl-, which react with water and increase the porous concrete's overall moisture absorption capacity. This effect is pronounced in concretes with high chloride contents and at higher atmospheric relative humidity, which could increase the time of wetness of steel reinforcement and, thus, prolonged periods of high corrosion currents.

For RC structures in tidal and splash zones, periodic wetting and drying cycles are the influential factors changing the moisture state in concrete. Investigations relating corrosion current to the changes in concrete moisture state explained that the net corrosion current in the cathodic branch during wetting is due to the combination of two contrasting effects: an increase in current due to lowered electrolytic resistance and a decrease in current due to increased oxygen reduction resistance (Raupach, 1996b, 1996c) (Andrade et al., 1990). Raupach (Raupach, 1996c) observed that electrolyte resistance played a dominating role in the short wetting phase of concrete. The corrosion current increased with moisture uptake by concrete and gradually decreased after the concrete started drying as the electrolyte resistance increased. Oxygen availability plays a dominating role in the longer wetting phase of concrete. From its dry state, the current increased with moisture intake to reach a maximum, followed by a swift drop as the oxygen supply was limited. During the drying stage, a comparison of the corrosion current from two concretes with w/b ratios of 0.4 and 0.65 revealed that for high-resistivity concrete (0.4 w/b in this case), the corrosion current was controlled by concrete resistance (Otieno et al., 2019). In comparison, the corrosion current varied with electrolyte and cathodic resistance for low-resistivity concrete of 0.65 w/b. Stefanoni extended this study to multiple wetting and drying cycles and observed that the peak current achieved in the wetting stage decreased with subsequent cyclic exposure (Stefanoni et al., 2020). A schematic of the relationship between corrosion current and different water saturation levels is provided in Figure 2.9.

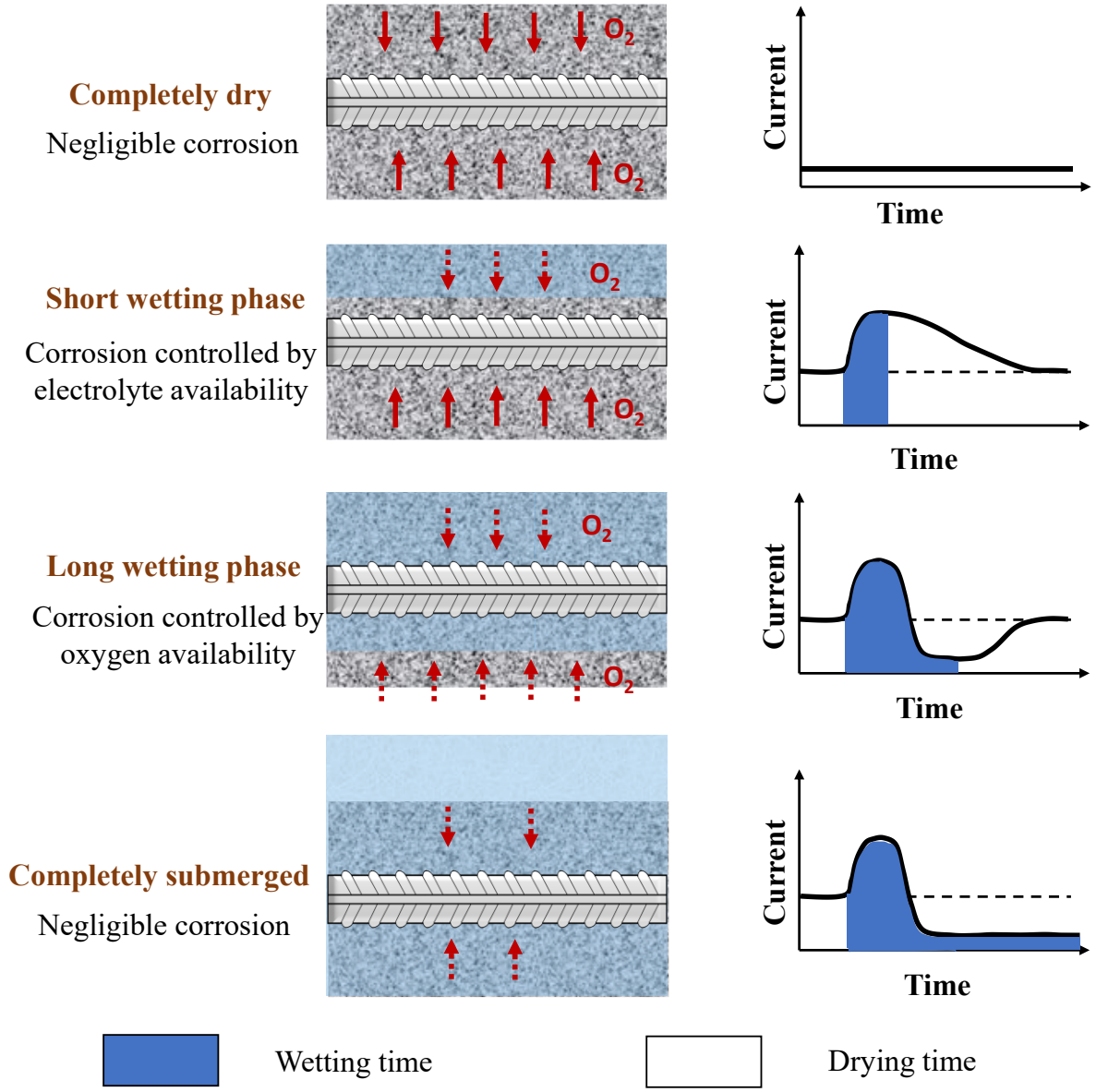

Figure 2.9. Schematic diagram for the accessibility of oxygen to the steel surface when reinforced concrete is subjected to four cases of exposure in periodic wetting and drying cycles of salt water, and the corresponding changes in corrosion current density controlled by electrolyte resistance and oxygen reduction resistance (Raupach, 1996c).

The moisture content in the concrete pores influences the transport rate of oxygen. The available oxygen at the steel surface influences the steel passivation behaviour even without chlorides. Alhozaimy et al. (Alhozaimy et al., 2016) observed that the initial current was low during passivation for reinforcing steel in concrete cured in a sealed condition or submerged in

water with minimal oxygen. However, these steel specimens showed high corrosion rates in long-term exposure. This was attributed to the poor passivation of steel reinforcement in the initial periods, thus making the steel vulnerable to corrosion. Decreasing the available oxygen decreases the cathodic current density and subsequently shifts the corrosion potential towards more negative values (Figure 2.10). The relation between oxygen availability and corrosion potential is also strongly observed in the pore solution of binders containing GGBS, where an oxygen deficiency shifts the corrosion potential to even values of -1V vs SCE in some cases (Criado & Provis, 2018; Das et al., 2023; Mundra & Provis, 2021). Some studies have reported that such a negative potential shift due to oxygen unavailability also helps to inhibit any corrosion risk (as the case for steel immersed in seawater) (Hussain & Ishida, 2010).

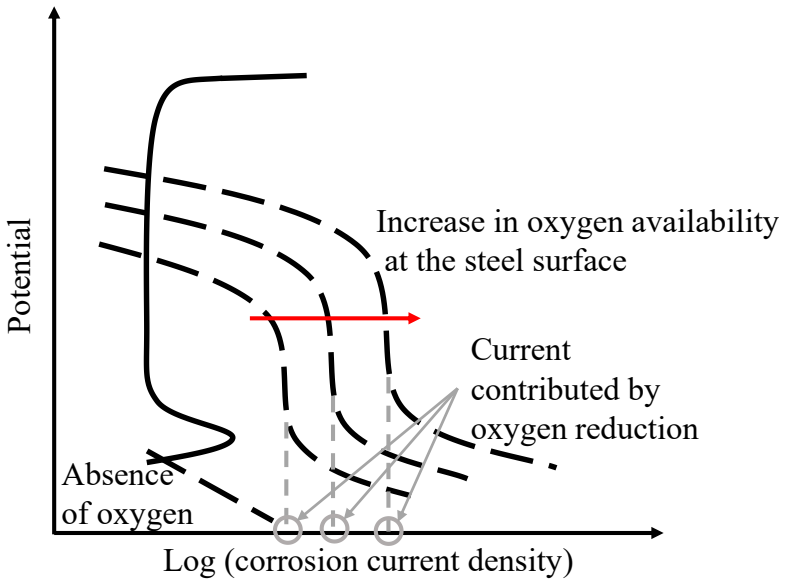

Figure 2.10. Schematic diagram for cathodic polarization curves, which shows (i) increasing corrosion current density due to greater availability of oxygen at steel surface and (ii) negligible electrochemical reaction in the absence of oxygen (Bertolini et al., 2013).

While this observation was based on microcell current, it can also be extended to macrocell corrosion. Macrocell corrosion currents between actively corroding and passivated steel rebars are negligible in dry concrete due to high electrolytic resistivity. However, moisture ingress

reduces resistivity, enabling significant galvanic currents. In partially submerged structures, submerged rebars (anodes) corrode aggressively, while aerated rebars (cathodes) sustain cathodic reactions, as demonstrated before (Chalhoub et al., 2020; Li, Xiong, Fan, Chen, et al., 2023). The time for corrosion initiation depends critically on the cathode-to-anode (C/A) area ratio. Li et al. (Li, Xiong, Fan, Gu, et al., 2023) reported that increasing the C/A ratio from 1 to 2 reduced the chloride threshold required for active corrosion by up to 50%, attributing this to intensified Cl^- adsorption at anodic sites. This adsorption promoted cation vacancy formation in the passive film, destabilizing its protective oxide layer and accelerating localized pitting. As a result, the corrosion initiation time was shortened.

2.4.3 Effect of temperature

A reinforced structure is constantly subjected to temperature fluctuations, which affect the corrosion rate. Jiang and Yuan (Jiang & Yuan, 2013) evaluated the variation of concrete's internal temperature based on natural climate and found that the variations in concrete's internal temperature followed the same trend as external climate. However, a difference of 1 to 2°F could be observed at the location of steel reinforcement when there are significant changes in concrete cover thickness (Liu & Weyers, 1998). Thus, many studies have been carried out by using concrete's pore solution at different temperatures to simulate different climatic conditions. When the environmental temperature is increased, keeping both the pH and dissolved oxygen (DO) constant, it has been observed that the changes in the curves follow the Arrhenius behaviour, leading to increased corrosion current density (Liu et al., 2021). The exposure temperature also affects the passive film growth rate and composition. It has been observed that an increase in temperature reduces the Fe(II)/ Fe(III) ratio as well as the ratio of Fe(oxides)/ Fe(hydroxides) in the developed passive film over carbon steel in an alkaline solution (Deus et al., 2012). These differences in passive film composition are attributed to one of the reasons for the negative shift in potential with high temperatures (Sánchez-Moreno et

al., 2009); (Abd El Haleem et al., 2010). An increased temperature has also been observed to alter the semiconductor properties of the formed passive film, which increases the passive current density (Wang et al., 2021). In addition to affecting the passive film properties, the exposure of steel rebars to higher temperatures causes a negative shift in the breakdown potential and decreases their localized corrosion resistance to chloride ions (Sharifi-Asl et al., 2015; Zha et al., 2022). However, the influence of temperature on corrosion risk does not feature a constant value and varies with the type of steel reinforcement (i.e., alloy composition). In a study comprising different stainless steels, it was observed that the low nickel duplex steels, due to their low nickel and high manganese content, exhibited higher sensitivity to temperature over austenitic steels (Gastaldi & Bertolini, 2014). This led to the pitting corrosion initiation of low nickel duplex steels at a much lower chloride content of 2.5% by mass of cement at 40˚C compared to 3% at 20˚C.

While most experimental studies involve exposure to a constant temperature, the temperature fluctuates with varying frequency and amplitude in real scenarios. A study by Feng et al. (Feng et al., 2020) observed that high frequency and high amplitude of temperature variations led to localized breakdown and cracks in the passive film due to the varying thermal expansion coefficients of steel and passive film. The temperature cycles also induce mechanical stresses at the steel-concrete interface due to the subsequent changes in the volume of oxide layers, leading to durability issues (Díaz et al., 2018). In addition to the prevailing temperature, some studies (Poursaee, 2016; Ruan et al., 2015) have observed that the previous exposure history of steel to high temperatures (such as in fire) can reduce the protectiveness of passive film formed on the steel surface when immersed in an alkaline solution. This developed passive film has also been observed to be sensitive to the use of different methods, such as air or water, to cool down the steel reinforcements, which can incur significant changes in the microstructure of steel specimens. The steel samples cooled with the use of water post-fire exposure show an

increase in the amount of martensite phase, which is primarily responsible for their poor passivation.

Some commonly occurring situations that can expose steel reinforcements to high temperatures are the different curing regimes or extreme environmental conditions. It has been observed that during concrete casting, high-temperature in rebars can increase the porosity at the steel/concrete interface (SCI), leading to lower bond strength (Pati, 2010). Subsequently, the porous SCI increases the corrosion susceptibility of the steel reinforcement in these members (Chen & Su, 2020).

However, it has been observed that the sensitivity of steel reinforcement to temperature changes decreases with an increase in the concrete resistivity (i.e., high-quality concrete) and increasing cover depth for reinforced concrete. Pour-Ghaz et al. (Pour-Ghaz et al., 2009a, 2009b) observed from experimental studies and numerical modelling that the corrosion process was controlled by the resistivity of concrete for high-quality concrete. Therefore, corrosion kinetics' dependence on such concrete's temperature was limited.

2.5 Discussion and future perspectives

Based on the review, a detailed illustration of the role of micro-climate parameters on the corrosion initiation process is provided in Figure 2.11, following equations by (Li & Song, 2022; Meira et al., 2008; Pour-Ghaz et al., 2009a).

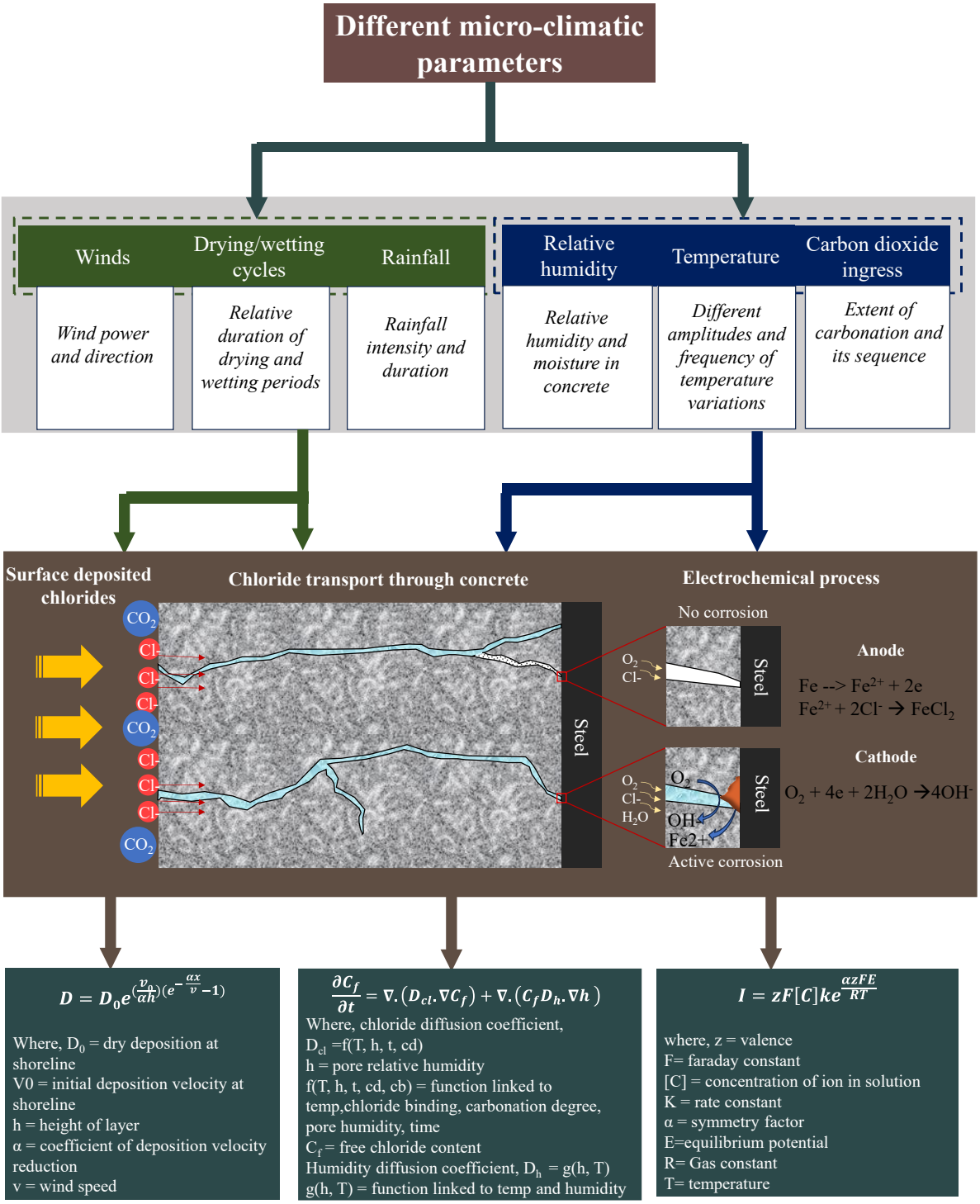

Figure 2.11. Schematic diagram showing the main micro-climate factors that affect (i) the nature and transport rate of chlorides through concrete and (ii) chloride threshold value required for steel corrosion initiation.

2.5.1 Chloride transport

Studies aimed to address micro-climates' effects have employed wet-dry cyclical exposure schemes or, in some cases, subjected them to field exposures. However, there are some main challenges associated with evaluating their effect:

i) Very limited studies have been conducted to specifically evaluate the changes in convection depth and peak chloride contents with wet/dry cycles for different concrete mixes. The role of SCMs is controversial regarding their use in concretes exposed to wet-dry cycles, considering contradictory results in the literature.

ii) There is an inconsistency in the number of wetting and drying period hours in different studies, which makes comparing different parameters difficult.

iii) The effect of rainfall and wind on chloride transport characteristics in concrete (i.e., chloride transport rate and chloride binding properties) is still relatively unexplored.

Even for the same mechanism of chloride transport through concrete, the exposure temperature changes the chloride transport rate (Al-Sodani, 2022; Yuan et al., 2008). This increase is considered to be governed by the activation energy of the concrete mix, which is obtained from diffusion experiments. There are three main concerns with the conducted studies:

i) The studies have calculated activation energy based on the chloride transport rate observed through diffusion experiments. These studies have been conducted at different concrete ages and for different chloride exposure conditions. Thus, the activation energy from different studies differs even for the same concrete mix.

ii) It is unclear how the activation energy changes when chloride transport is conducted under accelerated conditions (i.e., applied voltage).

iii) The inconsistency between the age of concrete when evaluating chloride binding ability at different temperatures among the available studies makes their

comparison difficult. There also seems to be no consensus on the mechanism behind chloride binding at different temperatures and the effect of concrete mix.

Considering the chloride transport through concrete pores, changes in pore distribution due to carbonation also affect the resultant chloride transport. The observations from the literature suggest that carbonation may have beneficial or detrimental effects on chloride transport rate based on concrete mix proportions. Over the last few decades, there has been an increasing addition of SCMs in concrete and the development of sustainable binder systems (LC3 and alkali-activated materials). Thus, it is imperative to understand how these binders perform under combined carbonation and chloride exposure. Additionally, volume change as a result of carbonation of C-(A)-S-H with different Ca/Si ranges could be conducted to consider changes in porosity.

2.5.2 Chloride threshold

In the event of carbonation, where the pH of the concrete pore solution may drop to about 9, literature studies reveal that corrosion may initiate even in the absence of chloride ions. Despite the available literature, some aspects need more investigation:

i) Studies evaluating the risk of carbonation on steel corrosion have added various dosages of carbonate and bicarbonate ions to simulated pore solutions, usually cement pore solutions or saturated $Ca(OH)_2$. It is worth mentioning that during carbonation, there are changes in the concrete pore solution with the uptake of alkali metals by carbonated hydrates (De Weerdt et al., 2019). This situation will not be reflected in the current setup, so the corrosion risk may be overestimated or underestimated. Thus, the reliability of results in simulated pore solutions should be further explored. Additionally, the correlation between simulated carbonated pore solution and the real concrete environment needs to be revealed.

ii) Available studies have only emphasized plain cement mixes. With the development of sustainable binders, which are more prone to carbonation, more studies are required to develop the necessary understanding.

Since oxygen reduction is the primary cathodic reaction, the availability of oxygen affects both the passivation in an alkaline environment and depassivation in the presence of chlorides. There are two aspects relating to oxygen availability and corrosion risk that require further investigation:

i) Once the chlorides have sufficiently ingressed the concretes, they will affect the concrete's internal humidity (pore saturation), affecting the wetness time of reinforcement and corrosion current. Thus, the changes in corrosion current due to this mechanism need further investigation.

ii) Limited studies are available to understand the corrosion risk in undersea transport tunnels where one side of the structure is exposed to seawater, and the other side is aerated. Such situations may pose the risk of macrocell corrosion.

iii) It is relatively unclear whether a combination of the reducing chemical nature of binder and dense matrix, which can reduce oxygen access to the steel surface, may restrict corrosion even in the presence of chlorides.

Very limited studies have tried to understand the effect of the corrosion risk of steel in alkaline solutions at different temperatures and the underlying mechanism, especially the effect on passivation and depassivation mechanism. With the development of different strength grades and alloy composition of steel, their corrosion susceptibility at different temperatures remains to be investigated.

Distinct microclimates within structural elements establish electrochemical potential differences between adjacent steel regions, driving macrocell corrosion currents. As mentioned

in previous sections, the severity of such corrosion depends on three key factors: (1) the chemical composition of the concrete (e.g., chloride content, pH), (2) the moisture content governing electrolytic conductivity, and (3) the cathode-to-anode (C/A) area ratio, which amplifies localized corrosion rates. Understanding this multi-faceted phenomenon—governed by coupled electrochemical, environmental, and material interactions—is essential for designing structures in harsh environments (e.g., marine, industrial).

Conventional durability design standards, including ACI, EN, GB, and AS, categorize marine exposure environments into distinct severity classifications such as fully submerged, tidal/splash, and airborne chloride conditions without addressing site-specific environmental variability (Hooton, 2019). The FIB Model Code 2010 introduces a progressive shift by adopting probabilistic modeling to accommodate data variability and forecast the probability of steel depassivation at defined chloride thresholds. While existing probabilistic frameworks acknowledge uncertainties in micro-climatic parameters (e.g., temperature gradients, CO_2 diffusion), their treatment of interactions between these factors and corrosion kinetics remains overly simplistic (Bastidas-Arteaga et al., 2010; Stewart et al., 2011). By establishing improved relationships between micro-climate parameters and electro-physical-chemical aspects of the corrosion process, these insights can be incorporated into service life models to refine stochastic variables and multi-physics coupling, thereby improving their accuracy. The prediction models can be further enhanced when combined with climate projections, which capture daily and seasonal variations and uncertainties associated with future climate in a location (Guo et al., 2020) Successfully incorporating these understandings would advance probability-based durability standards and ultimately enable the development of climate-resilient infrastructure in the long run.

2.6 Overall Summary

Based on the literature review, the following conclusions are drawn:

(a) The convection depth is formed in the top 15 mm layer of concrete due to rapid changes in pore moisture content brought by atmospheric humidity, rainfall, wetting and drying cycles of salt water. The convection depth and peak chloride content seem to be directly linked to the w/b ratio of the mixes due to the presence of larger pores. However, the concrete mix composition has limited effect. The convection depth increases with a greater drying/wetting period and an increasing exposure period, resulting in increased chloride contents in concrete interiors.

(b) The moisture state of concrete by micro-climatic factors influences the electrochemical reactions by changing the electrolyte and cathodic polarization resistance. When the concrete's moisture content increases from its original dry state during the wetting cycle, the reduced electrolyte resistance leads to increased corrosion current. However, with the prolonged wetting stage, the oxygen availability at the steel surface decreases, thereby reducing the corrosion current. When the concrete is dry, the corrosion current is controlled by electrolyte resistance for high-resistivity concrete and combined electrolytic and cathodic polarisation resistance for low-resistivity concrete.

(c) For the carbonated layer of concrete, the rate of chloride transport is changed considerably by pore redistribution and microcracking. The carbonation leads to a net reduction of porosity and chloride transport rate for OPC concrete with a low w/b ratio. For high w/b ratio and concretes with silica-rich SCMs (leading to low Ca/Si ratio based C-(A)-S-H gels), the carbonation causes the coarsening of pores and reduces the time for chlorides to reach the steel surface. The carbonation front progression into deeper chloride-

contaminated concrete layers leads to the release of bound chlorides, increasing free chloride amounts in the inner concrete layers.

(d) In addition to releasing the bound chlorides, the progress of the carbonation front near the steel surface in chloride-contaminated concrete reduces the pore solution pH, which sharply increases [Cl]/[OH] at the steel surface. As a result, the corrosion initiation time is shortened significantly. Only in those cases where the release of bound chlorides due to carbonation is compensated by reduced chloride transport rate could a net increase in corrosion initiation time be observed.

(e) The surrounding temperature directly impacts ionic mobility and the bound chloride contents, ultimately influencing the chloride distribution inside the concrete. The increased chloride transport rate can be explained by activation energy, which reduces with increasing SCM content in the concrete mix. The bound chloride contents do not show a definitive trend but vary significantly with exposed temperature.

(f) Increased temperature leads to a porous and defective passive film on steel, which reduces the chloride threshold for corrosion initiation. One reason for the localised defects is the different thermal coefficients of expansion for steel and passive film. Increasing temperature also leads to a negative shift in breakdown potential, which raises the localized corrosion risk.

(g) Considering the significant role of micro-climates, a more realistic assessment of chloride-induced corrosion initiation time should include chloride transport rate and threshold values modified by seasonal and daily temperature trends, humidity for the atmospheric zone and accurate wetting and drying periods of structural members for tidal and splash exposure zones. The effect of carbonation should account for the chemistry of the binder such that the net impact on the chloride transport rate is accurately considered. These steps will

ensure that the structure meets its design service periods without requiring extensive maintenance.

(h) It is suggested that design engineers should improve their understanding of the influence of micro-climate factors on chloride-induced corrosion. This would enable them to choose the appropriate environmental loads when designing coastal RC structures, leading to efficient resource allocation.

CHAPTER 3

STEEL CORROSION BEHAVIOUR IN SIMULATED CONCRETE ENVIRONMENT

3.1 Introduction

Despite decades of research, challenges arise due to the complex relationships between the different variables that influence the corrosion process (Das, Zheng, et al., 2025). As reviewed in Chapter 2, corrosion is affected by the physical properties of steel reinforcement embedded in concrete and the reaction chemistry. An important parameter that affects chloride-induced corrosion is the chloride threshold value (CTV), which initiates corrosion (Angst et al., 2009). Previous works have demonstrated that this CTV significantly varies with the steel composition (Cai et al., 2021; Gastaldi & Bertolini, 2014), the surface condition of the steel rebar (Kamde & Pillai, 2020; Mohammed & Hamada, 2006), and the steel-concrete interface (SCI) (Angst et al., 2019). The CTV has also been observed to vary with the changes in oxygen availability and pore solution composition brought about by concretes prepared with different water/binder ratios, strengths and supplementary cementitious material (SCM) additions (Hussain & Ishida, 2010; Mundra et al., 2017; Zheng, Poon, et al., 2020).

Most existing corrosion studies have focused on improving the CTV by changing the steel type and improving the surrounding concrete properties. However, relatively little research has been directed to understand how the different climatic factors (e.g., the temperature) affect the CTV in reinforced concrete, with most laboratory tests being conducted at standard temperature and humidity. This is significantly different from the situations in practice where the reinforced concrete (RC) structure is exposed to different climatic conditions during its service period. It is expected that with the looming risk of climate change and global warming, there will be a

greater exposure of different structures to high temperatures and frequent temperature fluctuations (Masson-Delmotte et al., 2018). Therefore, understanding the impact of temperature on steel corrosion susceptibility is of greater significance now.

From a chemical perspective, the corrosion reaction rate is greatly influenced by temperature, according to the Arrhenius equation. The temperature also changes the equilibrium potential of both anodic and cathodic processes, leading to significant changes in corrosion risk (Pour-Ghaz et al., 2009a; Wang et al., 2022). This influence on corrosion reaction rate is apparent in industrial boilers or gas and oil pipelines, which showed an increased corrosion-induced steel degradation when subjected to high temperatures (Nazari et al., 2010; Popova, 2007; Uusitalo et al., 2003). However, the fundamental aspect of steel corrosion in industrial systems is very different from that of reinforced concrete. The steel in reinforced concrete undergoes two chemical processes: the formation of oxide film (i.e., passivation) and passive film breakdown (i.e., depassivation). The protective oxide film is formed due to the alkaline nature of the concrete pore solution, and its protectiveness varies significantly with the pore solution composition (Zheng, Dai, et al., 2020a; Zheng, Dai, Poon, et al., 2018; Zheng, Poon, et al., 2020). The exposed temperature significantly affects the concentration of individual ions in the pore solution and the nature of hydration products (Hussain, 1993; Lothenbach et al., 2007). A high-temperature environment also results in a less protective passive film on the stainless steel surface (Deus et al., 2012; Feng et al., 2020) and increases the corrosion current density during the passivation period (Liu et al., 2021). In addition, the high-temperature environment has been observed to alter the already formed passive films on stainless steel by forming microscopic cracks and local breakdown points, even in the absence of chlorides (Feng et al., 2020).

The existing literature suggests that the exposed temperature significantly affects the chemical environment, electrochemical properties, and the transport of ions, which collectively

determine the service life of a structure. However, there is a lack of systematic investigation on the passivation process and the progressive changes in corrosion susceptibility with increasing temperatures. A previous study focusing on the characterization of passive film formed at different temperatures was conducted after less than one day of exposure, in the range of 1-2 hours (Deus et al., 2012). This is not representative of the actual passivation process, which usually requires several days for the development of a stable passive film (Poursaee & Hansson, 2007). Considering the nanosized thickness of the passive film, any changes in its properties arising from increased temperature can have significant implications on its protectiveness against chloride ions. This requires an in-depth investigation into the growth and nature of passive film during the exposure period.

The current study aims to experimentally investigate the corrosion performance of low-carbon steel when exposed to different temperatures (25 ˚C, 35 ˚C and 45 ˚C, commonly representing the summer daytime temperatures in Sydney, Hong Kong, and Dubai, respectively). Specifically, the study emphasizes the evolution of passive film characteristics, which is developed on steel surfaces during its exposure to alkaline solution and the effect on CTV due to the different exposed temperatures. This was achieved by employing electrochemical techniques such as cyclic voltammetry (CV), electrochemical impedance spectroscopy (EIS), open circuit potential (OCP), Mott-Schottky and surface characterization techniques such as x-ray photoelectron spectroscopy (XPS) and atomic force microscopy (AFM).

3.2 Experimental Program

3.2.1 Material preparation and exposure scheme

In this study, a ribbed steel bar (500B as per BS 4449:2005) with a diameter of 10 mm was employed. The detailed chemical composition of the steel bar is: (C: 0.20, Mn: 1.16, P:0.012, Si:0.593, Cr:0.037, Ni:0.032, Cu:0.047, Mo:0.003, S:0.004). For the electrochemical tests, the

steel rebar of the original length 6 m was sliced into 2-4 mm thick sections. These samples were soldered with wire on one side and then impregnated with epoxy. The opposite cross-sectional side of the steel rebar was then progressively ground by SiC abrasive papers from Grit size 180 to 1200. This was followed by polishing using different polishing agents (9μm, 3 μm and 0.05 μm) to get a smooth mirror-like surface. This was carried out to obtain a homogeneous surface on all steel surfaces. In the end, the edges of the steel section were sealed with epoxy to prevent any crevice corrosion, leaving an exposed area of 1 cm2 for electrochemical experiments. Finally, the samples were degreased with ethyl alcohol and distilled water before starting the tests.

The exposure scheme consisted of immersion of steel samples in saturated Ca(OH)2 solution, which was maintained in equilibrium at different temperatures (25 ˚C, 35 ˚C and 45 ˚C). The temperatures representing three climatic conditions were controlled through a thermostatic water bath. After 14 days of exposing steel rebars to saturated Ca(OH)2 solution, 0.2 M (moles/litre) of NaCl was added every 12 hours to the solution to monitor the interaction between chloride ions and the steel surface. De-ionized water and analytical-grade chemicals were used throughout the experiments.

3.2.2 Electrochemical measurements

All the electrochemical measurements were conducted using Metrohm Autolab Workstation PGSTAT302N. Five steel samples were prepared for each exposure scheme. The electrochemical setup was a three-electrode system consisting of a platinum plate (4 cm^2) as the counter electrode (CE), carbon steel as the working electrode (WE) and solid Ag/AgCl as the reference electrode (RE), as shown in Figure 3.1. Thus, all the subsequent potentials in this chapter are mentioned with reference to the Ag/AgCl electrode.

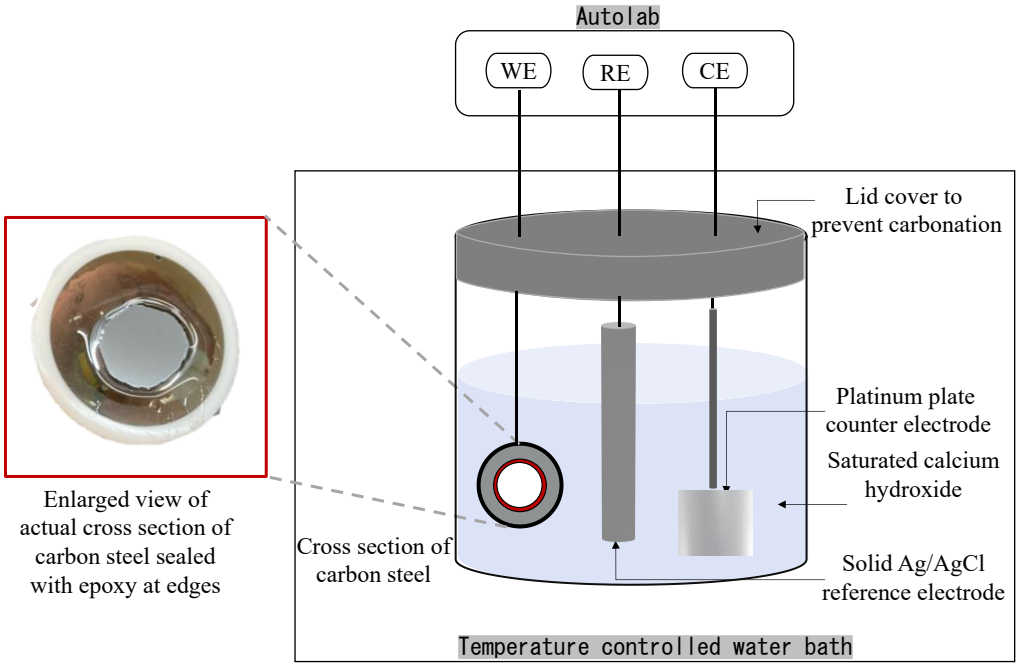

Figure 3.1. Test setup for electrochemical measurements at different temperatures.

Various electrochemical measurements were conducted during the exposure period to monitor the evolution of passivation and depassivation characteristics. Electrochemical impedance spectroscopy (EIS) and open circuit potential (OCP) were measured periodically to study the evolution of passivation and depassivation behavior. During the first day of immersion in an alkaline solution, the OCP of the steel specimen was recorded at 1, 3, 5, 7, 9, 12, and 24 hours. Subsequent OCP measurements were taken on the 3rd, 7th, and 14th days of passivation to evaluate corrosion risk over varying durations. Further, once chlorides were gradually introduced to the alkaline solution, OCP measurements were further taken periodically after every 0.2 M of chloride addition. Before each OCP measurement, the potential was allowed to stabilize sufficiently, such that the rate of potential change (dV/dt) was below 10^{-6} V/s.

The EIS was performed after 12 hours, 7 days, and 14 days of immersion in chloride-free alkaline solution to examine the growth and protective properties of the passive film. The EIS test was conducted using an excitation AC voltage of 10 mV at the OCP over a frequency range from 100kHz to 0.01Hz (Das et al., 2023; Mi, Yang, et al., 2023; Zheng et al., 2022). Ten points

per decade were recorded over the frequency range. Once chlorides were progressively added to the alkaline solution, EIS was further measured after every 0.4 M of chloride addition.

The steel passivation consists of a complex multi-step oxidation process from Fe metal to different Fe oxides (Joiret et al., 2002; Sánchez-Moreno et al., 2009). While EIS is capable of assessing the protective quality of passive films, it does not directly identify the predominant redox reactions on the steel surface at specific exposure times. In such cases, cyclic voltammetry (CV) can complement EIS by elucidating chemical alterations in the passive film within alkaline environments (Guzman et al., 1979). Thus, the CV test was also performed on one steel sample for every temperature exposure at 12 hours of immersion to correlate EIS findings with the surface redox mechanism. The test involved five consecutive cycles, sweeping from an initial potential of −1.5 V to a positive limit of 0.65V (measured with reference to the Ag/AgCl solid electrode), after which the scanning direction was reversed (Mundra et al., 2017). The five cyclical scans were intended to understand the changes in redox reactions with the continuous growth of the passive film, following previous studies (Yao et al., 2022). Following some trials, the scan rate was fixed at 50 mV/s to find a balance between the peak intensities and the number of visible peaks (M. Liu et al., 2017; Yao et al., 2022).

At the end of the passivation study (i.e., at 14 days of immersion in saturated $Ca(OH)_2$ solution), the semiconductor properties of the passive film were evaluated using Mott-Schottky analysis for the samples at each temperature. The frequency was fixed at 1kHz, and the potential varied from -1 V to 0.6 V measured vs. Ag/AgCl to obtain the capacitance-potential relationship for a perturbing AC signal of 10 mV (Cai et al., 2021). During the measurement, the stepping potential was 50 mV.

3.2.3 Composition and morphology of passive film

The composition of the developed passive film at different depths was investigated using X-ray photoelectron spectroscopy (XPS) after 14 days of immersion in an alkaline solution. The X-ray source consisted of a monochromatic Aluminium Kα beam with a beam spot size of 400 μm and an accelerating voltage of 12 kV. High-resolution scans (Fe 2p and O 1s) were conducted to compare the proportion of different iron oxides and hydroxides at different depths of 0, 1, 2, 3, and 5 nm from the surface of the passive film developed on steel exposed to different temperatures (Cai et al., 2021; Zheng, Poon, et al., 2020). These scans were performed by ion sputtering using an Argon gun at 4 keV with 140μA current over a 2 x 2 mm area. Subsequently, the peaks were analyzed using XPS Peak 41.

The surface morphology of the developed passive film was observed using atomic force microscopy (AFM) after 14 days of immersion in the alkaline solutions. AFM measurements were conducted under tapping mode on an area of 500 nm X 500 nm, and the results were analyzed using NanoScope Analysis Software (Zhou et al., 2022).

3.3 Results

3.3.1 Electrochemical analyses of passivation behaviour

Cyclic voltammetry (CV)

The E/I plots for the 5 cycles of cyclic voltammetric (CV) experiment of the steel samples in alkaline solutions measured at 12 hours of immersion are presented in Figure 3.2 (a-c). Figure 3.2 (d) presents the combined CV plots of samples obtained in the 5^{th} cycle of measurement for comparison. The main aim was to understand the predominant reactions occurring on the steel surface and the products formed at an early age, and in the presence of the passive film.

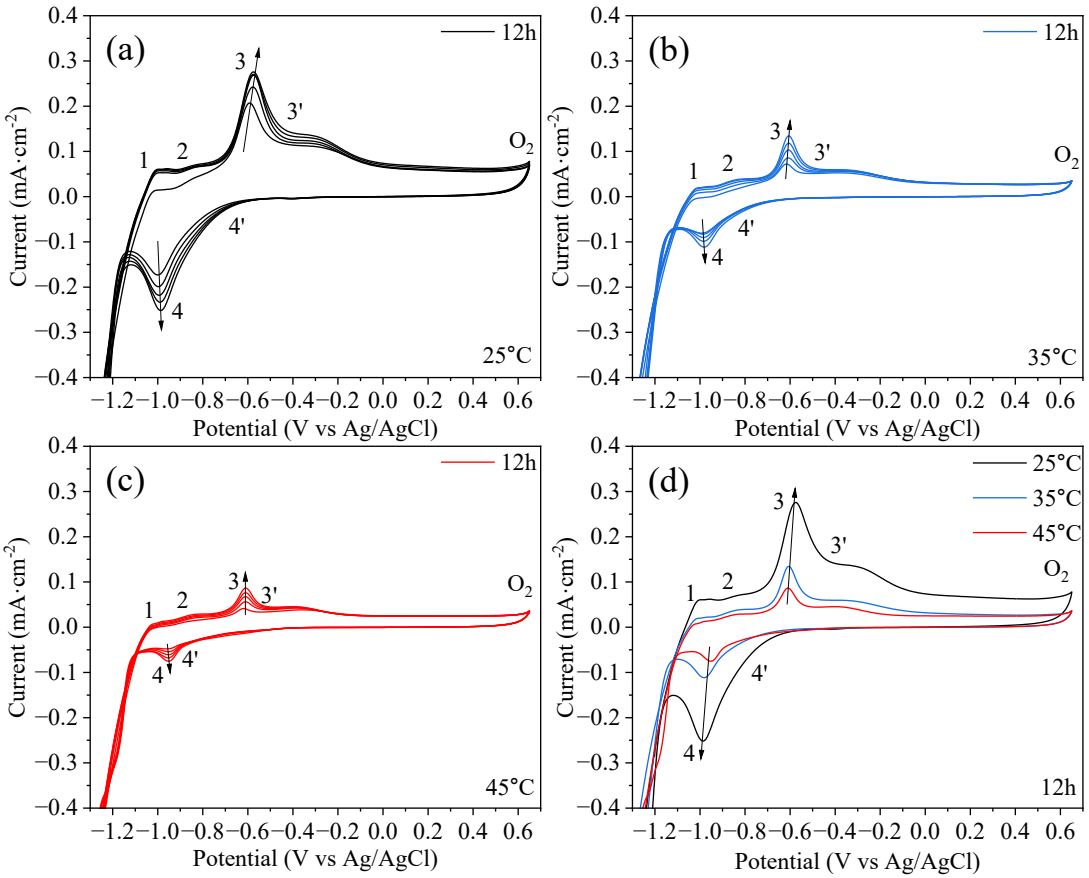

Figure 3.2. Current vs. Potential curves from cyclic voltammetry tests at (a) 25 ˚C, (b) 35 ˚C, (c) 45 ˚C and (d) comparison of plots on the 5th scan.

A closer look at the figures denotes the existence of 6 peaks in each CV scan, representing the various redox reactions occurring on the steel surface. It was observed that the intensity of these peaks increased with each successive cycle and decreased with an increase in exposure temperatures. Four anodic peaks were observed in the forward scan with different intensities, followed by oxygen evolution at about 0.65V. The first anodic peak (Peak 1) was observed at about -1.05V, followed by a second peak (Peak 2) at about -0.85V. These peaks have been well-known previously to be contributed by the electro-oxidation of Fe (metal) to $Fe(OH)_2$/ Fe(II) oxides (Guzman et al., 1979; Joiret et al., 2002). On a slight increase in potential, the third peak (Peak 3) appeared at about 0.7V with the highest current intensity and a somewhat asymmetric feature that included a broader shoulder on the positive potential side, denoting the fourth

anodic peak (Peak 3'). Peaks 3 and 3' are generally assumed to be related to the oxidation of $Fe(OH)_2$ to Fe_3O_4 /Fe(III) (Guzman et al., 1979; Zhou et al., 2022). In the backward scan, two cathodic peaks (Peak 4 and Peak 4') were distinctly observed at about -0.75V with a characteristic feature similar to the Peak 3 and 3' couple. These two peaks were related to the reduction of formed Fe_3O_4.

Comparing the peaks at different temperatures helps to identify the difference in passivation abilities at different temperatures. One clear trend observed was an increase in current intensity at all peaks with a decrease in exposure temperature. This demonstrated increased currents due to redox reactions at the metal surface and denoted a higher oxidation tendency of iron (i.e., formation of high oxide contents) with decreasing temperature. This suggests that more oxides may be formed in steel exposed to alkaline environments at low temperatures. Another feature that is more distinctive in Figure 3.2 (d) is the location of peaks for different temperatures. With a decrease in temperature, there was a clear positive shift in the potential corresponding to peak current density in the forward scan and a negative shift in the backward scan. This potential shift represents the overpotential required for redox reactions, indicating the higher protection ability of the passive film, which limits the charge transfer process (Volpi et al., 2015).

The effect of multiple scanning, representing the changes in redox reactions on a steel surface with the development of passive film, differed for the six analyzed peaks while exposed to varying temperatures. This suggests that the exposure temperature affected redox reaction processes differently in the presence of the passive film. For peaks 1 and 2, which denote oxidation of the metallic iron to Fe(II) oxides, the peaks varied significantly from the first to the second scan and stabilized later at 25 ˚C. On increasing the temperature to 35 ˚C, the increase in peak current intensity was only marginal, while there were no observable changes in the sample at 45 ˚C. However, the effect of successive scans was reversed for peak 3 at the three exposure temperatures. At 25 ˚C, the net current intensity increased from about 0.206

mA·cm-2 to 0.276 mA·cm^{-2}, about a 33% increase. For the sample at 35 ˚C, the current intensity increased from 0.07 mA·cm^{-2} to 0.132 mA·cm^{-2}, an increase of about 88%. In addition, the increase for the sample at 45 ˚C was about 110% from 0.041 mA·cm^{-2} to 0.086 mA·cm^{-2}. Thus, comparing the results from successive scans, it is evident that at high temperatures (e.g., 45 ˚C), most of the Fe metal is completely oxidized to Fe(II) at a much earlier age. During prolonged exposure, these Fe(II) oxides only tend to oxidize to Fe(III), thus modifying the developed passive film. On the contrary, the samples exposed to low temperatures (e.g., 25 ˚C) undergo two processes for a longer time, i.e., oxidation of Fe metal to Fe(II) oxide and also the oxidation of Fe(II) to Fe(III). Thus, there is a combined growth/development of passive film and its structural modification.

One primary implication of this result is that for the passive film formed at higher temperatures, a longer exposure period will promote higher oxidation of magnetite to Fe(III) such that Fe(III)/Fe(II) will increase. This may influence the corrosion potentials, which will be reported later. It also suggests that the rate constant for the oxidation of Fe metal to Fe(II) is increased more than that of oxidation of Fe(II) to Fe(III) with an increase in temperature, i.e., if the relationship is expressed in Arrhenius type equation, the activation energy of the former process should be higher.

Electrochemical impedance spectroscopy (EIS)

The EIS response of the steel samples in chloride-free saturated $Ca(OH)_2$ solutions maintained at different temperatures is presented through Nyquist and Bode plots in Figure 3.3. It can be observed that there is a progressive increase in the capacitative arc radius of the Nyquist plot with exposure time in the solution. This is also accompanied by an increase in the phase angle at the low-frequency region of Bode's plot. The features were most prominent in samples at 25

˚C and least apparent in samples at 45 ˚C, demonstrating the significant effect of exposure temperatures on electrochemical properties.

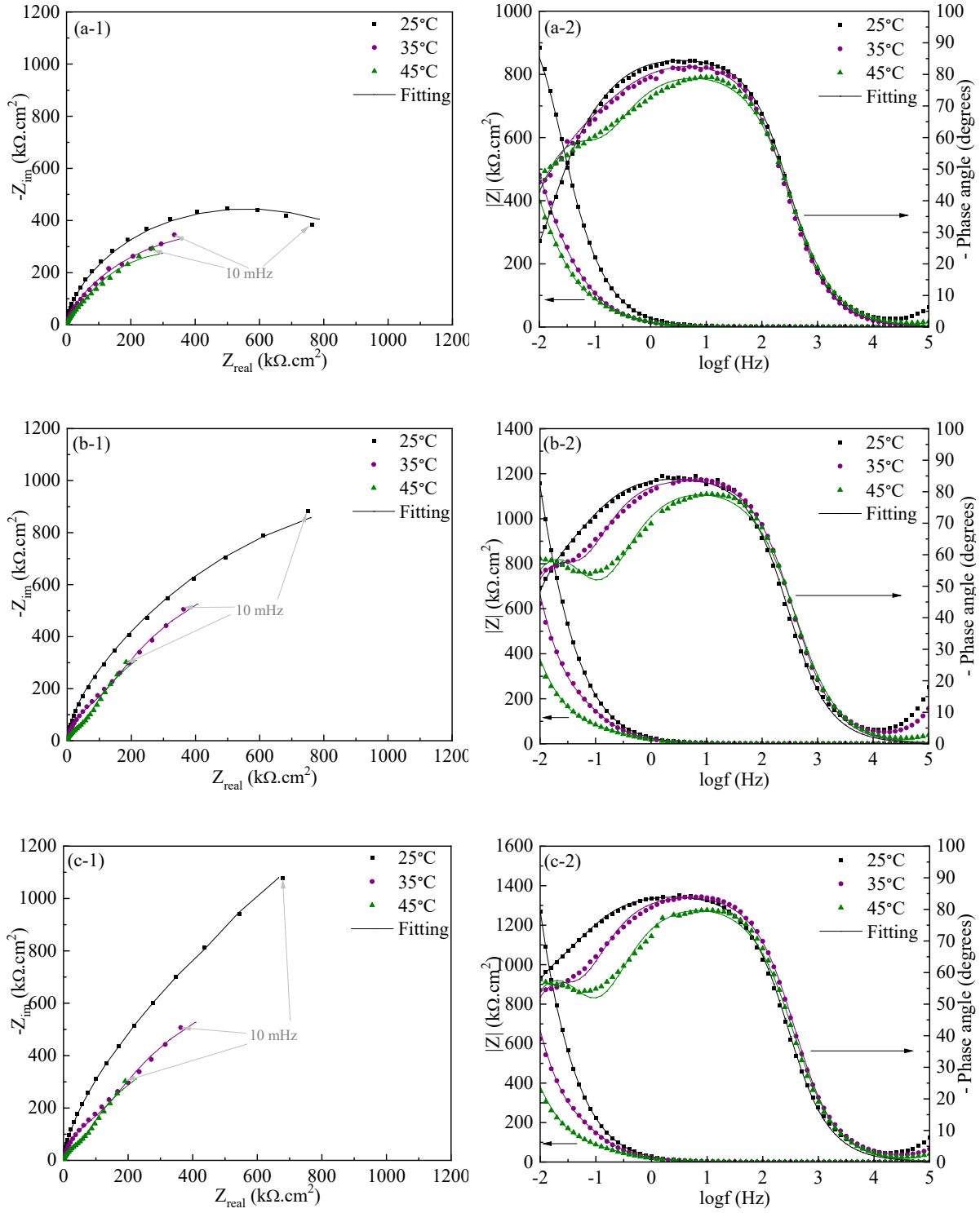

Figure 3.3. EIS response of steel at (a) 12 hours, (b) 7 days and (c) 14 days expressed in terms of (1) Nyquist plot and (2) Bode plot.

Different electrical equivalent circuits were tried to improve the understanding of the effect of elevated temperatures on EIS response. The circuits were selected based on the physical interpretation of different corrosion cell components and previous studies (M. Liu et al., 2017; Zheng, Poon, et al., 2020). Finally, an equivalent circuit with two hierarchical parallel RC loops, as shown in Figure 3.4, was adopted to fit the EIS data. The two-time constants consider the influences of exposed $Ca(OH)_2$ solution, passive film properties and steel-to-solution interface. A constant phase element (CPE) was used instead of an ideal capacitance in different RC time constants. This aimed to consider the deviation from ideal capacitance properties arising due to surface inhomogeneities.

CPE is generally defined as:

$CPE = Y_0 (jw)^n$ where n is a value between 0 and 1, Y_0 is the magnitude, j is the imaginary root, and w is the angular frequency.

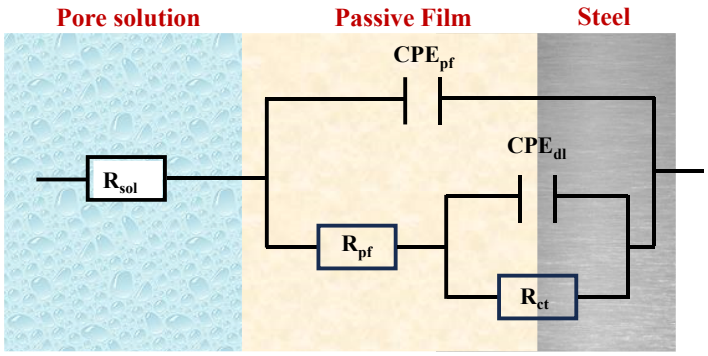

Figure 3.4. Equivalent electrical circuit (EEC) for the proposed study.

In the adopted equivalent circuit, the high-frequency RC constant corresponds to the passive film properties (i.e., passive film resistance, R_{pf} and passive film capacitance, CPE_{pf}), and the low-frequency time constant corresponds to the processes at the steel-solution interface (charge transfer resistance, R_{ct} and faradaic pseudo double layer capacitance, CPE_{dl}). Rsol denotes the resistance of the simulated pore solution at different temperatures.

The variation of resistances and capacitances is shown in Figure 3.5. It can be observed that there was a progressive increase in different resistances (R_{ct} and R_{pf}) with exposure time. This indicated the growth and formation of a stable passive film in an alkaline solution, which offered better resistance against electrochemical processes at the steel surface. However, the increase was not linear over the exposure period and temperatures. For example, the samples at 25 ˚C showed a continuous increase in both R_{ct} (1565 kΩ·cm^2 to 3750 kΩ·cm^2) and R_{pf} (812 kΩ·cm^2 to 1053 kΩ·cm^2) between 7 and 14 days of exposure. By contrast, the samples at 45 ˚C showed a minimal increase of R_{ct} (1048 kΩ·cm^2 to 1052 kΩ·cm^2) and R_{pf} (50.5 kΩ·cm^2 to 57.5 kΩ·cm^2) at an exposure period beyond 7 days. This suggests that the passive film was fully developed at an early age when immersed in the alkaline solution at 45 ˚C, supporting the observations from cyclic voltammetry. However, faster passive film growth did not necessarily mean enhanced protectiveness. This was evident in R_{pf} for 25 ˚C (1053 kΩ·cm^2), which was 7 times and 20 times higher than that for 35 ˚C (144 kΩ·cm^2) and 45 ˚C (57.5 kΩ·cm^2), respectively, at 14 days. The implications of exposure temperature were observed in the solution resistance (Rsol), which decreased with an increase in temperature. For example, the solution resistance for the alkaline solution at 45 ˚C was 82 Ω·cm^2, which increased to 98 Ω·cm2 and 117 Ω·cm^2 at 35 ˚C and 25 ˚C, respectively. As is generally well known, this could be attributed to the increased ionic mobility at elevated temperatures, which contributed to low resistance values.

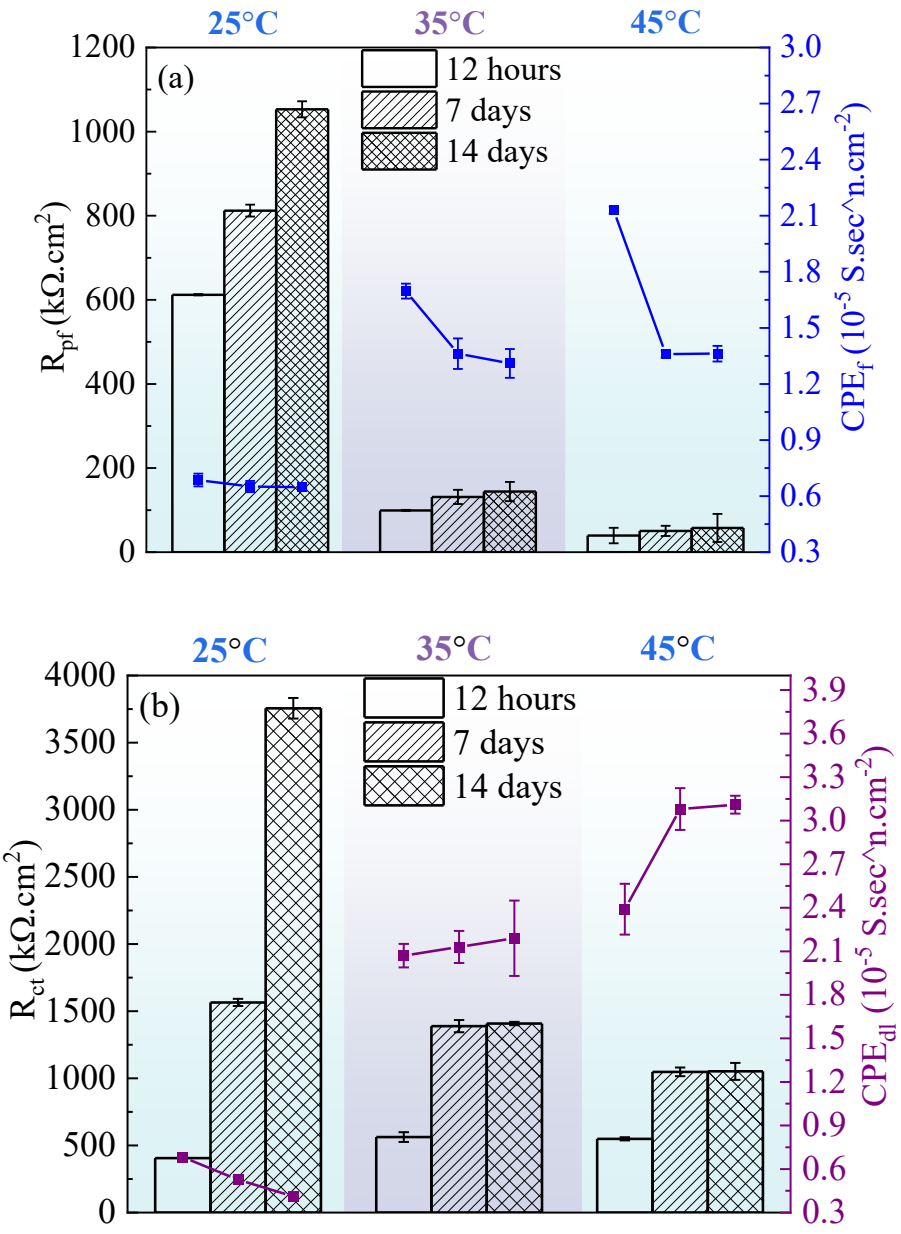

Figure 3.5. Variation of steel (a) passive film resistance and capacitance, and (b) charge transfer resistance and double layer capacitance with immersion time at different temperatures.

The effect of temperature was also evident in the capacitance values. At all exposure days, the lowest capacitance values were observed for samples immersed at 25 ˚C. A lower passive film capacitance (CPE_{pf}) and double layer capacitance (CPE_{dl}) represent the development of fewer defective layers at steel-passive film-solution interfaces. Comparing the evolution of CPE_{pf}

with time, it can be observed that there was a progressive decrease in its value, which reflects the increasing protectiveness of passive film with ageing. CPE_{dl} is generally formed due to the adsorbed layer of ions and water molecules on steel surfaces. On a closer look at the evolution of CPEdl for different samples, an opposite trend can be observed in different samples. For the sample at 25 ˚C, CPE_{dl} decreased with exposure time, but for higher temperatures (i.e., 35 ˚C and 45 ˚C), there was an increasing trend. This increasing trend of CPE_{dl} contrasts with most studies on passivation (Z. Jin et al., 2022; Zheng, Poon, et al., 2020). However, it is worth mentioning that these previous studies did not consider the influence of temperature (as an external factor) on passivation. One possible reason for this behavior could be derived from a decrease in adsorbed ions, arising from either the higher kinetic energy of ions at high temperatures or a higher dissolution rate. However, an in-depth study may be necessary to accurately explain the continuous evolution of steel surface features.

Open circuit potential (OCP)

The variation of open circuit potential (OCP) of steel samples with exposure time for steel samples immersed in an alkaline solution of different temperatures is provided in Figure 3.6. It can be observed that the samples at 45 ˚C showed the most negative potential in the initial period of immersion (< 3 hours), which was similar to the observations by Deus et al. (Deus et al., 2012) in stainless steel and Haleem et al. (Abd El Haleem et al., 2013). They proposed that the initial low potential observed in steel exposed to elevated temperatures was linked to the reduced dissolved oxygen concentration in alkaline solutions. While their experiments were not continued beyond 5000 s (80 min), they also observed the potential to become nobler as the immersion period of steel was extended, similar to what was observed in this study beyond three hours. Thus, the hypothesis that only oxygen availability influences the steel potential may not be accurate for prolonged immersions. Instead, this could also be related to the different Fe(II) and Fe(III) proportions formed in the passive film as evaluated from cyclic

voltammetry. Some previous literature studies have also reported that the steel potential varies with the nature and composition of the passive oxide film formed on the surface (Abd El Haleem et al., 2010; Alonso et al., 1998; Díaz et al., 2018; Sánchez-Moreno et al., 2009). A higher Fe(III)/Fe(II) ratio could shift the potentials to more positive values through the oxidation of magnetite to form Fe_2O_3 (Andrade et al., 2001; Sánchez et al., 2007). Thus, the oxidation of Fe(II) to Fe(III) (i.e., increasing the Fe(III)/Fe(II) ratio) during the ageing of passive film formed at 45 ˚C leads to a positive shift in potential values. Therefore, to quantify the Fe(III)/Fe(II) ratio, the nature of the passive films formed at different temperatures has been investigated in the latter section of the paper using XPS.

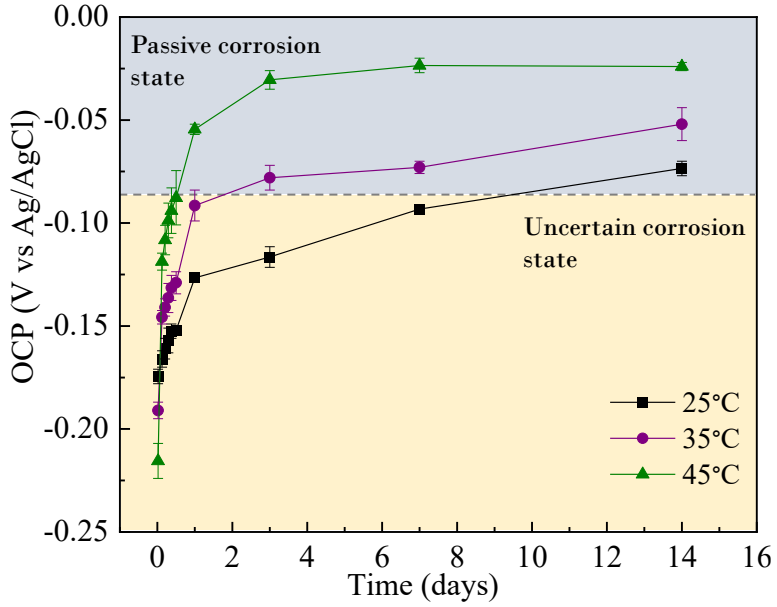

Figure 3.6. Evolution of open circuit potential (OCP) of steel at different temperatures.

Mott Schottky analysis (M-S)

The M-S analysis represents a plot of the inverse of the square of overall capacitance against applied potential and is useful for understanding the semiconductor properties of oxide film (either p or n-type) formed on the steel surface. Additionally, it helps to identify the donor density, N_D, of the developed passive film. Previous studies have observed an *n*-type passive

film on iron-based alloys. The relationship between capacitance (C) and the applied potential (E) can be represented using Eqs. 1 and 2 (Sánchez et al., 2006).

$$\frac{1}{C^2} = \frac{1}{C_H^2} + \frac{1}{C_{sc}^2} \tag{3.1}$$

$$\frac{1}{C_{sc}^2} = \pm\frac{2}{\epsilon\epsilon_0\, eN_D}\left(E - E_{FB} - \frac{kT}{e}\right) \tag{3.2}$$

$$N_D = \pm\frac{2}{\epsilon\epsilon_0\, eS} \tag{3.3}$$

Where the sign is negative for *p*-type semiconductors and positive for *n*-type semiconductors, C_{sc} represents space charge capacitance, C_H represents Helmholtz double-layer capacitance, e is the charge of one electron (1.602e-19 C), E_{FB} is the flat band potential, ε is the relative dielectric constant of iron oxides (12), and ε_0 is the permittivity of vacuum (8.85e-12). Considering the magnitude of C_H to be 2 to 3 orders of magnitude higher than C_{sc}, Eq 1, 2 and 3 can be combined as follows:

$$\frac{1}{C^2} = \pm\frac{2}{\epsilon\epsilon_0 eN_A}\left(E - E_{FB} - \frac{kT}{e}\right) \tag{3.4}$$

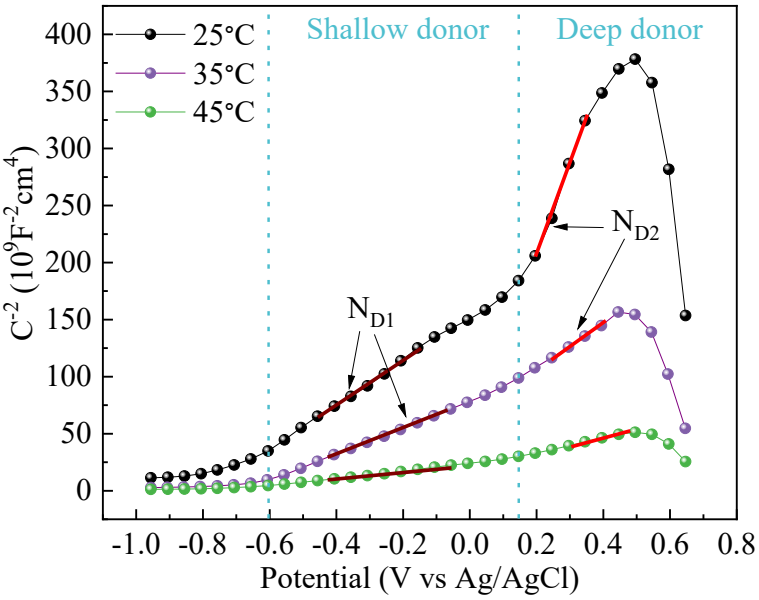

Figure 3.7. Mott Schottky curves of steel after 14 days of passivation at different temperatures.

The M-S plot for samples in alkaline solutions at different temperatures after 14 days of immersion is presented in Figure 3.7. The steel samples all showed *n*-type semiconductor properties (positive slopes), aligning with previous studies (Cai et al., 2021; M. Liu et al., 2017). The M-S plot can be divided into two linear sections representing two different donor levels: shallow (N_{D1}) and deep (N_{D2}). The shallow donor level corresponds to the inner Fe(II) layer, and the deep donor density corresponds to the outer Fe(III) layer, which may be in the form of oxides and hydroxides (Cai et al., 2021; Gadala & Alfantazi, 2015). Table 3.1 presents the shallow and deep donor densities observed for samples exposed to alkaline solutions at different temperatures. It can be observed that both the defect densities showed an increasing trend with the increase in exposure temperature. A higher donor density represents a higher concentration of local defects on the passive film and low resistance, which may result in inferior protective ability (Sánchez et al., 2007). A comparison of the donor densities of the samples further confirms the EIS results that although higher temperatures increased the formation rate of the passive film, the developed film has a higher concentration of flaws on the surface. Thus, the resistance of the passive film was significantly lower.

Table 3.1. Calculated donor densities (N_D) of steel at different exposure temperatures.

	25 °C	**35 °C**	**45 °C**
N_{D1}	5.94E19	1.02E20	3.387E20
N_{D2}	1.44E19	6.38E19	1.936E20

3.3.2 Passive film composition

The observations from potential measurements of the steel sample and the Mott Schottky analysis suggest that exposure temperature also modifies the composition of the developed passive film. Hence, this requires applying additional techniques to understand the composition of passive film at a nanoscale. Therefore, XPS was used as a tool to investigate the variation of Fe^{2+} and Fe^{3+} at varying depths of the passive film formed after 14 days of immersion in the alkaline solution. Figure 3.8 presents the high-resolution spectrum of Fe $2p_{3/2}$ obtained at different depths of the passive film formed on the steel samples after 14 days of immersion in alkaline solutions at different temperatures. Additionally, the Fe $2p_{3/2}$ XPS spectra was fitted using five peaks representing Fe metal (Fe-1), Fe_3C (Fe-2), Fe_3O_4/FeO (Fe-3), Fe_2O_3/FeOOH (Fe-4) and Fe_2O_3-satellite (Fe-5) as suggested by Ghods et al. (Ghods et al., 2011).

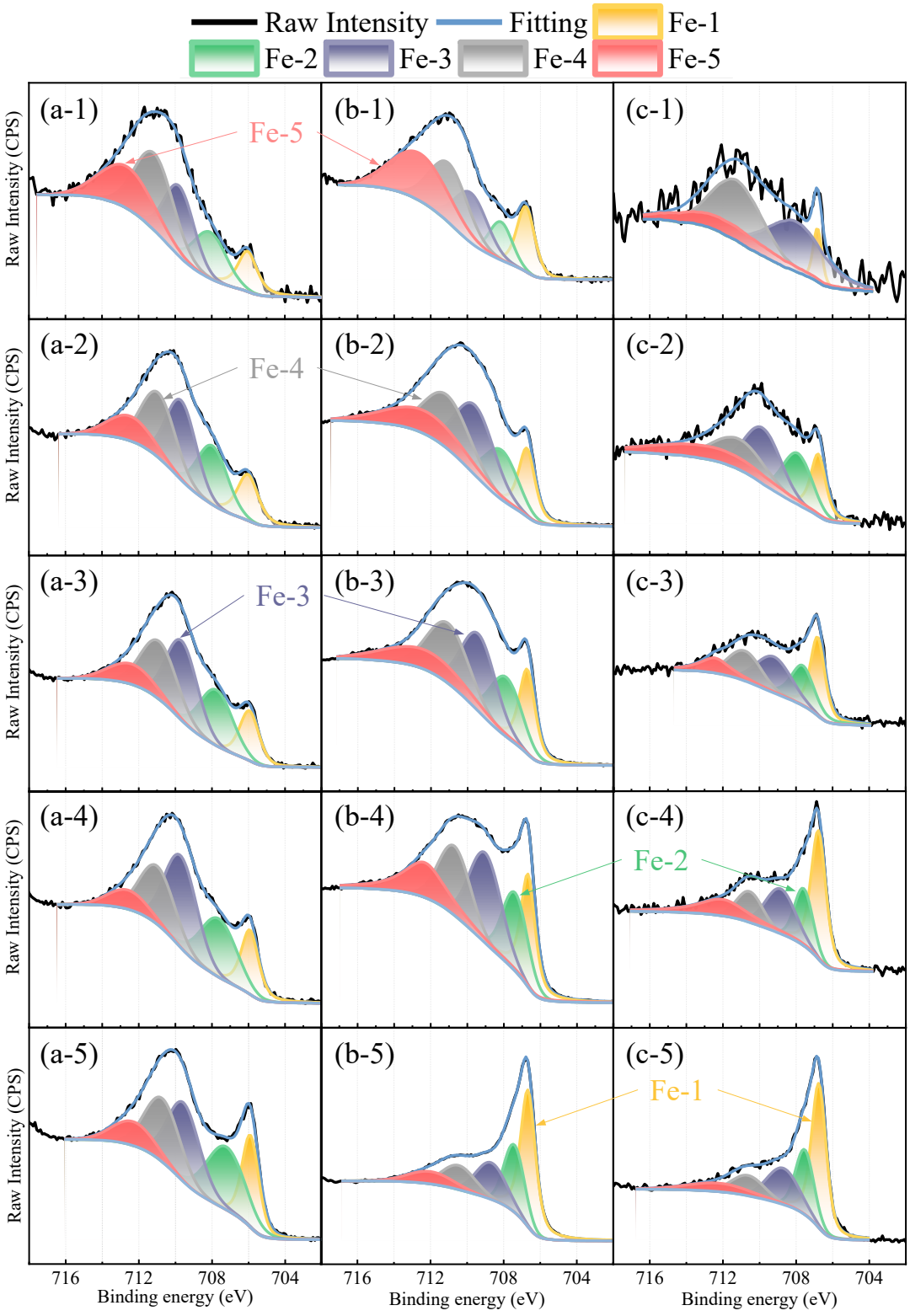

Figure 3.8. High-resolution of Fe 2p XPS spectra after 14 days of passivation in alkaline solution maintained at temperatures of (a) 25 ℃, (b) 35 ℃ and (c) 45 ℃ at sputtered depths of (1) 0 nm, (2) 1 nm, (3) 2 nm, (4) 3 nm and (5) 5 nm.

Based on the curve fitting, the XPS spectra can be analyzed to find the atomic concentration of iron and oxygen and determine the ratios of different compounds of Fe at different depths. The most general ratios that have been used in previous studies to determine the protectiveness of passive film are the ratio of total iron oxides to metallic iron (shown in Eq 3.5) and the ratio of Fe_2O_3/FeOOH (Fe (III)) to Fe_3O_4/FeO (Fe (II)) as shown in Eq 3.6.

$$\text{Total iron oxides/ Metallic iron} = \frac{(\text{Fe}-3) + (\text{Fe}-4) + (\text{Fe}-5)}{(\text{Fe}-1)} \quad (3.5)$$

$$\text{Fe(II)/ Fe(III)} = \frac{(\text{Fe}-4) + (\text{Fe}-5)}{(\text{Fe}-3)} \quad (3.6)$$

The atomic concentrations and ratios of Fe compounds are presented in Figure 3.9. From Figure 3.9 (a, b), it can be observed that with an increase in depth of analysis of the passive film towards the in-contact steel surface, there was an increase in iron content and a decrease in oxygen content. Figure 3.9 (c) represents the ratio of iron oxides to metallic iron at various depths. For all the depths, a greater iron oxide to metallic iron ratio can be observed in samples exposed to 25 ℃, while the lowest ratio is for samples at 45 ℃. It is worth mentioning that, considering the higher oxide content and higher oxygen atomic concentration at different depths, it can be confirmed that the samples exposed to alkaline solutions at 25 ℃ have a thicker passive film. However, a thicker passive film does not necessarily mean higher protection, as has been reported in some studies previously (Liu & Shi, 2022). Hence, through curve fitting of XPS spectra, the ratio of Fe(II) to Fe(III) was determined and is presented in Figure 3.9 (d). It can be observed that Fe(III) clearly dominates the outer layer, and Fe(II) dominates the inner layer in all the samples. A greater Fe(II)/ Fe(III) ratio is generally desirable and has been shown to provide better corrosion protection of steel (Ghods et al., 2011). Thus, comparing the ratios, it is apparent that the passive film formed in samples exposed to an alkaline solution at 25 ℃ developed a thicker and highly protective passive layer. A lower

Fe(II)/ Fe(III) ratio in the inner depths of the passive layer with high temperatures also denotes that high temperature probably promotes the oxidation of Fe(II), which was already observed during the CV test. This primarily led to a positive shift in the potential of steel exposed to alkaline solution at 45 °C.

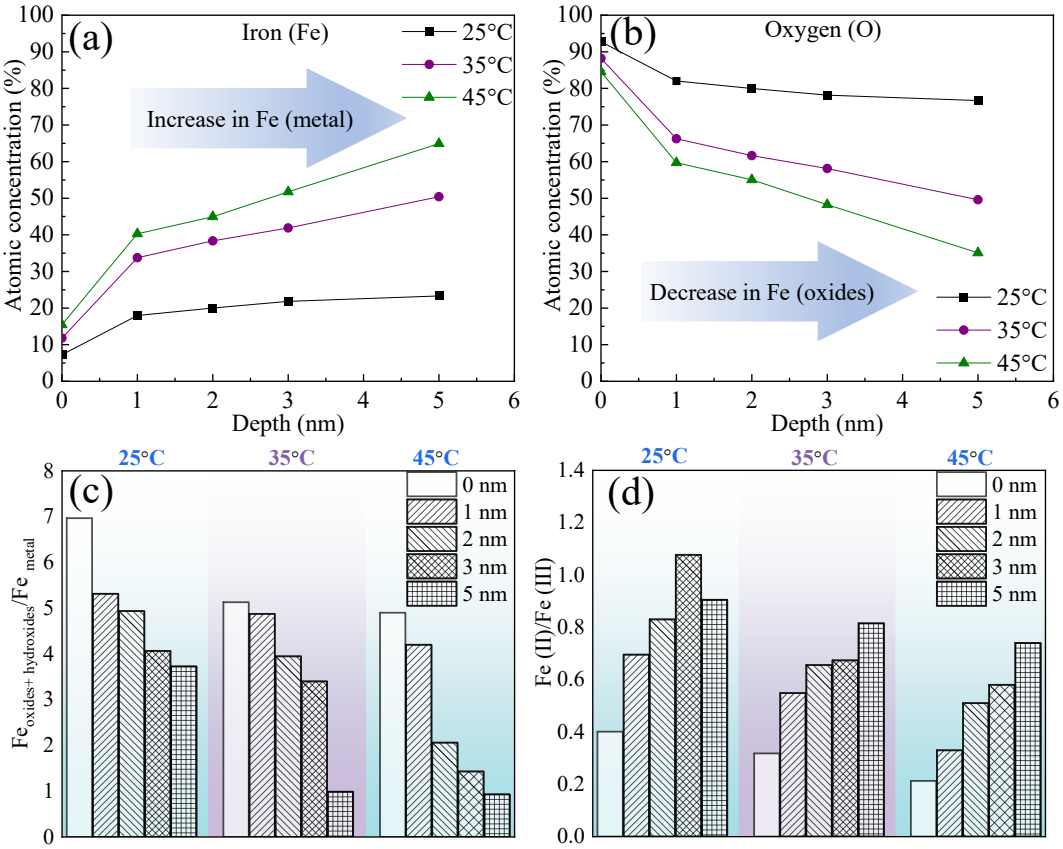

Figure 3.9. EIS fitting data to obtain the (a) atomic ratio of iron, (b) atomic ratio of oxygen, (c) ratio of iron oxides formed and (d) ratio of Fe^{2+}/Fe^{3+} at different depths after 14 days of passivation.

In addition to the qualitative analysis, XPS results can also be used to quantify the passive film thickness, using Eq. 3.7-3.11 (Ghods et al., 2011; Zhou et al., 2022)

$$d = \lambda_{ox}^{Fe} \cos\theta \ln\left(\frac{I_{ox}^{Fe}}{I_{m}^{Fe}} \cdot \frac{N_{m}^{Fe}}{N_{ox}^{Fe}} \cdot \frac{\lambda_{m}^{Fe}}{\lambda_{ox}^{Fe}} + 1\right) \tag{3.7}$$

$$\lambda_{ox}^{Fe} = 0.72\ (\propto_{ox})^{1.5} .(\ E_k^{0.5} \tag{3.8}$$

$$\lambda_{m}^{Fe} = 0.41\ (\propto_{m})^{1.5} .(\ E_k^{0.5} \tag{3.9}$$

$$\propto_{ox} = \ (\frac{1}{N_{ox}^{Fe}})^{0.33} \tag{3.10}$$

$$\propto_{m} = \ (\frac{1}{N_{m}^{Fe}})^{0.33} \tag{3.11}$$

Where d is the passive film thickness obtained by XPS, θ is the take-off angle with respect to the normal to sample surface (0 in this study), and I_{ox} and I_m represent the total iron oxide and metallic iron, respectively. N_m^{Fe} and N_{ox}^{Fe} represent the atomic densities of metallic iron (i.e., 84 atom/nm^3) and metal oxides (i.e., 38 atom/nm^3), and E_k is the kinetic energy of iron (i.e., 779 eV).

Based on the equations, the passive film thickness was obtained to be 6.295 nm, 5.457 nm, and 5.28 nm, which supports our previous qualitative estimation. The value obtained at 25℃ was in the same range as those in some previous studies conducted on the same steel (Zheng et al., 2022; Zheng, Poon, et al., 2020).

3.3.3 Passive film morphology

The combined electrochemical and XPS measurements provided an understanding of the composition and the quality of passive film formed on steel surfaces at different temperatures. The AFM technique was used to understand the morphology of the developed passive film on the steel surfaces. Figure 3.10 presents the surface morphology of steel after 14 days of passivation. A clear trend could be observed in the surface morphology between samples. The samples exposed to 25 ℃ demonstrated a more uniform passive film. However, as the temperature increased, the developed passive films were more non-uniform (increased roughness) with local thinner areas. The average roughness (r_a) of passive film formed at 25 ℃, 35 ℃, and 45 ℃ was 2.04 nm, 2.55 nm and 3.81 nm. The passive film quality was most

detrimental for samples at 45 °C, where the passive film observed had more localized defects that can allow an easier pathway for an attack of aggressive ions.

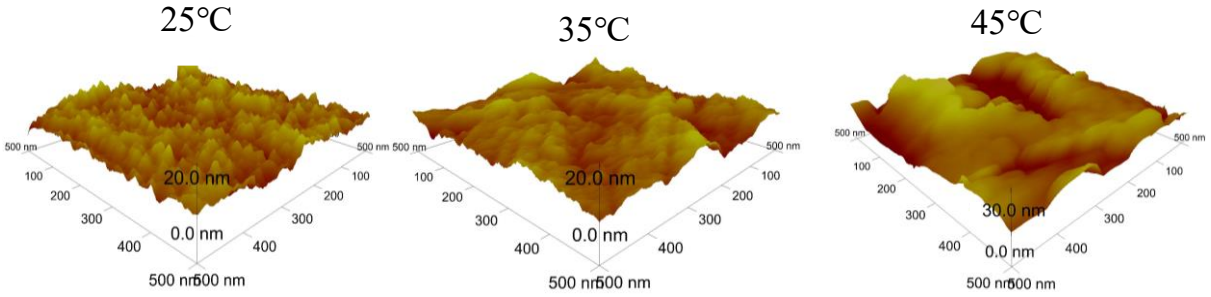

Figure 3.10. Surface morphology of passive film formed after 14 days of immersion.

While an investigation of the developed passive film helps to understand its quality and the possible implications on protection ability, a quantitative estimation of corrosion risk can be obtained only after exposure of the passivated steel samples at different temperatures to chloride ions, which has been explored in the subsequent section.

3.3.4 Depassivation and chloride threshold value

After 14 days of immersion in chloride-free alkaline solutions, the samples were exposed to chloride ions. The chloride addition was in the form of a fixed amount of 0.2 M, which was added at 12-hour intervals to allow sufficient time for the chlorides to react with the steel surface. Moreover, EIS measurements were done after every 0.4 M of chloride addition to understand the effect of added chlorides. The variation of EIS response, in the form of Nyquist plots, is presented in Figure 3.11. A reduction of impedance values and a decrease in capacitative arc radius can be observed for steel samples with increased chloride addition, irrespective of the exposure temperature. The primary reason for this behaviour is the increased dissolution of the oxide layer and the resultant decrease in the protectiveness of the passive film (Ghods et al., 2011; Ghods et al., 2013). However, it is worth noting that with increasing chloride addition, the decrease in the capacitative arc and impedance is not uniform and varies

with the temperature of the solution. This is evident when comparing the impedance curves at 25 °C, where there was a gradual drop in impedance with higher chloride addition. On the contrary, the drop in impedance for the steel in the alkaline solution at 45 °C was insignificant until corrosion initiation, i.e., the steel sample abruptly shifted from a passive to an active corrosion state.

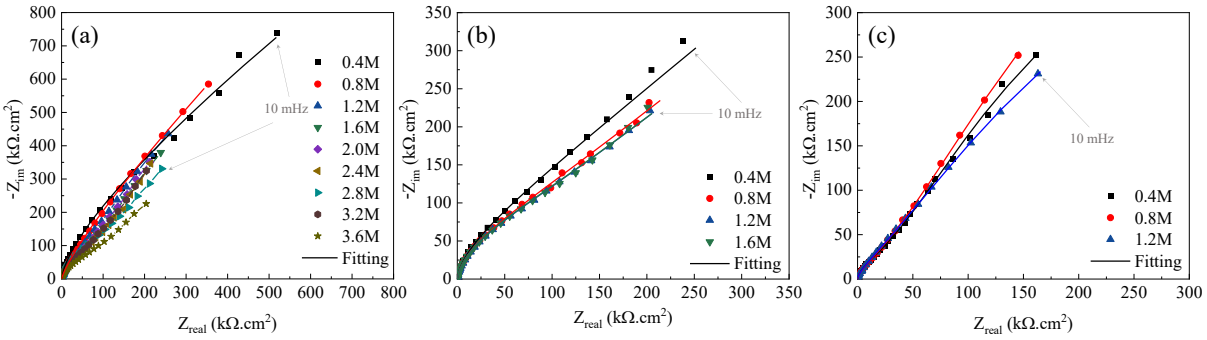

Figure 3.11. Nyquist response plots of steel after different contents of chloride addition at different temperatures.

The EIS data for steel samples exposed to varying chloride concentrations before depassivation were analyzed using the EEC model shown in Figure 3.4. The obtained electrochemical parameters can be explained in terms of solution resistance (R_{sol}) and polarization resistance (R_p), representing the sum of passive film and charge transfer resistance, as shown in Figure 3.12. As chloride ions were incrementally added, R_{sol} decreased significantly across all temperature conditions (Figure 3.12 (a)). The decreased R_{sol} was due to the increased conductivity of the solution, which is primarily responsible for electron transfer from anodic to cathodic sites of corroding metal (Raupach, 1996a). Thus, reduced R_{sol} can cause a decrease in ohmic drop due to electrolytic resistance and facilitate higher corrosion current. For samples at 25 °C, the R_{sol} decreased from 117 Ω·cm^2 in the alkaline solution free from chlorides to 48.6 Ω·cm^2 with a chloride addition of 0.4M and about 5.04 Ω·cm^2 when chloride contents reached 3.6M at depassivation stage. For samples exposed to 35 °C, the average R_{sol} reduced from 98

$\Omega \cdot cm^2$ in a chloride-free environment to 4.67 $\Omega \cdot cm^2$ at 1.6M during depassivation. Following the same trend, the R_{sol} for samples at 45 ℃ dropped from 82 $\Omega \cdot cm^2$ to 5.029 $\Omega \cdot cm^2$ with a chloride addition of 1.2M during depassivation.

The evolution of R_p with gradual chloride addition is shown in Figure 3.12 (b). With chloride addition, the R_p of steel samples was reduced for all temperature exposures. The decreased R_p could be attributed to the gradual dissolution and reduced protective ability of the passive film with higher chloride contents (Z. Jin et al., 2022; G. Liu et al., 2017; Zuo et al., 2019). This consequently promotes greater interaction between the steel surface and chloride ions, ultimately leading to rust formation once depassivation has been achieved. The trend denotes a drop in R_p of steel samples at 25 ℃ from 4700 $k\Omega \cdot cm^2$ in the fully passivated state to about 594 $k\Omega \cdot cm^2$ at depassivation, representing a drop of one order in magnitude. For samples at 35 ℃, this drop was from 1427 $k\Omega \cdot cm^2$ to 582 $k\Omega \cdot cm^2$ and for samples at 45 ℃, the drop was from 1106 $k\Omega \cdot cm^2$ to 493 $k\Omega \cdot cm^2$. One key observation from the trend of R_{sol} and R_p for samples exposed to chlorides is that, irrespective of exposure temperature, the onset of depassivation was triggered at nearly the same values in each case, which was at about a solution resistance of 5 $\Omega \cdot cm^2$ and polarization resistance of 450-600 $k\Omega \cdot cm^2$. This suggests that pore solution conductivity (directly linked to R_{sol}) may be able to indicate chloride-induced corrosion (Azarsa & Gupta, 2017), even for different exposure temperatures.

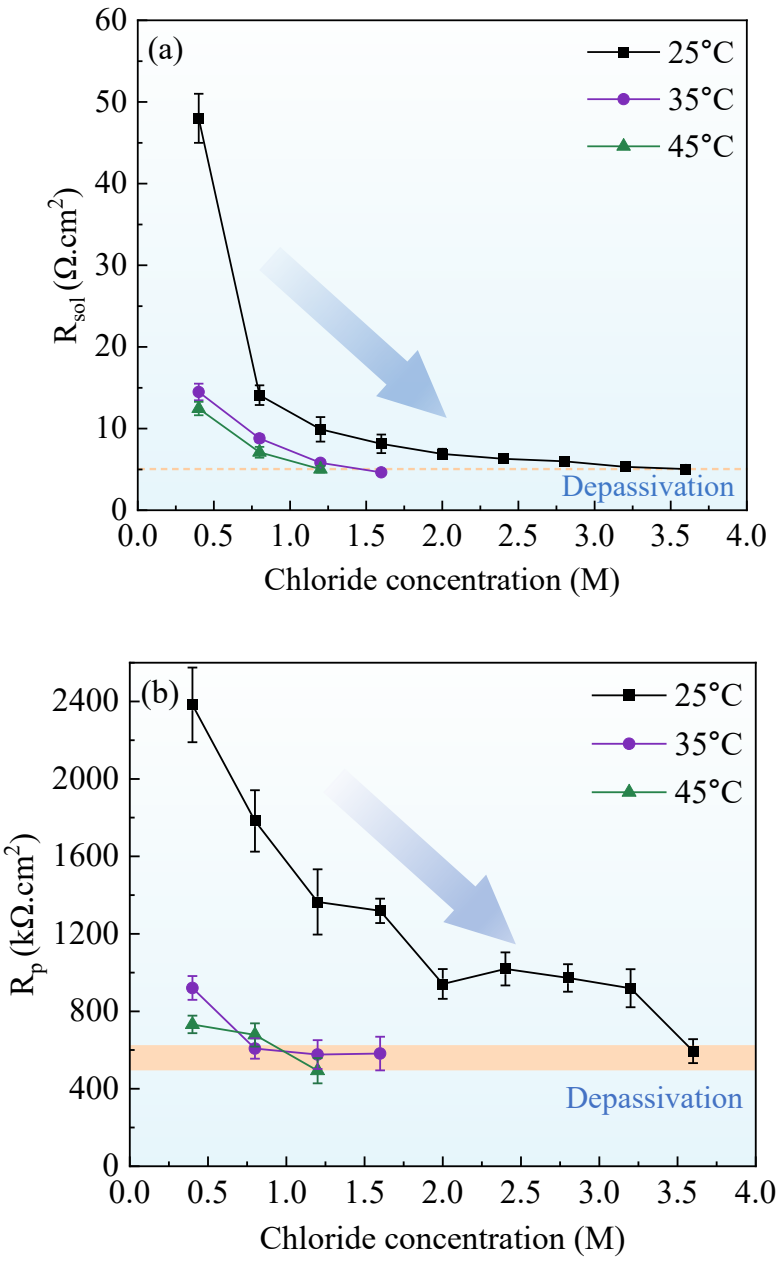

Figure 3.12. Evolution of (a) solution resistance (R_{sol}) and (b) polarization resistance (R_p) with different chloride additions for steel samples exposed to different temperatures.

Another implication of this test was determining the chloride concentration required for corrosion initiation in steel samples at different temperatures. This was evaluated by measuring the open circuit potential (OCP) periodically after every chloride addition until the OCP dropped into the active corrosion zone (-0.232 V vs. Ag/AgCl based on ASTM C876-15 (ASTM International, 2015)). It can be observed that the two samples used to check chloride

threshold values at different temperatures demonstrated nearly similar chloride thresholds, thus highlighting the repeatability of the experiment. The chloride threshold value decreased with an increase in temperature, as shown in Figure 3.13. As observed earlier, the effect of temperature rise on the corrosion susceptibility of steel is not uniform. For samples at 25 ℃, the chloride threshold value was in the range of 3.4M to 3.6M chloride concentration. With an increase in temperature to 35 ℃, the chloride threshold value dropped significantly to about 1.8M, which means the corrosion resistance halved at just a 10 ℃ temperature rise. With another 10℃ temperature increase, the chloride threshold further dropped to about 1-1.2M of chloride concentration, which denotes a sharp decrease in corrosion resistance at 45 ℃ to less than one-third of that at 25 ℃. This can be attributed to a combined effect of two factors, which include: structural and chemical modification of the passive, which reduced the passive film's protectiveness; elevated temperature could have promoted the reaction between chlorides and passive oxide film and accelerated the oxide film dissolution, which is crucial for protectiveness.

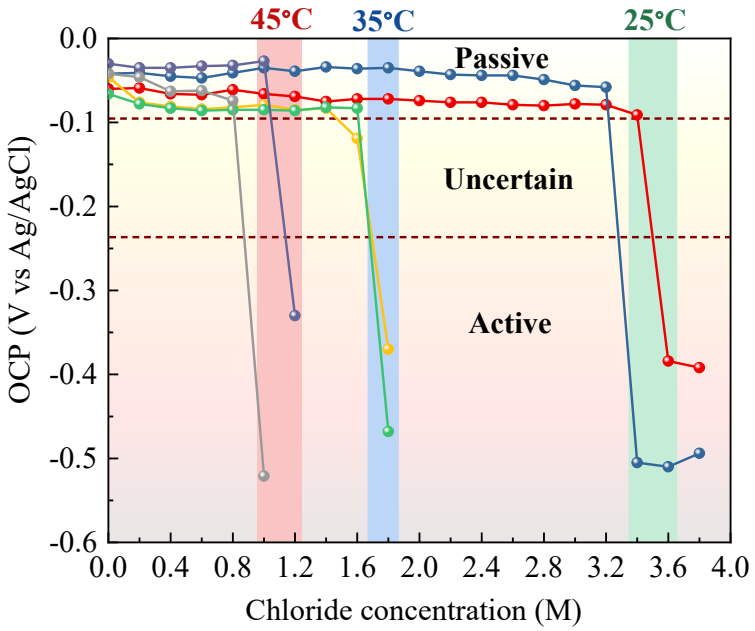

Figure 3.13. Evolution of OCP with chloride addition for steels at different temperatures.

3.4 Discussion

In order to understand the overall impact of temperature on chloride-induced corrosion of steel in simulated alkaline pore solution, a schematic diagram (Figure 3.14) is presented, considering the results from electrochemical tests and surface characterization techniques. Figure 3.14 illustrates three series of steps involved in chloride induced corrosion process of passivated steel. Stage (a) represents the passive surface of the steel after 14 days of immersion at different temperatures. Stage (b) represents the interaction/attack of chlorides to passivated steels, and stage (c) represents the corrosion initiation after the chloride threshold has been achieved.

Stage (a) represents the fully passivated steel surface after immersion in alkaline solutions at different temperatures. Previous experimental results helped to understand that the developed passive films are not the same in all samples but vary in structure and composition. In coherence with XPS results, the passive film formed on the steel surface is illustrated to be multilayered, with the outer layer dominated by Fe(III) oxides and an increasing concentration of Fe(II) oxides in the inner layers. With the increase in temperature (from 25 ℃ to 45 ℃), there is increased oxidation of the passive film from Fe(II) to Fe(III) and an increased dissolution, leading to its reduced thickness. Additionally, the high temperature also increased the concentration of surface defects, which was evident from AFM and Mott-Schottky analysis. All these factors subsequently lead to a less protective passive film on steel exposed to 45 ℃ and the most protective on steel at 25 ℃, as proven through EIS (Figures 3.3 & 3.5).

Stages (b) and (c) represent the subsequent effect on the corrosion initiation process. When chlorides are added to an alkaline solution, the dissolution of iron is accelerated, reducing the thickness of the passive film and its overall protectiveness (Lin et al., 1981; Montemor et al., 2003). This is reflected in the Nyquist plots, which demonstrate a decrease in the impedance of steel with increasing chloride concentration (Figures 3.11 and 3.12). Subsequently, the

gradual decrease of impedance is continued until the chloride content reaches a threshold concentration, after which there is a sudden drop of potential (OCP) to highly negative values, representing an active corrosion state (Figure 3.13). This threshold chloride content varies significantly with the temperature and is illustrated in stage (b).

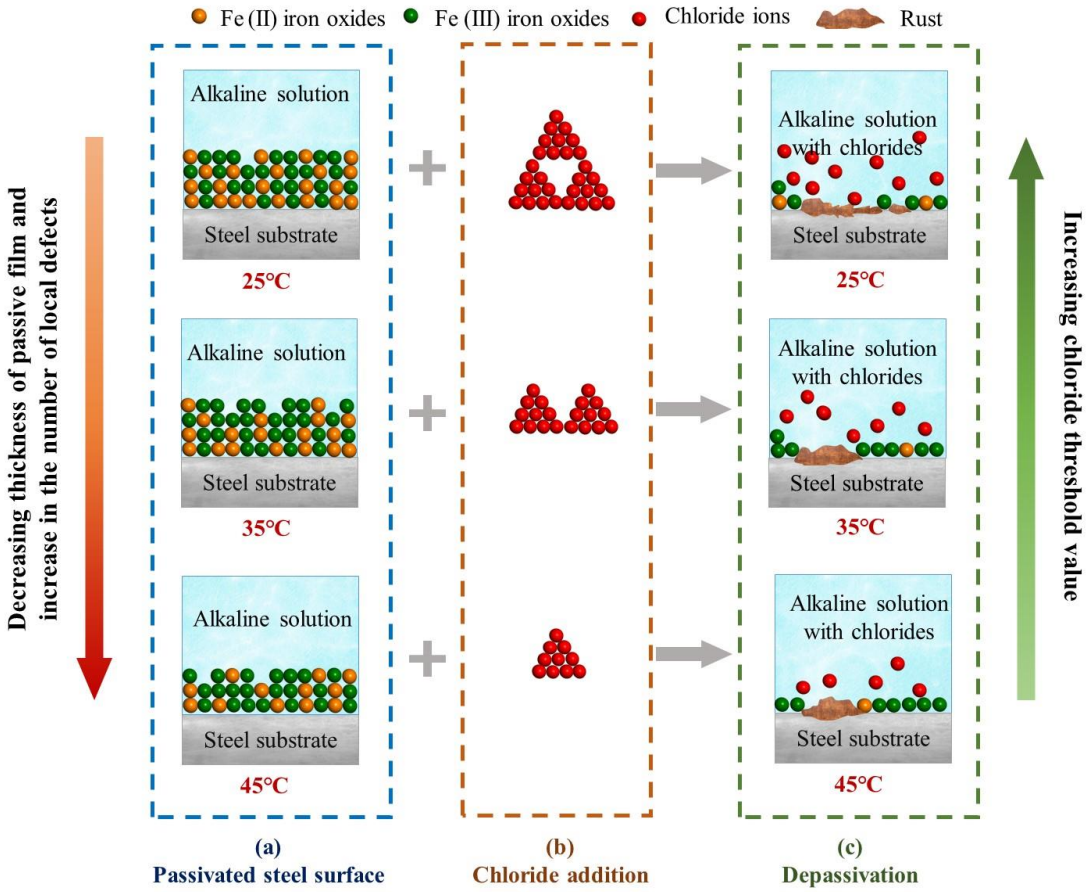

Figure 3.14. Schematic of the developed passive film and corrosion initiation at different exposure temperatures.

3.5 Overall Summary

In the current study, the effect of exposure temperature (namely 25 °C, 35 °C and 45 °C) on the passivation ability of steel and its implications on chloride threshold value was investigated through electrochemical measurements and surface analysis. Based on the study, the following conclusions can be drawn:

(a) Elevated temperatures significantly accelerated the initial oxidation kinetics of metallic iron (Fe) to Fe(II) oxides. At a high temperature of 45 ℃, the Fe(metal) undergoes rapid oxidation to Fe(II) oxides, such that the oxide film growth is fully completed in a short immersion time of less than 12 hours. Only the structural transformation from Fe(II) oxides to Fe(III) oxides was observed with prolonged immersion. For samples at lower temperatures (e.g., 25 ℃ and 35 ℃), metal oxidation to Fe(II) continued for a prolonged period, accompanied by further oxidation to Fe(III) oxides. These observations indicate that temperature predominantly governs the rate of the initial oxidation step rather than subsequent oxidation processes.

(b) Electrochemical characterization via CV and EIS demonstrated that the net oxide formed and the resulting impedance were inversely correlated with exposure temperature. A comparison at the end of passivation (i.e., 14 days) reveals that the average passive film resistance of samples exposed to 25 ℃ was 1053 kΩ·cm^2 while the average for those at 35 ℃ was 144 kΩ·cm^2 and at 45 ℃ was 57.5 kΩ·cm^2.

(c) The reduced impedance at higher temperatures was attributed to three interrelated mechanisms: (i) a reduction in passive film thickness, (ii) increased defect density within the oxide layer, and (iii) an increased proportion of porous, less protective Fe(III) oxides due to enhanced oxidation conditions.

(d) The reduced protectiveness of passive film significantly impacted the chloride threshold value (CTV) for corrosion initiation. Increasing the temperature from 25 ℃ to 35 ℃ reduced the average CTV of samples from 3.5M (moles/litre) to 1.8M. The CTV further reduced to 1.1M when the exposure temperature was 45 ℃.

(e) Even though the CTV for steel samples exposed to different temperatures had a significant difference, the transition from passive to active state occurred at a nearly similar average solution resistance of 5.04 Ω·cm^2 for those at 25 ℃, 4.67 Ω·cm^2 for

those at 35 ℃ and 5.029 Ω·cm^2 for those at 45 ℃. The trend suggests that pore solution resistivity can potentially indicate chloride-induced corrosion, and further research is required.

This study helped to identify the influence of exposure temperature on corrosion risk in concrete structures, which has not been explored extensively. Although the results from the simulated solution cannot be directly extended to real-world structures, the study highlights that ignoring the effect of temperature may significantly overestimate a structure's service years in the long run.

CHAPTER 4

CHLORIDE BINDING BY CEMENT HYDRATION PRODUCTS

4.1 Introduction

In Chapter 3, it was revealed that elevated temperature adversely affects the passive film thickness and composition, which is developed on the steel reinforcement. This subsequently reduces the amount of chlorides required in the pore solution near the steel surface to cause a breakdown of the passive film and initiate corrosion. It is important to highlight that the chlorides present in the pore solution constitute only a fraction of the total chlorides that penetrate the concrete, as a substantial portion becomes bound to cement hydration products and is immobilised. Thus, it is essential to understand the net-bound chlorides by cement hydrates to quantify the chlorides present in the pore solution. The bindings can be both physical and chemical in nature. The primary chemical reaction is with AFm phases to form Friedel and/or Kuzel salt (Delagrave et al., 1997; Suryavanshi et al., 1996). Some chloride parts are also physically absorbed into the calcium silicate hydrate (C-S-H) surface (Yuguo Zhang et al., 2023). As a consequence of the binding, the chloride concentration in the concrete pores becomes lower. This subsequently reduces the corrosion risk of the structure and significantly affects the overall service life (Li & Shao, 2014; Martın-Pérez et al., 2000).

However, accurately predicting bound chloride amounts in different matrices remains a significant challenge. This difficulty arises from the variability in chloride binding, which is influenced by several factors: the concentration of salts, the source of chlorides and their associated cations, the presence of any other deleterious ion during ingress of chlorides, mix composition of concrete and microclimate parameters such as carbon dioxide concentration (which poses a carbonation risk) and temperature (Arya et al., 1990; He et al., 2024; Yuan et al., 2009; Zhu et al., 2012). Various studies have demonstrated that the relationship between

bound and free chlorides at different concentrations can be explained by certain isotherms (e.g., linear, Langmuir, Freundlich and BET binding) (Florea & Brouwers, 2012). For a given temperature, the chloride binding increases with increasing concentration of chlorides. The chloride binding is generally higher for calcium salts, followed by magnesium and sodium salts (De Weerdt et al., 2015). This is associated with the reduction of pH for calcium salts and increased sorption of calcium ions on the C-S-H surface, leading to higher adsorption of chlorides in the diffuse layer of C-S-H. It has been observed that the chloride binding in binders increases as pH decreases until it reaches 12, beyond which binding starts to decline (Hemstad et al., 2020). A decrease in binding has been observed in the presence of other deleterious ions, such as sulfates or dissolved carbon dioxide, as AFm transforms to monosulfoaluminate and monocarboaluminate instead of Friedel salt (Sun et al., 2021; Ukpata et al., 2019). This reduces the ability to bind chlorides chemically. Thus, the overall chloride binding is influenced by the properties of C-S-H, a major hydrate phase in cement, and the availability of AFm for Friedel salt.

Different methods to increase chloride binding and improve durability include adding alumina-rich SCMs like metakaolin, ground granulated blast furnace slag (GGBS), fly ash, and direct addition of nano-alumina (Yang et al., 2019; Yang et al., 2020). It is worth mentioning that concrete, over its service life, is exposed to different temperature cycles (based on its service location and environment), which affects the chloride transport process (Hayat et al., 2024; Yuan et al., 2008; P. Zhang et al., 2023a). This makes it questionable to predict service life by extrapolating chloride binding results from experiments conducted at room temperature (20-25°C). Studies evaluating the exposure temperature effects on chloride binding are relatively scarce, with the findings reporting very contrasting results (Dousti & Shekarchi, 2015; Nguyen et al., 2009; Ogirigbo & Black, 2017; Panesar & Chidiac, 2011; Qiao et al., 2019; Zibara, 2001). Table 4.1 summarizes the conclusions from previous studies. An earlier study by Zibara

(Zibara, 2001) found that chloride binding at different temperatures depended on chloride concentration. For a low chloride concentration (i.e., 0.1 M), elevated temperature decreased chloride binding. In contrast, at high concentrations (e.g., 3M), elevated temperatures increase chloride binding. These findings were supported by Ogirigbo and Black (Ogirigbo & Black, 2017), who found that chloride binding increased at elevated temperatures for slag-mixed concrete mixes, and the increase in binding was more prominent at higher chloride concentrations. However, Dousti and Shekarchi (Dousti & Shekarchi, 2015) claimed that chloride binding decreased as the exposure temperatures were increased from 22℃ to 70℃ for different mixes, irrespective of chloride concentrations. However, these studies did not provide insights into how temperature specifically affects chloride binding to individual phases. Only one study (Qiao et al., 2019) evaluated the physical and chemical bound chloride contents at two different temperatures of 5 ℃ and 23 ℃ and found that physically bound chlorides increased with temperature, while chemically bound chlorides remained unaffected. It is worth noting that this study used a high curing temperature of 50℃, which might affect the hydrate phase and ionic composition of mixes (Lothenbach et al., 2007).

Table 4.1. Summary of the temperature effect on chloride binding in different binders

References	Binder	Temperature	Chloride concentration	Curing of binder before exposure	Remarks on the effect of temperature
(Panesar & Chidiac, 2011)	Type 10 OPC and GGBS from 0 to 60% replacement	Exposure temperature: -3, 5, 13, and 22°C	0.1, 0.5, 0.75, 1, and 3 M	4 weeks	Chloride binding increased with temperature: 22°C > -3°C > 13°C > 5°C
(Dousti & Shekarchi, 2015)	OPC, OPC+8%SF, OPC+8%MK, OPC+10%NZ	Exposure temperature: -3, 3, 22, 35, 50, and 70°C	0.1, 0.5, 1.0, 2.0 and 3.0M	2 months	Chloride binding reduced with temperature: 22°C > -4°C > 3°C > 35°C > 50°C > 70°C XRD shows reduced Friedel salt with increasing temperature
(Ogirigbo & Black, 2017)	CEM I 52.5R with 30% slag of two types	Cured and exposed to temperatures of 20°C and 38°C	0.1, 0.5, 1.0, 2.0 and 3.0 M	8 weeks	At 0.1M, the temperature had no influence. At 0.5M or higher chloride concentration, binding increased with increased temperature. Attributed to higher slag hydration at higher temperatures

(Nguyen et al., 2009)	CEM I and CEM V	Exposure temperature: 5, 21, and 35°C	5, 10 and 20 g/l	CEM I: 7 months CEM V: 18 months	For CEM V, chloride binding increases with a temperature rise from 5 to 35°C For CEM I, chloride binding does not change significantly with temperature.
(Zibara, 2001)	OPC, OPC+8%SF, OPC+8%MK	Exposure temperature: 7, 23, and 38°C	0.1, 0.5 and 3M	2 months	For 0.1 and 0.5M, chloride binding decreases with temperature rise (38°C< 23°C<7°C) For 3M chloride concentration, binding increases with temperature (38°C> 23°C>7°C)
(Qiao et al., 2019)	OPC, OPC + 10-60% FA	Curing temperature 50°C Exposure temperature: 5 and 23°C	0.1, 0.3, 0.5, 0.7, 1.0, 1.5, 2.0 , 2.5, 3.0, 3.5, 4.0, 4.5, 5.5 and 7.0 M	28 days	Physically bound chlorides increased with temperature. Highest physical binding in 20% FA. Chemical binding was not influenced by temperature

Thus, in light of the contradicting results and lack of clarity in existing research, further studies are necessary to understand the chloride binding phenomena in different mixes at varying temperatures. The current study aims to experimentally investigate the chloride binding in binary and ternary blended mixes when exposed to temperatures of 25 ˚C and 45 ˚C. Four mixes were investigated: two binary blends containing a mix of OPC and fly ash in various weight ratios, one ternary blend containing OPC, fly ash, and silica fume, and a control OPC-based mix. The four mixes were chosen to understand the changes in physical binding ability when adding two different SCMs (with different silica and alumina contents) at different temperatures. The study was further extended to understand their implications on chloride-induced corrosion risk for steel embedded in such concretes.

The main objectives of the study are to investigate (1) chloride binding isotherms at different temperatures, (2) quantifying the physical and chemically bound chlorides for the mixes, and (3) exploring the implications of chloride binding at different temperatures on steel corrosion. Different chemical techniques, such as X-ray diffraction (XRD), thermogravimetric analysis (TGA), Fourier Transform Infrared spectroscopy (FTIR), and Energy dispersive spectroscopy (EDS), chloride titration, were used in the study.

4.2 Experimental Program

4.2.1 Raw materials

The raw materials used to prepare the blended cement mixes were ordinary Portland cement, fly ash, silica fume, and deionized water. The chemical composition of the raw materials as determined by X-ray Fluorescence (XRF) test is provided in Table 4.2.

Table 4.2. Oxide composition of raw materials from XRF.

	CaO	SiO_2	Al_2O_3	Fe_2O_3	MgO	K_2O	TiO_2	MnO	SO_3
Cement	70.3	15.3	4.35	3.74	0.855	0.662	0.342	0.050	4.06
Fly ash	6.45	56.2	21.8	8.33	2.25	1.68	1.70	0.073	0.752
Silia fume	0.21	97.1	0.40	0.13	0.51	0.50	-	-	1.03

4.2.2 Preparation of paste samples

Four different paste samples were prepared with the fixed water to binder of 0.38. The detailed mix design is provided in Table 4.3.

Table 4.3. Mix proportions of control and blended cement pastes (weight relative to cement)

Sample ID	Cement	Fly Ash	Silica Fume
OPC	1	-	-
15FA	0.85	0.15	-
35FA	0.65	0.35	-
35FA8SF	0.57	0.35	0.08

The raw materials were mixed in a standard Hobart mixer (Fargo: CE-212 XG 12 Litres) containing 500 grams of cementitious binder and 190 grams of deionized water. The dry constituents were mixed for 3 minutes at low speed, followed by the addition of water and mixing for another 7 minutes. Once the mixing procedure was completed, a series of steps were

adopted, as shown in Figure 4.1, to expose the different samples to chloride solutions under controlled temperatures.

Step 1: Fresh cement paste slurry was poured inside the sealed plastic bags and cured in a controlled environmental chamber maintained at 90% relative humidity and 20℃ for 14 days.

Step 2: The hydrated cement pastes in plastic bags were ground into powders with sizes finer than 0.5 mm by a laboratory grinder.

Step 3: The hydrated cement powder was then placed in plastic bottles with an additional 30% water by weight of the powder to ensure continuous curing and further rehydration of the cement powder slurry (Hemstad et al., 2020). The primary purpose of rehydrating cement powder was to achieve maximum and uniform hydration. Such a procedure has also been followed previously (De Weerdt et al., 2015; Shi et al., 2017).

Step 4: After seven days, the rehydrated cement powders were removed from the bottle, further reduced to particle sizes of about 0.1 mm, and stored in zip-locked plastic bags.

Step 5: After storing for 90 days in plastic bags, the rehydrated cement powders were analyzed for their free water content and exposed to chloride solutions of different concentrations at two temperatures.

The above process was carefully done to avoid carbonation as much as possible.

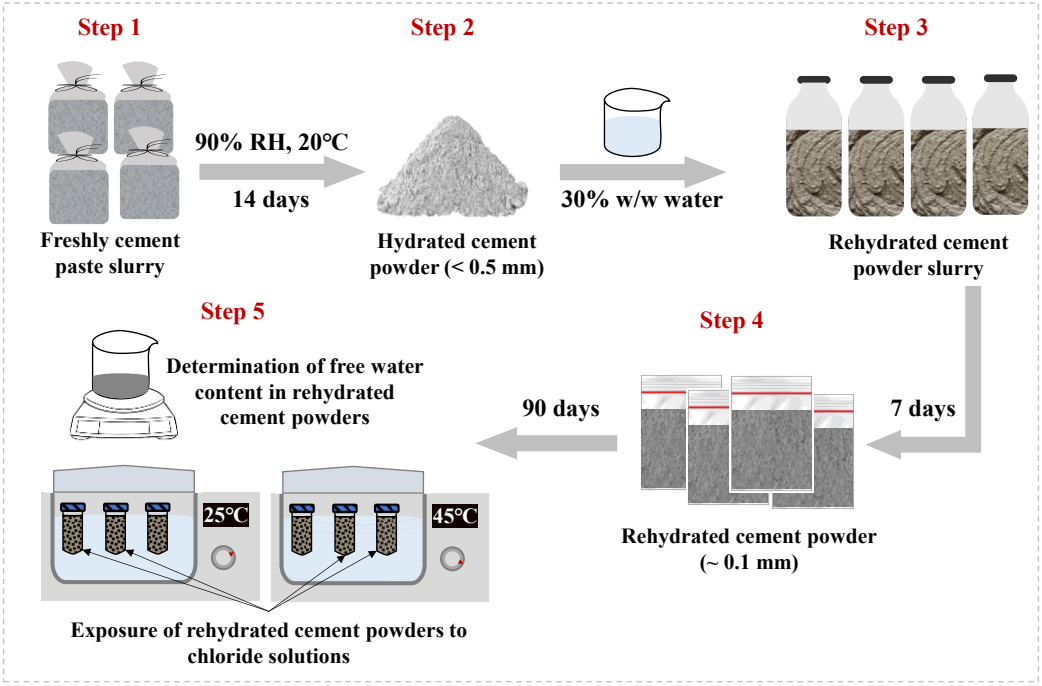

Figure 4.1. Schematic of sample preparation for chloride binding experiment.

4.2.3 Free water content of the rehydrated cement powders

Free water constitutes the excess water present in the rehydrated cement powders before exposure to chloride solutions. Thus, to ensure accurate determination of chloride concentrations, it is crucial to account for the dilution effect caused by this free water. Hence, a small amount (about 10 grams) of the rehydrated powder samples was dried in an oven at 40℃ for seven days. The weight of samples was measured before and after drying, and the % loss in weight of samples due to free water is provided in Table 4.4. The free water contents were in the range of 29-34%.

Table 4.4. Water contents in rehydrated cement powder (%)

OPC	15FA	35FA	35FA8SF
29.87	31.203	33.00	33.48

This % weight loss was later used to calculate the volume of free water (V_{fw}), assuming the specific gravity of water to be unity, and to calculate the chloride concentrations, as detailed in section 4.2.5.

4.2.4 Chloride exposure

For the chloride exposure study, 30 grams of rehydrated cement powder and 15 ml of chloride solution were mixed in 50 ml centrifuge tubes. These tubes were stored in sealed plastic boxes and kept inside water baths for eight weeks to enable sufficient time for chloride binding by powders. The duration of 8 weeks was chosen based on the available literature (Babaahmadi et al., 2022; Wang et al., 2020). During this period, the centrifuge tubes were shaken every week. Two sets of identical centrifuge tubes were used for each mix, and the reported results are an average of values from both tubes.

4.2.5 Analysis after chloride exposure

Determination of free and bound chlorides

During the exposure of rehydrated cement powders to chloride solutions, chlorides continued to bind to the cement hydration products. The concentration of free chlorides (Cl_{free}) after 8 weeks of binding was determined through titration of supernatant liquid, which was extracted after centrifugation using the Mettler Toledo Auto titrator. For this procedure, 0.2-0.4 ml (depending on the exposed chloride concentration) of extracted liquid was collected via a pipette and added to a beaker containing about 40 ml of deionized water and 1 ml of diluted 5% HNO_3. The solution was then titrated with 0.01M $AgNO_3$ using an automatic titrator. Two measurements were conducted for each extracted liquid, and the reported results represent the average of the two measured values.

Considering a part of the chloride introduced in exposure solutions remained free, while the other part remained bound to the hydration products, the total bound chlorides concentration

can be calculated based on the initial concentration of chlorides inside the centrifuge tubes before chloride binding ($Cl_{initial}$) and the concentration of free chlorides obtained through titration after allowing binding for 8 weeks (Cl_{free}). The initial chloride concentration inside centrifuge tubes differs from the reference chloride concentrations (Cl_{ref}) due to the free water contents in powders, as described in Section 4.2.3.

The $Cl_{initial}$ can be calculated as

$$Cl_{initial} = \frac{Cl_{ref} \times V_{cl,\ solution}}{V_{fw} + V_{cl,\ solution}} \tag{4.1}$$

The mass of bound chlorides relative to the mass of dry powder can be expressed as $\varphi_{cl,bound}$:

$$\varphi_{cl,bound} = \frac{M_{cl} \times \left(Cl_{initial} - Cl_{free}\right) \times (V_{fw} + V_{cl,solution})/1000}{m_{dry\ powder}} \tag{4.2}$$

where, M_{cl} is the molar mass of chlorine = 35.45 g, $V_{cl,\ solution}$ is the volume of chloride solution (15 ml), V_{fw} is the free water content in the rehydrated cement powders in ml, and $m_{dry\ powder}$ is the mass of powders in grams without any free content water in them.

Determination of ionic composition

After chloride exposure, the supernatant liquid was subjected to Inductively Coupled Plasma atomic emission spectroscopy (ICP-OES) analysis using Agilent 720 ICP-OES to obtain calcium and aluminium ions in the supernatant liquid, since they have been shown to significantly affect the physical chloride adsorption in C-(A)-S-H. The pH of the supernatant liquid was also measured using a standard Mettler Toledo pH meter.

Analysis of powder residue post chloride exposure

The powder samples after chloride exposure were analyzed using XRD, TGA, FTIR, and EDS to determine the proportion of chlorides bound physically and chemically.

For XRD measurements, a Rigaku SmartLab Advance with Cu-Kα radiation and a fast 1D solid state detector was used. The dried powder was scanned at a scanning speed of 2 steps per second and a step size of 0.02° 2θ with Bragg Brentano diffraction mode. The scanning range of 2θ was set from 5° to 45°.

For the TGA, approximately 10 mg of each dried powder was placed into an aluminium crucible for measurements using Rigaku Thermoplus EVO2. The mass loss was measured from 25 ℃ to 1000 ℃ at a heating rate of 10℃/min. The different hydration phases of the mixes can be identified based on the mass loss observed between specific temperature ranges. The main objective of TGA analysis was to determine the portlandite contents and the chloride bound by Friedel salt (i.e., chemically bound chlorides).

Since the C-(A)-S-H in cement hydrates is responsible for physical chloride adsorption, FTIR was conducted to examine whether chloride exposure at different temperatures affected C-(A)-S-H composition and structure. The powder samples containing 0.5 and 3M NaCl solutions were dried and scanned in the 400 to 4000 cm-1 range in transmission mode. The scanning resolution was 2 cm-1, and a total of 16 scans were accumulated for the measurement. Each mix proportion was tested twice, and the average results are reported in the paper.

Finally, EDS point analyses were conducted on the dried powder residues after chloride exposure to clarify and quantify the most dominating property of C-(A)-S-H affecting chloride adsorption using VEGA3 TESCAN in SE mode at an accelerating voltage of 15 kV. EDS point analysis was performed at 3kx magnification to calculate the Cl/Si, Ca/Si, Cl/(Si+Al), and Al/(Si+Al), which were then used to explain the variations in the physical binding of chlorides in different mixes.

4.3 Results

4.3.1 Chloride binding Isotherms

The total bound chloride contents for the cement paste samples after exposure to chlorides at 25 and 45 °C corresponding to the reference chloride concentrations are presented in Figure 4.2.

Influence of SCM addition

At 25°C (Figure 4.2 (a)), the chloride binding isotherm showed an increasing trend with fly ash addition, which is consistent with previous studies (Cheewaket et al., 2010; H. Li et al., 2024). However, adding silica fume into the mix reversed the beneficial effect of fly ash. As a result, the chloride binding capacity for OPC and 35FA8SF was nearly the same. This aligns with the investigations of previous researchers who have identified the detrimental effect of silica fume addition on chloride binding ability (Zibara et al., 2008).

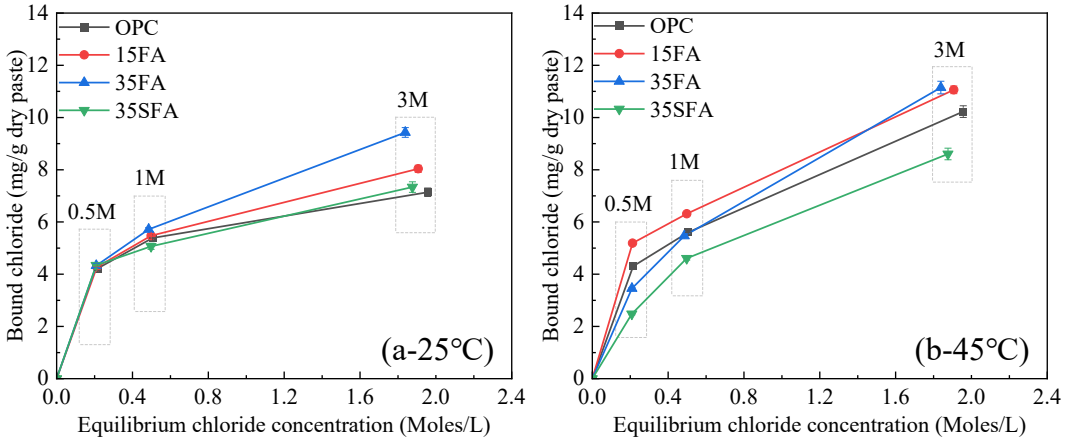

Figure 4.2. Bound chloride contents for the four mixes at (a) 25 °C and (b) 45 °C

Influence of temperature on chloride binding in samples exposed to 0.5M and 1M chloride concentrations

The effect of exposure temperature on chloride binding ability can be identified by comparing Figures 4.2 (a) and 4.2 (b). For chloride concentrations of 0.5 and 1M, the OPC mixes did not show a significant difference in chloride binding ability at different exposure temperatures. For mix 15FA with low fly ash contents, the chloride binding was higher at 45 ℃ compared to 25 ℃. However, on further addition of fly ash and silica fume to the mixes (i.e., 35FA and 35FA8SF), the elevated exposure temperature of 45 ℃ had a detrimental effect on the chloride binding ability of binders.

Influence of temperature on chloride binding in samples exposed to 3M chloride concentrations

At the highest chloride exposure concentration (3M), elevated exposure temperature positively affected chloride binding ability regardless of the mix composition. Mix 35FA8SF had the lowest chloride binding, while 15FA and 35FA showed nearly the same bound chlorides. It is worth mentioning that, except for the 3M concentration, the chloride binding for sample 15FA at 45 ℃ was higher than 35FA. This is contradictory to the usual understanding that higher fly ash contents increase the chloride binding ability due to increased alumina contents in the binder. It is important to mention that this observation is from chloride binding experiments at room temperature. As observed here and will be discussed subsequently, the effect of exposure temperature on chloride binding is linked to alumina contents in the mix and their preferential reaction in the presence of chloride ions.

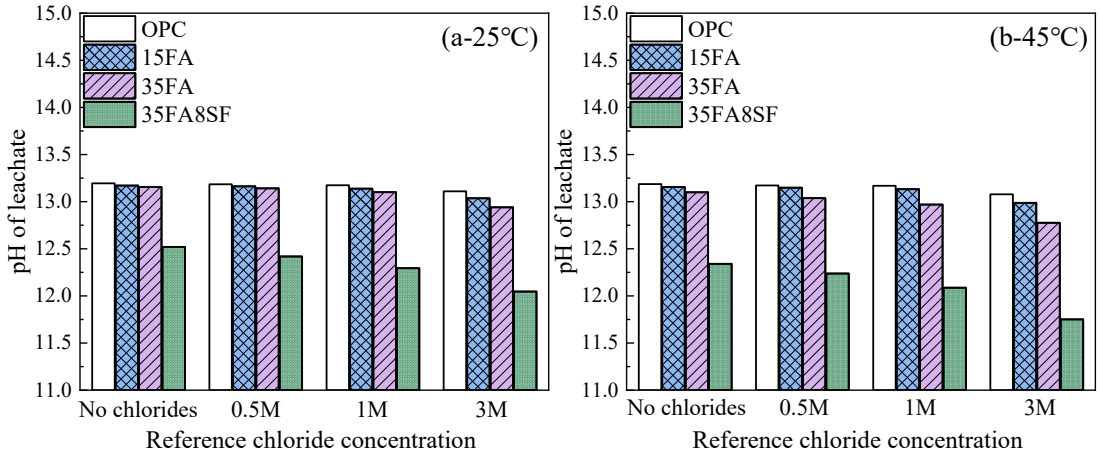

Figure 4.3. pH of leachates after exposure to chlorides at (a) 25 ℃ and (b) 45 ℃

The pH of the supernatant liquid extracted through centrifugation after exposure of rehydrated cement powders to chlorides at 25 ℃ and 45 ℃ is provided in Figures 4.3 (a) and 4.3 (b). Adding fly ash and silica fume reduced the pH of the pore solution due to the pozzolanic reaction (e.g. consumption of portlandite). The pH of the extracted liquid was also observed to vary with exposure to different temperatures and chloride concentrations. When considering the effect of temperature on the pH of the supernatant liquid, the dissolution of portlandite decreases at elevated temperatures, leading to a drop in pH. However, in the presence of high chloride concentrations, it has been reported that the dissolution of portlandite can be accelerated (Glasser et al., 2005). Thus, the measured pH in this study resulted from the above two effects of temperature and chloride concentration. The most notable reduction in pH was observed in mix 35FA8SF, which showed a pH of less than 12 when exposed to 3M chloride concentrations at 45 ℃.

4.3.2 Hydration phases changes of binders under chloride exposure

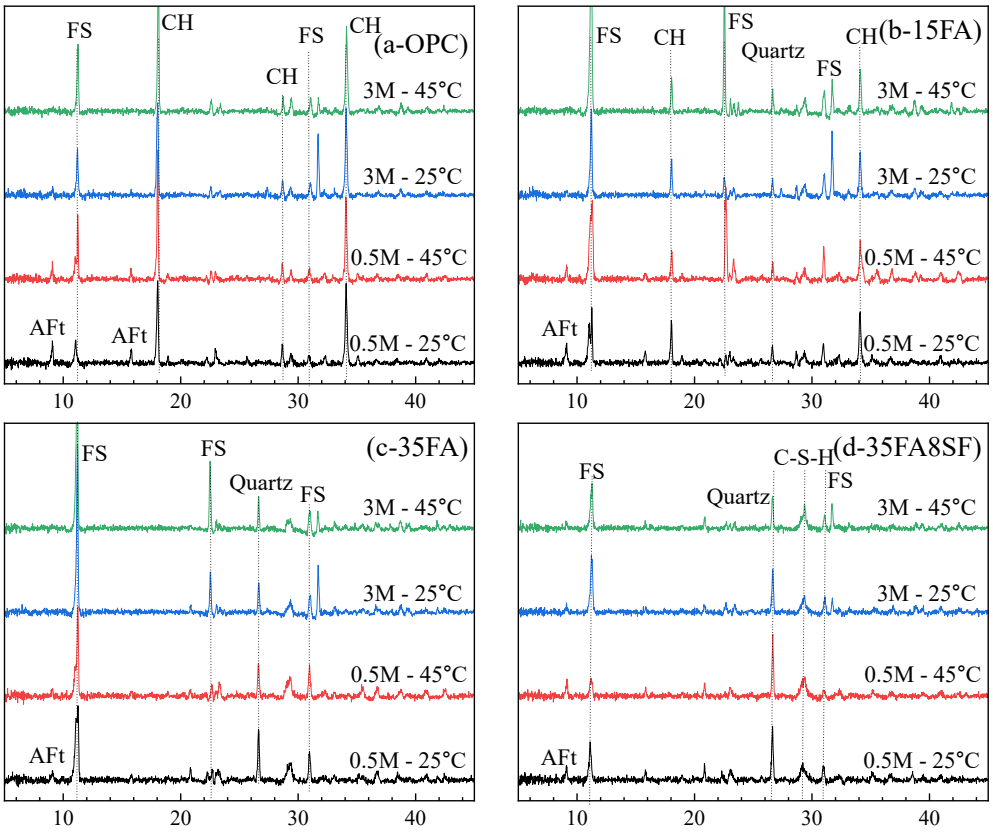

Figure 4.4. XRD patterns for samples (a) OPC, (b) 15FA, (c) 35FA and (d) 35FA8SF post chloride exposure.

The chloride exposure to binders causes significant changes to phase compositions. The effect of temperature and chloride concentrations on the changes in binder phases was analyzed by XRD measurements, as shown in Figure 4.4. The portlandite (CH) content of mixes followed the expected trend, with OPC (Figure 4.4 (a)) showing the highest peak intensity. As the SCM content increased in the mix, the peak intensity dropped significantly and disappeared for 35FA and 35FA8SF (Figures 4.4 (c & d)). The other distinguishable peak was that of AFt, the intensity of which dropped significantly in samples exposed to high chloride concentrations (3M). This is attributed to the substitution of sulphate ions by chloride ions from AFt at a higher chloride concentration, which leads to the formation of more Friedel salt (Birnin-Yauri &

Glasser, 1998; Ekolu et al., 2006). The AFt content was lowest for sample 35FA8SF, suggesting the dilution effect of silica fume. Furthermore, elevated temperatures appear to accelerate the transformation of AFt to Friedel salt. This is evident from comparing AFt peak intensity for 0.5M NaCl exposure, where a higher temperature reduced the peak intensity (refer to Figures 4.4 (b & c)). This was accompanied by an increase in peak intensity corresponding to Friedel salt. At 3M chloride exposure, the peaks of AFt disappeared in all mixes, suggesting the complete transformation of AFt to AFm. The peak corresponding to Friedel salt increased with exposure to higher chloride contents and fly ash addition. Thus, the peak intensity was strongest for the 35FA mix (Figure 4.4 (c)) when exposed to 3M chloride concentrations at 45 ℃. Contrary to other mixes, in the ternary mix (35FA8SF, Figure 4.4 (d)), the peak intensity corresponding to Friedel salt decreased when the temperature increased. One possible reason could be the drop in pH below 12, as observed in Figure 4.3 (b), which is known to reduce the stability of Friedel salt (Jain et al., 2021).

4.3.3 Thermogravimetric/Differential thermogravimetric analysis

Considering the observed variations in hydration phases of binders from XRD analysis, TGA was conducted to quantitatively assess the phase compositions of binders exposed to chlorides at varying temperatures. The corresponding derivative thermogravimetric (DTG) plots for powders exposed to 3M reference chloride concentrations are provided in Figure 4.5, with additional data for other chloride concentrations available in the Appendix 2. The DTG curves show a peak centred around 100℃ with a shoulder at about 150℃, which is associated with the presence of AFt and C-(A)-S-H phases. Moreover, it should be noted that C-(A)-S-H gel shows mass loss over a wide range of temperatures from 50 to 600℃ due to the loss of water from interlayer and dihydroxylation (Scrivener et al., 2016), overlapping with other phases (e.g., ettringite at ~100°C). This makes the quantification of C-(A)-S-H gel more challenging by TG/DTG. Nonethless, higher consumption of portlandite in the 35FA mix strongly supports

enhanced pozzolanic reactivity and higher volume of C-A-S-H gel presence, as compared to OPC and 15FA mixes. A minor peak between 230℃-400℃ corresponds to the decomposition of Friedel salt (Scrivener et al., 2016), which plays a crucial role in chemically binding chlorides (Shi et al., 2017). The major peak between 400℃ and 500℃ represents the decomposition of portlandite, which is essential to maintain a high pH environment in pore solution. When comparing different mixes, it can be observed that the portlandite content decreased with the addition of SCMs, and for 35FA8SF Figure 4.5 (d)), the entire portlandite was consumed and corroborated the XRD findings and lowest pH in 35FA8SF as observed before.

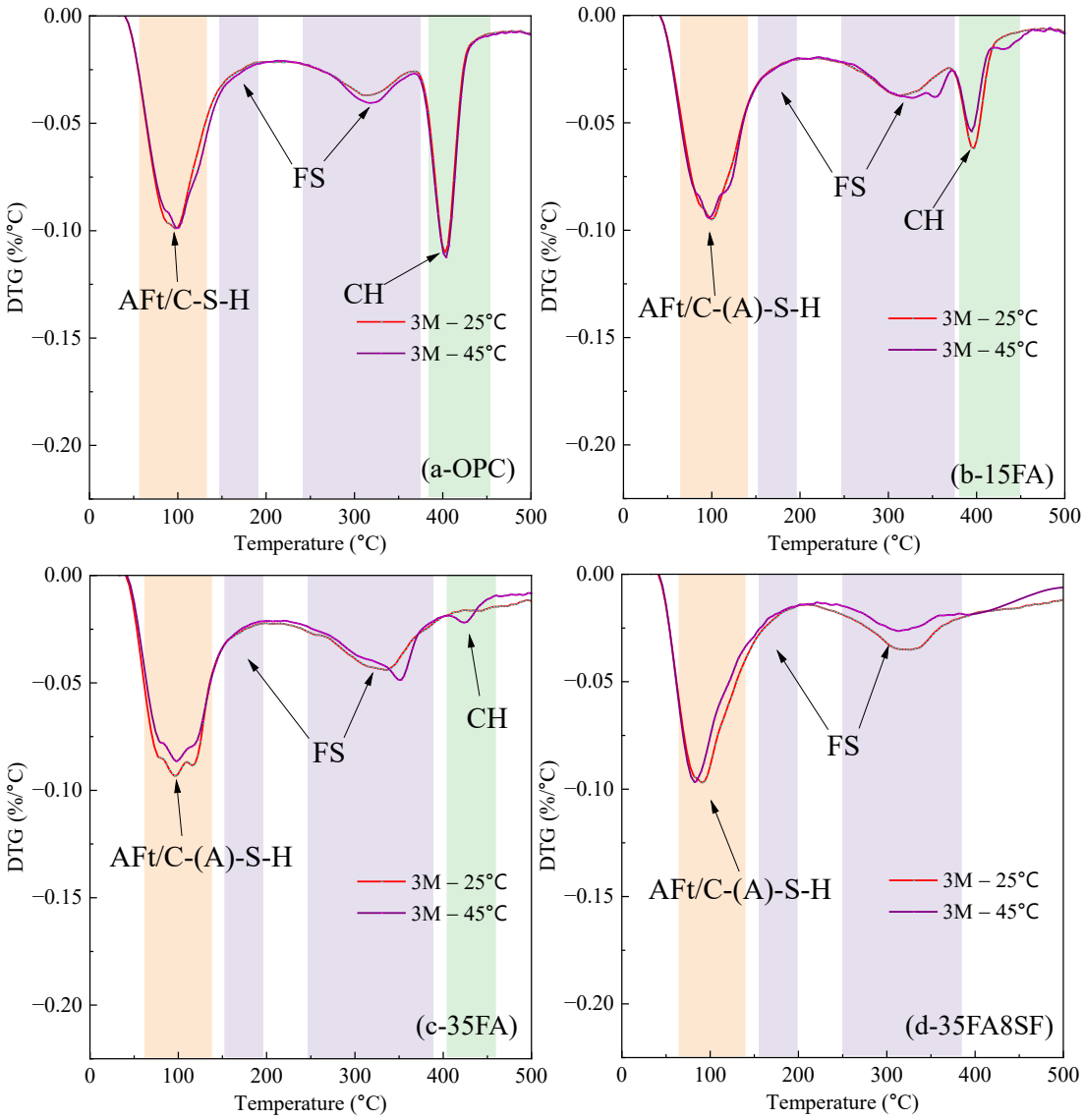

Figure 4.5. DTG plots of powders (a) OPC, (b) 15FA, (c) 35FA and (d) 35FA8SF after exposure to 3M reference chloride concentrations.

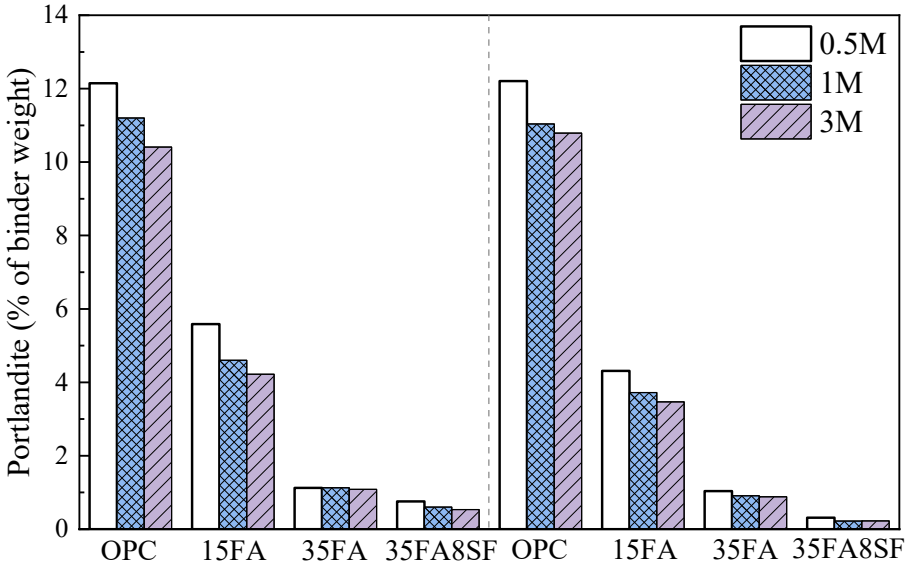

Figure 4.6. Portlandite content in paste samples obtained from DTG curves

The quantity of portlandite and Friedel salt was subsequently measured using the integration of mass loss over the temperature range using the tangential method recommended in a previous study (Scrivener et al., 2016). The contents of portlandite for different temperatures and chloride contents are plotted in Figure 4.6. The amount of portlandite measured is directly related to the pH of the supernatant liquid, i.e., a greater portlandite content enables a high pH. The higher temperature has little effect on portlandite consumption for the same chloride concentration, likely because of the longer curing time of mixes. It is worth pointing out that mix 35FA8SF was depleted of portlandite reserve, with most of it consumed during the pozzolanic reaction. This explains the lowest pH in the 35FA8SF mix.

During the temperature range of 230℃-400℃, Friedel salt loses 6 water molecules present in the crystal structure. Thus, the mass % of Friedel salt (FS) can be calculated as:

$$FS = \frac{M_{FS}}{6M_{water}} \times \Delta m_{230\text{-}400℃}$$

Where, M_{FS} is the molar mass of Friedel salt (561.3 grams) and M_{water} is the molar mass of water (18.02 grams) and $\Delta m_{230\text{-}400°C}$ represents mass loss between 230 and 400°C. This mass loss was also calculated for mixes that were not exposed to chlorides and deducted from chloride-exposed mixes. This was done to ensure the mass loss was only for Friedel salt. Subsequently, the maximum chloride content bound in Friedel salt was calculated as:

$$Max\ chemically\ bound\ chloride\ (mg/g) = \frac{FS \times 2M_{Cl}}{100 \times M_{FS}} \times 1000$$

Where M_{Cl} is the molar mass of chlorides (35.45 grams), and each mole of Friedel salt contains 2 moles of chlorides.

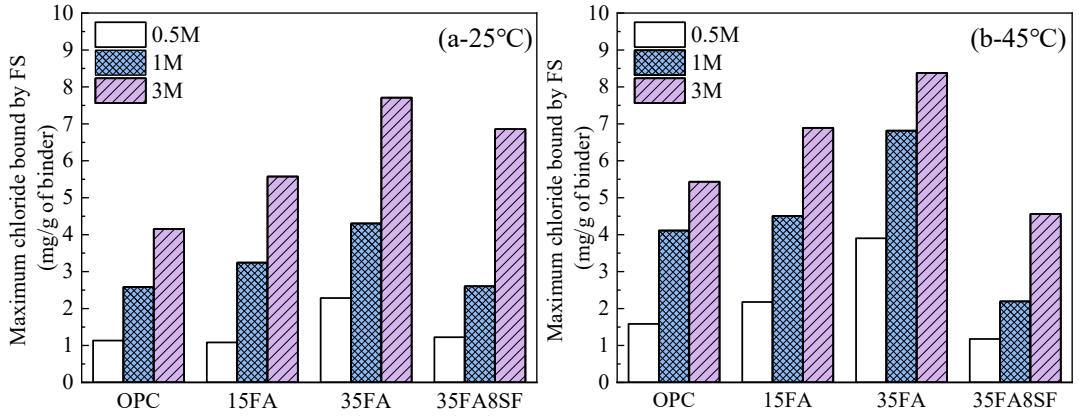

Figure 4.7. Variations of chemically bound chloride by Friedel salt in samples exposed to different chloride concentrations and temperatures.

The maximum chloride bound in Friedel salt in different mixes is provided in Figure 4.7. The stoichiometry of Friedel's salt is known to vary with pH, with a Cl/Al ratio of approximately 0.5 at pH 13, increasing to 1 at pH 12, before declining (Hemstad et al., 2020). It has also been reported that Friedel salt changes its structure from monoclinic to rhombohedral at a temperature above 28°C, but its effect on Cl/Al stoichiometry is not yet clear (Balonis et al., 2010; Renaudin et al., 1999). Thus, considering the variability associated with the stoichiometry of Friedel salt due to pH and possible interference due to temperature, an ideal

stoichiometry wherein a mole of Friedel salt binds 2 moles of chloride has been assumed for calculations. The chemically bound chloride was expressed relative to the dry powder mass corresponding to the powder's mass at 40°C at TGA measurement. It can be observed that the temperature had a profound impact on Friedel salt formation. This was consistent for mixes OPC, 15FA, and 35FA, where increasing exposed temperature from 25 to 45 °C increased Friedel salt and thus chemically bound chloride contents. This phenomenon can be explained by two possible reasons. First, the formation of additional AFm due to the reaction of unhydrated C_3A with portlandite can partially contribute to the formation of Friedel salt. Second, temperature has an accelerating effect on the transformation of AFt to Friedel salts. This is observed in XRD results (Figure 4.4), where a lower peak intensity corresponding to AFt is visible for mix OPC, 15FA and 35FA exposed to 0.5M chlorides at 45 °C compared to 25°C. On the contrary, for mix 35FA8SF, there was a reduction in chemically bound chlorides when the exposure temperature was increased, particularly at a higher chloride concentration of 3M, where chemically bound chlorides at 45 °C were about 60% of those at 25°C.

The chemically bound chloride contents also increased with fly ash addition due to a rise in alumina in the mix and with increased chloride exposure. However, this is valid as long as the pH of the pore solution remains higher than 12 even after the pozzolanic reactions, after which the chemically bound chlorides get destabilized (Hemstad et al., 2020). The increase in Friedel salt amount for all the mixes with increased chloride addition was related to the transformation of all available OH-AFm, ettringite and monosulfoaluminates phases into Friedel salt (Balonis et al., 2010; Galan & Glasser, 2015; Wang et al., 2020).

4.3.4 Physically bound chlorides on C-A-S-H

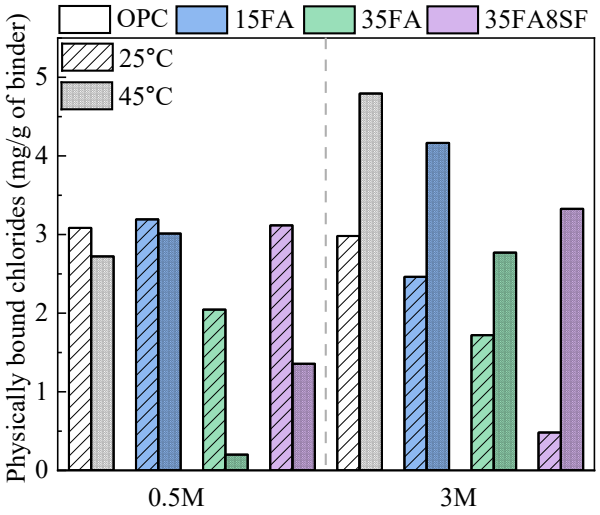

Figure 4.8. Effect of temperature on physical chloride binding for different chloride exposures.

The amount of chlorides physically bound to the C-S-H and C-(A)-S-H is provided in Figure 4.8. At a low chloride concentration of 0.5M, the physical binding decreased with an increase in temperature. The drop was marginal for OPC and 15FA mixes but more significant for mixes with high fly ash and silica fume (35FA and 35FA8SF). Subsequently, this led to a drop in overall bound chloride contents, as shown in Figure 4.2. The physical chloride binding has a key role in such chloride concentrations, as reported previously (Elakneswaran et al., 2009). This implies that the general understanding that higher alumina contents in raw materials will increase the chloride binding ability of the binder might not be true for low chloride concentrations at elevated exposure temperature (e.g. reduction in physical chloride binding for 0.5M from 25 ℃ to 45 ℃).

At high chloride concentrations of 3M, a general increasing trend in physical chloride binding can be observed in all mixes with increased exposure temperature. Irrespective of chloride contents, physical binding in C-S-H and C-(A)-S-H is significantly higher for 15FA and OPC mixes than 35FA and 35FA8SF at elevated temperatures. This is despite the fact that increased SCM contents (e.g., in 35FA and 35FA8SF) will have more C-(A)-S-H contents in the binders.

Thus, the Ca/Si ratio has a more prominent role than the amount of C-(A)-S-H formed, supporting observation from a previous study (Zibara et al., 2008). The observation that SCM addition reduces physically bound chlorides aligns with other studies (Wilson et al., 2022), which attributes this to the formation of higher proportions of C-(A)-S-H with a low Ca/Si ratio.

It is worth pointing out that the accurate values of physically bound chlorides may vary based on the stoichiometric ratios of Friedel salt formed at specific chloride concentrations and exposure temperatures. The values in this work have been obtained by subtracting the free and maximum chemically bound chlorides (assuming a Cl/Al ratio of 2 in Friedel salt) from the initial chloride contents. This could have led to an overestimation of chloride binding by Friedel salt, resulting in relatively lower values of physically bound chlorides at 3M chlorides exposure compared to 0.5M at 25°C. Previous studies have also indicated such overestimation (Machner et al., 2018).

4.3.5 Effect of temperature and chlorides on the structure of C-S-H and C-(A)-S-H

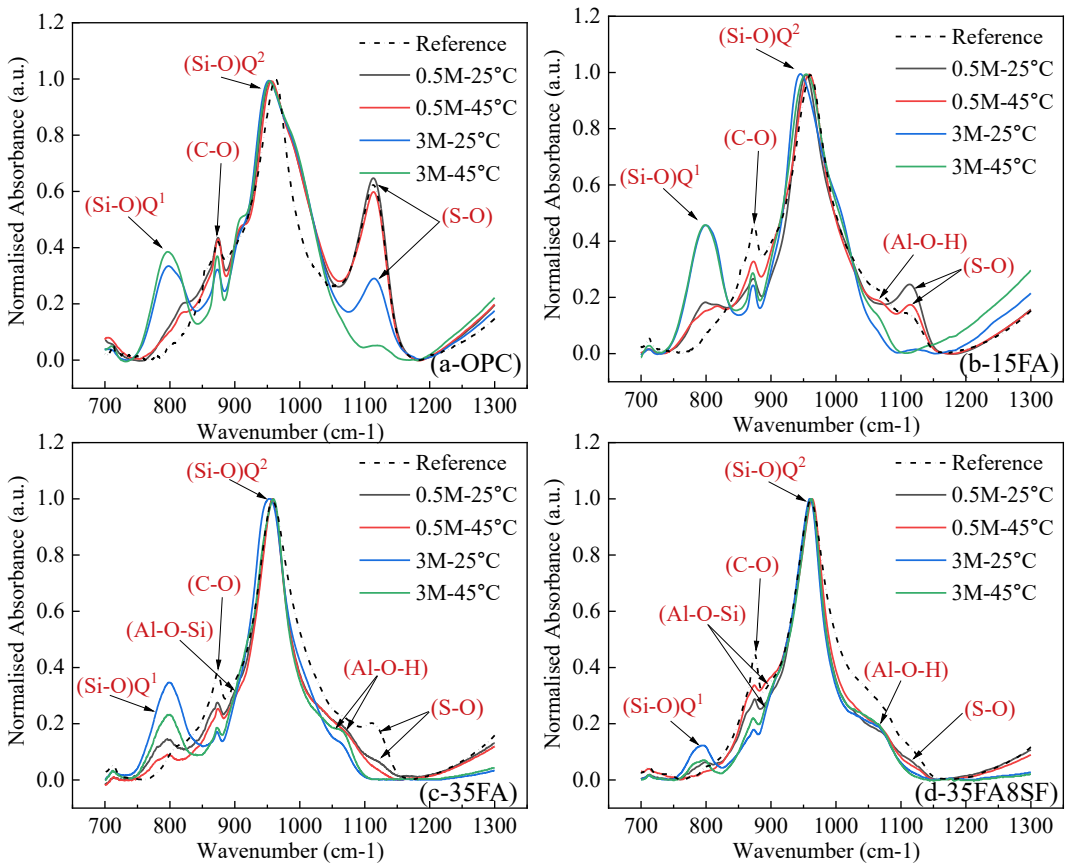

Figure 4.9. FTIR spectra of paste samples (a) OPC, (b) 15FA, (c) 35FA and (d) 35FA8SF exposed to chlorides at different temperatures.

The changes in the structure of C-S-H and C-(A)-S-H due to different temperatures and chloride concentrations were investigated to correlate with the physically bound chloride contents. Figure 4.9 presents the FTIR spectrum for the four mixes before exposure to chloride solutions and when exposed to 0.5 and 3M chloride solutions. The values were normalized, corresponding to the peak at about 950 cm^{-1}. The FTIR spectra show absorption bands between 750 and 1200 cm^{-1}, typically representing the symmetric and asymmetric stretching vibrations of Si-O-Si and Si-O-Al bonds in aluminosilicates (H. Li et al., 2024).

The presence of minor calcium carbonate ($CaCO_3$) in the mixes, formed during the sample preparation process, was identified by a characteristic peak at approximately 875 cm^{-1},

corresponding to ν3 vibration mode of CO_3^{2-} (Choudhary et al., 2015). Following exposure to chloride solutions, the intensity of this carbonate peak diminished, reaching its lowest magnitude in the 3M chloride exposure case. This reduction may result from reactions between calcium carbonate and aluminate phases or partial substitution of sulfate ions within the AFt.

Another peak distinctly visible at about 1100 cm^{-1} is typically assigned to the υ3 vibration of the SO_4^{2-} group, indicative of sulphate species. These sulphates can react with aluminate and ferrite phases of cement to form AFm and AFt phases (Qu et al., 2022; Ylmén et al., 2009). Consequently, the intensity of this sulfate peak decreased with the replacement of OPC by SCMs, likely due to reduced sulfate availability. Furthermore, exposure to increased chloride concentrations significantly diminished the sulfate peak intensity. This suggests the progressive transformation of AFt and AFm to Friedel salt.

Changes in Ca/Si ratio

The signals at about 800 cm^{-1} and 1005 cm^{-1} are related to the Si-O stretching of Q^1 tetrahedra (Yu et al., 1999). After exposure to chlorides, which could have promoted some extra hydration, we can see an increase in peak intensity at 800 cm^{-1} for all the mixes. For the mixes below, the band at 1005 cm^{-1} is only visible as a shoulder for mix OPC (Figure 4.9 (a)) and 15FA (Figure 4.9 (b)). It has been previously suggested that this peak intensity increases for a higher Ca/Si ratio. A higher Ca/Si ratio based C-S-H has a greater ability to physically bind chlorides (Zhou et al., 2018). This justifies the higher physically bound chlorides in OPC and 15FA (refer to Figure 4.8). The next intense band is centred at about 950-970 cm^{-1} and corresponds to Q^2 units of C-S-H (Kapeluszna et al., 2017; H. Li et al., 2024). This signal can either be in the form of a single band or several overlapping bands. It can be observed that the main peak in this region shifts towards a higher wave number when the exposure temperature increases for mixes 15FA, 35FA, and 35FA8SF. The shift of this peak towards a higher wavenumber is associated with the reduction in the Ca/Si ratio and increased depolymerization of the silicate chains

(Kapeluszna et al., 2017; H. Li et al., 2024). Another notable effect was the role of chloride exposure on the Ca/Si ratio. It could be observed that increasing chloride concentration in the exposure solution shifted this peak towards a lower wave number. This shift was more pronounced in mixes 15FA and 35FA, compared to OPC and 35FA8SF.

Changes in aluminium uptake

The FTIR spectra can also denote the incorporation of aluminium into C-S-H gels. Comparing the FTIR spectra of the different mixes (15FA, 35FA and 35FA8SF), the presence of aluminium in C-(A)-S-H gels resulted in a shoulder formation at about 880 cm^{-1}, corresponding to the stretching vibration of Al-O-Si. Similarly, the shoulder formed around 1050 cm^{-1} suggests the symmetric bending of Al-O-H (Barzgar et al., 2021). This has been reported to increase with higher alumina substitution in C-(A)-S-H. By comparing the FTIR spectra of different mixes, it could be observed that the band at 1050 cm^{1} is absent in OPC (Figure 4.9 (a)) and more prominent in mixes 35FA and 35FA8SF (Figures 4.9 (c, d)) compared to 15FA. This supports the earlier observations that C-S-H with low Ca/Si has a higher affinity for aluminium (Kapeluszna et al., 2017). In the sample with silica fume (35FA8SF), where there is complete consumption of CH, there will be a larger content of C-(A)-S-H with a low Ca/Si ratio, with more aluminium uptake (Kapeluszna et al., 2017). This has two implications: A part of aluminium released from the dissolution of fly ash goes into C-(A)-S-H and cannot form Friedel salt; The uptake of aluminium in C-(A)-S-H reduces its ability to physically bind the chlorides (Yoshida et al., 2021).

Two distinct observations can be made when comparing the effect of temperature and chloride exposure on FTIR spectra. An increase in chloride content in the exposure solution increases the peak corresponding to Q^1 tetrahedra for all mixes. The peak intensity is also observed to be slightly reduced when the exposure temperature is increased (except for OPC), suggesting changes in the Ca/Si ratio. Another observation is the peak intensity corresponding to Al-O-H

and Si-O-Al bond, indicating aluminium uptake in C-(A)-S-H. For mixes 35FA and 35FA8SF, the shoulder formed at 880 cm^{-1} is more intense for mixes exposed to 0.5M NaCl than 3M. This trend is also visible in the shoulder formed at 1050 cm^{-1} for sample 35FA. This indicates that the substitution of silicon by aluminium in C-(A)-S-H could be inhibited in the presence of high chloride exposure.

4.3.6 Relation between C-(A)-S-H gel composition and physical chloride binding

Following the results of FTIR tests, which demonstrated that both exposure temperature and chloride concentrations changed the composition of C-S-H and C-(A)-S-H gel composition, EDS point analysis was conducted on the binders to quantify the chlorides physically bound to C-(A)-S-H gels of different compositions. Two mixes (15FA and 35FA) were selected for this analysis since the effect was more pronounced in these binders. An average of at least 100 points was taken on C-(A)-S-H gel to report the results. The scattered plot of the EDS point scans is also provided in the Appendix 2.

The average EDS point ratios of Cl/Si vs Ca/Si are plotted in Figure 4.10 (a) and represent the variation of physically bound chlorides with different Ca/Si.

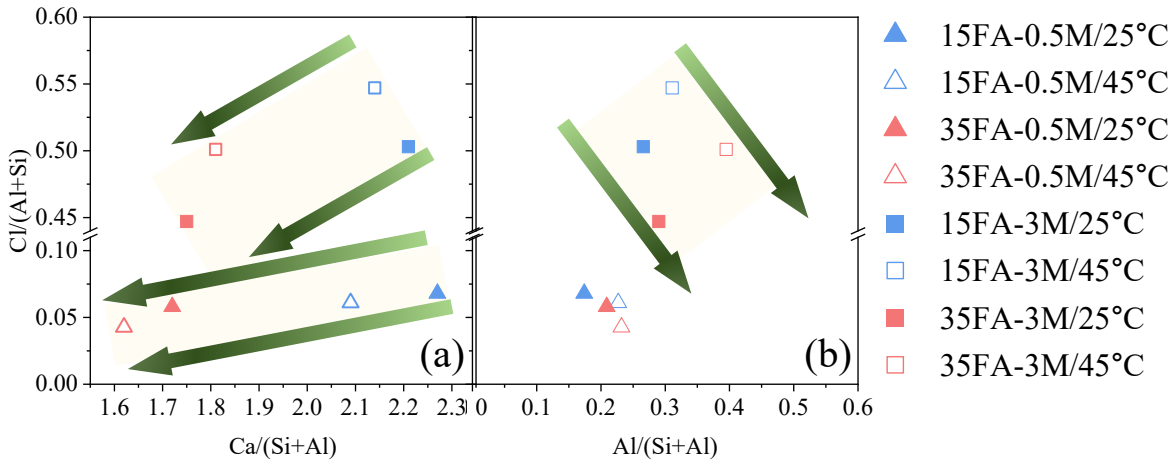

Figure 4.10. EDS analysis of samples after chloride exposure (a) Cl/(Al/Si) vs Ca/(Si+Al) and (b) Cl/(Si+Al) vs Al/(Si+Al).

Results show that increased chloride exposure concentrations increased the physically bound chlorides (Cl/Si) in C-(A)-S-H gel. This was linked to higher availability and ionic mobility of chloride at higher concentrations, leading to increased physical binding with C-(A)-S-H gel.

Influence of SCM addition

At a constant temperature and chloride concentration, the increase in FA content from 15% to 35% resulted in the formation of C-(A)-S-H gel with lower Ca/Si. This lower Ca/Si ratio slightly reduced the physically bound chloride. This is based on the hypothesis that in highly alkaline environments, the silanol site (≡SiOH) deprotonates to ≡SiO−, imparting a negative charge to C-(A)-S-H. Thus, the higher the concentration of negatively charged hydroxyl ions, the greater the number of deprotonated sites in C-(A)-S-H. These deprotonated sites lead to Ca^{2+} ions adsorption, which increases the Ca/Si ratio, ultimately leading to a net positive charge on the C-(A)-S-H surface and enhancing chloride accumulation in the diffuse layer (H. Li et al., 2024). Due to the pozzolanic reaction, the pH of the pore solution is reduced (i.e., alkalinity decreases) with an increase in FA contents. This caused the physically adsorbed chlorides per unit of Si to reduce as the fly ash content was increased from 15% to 35% due to a higher volume of C-(A)-S-H with low Ca/(Si+Al).

Influence of temperature on samples exposed to low (0.5M) and high chloride (3M) concentrations

For low chloride exposure (0.5M), an increase in the temperature from 25 ℃ to 45 ℃ led to a reduction in the Ca/Si, which reduced the chloride adsorption on the C-(A)-S-H gel. However, an increase in temperature at higher chloride concentration (3M) had a very marginal effect on Ca/Si, with only a slight increase in Ca/Si ratio and physically bound chlorides observed in 35FA. This aligns with the trend observed from the net physically bound chlorides calculation

by subtracting chemically bound chlorides from total chlorides. The underlying reason for this is based on the solubility trends of portlandite and C-(A)-S-H, which will be discussed later.

Influence of aluminium uptake in C-(A)-S-H

The average EDS point ratios of Cl/(Al+Si) vs Al/(Al+Si) are plotted in Figure 4.10 (b) and represent the effect of aluminium incorporation into C-(A)-S-H on chloride binding ability. Increased aluminium content in C-(A)-S-H reduced its chloride adsorption capacity, aligning with previous studies (Liu et al., 2024; Wilson et al., 2022; Yoshida et al., 2021). When increasing the chloride concentration, there was just a marginal change in the aluminium contents in C-(A)-S-H. However, the FA content significantly affected aluminium uptake, with greater FA contents leading to higher Al/(Al+Si) ratios. This supports the FTIR results and aligns with previous study observations (Kapeluszna et al., 2017). Elevated temperature also increased the aluminium uptake in C-(A)-S-H, which was more evident at exposure to higher chloride concentrations. However, no such definite trend could be observed for low chloride contents.

Overall, from the EDS point analysis, it can be summarized that chloride adsorption in C-(A)-S-H is strongly linked to the Ca/Si ratio, with aluminium content having a lower impact.

4.3.7 Ionic composition of binder pore solution

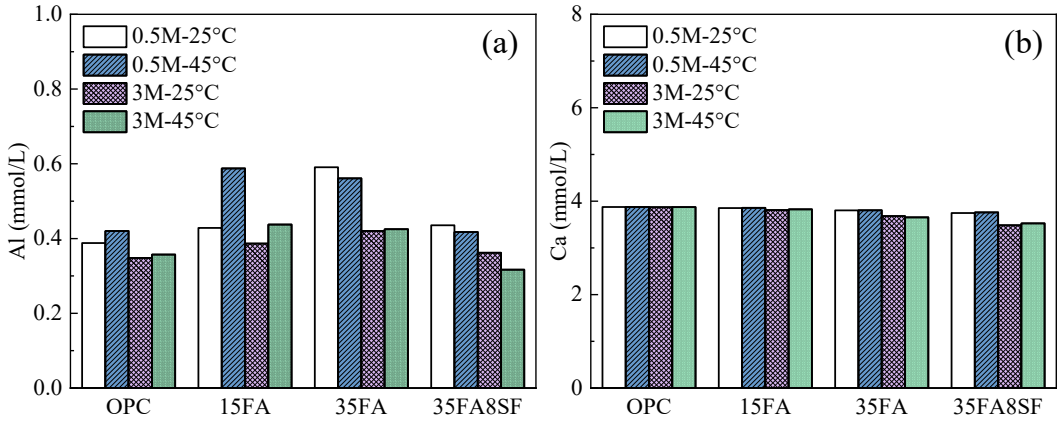

Figure 4.11. Aluminium and calcium ion concentration in pore solution

The reaction of aluminium with different cement hydration phases will inevitably change its concentration in the pore solution. In addition, calcium has been known to affect the chloride adsorption in C-A-S-H. Thus, the concentration of aluminium and calcium ions was determined by ICP-OES and is provided in Figure 4.11. The amount of aluminium was within the limits of 0.4 mmol and 0.8 mmol, as has been reported in previous literature (Vollpracht et al., 2016). The aluminium concentration increased in the pore solution with the increase in fly ash substitution. (Yoshida et al., 2021). The calcium concentration for all the solutions was similar to that of the previous study (Vollpracht et al., 2016). Between the different mixes, there were minimal changes in calcium concentrations.

4.3.8 Discussions

A series of tests was conducted to evaluate the effect of chloride concentration and temperature on the physical and chemical chloride binding of blended cement pastes, with a particular focus on the properties of C-S-H and the contents of Friedel salts formed. The resultant free and bound chloride contents in different phases are summarized in Figure 4.12. The conventional understanding that increasing alumina-rich SCM proportions in cement mix increases chloride

binding is only valid to exposure at normal temperatures (25℃ in this study). However, at elevated temperatures (45 ℃), multiple factors affect the chloride binding process, making it challenging to establish a definitive trend. Based on the findings from this study, a new hypothesis has been proposed.

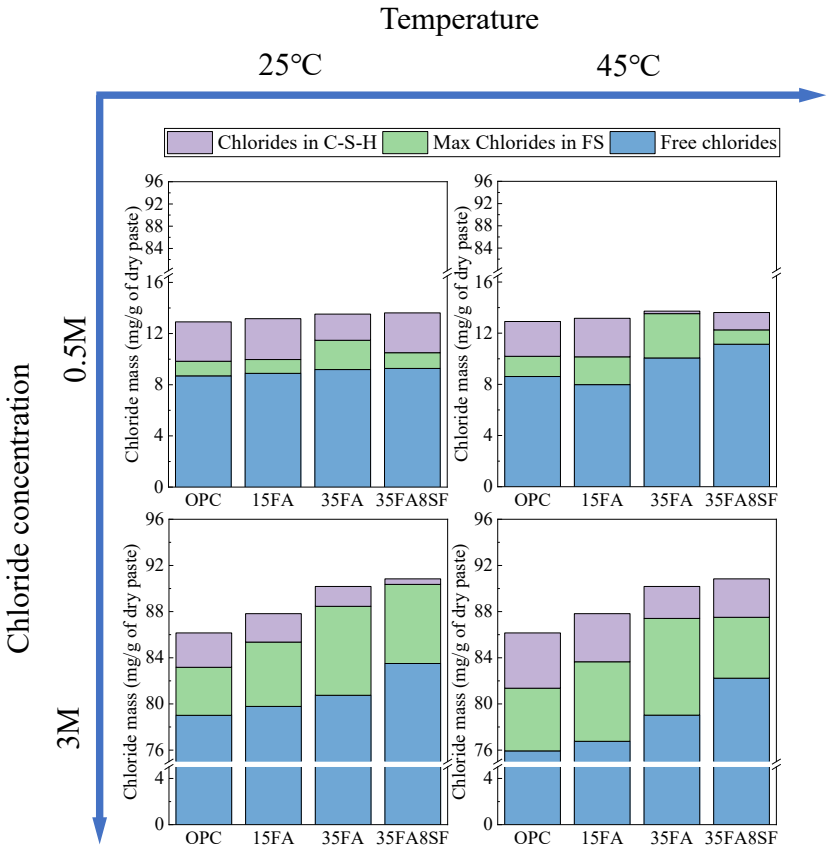

Figure 4.12. Chloride distribution in different phases at different chloride exposure concentrations and temperatures

The hydrated calcium aluminate phase (AFm) in cement usually coexists with certain anions such as hydroxyl, carbonates, sulphates, or chlorides. The presence of any of these anions depends on their relative concentrations. At low chloride concentrations, a part of AFm exists in the form of monosulphoaluminates, which, along with ettringite (AFt), transforms into Fridel salt at higher chloride contents. This transformation is facilitated by a lower pH, which reduces hydroxide ion concentration and competitive adsorption. Therefore, it can be assumed that all

AFm phases convert to Friedel's salt at high chloride concentrations, provided the aluminium content in the pore solution remains constant. With the use of SCMs like fly ash, which have low reactivity, the dissolution process can proceed slowly for prolonged periods. As the exposure temperature increases, the dissolution of fly ash accelerates, releasing more aluminium into the pore solution. These extra alumina can react with portlandite to form an additional AFm phase or partially replace silica in C-(A)-S-H (Wang et al., 2020).

The chemically bound chloride at different temperatures is related to Friedel salt contents and stability. At 25℃, the net-bound chloride content increased with the alumina content of the mix. For OPC, 15FA, and 35FA, the increase in Friedel salt with an increase in temperature is because of the accelerated transformation of AFt to Friedel salt and increased AFm formation due to the reaction of alumina with portlandite, which was observed through XRD. This was consistent for all chloride concentrations. In the 35FA8SF mix, at chloride levels of 0.5M and 1M, limited portlandite content hinders additional AFm formation, resulting in minimal changes in Friedel salt with temperature. (Saillio et al., 2019; Wang et al., 2020). When the chloride concentration was increased to 3M, the different aluminium-rich phases were transformed into Friedel salt. Thus, at 3M-25℃, the maximum chemically bound was nearly similar in both 35FA and 35FA8SF due to the equal amount of alumina in raw materials. However, when the portlandite was fully consumed (in the case of 3M-45 ℃), the pH dropped below 12, leading to the instability of Friedel salt and a significant drop in chemically bound chlorides (Hemstad et al., 2020; Jain et al., 2021).

The physically bound chloride was observed to be strongly linked to the Ca/Si of the C-(A)-S-H. The aluminium incorporation in C-(A)-S-H also limited its ability to adsorb chlorides. At a low chloride exposure of 0.5M, physically bound chlorides decreased with increased temperature exposure. EDX point analysis of 15FA and 35FA mixes showed a drop in Ca/Si ratios as temperature increased. Conversely, at a higher chloride concentration of 3M, the

Ca/(Si+Al) ratio increased with temperature. These phenomena can be explained by the solubility trends of portlandite and C-S-H at different temperatures and chloride levels. Temperature plays a predominant role at low chloride exposure, with elevated temperature leading to low dissolution. Thus, a reduced number of Ca^{2+} ions are adsorbed on deprotonated surface sites of ≡SiOH and ≡AlOH in C-(A)-S-H, which causes a net reduction in the ability of C-(A)-S-H to adsorb chlorides. At higher chloride contents, the inhibition effect of temperature on portlandite and C-(A)-S-H dissolution is minimal (Glasser et al., 2005). As a result, the chloride adsorption amount (physically bound chlorides) was directly linked to the nature of the endothermic reaction and increased for 45 °C compared to 25 °C (Tran et al., 2021).

Based on the above hypothesis, a schematic figure showing the variations in chemically and physically bound chlorides with temperature and chloride concentrations is presented in Figure 4.13.

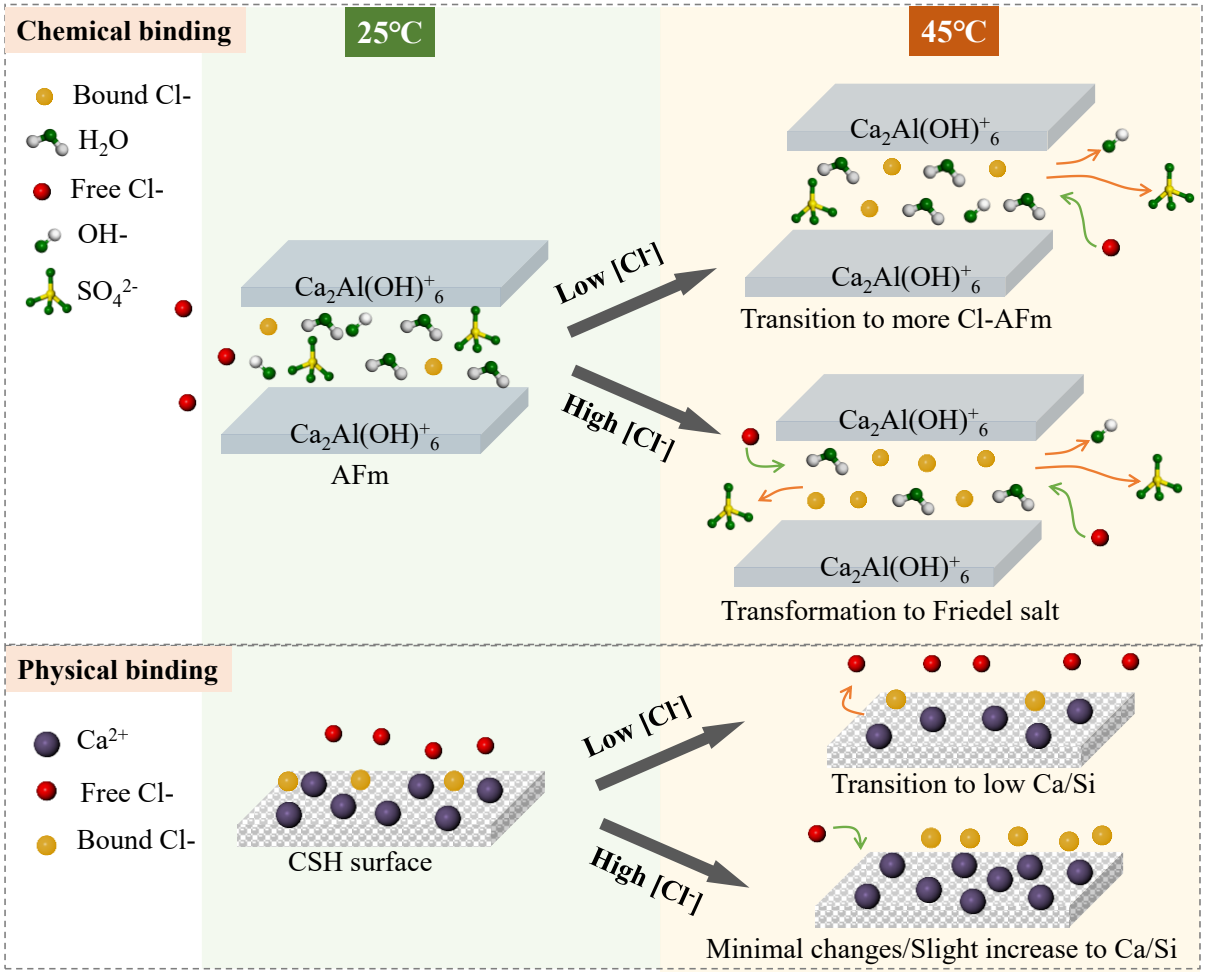

Figure 4.13. Schematic figure of chloride bound by AFm phase and C-(A)-S-H surface at different temperature exposures and chloride concentrations.

Implications on steel corrosion

The seawater usually has a concentration of about 0.5-0.6M of chlorides. In marine environments, pitting corrosion initiates when the chloride to hydroxyl ions ($[Cl^-]/[OH^-]$) in the pore solution exceeds a threshold value. The corresponding chloride content is usually referred to as threshold chloride concentration or critical chloride content (Angst et al., 2009; Li et al., 2020). While this critical value is often debated and has wide variations (Angst et al., 2009), it is acknowledged that a higher $[Cl^-]/[OH^-]$ in concrete pore solution leads to a high corrosion probability (Fan et al., 2021; Mundra et al., 2017). Thus, the susceptibility of steel to corrosion was evaluated for four binder compositions at two temperatures (25 °C and 45 °C)

when exposed to a fixed 0.5M total chlorides concentration, as shown in Figure 4.14. It can be observed that under the combined influence of elevated temperature and silica fume addition, which leads to a drop in pH and low chloride binding, the amount of chlorides necessary at the steel surface to initiate corrosion will be much lower. This suggests the importance of considering the temperature-influenced chloride binding for individual mixes when estimating service life against corrosion damage.

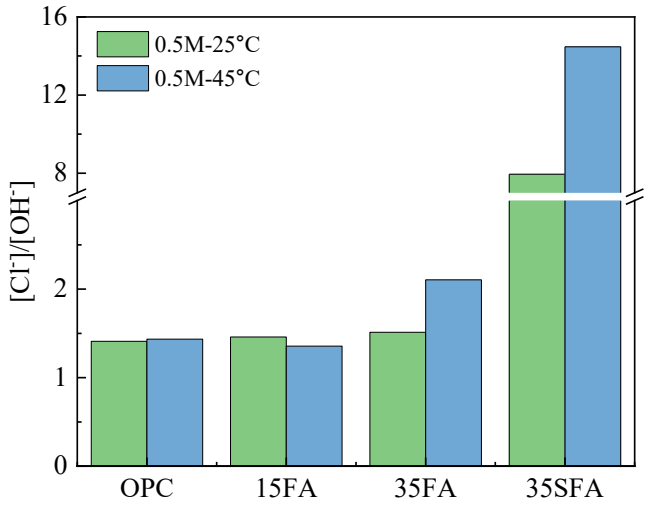

Figure 4.14. Impact of temperature on Cl/OH ratio in different binders

4.4 Overall Summary

Four different OPC-based mixes with two different contents of fly ash (15FA and 35FA) and a ternary blend (35FA8SF) were crushed into powder and exposed to different chloride concentrations (e.g., 0.5M, 1M and 3M) at two different temperatures of 25 ℃ and 45 ℃. After exposure for 8 weeks, the equilibrium solution was titrated for free chloride concentration and different characterization techniques were used for the binder. The conclusions from the study can be summarized as below:

(a) The chloride binding in mixes exposed to chlorides at room temperature increased with increasing fly ash content. This was due to the increase in alumina content of the mix.

For the mix containing a mixture of fly ash and silica fume, the chloride binding was nearly the same as OPC, thus negating the beneficial effect of adding fly ash. This was due to a reduced Friedel salt formation and reduced physically bound chlorides in low Ca/Si ratio based C-S-H/C-(A)-S-H.

(b) Increasing exposure temperature from 25 ℃ to 45 ℃ increased the chloride binding in mixes without silica fume for a high chloride exposure of 3M. This was due to an increase in chemically and physically bound chlorides.

(c) At a low chloride exposure of 0.5M, the chemically bound chloride increased at elevated exposure temperature for mixes without silica fume. But, there was a drop in physically bound chlorides in C-S-H. The two counter effects led to only a marginal drop in total bound chlorides for mixes OPC and 15FA. However, the total bound chlorides dropped significantly for mixes 35FA and 35FA8SF.

(d) TGA and XRD results suggested that higher Friedel salt at an elevated temperature of 45 ℃ could be linked to the faster transformation of ettringite (AFm) and other AFm phases to Friedel salt and also additional AFm formed by the reaction between C3A and portlandite. The change in trend for 35FA8SF was primarily linked to the absence of portlandite for additional AFm and low pH, which led to the instability of Friedel salt.

(e) The physical binding of chlorides was strongly linked to the Ca/Si in C-(A)-S-H and had a weak correlation with aluminium contents, i.e., Al/(Al+Si). At low chloride concentrations, portlandite's low solubility reduced Ca/Si at higher temperatures. However, at 3M chloride exposure, this temperature effect on portlandite solubility was countered, leading to increased physically bound chlorides due to the endothermic nature of the reaction.

CHAPTER 5

CHLORIDE THRESHOLD VALUE AND STEEL CORROSION SUSCEPTIBILITY IN DIFFERENT MORTARS

5.1 Introduction

Chapters 3 and 4 provided insights into how temperature influences the mechanism of interactions between steel and chloride ions and cement hydrates and chloride ions. While these two studies help to understand the impact of elevated temperatures on corrosion risk, they considered isolated cases of interaction, which may not fully capture the complexity in real service conditions. For example, in Chapter 3, the use of saturated $Ca(OH)_2$ simplifies the cement pore solution and does not consider the effect of different concrete micro-structures and pore solution chemistry. Chapter 4 ignores the nature of chloride transport through concrete pores.

Steel corrosion in concrete, as an electrochemical reaction comprising anodic oxidation of iron and cathodic reduction of oxygen, is influenced by micro-climate parameters like temperature, which varies based on geographic locations and also service conditions (Das, Ahmad, et al., 2025; Das, Zheng, et al., 2025; Michel et al., 2013; Otsuki et al., 2009; P. Zhang et al., 2023b). Elevated temperatures influence three critical aspects: (i) increase the diffusion coefficient of chlorides through concrete by a factor that depends on the activation energy of mixes (Care, 2008; Yuan et al., 2008), (ii) alter the stability and protectiveness of the passive film on steel (Deus et al., 2012) and (iii) influence chloride binding by the cement hydrates (Das, Ahmad, et al., 2025; Xiang-peng et al., 2023; Xu et al., 2016). These competing effects create a complex interplay, where the overall corrosion risk in steel reinforcement is governed by the dominance

of one mechanism over others. Studies evaluating corrosion susceptibility in concretes at elevated temperatures have focused on some specific aspects. For example, a few studies (Alhozaimy et al., 2012; Deus et al., 2014; Gastaldi & Bertolini, 2014) investigated the change in corrosion currents in chloride-admixed OPC mixes when exposed to elevated temperatures. Some other studies focused on the effect of temperature on passive film properties and corrosion potentials in alkaline solutions (Abd El Haleem et al., 2013; Deus et al., 2012; Poursaee, 2016). These studies provide some critical information on corrosion currents on passive and actively corroding steels. However, without a systematic investigation into reinforced concretes and mortars, it is unclear what chloride contents can cause the transition from passive to active steel (i.e., passivity breakdown) at elevated temperatures under real service conditions. Without this important information, as seen in a few studies (Chauhan & Sharma, 2019; Guo et al., 2020; Tong et al., 2025), the numerical models will have limited accuracy in predicting service life against reinforcement corrosion. The inaccurate assessment ultimately affects maintenance strategies for coastal infrastructures.

This study systematically investigates the corrosion performance of low-carbon steel embedded in four different OPC mortars modified with commonly used SCMs when exposed to chlorides at elevated temperatures of 45 ˚C, which is frequently observed in many cities around the tropical region. The corrosion performance is compared with identical mortars exposed to standard laboratory temperatures of 25 ˚C. The objectives are threefold: (1) to quantify temperature-dependent chloride threshold values, (2) to assess any benefits of adding siliceous SCM contents in these extreme conditions, and (3) to characterize the evolution of mortar properties. The investigation employs electrochemical techniques such as electrochemical impedance spectroscopy (EIS) and open circuit potential (OCP), along with chemical techniques such as chloride titration, thermogravimetric analysis (TGA), Raman spectroscopy and porosity estimation.

5.2 Experimental Program

5.2.1 Material preparation

The ribbed steel bars (500B as per BS 4449:2005) were used with chemical composition (C: 0.20, Mn: 1.16, P:0.012, Si:0.593, Cr:0.037, Ni:0.032, Cu:0.047, Mo:0.003, S:0.004). The steel bars, each 6 m in length, were cut into small sections of length 120 mm for chloride exposures. Then, they were sandblasted for about 5 minutes to remove any mill scale and contamination from the surface. This was done to ensure more repeatable test data. These steel sections were later soldered with wire at one end for electrical connections. This was followed by covering the rebar with epoxy for a length of 20 mm at both ends, leaving an overall exposed length of 80 mm in the middle. As a double protection, the epoxy-coated area of steel was also covered with heat shrinkage tubes, thus leaving an exposed area of 25.12 cm^2 (80 mm length) for electrochemical measurements. The prepared steel bars were later kept inside a vacuum container to prevent any oxidation until the day of casting.

Four mortar mixes were prepared for the study, as listed in Table 5.1. The rationale behind the second and third mixes was to evaluate the effect of different fly ash addition contents, which is one of the most commonly used SCMs. The fourth mix represents the mix proportion that is currently being used for coastal RC structures (e.g., piers) in Hong Kong. The cementitious materials (cement, fly ash, and silica fume) were obtained from a local supplier, and their oxide composition, as measured through XRF, is provided in Table 5.2. Normal river sand with particle sizes less than 4.72 mm was used for the preparation of mortar, and distilled water was used for all mixes. A water-reducing superplasticizer, Master Glenium SKY8588, was added during mixing to maintain proper flowability. The mortar mixing was done in a Hobart mixer to ensure a homogeneous distribution of fine aggregates in the mix. The mortar mix was then poured into molds of dimensions 100 mm × 44 mm × 44 mm, along with prepared steel rebar,

as discussed before. Four specimens were prepared for each mix, and the specimens were vibrated in their fresh state to ensure compaction and remove any air voids that may negatively affect the test results. Six cube samples of side 50 mm were also cast to determine the compressive strength of the mixes after 28 days and 90 days of curing.

Table 5.1 Weight ratios of raw materials for preparation of mortar samples

Sample ID	Cement	Fly Ash	Silica Fume	Water	Sand	Superplasticizer
OPC	1	-	-	0.38	3	0.01
15FA	0.85	0.15	-	0.38	3	0.01
35FA	0.65	0.35	-	0.38	3	0.01
35FA-8SF	0.57	0.35	0.08	0.38	3	0.01

Table 5.2 Oxide composition of raw materials obtained through XRF.

	CaO	SiO_2	Al_2O_3	Fe_2O_3	MgO	K_2O	TiO_2	MnO	SO_3
Cement	70.3	15.3	4.35	3.74	0.855	0.662	0.342	0.050	4.06
Fly ash	6.45	56.2	21.8	8.33	2.25	1.68	1.70	0.073	0.752
Silia fume	0.21	97.1	0.40	0.13	0.51	0.50	-	-	1.03

The cast samples were wrapped with a plastic sheet, demolded after 24 hours and cured in a sealed box for 28 days at a constant humidity level of above 90% and a temperature of about 20 ℃. During the curing period, the samples with steel reinforcements were periodically measured for their evolution of electrochemical behavior.

After the end of the curing period, the samples were sealed with epoxy and waterproof tapes on five sides, leaving one side for exposure. Since there is a higher chance of defects at the steel-concrete interface on the casting surface and bottom side, one of the two lateral sides was considered for exposure to chloride solution (K. Li et al., 2024). The exposure scheme consisted of immersion of steel samples in 3.5% NaCl solutions, which was increased to 5% after 50

weeks of exposure and 16.5% after 60 weeks of exposure to accelerate chloride ingress and reduce the time for corrosion initiation. The same steps were followed for both samples exposed to different temperatures (25 ˚C and 45 ˚C). The temperatures representing the two conditions were controlled through a thermostatic water bath. The experimental setup is presented in Figure 5.1. Analytical-grade NaCl was used throughout the experiments.

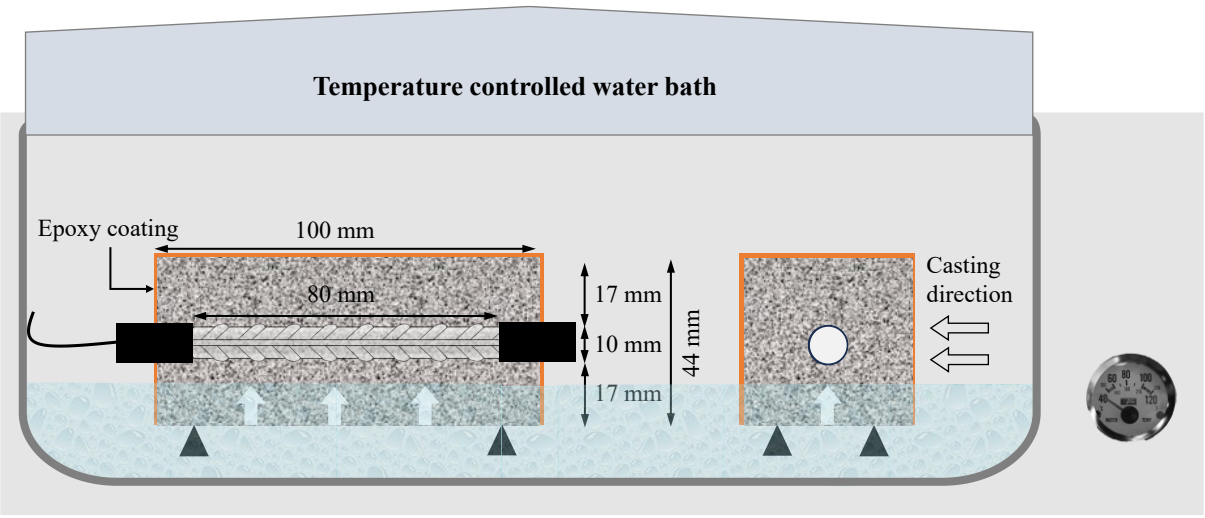

Figure 5.1. Test setup for chloride exposure at 25 ℃ and 45 ℃.

5.2.2 Electrochemical measurements

The different electrochemical measurements were conducted using Metrohm Autolab Workstation PGSTAT302N. The electrochemical setup was a three-electrode system consisting of a stainless steel plate as the counter electrode (CE), a steel rebar as the working electrode (WE), and a saturated calomel electrode as the reference electrode (RE). Thus, all the subsequent potentials in this paper are mentioned with reference to a saturated calomel electrode (SCE). The counter electrode had an area of 40 cm^2 and was placed on the exposed surface of the mortar during electrochemical measurement (Das et al., 2023). A wet sponge was placed between the CE and the mortar for contact during the electrochemical measurements.

The open circuit potential (OCP) was measured periodically every 2 weeks for all the samples. The OCP data was noted once the values stabilized ($\frac{dV}{dt} = 10^{-6}$V). The electrochemical impedance spectroscopy (EIS) measurements were conducted over a frequency range of 0.01 Hz to 100 kHz using an AC perturbation voltage of 10 mV (Das et al., 2023). Five points were noted for every decade in the frequency range.

5.2.3 Corrosion morphology and rust characterization

At the end of the exposure period, the samples were split to observe the morphology of the steel surface and evaluate the severity of steel corrosion in different mixes exposed to chloride solutions at the two temperatures.

The steel samples were immediately vacuum-sealed to preserve them for rust characterization. The characterization of rust products was conducted using Micro-Raman spectroscopy with a 532 nm laser. The Raman mapping technique was used to capture the heterogeneity associated with the distribution of different iron oxides generated over the steel surface. Raman mapping was conducted over a spectral region of 72 to 1843 cm^{-1} with an exposure time of 100 seconds and a laser power of 1 mW (Mi, Wang, et al., 2023). The scanning area of the sample comprised a square region with an edge length of 188.5 μm. The two samples scanned were 35FA-25℃ and 35FA-45℃ to identify the effect of temperature on corrosion products formed.

5.2.4 Chloride contents at the steel surface

The corresponding chloride contents that led to corrosion were then evaluated by scraping some mortar powders near the corroded areas. These powder samples were ground further and passed through a 75 μm sieve. For analyzing the total chloride content, about 0.4 gram of powder sample was added to 4 ml of 10% nitric acid and continuously shaken for 24 hours, after which the leachate was filtered through a 0.45 μm filter and titrated using 0.01M $AgNO_3$ through a

Mettler Toledo auto titrator (Angst et al., 2011). About 0.2-0.3 grams of powders were diluted ten times with deionized water and shaken for 24 hours in airtight centrifuge tubes to analyze water-soluble chlorides (Maradani & Pradhan, 2024). The suspension was filtered through a 0.45 μm filter and tested for pH using a standard pH meter and chloride content by an auto-titrator.

5.2.5 Characterization of mortar properties

The compressive strength of the different mortars was measured on cubes of dimensions 50 mm after 28 days and 90 days of curing at normal room temperature (20 ℃) in sealed boxes maintained at 90% humidity. The compressive strength was determined as per ASTM C109. The results reported are average compressive values of three samples at each testing age.

The pH of the mortars during passivation was measured using the cold water leaching method (Ranger et al., 2023). Small pieces of mortar obtained after compressive strength tests at 28 days were ground into powders using a mortar and pestle and sieved through a 75 μm sieve. About 10 grams of powder were mixed with 10 grams of deionized water and stirred with a magnetic stirrer for 5 minutes. The solution was then filtered using a 0.45 μm filter and tested using standard pH.

In order to assess the effect of exposing the steel-embedded mortars to chlorides at elevated temperatures on concrete degradation, the surface 3 mm layer of samples was chiselled out and ground to powder using a mortar and pestle. About 10-15 mg of the ground powders sieved through a 75 μm sieve were then tested to compare the changes in mineral phases using Thermogravimetric analysis (TGA) in Rigaku Thermoplus EVO2. For TGA, two representative mixes (15FA and 35FA8SF) were heated in an aluminium pan from 40 ℃ to 1000 ℃ at a heating rate of 10 ℃/min.

The porosity of two mortars (15FA and 35FA8SF) was also analyzed to identify the effect of changes in the mineral phases on the overall porosity of the samples. For this, the samples were crushed to dimensions of about 3-5 mm, and 6 grams of each sample were analyzed using mercury intrusion porosimeter (MIP, AutoPore IV 9500, Micromeritics, USA).

5.3 Results

5.3.1 Open circuit potential of steel bars

Figure 5.2 represents the variation of OCP of steel samples during the experiment period. After casting steel bars in the different mixes, the samples showed negative potential values (about -0.2V vs SCE), denoting the uncertain corrosion stage of steel bars. However, with further curing, the OCP of samples underwent a positive shift and went into the passive zone (> -0.126V vs SCE as per ASTM C876-15) after about two weeks. The passive state potential of steel samples varied with the binder chemistry, with OPC samples showing a slightly negative stable passivation potential compared to the samples containing fly ash and silica fume. Two possible reasons are attributed to this behavior: a lower oxygen availability due to the dense microstructure in SCM-modified concrete, which limits the oxidation from Fe(II) to Fe(III), leading to greater Fe(II)/ Fe(III) and more negative potential (Zheng, Dai, et al., 2020b). A higher pH of the pore solution also results in partial dissolution of the passive oxide film with a reduction of the activity of Fe(II) (Abd El Haleem et al., 2010). This led to the ennobling of potential for steel in 35FA8SF samples where pH was lowest due to the pozzolanic reaction (refer to Section 3.6). With the addition of chloride ions, the potential of steel samples gradually shifted towards negative values, representing a transition from a passive to an active state. For OPC samples, the increase in temperature from 25 ℃ to 45 ℃ reduced the time of corrosion initiation from 36 weeks to 12 weeks (67% reduction). When replaced by 15% FA in the binder, the reduction in corrosion initiation time was 62%, which further reduced to 61% in 35FA

samples and 55% for 35FA8SF samples. Thus, elevated temperature significantly increased the corrosion susceptibility in all mortars. However, with high SCM addition (e.g., 35FA and 35FA8SF), the increased corrosion risk due to elevated temperature could be partially alleviated.

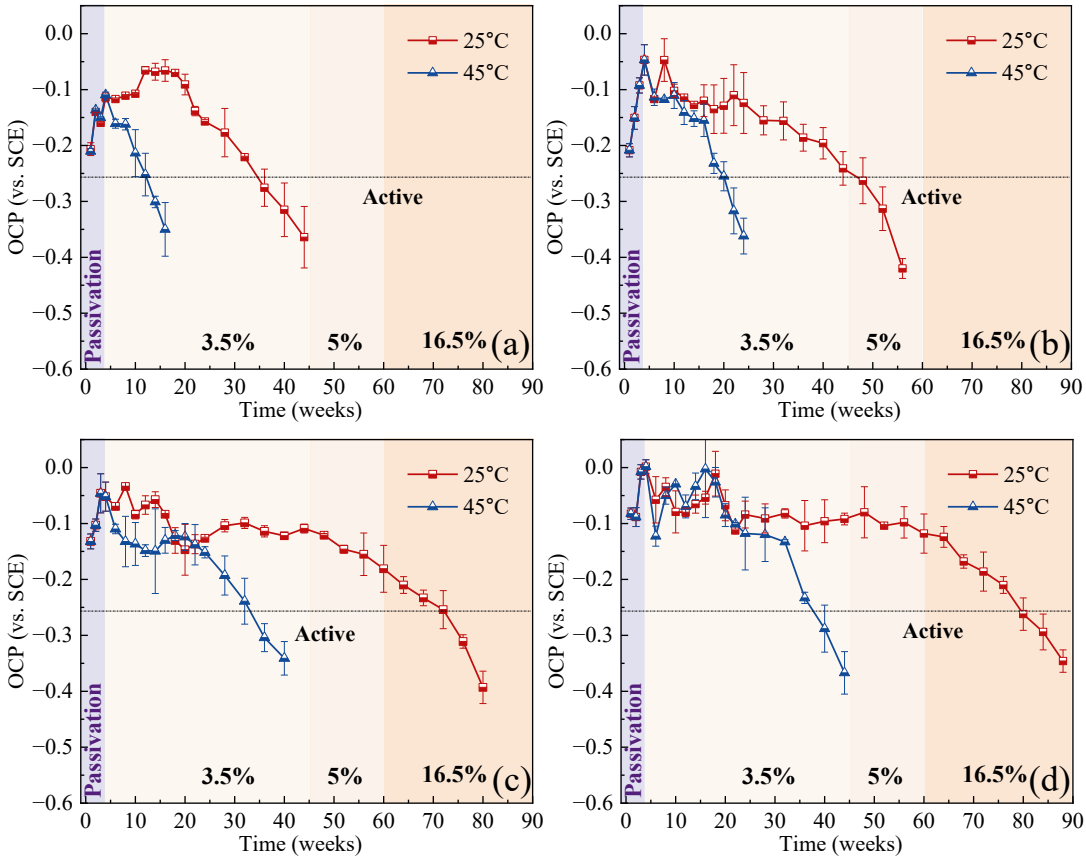

Figure 5.2. Variation in open circuit potential values during the exposure period for steel embedded in (a) OPC, (b) 15FA, (c) 35FA and (d) 35FA8SF binders at 25 ℃ and 45 ℃.

5.3.2 Electrochemical Impedance Spectroscopy (EIS) analyses

Passivation behaviour during curing

In addition to periodical OCP measures, which provided qualitative information about the corrosion potential of steel bars, EIS measurements were conducted to gain an in-depth

understanding of the state of the steel bar embedded in mortars. The EIS response of the embedded steel rebars in the three different mixes during their curing stage, as observed from Nyquist and Bode plots, is presented in Figure 5.3. It can be observed that there is a progressive increase in the capacitative arc radius of the Nyquist plot with exposure time in the solution. This is also accompanied by an increase in the phase angle at the low-frequency region of Bode's plot. On comparing different mixes, the lowest point of the Nyquist plot, which represents the mortar cover resistance, can be observed to be higher for Mix 35FA8SF and lowest for Mix OPC. In addition, the total impedance at the low-frequency part (observed in Bode's impedance plot) followed an increasing trend with silica contents from fly ash and silica fume.

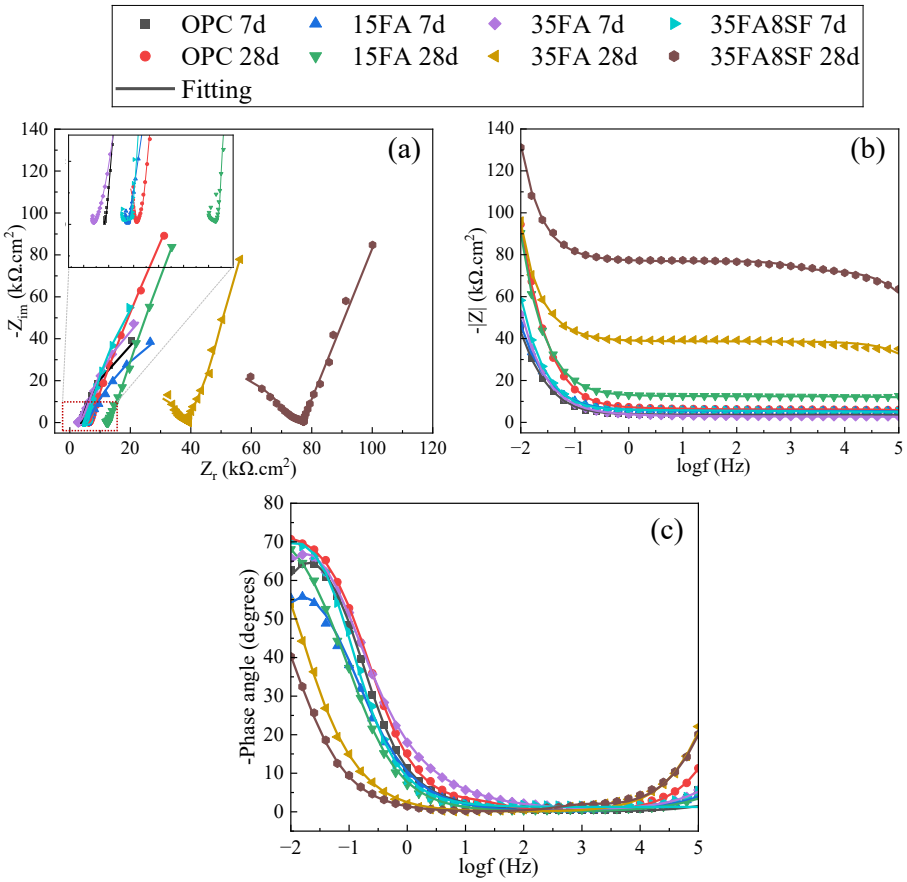

Figure 5.3. EIS response of steel bar cured in different binder systems expressed in terms of (a) Nyquist plot, (b) Bode impedance plot and (c) Bode phase angle plot.

Thus, to clarify the impedance response from different processes (e.g., mortar cover, steel-pore solution interface and steel passive film) contributed at different frequencies, the Nyquist and Bode plots were fitted following different equivalent electrical circuits. The choice of the circuits was based on the physical interpretation of different corrosion cell components (M. Liu et al., 2017; Zheng, Poon, et al., 2020). Finally, one equivalent circuit with one loop in series with two hierarchical parallel RC loops (Figure 5.4 (a)) and another equivalent circuit with three loops in series (Figure 5.4 (b)) was adopted to fit the EIS data. The three-time constants consider the evolution of mortar properties, passive film properties, and reactions at the steel-pore solution interface. For the different RC loops, a constant phase element (CPE) was used instead of capacitance during analysis to account for the deviation from ideal capacitance behavior. The deviation is primarily linked to the different surface inhomogeneities, such as the roughness of the steel substrate.

The relationship between capacitance (C) and CPE:

$C = \frac{(CPE.\ R)^{-n}}{R}$ where n represents the phase shift value (ranging from 0 to 1)

CPE is generally defined as:

$CPE = Y_0\ (jw)^n$ where n is a value between 0 and 1, Y_0 is the magnitude, j is the imaginary root, and w is the angular frequency.

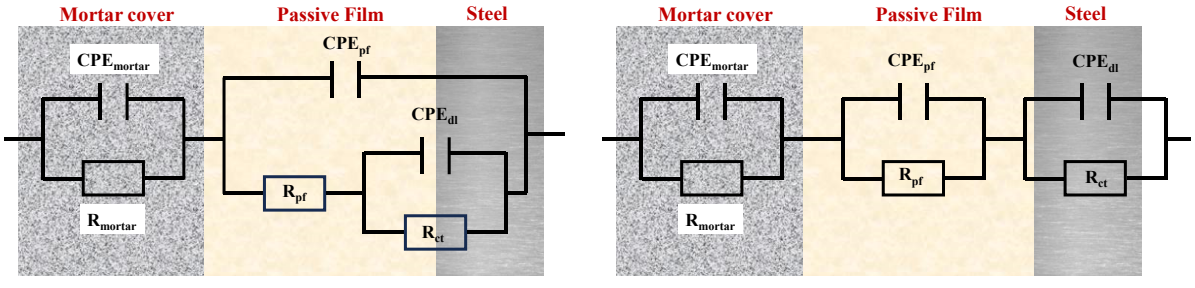

(a) (b)

Figure 5.4. Equivalent electrical circuit (EEC) for the proposed study.

In the equivalent circuit shown in Figure 5.4, the high-frequency RC time constant is related to the mortar properties (mortar resistance, R_m and capacitance, CPE_m), which vary with the mix proportions and evolve due to the exposure to chloride solution at different temperatures. The RC time constant corresponding to the medium frequency range represents the passive film properties (i.e., passive film resistance, R_{pf} and passive film capacitance, CPE_{pf}), and the low-frequency time constant corresponds to the processes at the steel-solution interface (charge transfer resistance, R_{ct} and faradaic pseudo double layer capacitance, CPE_{dl}).

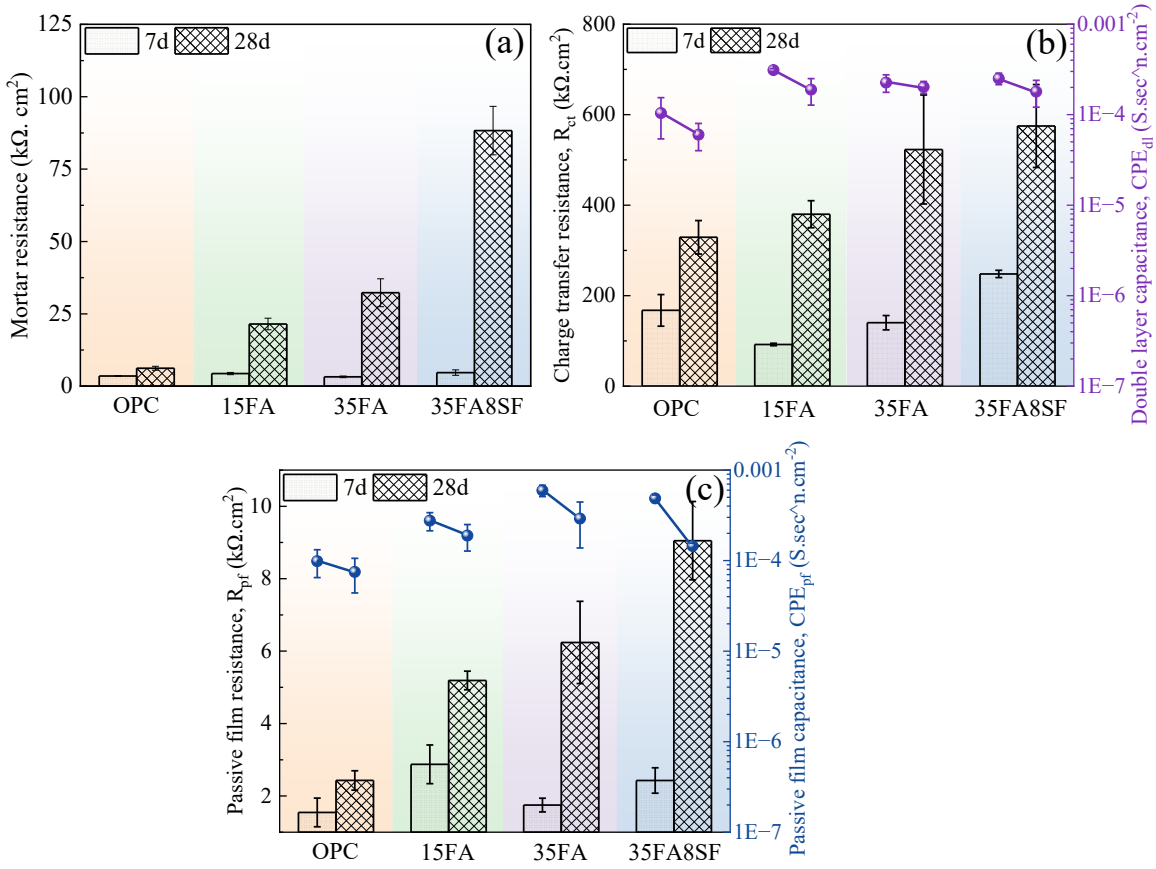

Figure 5.5. Variation of (a) mortar resistance, (b) passive film properties and (c) charge transfer behaviour of passive film during curing conditions.

For fitting the EIS data during the passivation stage (before chloride exposure), EEC from Figure 5.4 (a) was used. The impedance characteristics (comprising resistive and capacitive components) of three mortar mixes were analyzed from the EIS response throughout the curing process, as shown in Figure 5.5. Between 7 and 28 days of curing, a steady rise in resistive parameters (R_m, R_{pf}, R_{ct}) was observed across all mixes. This reflects the formation and growth of passive film during the curing period of 28 days. The CPE values corresponding to passive film and double-layer capacitances also experienced a drop, confirming the growth of a stable passive film on the steel surface, reducing its permeability and the charge accumulated at the metal-pore solution interface.

Comparing the impedances of the four different mixes at 7 or 28 days, it can be observed that the addition of SCMs at different levels led to changes in all of R_m, R_{pf}, and R_{ct}. The 35FA8SF blend (35% fly ash, 8% silica fume) exhibited the highest matrix resistance, while the ordinary Portland cement (OPC) mix showed the lowest. This variation is primarily linked to higher pozzolanic reactions in 35FA8SF, which consumes calcium hydroxide to form a denser matrix over time and refinement of pore structure. While differences in matric resistance were marginal in the early days of curing, they became much more pronounced after 28 days. This pore structure densification also reduced oxygen diffusion to the steel surface, thereby limiting the oxidation of Fe to Fe(II) and Fe(III). Fe(II) based oxides generally have a greater protection ability (i.e., greater resistance) than Fe(III) (Ghods et al., 2011; Zheng, Poon, et al., 2020). Hence, with greater fly ash and silica fume in the mix (i.e., 35FA8SF), the passive layer had higher Fe(II)/Fe(III) ratios and demonstrated the highest passive film resistance among the four mixes. This finding challenges the traditional belief that a lower pH level should weaken the protective passive film, as seen in experiments with simulated pore solutions.

The reduced pore solution alkalinity due to pozzolanic reactions, as subsequently shown in Section 5.3.6, can slow down redox reactions involving hydroxyl ions (OH^-). This reduction in electrochemical reactions at the steel surface increases the corrosion resistance, leading to reduced corrosion current densities in supplementary cementitious material (SCM)-modified mortars compared to OPC (Zheng, Poon, et al., 2020) (Ortolan et al., 2016; Scott & Alexander, 2016; Simões et al., 2024; Zheng, Poon, et al., 2020). Therefore, the effectiveness of the passive film is not solely dependent on the pH of the pore solution but instead has to be supplemented with the local microstructure and oxygen availability at the steel surface. Considering that experiments conducted in simulated pore solutions cannot capture these changes, the observed passivation trend is directly related to the pH of the solution.

Exposure to NaCl solutions at different temperatures

After curing at room temperature, the samples were exposed to chloride solutions at different temperatures. The chloride transport was unidirectional, and the resulting changes in impedance spectra, represented through Nyquist and Bode plots, are provided in Figure 5.6. Three trends can be distinctly identified from the plots. First, Prolonged chloride exposure progressively reduced the capacitive arc radius in Nyquist plots, signifying diminished corrosion resistance. Second, extended chloride exposure lowered the phase angle at the lowest frequency (10 mHz) across all samples, confirming chloride-induced deterioration of the steel's passive film. Third, incorporating supplementary cementitious materials (SCMs), such as fly ash (FA) and silica fume (SF), shifted Nyquist plots toward higher real impedance values at elevated temperatures, indicative of improved bulk resistance.

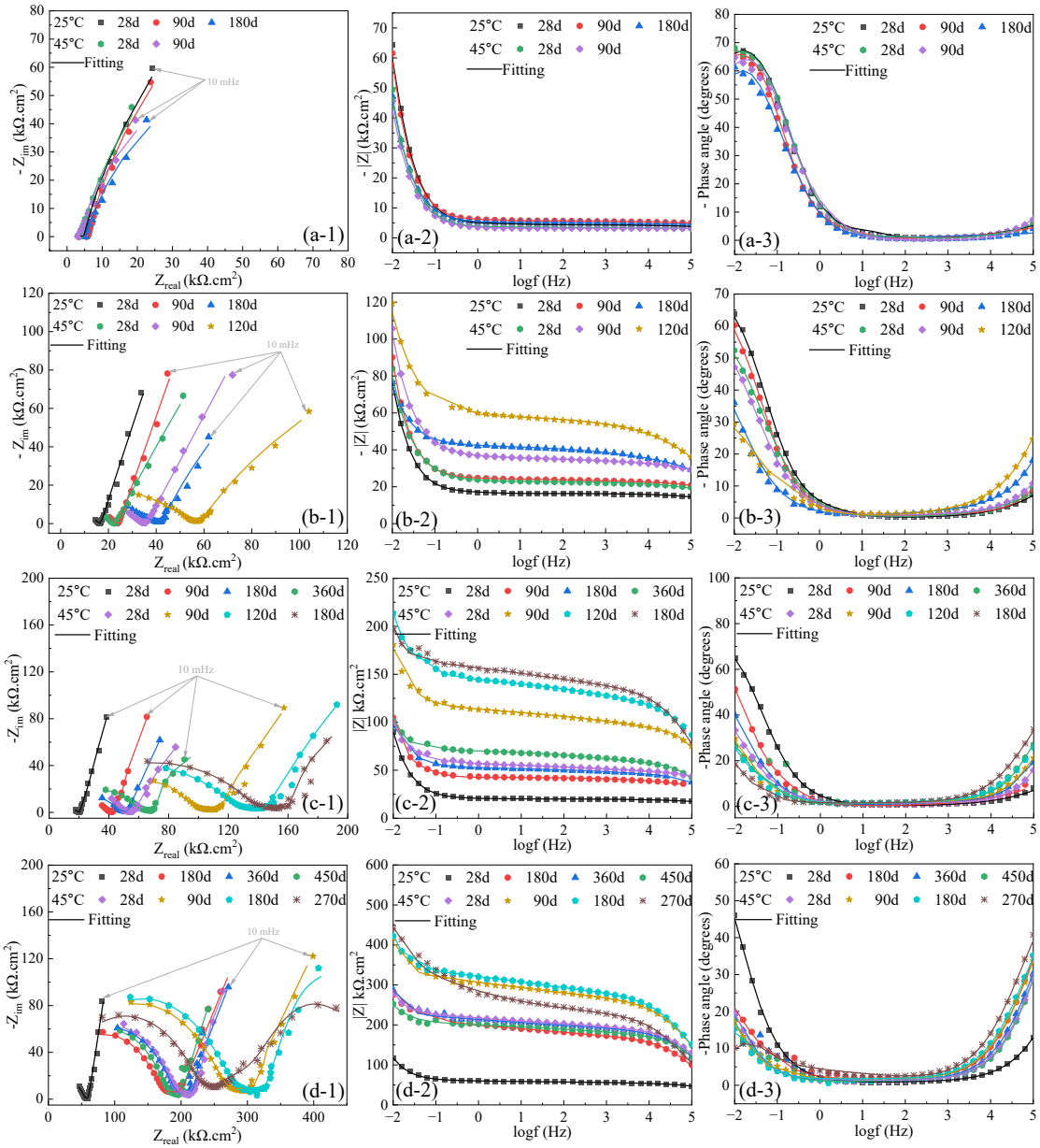

Figure 5.6. Evolution of EIS spectrum during chloride exposure in the format of (1) Nyquist plot, (2) Bode impedance plot and (3) Bode phase angle plot for steel samples embedded in (a) OPC, (b) 15FA, (c) 35FA and (d) 35FA8SF binders at 25 °C and 45 °C.

The EIS data were modeled using equivalent electrical circuits (EECs) featuring three RC time constants, selected based on physical relevance and prior studies. While choosing one of the two EECs provided in Figure 5.4, care was taken to ensure that the chi-squared values were in the range of 10^{-3} or even lower to minimize the fitting error. The detailed fitting parameters for

two samples of each mix representing the evolution of resistances and capacitances for different samples are provided in Table 5.3. Additionally, the variation of polarization resistance, Rp (denoted as the sum of passive film and charge transfer resistance) for different samples during exposure to NaCl solution is provided in Figure 5.7.

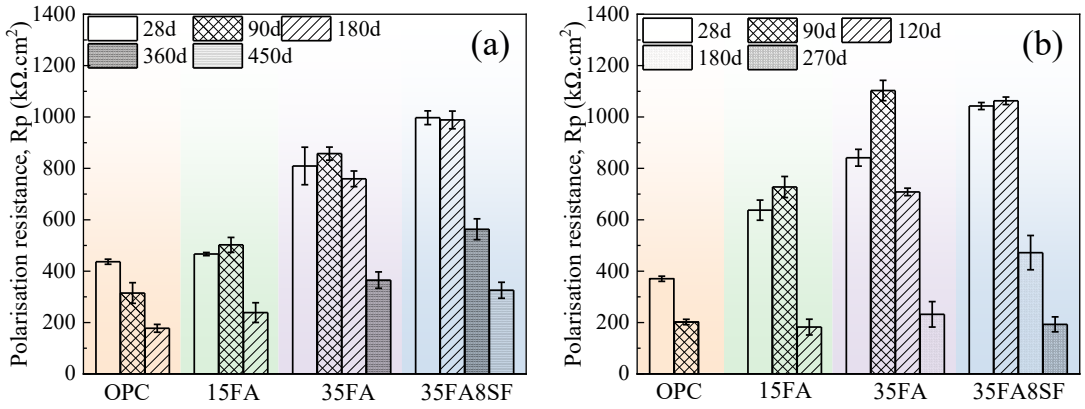

Figure 5.7. Evolution of polarization resistance, Rp, during chloride exposure for samples exposed to chlorides at (a) 25 ℃ and (b) 45 ℃.

Comparative analysis of the four mixes after 28 and 90 days of exposure revealed that SCM incorporation (FA and SF) enhanced mortar resistance and passive film resistance, highlighting their efficacy in mitigating chloride ingress. For instance, the mortar resistance for 35FA8SF samples at 28 days was more than 10 times higher than that of control OPC samples when exposed at 25 ℃ and about 30 times higher when the exposure temperature was 45 ℃. On the contrary, OPC samples showed reduced mortar resistance at higher temperatures due to accelerated ionic mobility. The superior resistance of SCM-modified mortars at elevated temperatures was attributed to more pronounced pozzolanic reactions, which consumed hydroxyl ions (OH^-) and refined the pore structure, limiting oxygen diffusion to the steel. This microstructural refinement likely increased the Fe(II)/ Fe(III) ratio in the oxide film, enhancing charge transfer resistance. As a result, the passive film resistance and charge transfer resistance

were significantly higher for SCM-modified samples (15FA, 35FA and 35FA8SF) exposed to chlorides at 45 ℃ compared to their counterparts at 25 ℃ during the initial days of exposure (e.g., 28 days and 90 days) before chlorides have reached the steel reinforcement. For example, after 28 days of exposure, the Rp was higher by 36% for the 15FA mix, 11.7% for the 35FA mix, and 6% for the 35FA8SF mix compared to their corresponding samples at 25 ℃. In addition to higher resistance, the samples exposed to elevated temperatures demonstrated lower capacitance values for the passive film. This has two implications: (1) the formation of a denser, more protective passive layer and (2) reduced pore solution alkalinity from ongoing pozzolanic reactions, which may lower the critical Cl^-/OH^- ratio required for corrosion initiation.

However, despite the improved polarization and mortar resistance for SCM-modified samples at earlier exposure periods, the chloride-induced corrosion risk was more severe for samples exposed to NaCl solutions at 45 ℃ in prolonged exposure. This could be observed in the trend of both passive film and charge transfer resistance, which dropped significantly earlier than those at 25℃. Thus, in summary, the electrochemical behaviour of steel at elevated temperature exposure can be summarized in two stages:

1. Initial Stage (Pre-Chloride Arrival): Enhanced pozzolanic activity at 45 °C improves passive film stability and charge transfer resistance.
2. Later Stage (Post-Chloride Arrival): Despite early benefits, prolonged exposure accelerates corrosion due to synergistic effects of elevated temperature promoting higher chloride ingress.

Table 5.3: Fitting data from EIS analysis of samples after different exposure days

Mix	Time (days)	CPE_{mortar} μS·sec^n·cm^{-2}	N1	R_{mortar} kΩ.cm^2	CPE_{pf} μS·sec^n·cm^{-2}	N2	R_{pf} kΩ.cm^2	CPE_{dl} μS·sec^n·cm^{-2}	N3	R_{ct} kΩ.cm^2	Chi sqrd	Error %
OPC25	28d	0.19 ±0.01	0.69±0.1	4.32±0.11	16.25±10.8	0.59	0.58±0.08	134.00±22.2	0.87±0.1	436.00±10	3.14E-04	1.55
	90d	0.63±0.01	0.47±0.1	5.93±0.18	31.30±9.8	1.00	0.65±0.12	129.10±14.4	0.87±0.1	314.20±40	2.54E-04	1.52
	180d	3.36±0.31	0.54±0.1	5.90±0.35	147.25±34	1.00	1.05±0.26	109.90±6.1	0.80±0.1	176.60±15	5.95E-04	2.44
OPC45	28d	0.035±0.01	0.55±0.1	4.24±0.75	31.47±16.6	1.00	1.19±0.15	145.11±71.6	0.83±0.1	369.20±10	1.96E-04	1.36
	90d	0.022±0.01	0.79±0.1	3.46±0.21	81.47±5.233	1.00	1.60±0.16	113.28±32.8	0.83±0.1	200.45±10.6	4.74E-04	2.25
15FA25	28d	0.045±0.01	0.43±0.1	15.23±0.70	110.00±0.01	1.00	19.24±1.3	103.30±0.7	1.00±0.1	447.50±7.5	3.37E-04	1.83
	90d	0.027±0.01	0.44±0.1	24.95±0.76	103.90±1.20	1.00	30.83±2.5	111.25±12.6	1.00±0.1	471.50±31.5	4.38E-04	2.09
	180d	0.37±0.02	0.28±0.1	32.66±1.82	392.40±41.4	1.00	14.30±2.8	548.00±365	0.79±0.1	224.50±35.5	1.29E-04	1.06
15FA45	28d	0.447±0.04	0.17±0.1	22.68±3.92	12.15±2.15	1.00	26.9±0.5	152.05±27.6	0.79±0.1	610.50±40.5	1.65E-04	1.51
	90d	0.019±0.01	0.31±0.1	35.37±0.11	76.06±0.71	1.00	36.59±2.93	137.52±59.5	0.88±0.1	691.00±43	3.99E-04	1.97
	180d	0.53±0.05	0.40±0.1	46.41±8.93	92.02±8.99	1.00	6.97±1.07	397.15±143	0.74±0.1	175.50±4.5	4.39E-04	2.10
35FA25	28d	0.021±0.01	0.47±0.1	19.15±1.01	2.92±0.33	0.84	17.17±2.3	174.75±35	0.91±0.1	742.25±20.8	1.33E-04	1.15
	90d	0.022±0.01	0.45±0.1	40.88±1.72	60.71±11.29	1.00	20.64±1.32	115.45±18.7	1.00±0.1	836.85±26.9	4.40E-04	2.04
	180d	0.356±0.04	0.49±0.1	46.66±0.84	61.98±0.6.98	0.66	20.21±2.69	131.55±10.4	0.44±0.1	739.20±27.9	3.03E-05	0.53
	360d	0.007±0.01	0.32±0.1	64.55±1.66	84.60±10.6	1.00	15.72±1.43	275.90±73.9	1.00±0.1	349.50±30.5	5.91E-04	1.92
35FA45	28d	0.00003	1.00	30.65±3.11	2.50±0.47	0.17	35.26±1.12	120.15±32	0.76±0.1	806.25±33.7	1.84E-04	1.27
	90d	0.00003	1.00	41.96±1.76	0.86±0.13	0.12	91.47±13.84	133.27±33	0.91±0.1	1011.55±53.4	4.12E-04	2.03
	180d	0.00014	0.88±0.1	114.40±4.20	4.03±0.85	0.21	68.01±14.01	77.43±2	0.75±0.1	640.50±6	4.98E-05	0.67
	360d	0.00039	0.74±0.1	104.10±3.20	19.21±5.9	0.65	44.48±5.87	87.31±5.3	0.49±0.1	147.55±43.6	1.27E-04	1.09
35FA8SF25	28d	0.00085	0.80±0.1	51.59±3.16	0.52±0.22	0.63	35.61±3.71	119.80±8.7	0.82±0.1	961.65±30.4	7.84E-05	0.86
	180d	0.00224	0.77±0.1	74.59±13.74	0.47±0.07	0.60	52.11±8.06	131.65±22	0.90±0.1	936.55±43	3.09E-04	1.49
	360d	0.00018	0.77±0.1	136.50±5.70	2.19±0.1	0.64	46.69±5.5	162.70±58.7	0.77±0.1	516.50±35	3.84E-04	1.70
	450d	0.00027	0.76±0.1	130.15±3.75	3.36±0.39	0.67	35.32±2.9	313.2±37.8	0.81±0.1	290.35±28	4.91E-04	2.12

35FA8SF45	28d	0.00002	1.00	115.98±6.77	0.22±0.05	0.25	120.25±18.8	63.79±13.9	0.68±0.1	922.50±32.5	3.08E-04	1.88
	180d	0.00024	0.72±0.1	247.60±7.50	5.83±0.35	0.20	98.08±4.8	12.8±1.56	1.00	965.10±9.8	2.69E-04	1.58
	360d	0.00036	0.72±0.1	240.75±2.55	5.95±1.7	0.24	88.80±4	88.93±9.8	1.00	383.30±70.6	1.11E-04	1.04
	450d	0.00040	0.72±0.1	220.65±8.25	12.95±4.07	0.32	73.45±2.91	99.89±6.3	1.00	119.40±32	7.20E-05	0.84

5.3.3 Chloride threshold value for corrosion initiation

After splitting, mortar powder (about 0.6-1 grams) was extracted from the vicinity of steel reinforcement on the exposure side using a small drilling machine and immediately sealed in airtight tubes to avoid any carbonation. These powder samples were analyzed for total chloride contents and free chloride contents, and the results obtained are provided in Figure 5.8. The samples where corrosion was observed to initiate at the ends of the steel bar (indicating flaws during sample preparation) were not considered for chloride threshold calculation.

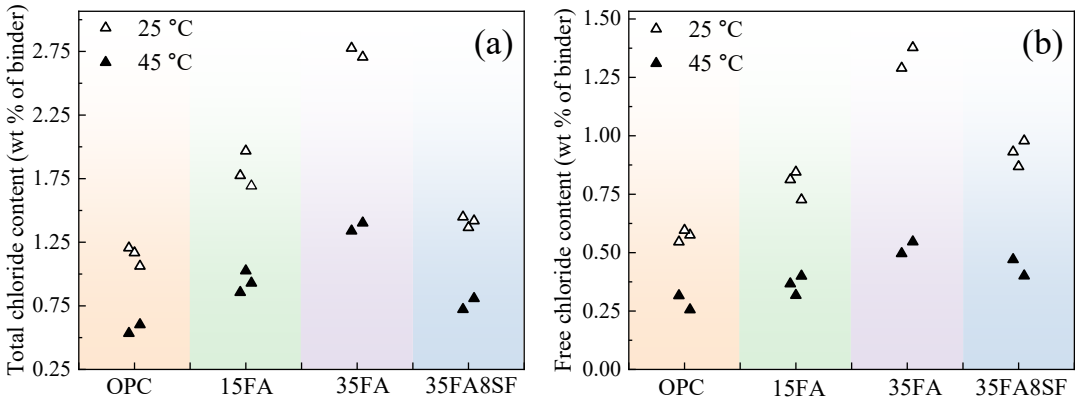

Figure 5.8. Chloride threshold value of steel embedded in different mortars expressed in terms of (a) Total chloride content and (b) Free chloride content.

It was observed that adding fly ash to mortars increased the total chloride threshold value (refer to Figure 5.8 (a)) for corrosion initiation. For example, replacing 15% of cement with fly ash

increased the chloride content for corrosion initiation at 25℃ from 1.2% to 1.7% by binder weight, representing an increase of about 40%. The total chloride threshold value further increased to 2.75% by binder weight when fly ash content in the mix was increased to 35% (FA35). The beneficial effect of fly ash has been observed previously in literature studies (Angst et al., 2009; Yao et al., 2022). However, silica fume incorporation in the mix had a severe detrimental effect. In fact, the beneficial effect of fly ash on the chloride threshold was entirely neutralized by further adding 8% silica fume, resulting in a total chloride threshold value of about 1.30% in 35FA8SF samples, with only a minor increment as compared to the control OPC sample. This suggests that while silica fume addition significantly improves the pozzolanic effect in mortars and reduces the porosity, it has a negative effect even when used with high aluminium-rich SCM, like fly ash.

When comparing the free chloride contents (refer to Figure 5.8 (b)), the same trend was observed as the total chloride contents. Compared to the control OPC samples, adding 15% fly ash in mortars (15FA) improved the free chloride for corrosion initiation from 0.6% by binder weight to 0.85%, which further increased to 1.25% in 35FA samples. However, this was reduced to about 0.9% by binder weight in 35FA8SF samples. A comparison of the free and total chloride contents at the steel-mortar interface after corrosion initiation gives essential information about the amount of chloride bound to hydration products. When comparing the different mixes, it can be observed that about 50% of the chlorides remained bound to hydration products during corrosion initiation. With fly ash addition, the net-bound chlorides stayed fairly similar for 15FA samples but increased to about 55% for 35FA samples. This suggests that chloride binding was enhanced with fly ash addition in mortars due to higher aluminium content (He et al., 2024; H. Li et al., 2024). The most notable difference was observed in the 35FA8SF samples, where the bound chlorides were significantly lower, ranging only to 32%.

Exposing samples to chlorides at elevated temperatures of 45 ℃ significantly affected both total and free chloride contents, which initiated steel corrosion. For OPC samples, the drop in total chloride content was about 55% compared to values obtained during chloride exposure at 25 ℃. By increasing fly ash in mixes, i.e., in 15FA and 35FA, the drop in chloride threshold reduced to about 45% for 15FA but was about 62% for 35FA samples. The drop was also around 50% in a sample containing silica fume. No observable relation could be obtained for the effect of mix composition on the increased susceptibility of steel corrosion at elevated temperatures. However, all the samples showed a reduced chloride threshold of about 45% to 62% due to chloride exposure at elevated temperatures. One possible reason for the drop in corrosion threshold could be variations in passive film properties based on different temperature conditions, as observed in Chapter 3.

Considering chloride-induced corrosion susceptibility is sometimes expressed as [Cl-]/[OH-], the pH of the leachate was measured, and the ratios of free chloride content and hydroxyl ion concentration for different samples are provided in Figure 5.9. It was observed that the critical [Cl-]/[OH-] ratio, which marks the onset of corrosion, increased with the addition of mineral admixtures. The critical ratio for OPC when exposed to chlorides at 25℃ was 0.75, which was higher than the proposed value of 0.6 by Hausmann (Hausmann, 1967). A significant rise in this ratio was noted for mixtures containing only fly ash (i.e., 15FA and 35FA). The increase can be attributed to two main reasons: an improved chloride threshold and a reduction in the pore solution's pH due to the pozzolanic reaction. Upon further addition of silica fume to the 35FA8SF mix, the ratio increased marginally compared to 35FA. By increasing the exposure temperature to 45 ℃, the critical [Cl-]/[OH-] dropped by more than 50% for OPC and 15FA samples. In mixes with high SCM contents (35FA and 35FA8SF), the impact of temperature was even more pronounced, reducing the critical [Cl-]/[OH-] ratio to approximately one-third of the values recorded at 25 ℃. This indicates that the adverse effect of higher temperatures on

the chloride threshold is more severe for binders modified with high SCM content, thereby heightening the risk of corrosion.

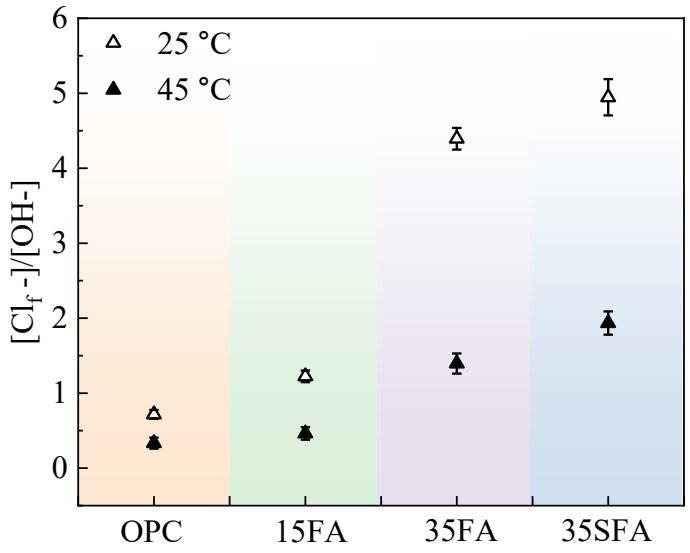

Figure 5.9. Ratio of [Cl-]/[OH-] at the steel mortar interface after corrosion initiation.

5.3.4 Corrosion Morphology

The mortar samples were split to reveal the steel surface after corrosion initiation was detected through OCP measurements. The morphology of observed corrosion in the steel reinforcements is presented in Figure 5.10. The corroded regions in the figures were primarily located in localized regions of the samples, particularly towards the central region, suggesting that there were no sealing defects at the ends that could accelerate corrosion. The samples exposed to chlorides at elevated temperatures of 45 ℃ showed darkish and orange spots, probably indicating more severe pit formation. This suggests that the formed corrosion products could differ based on the exposure condition, as previously reported in the literature (Zhao et al., 2011). Notably, no obvious casting defects were observed near the steel-mortar interface that could have adversely affected the corrosion initiation.

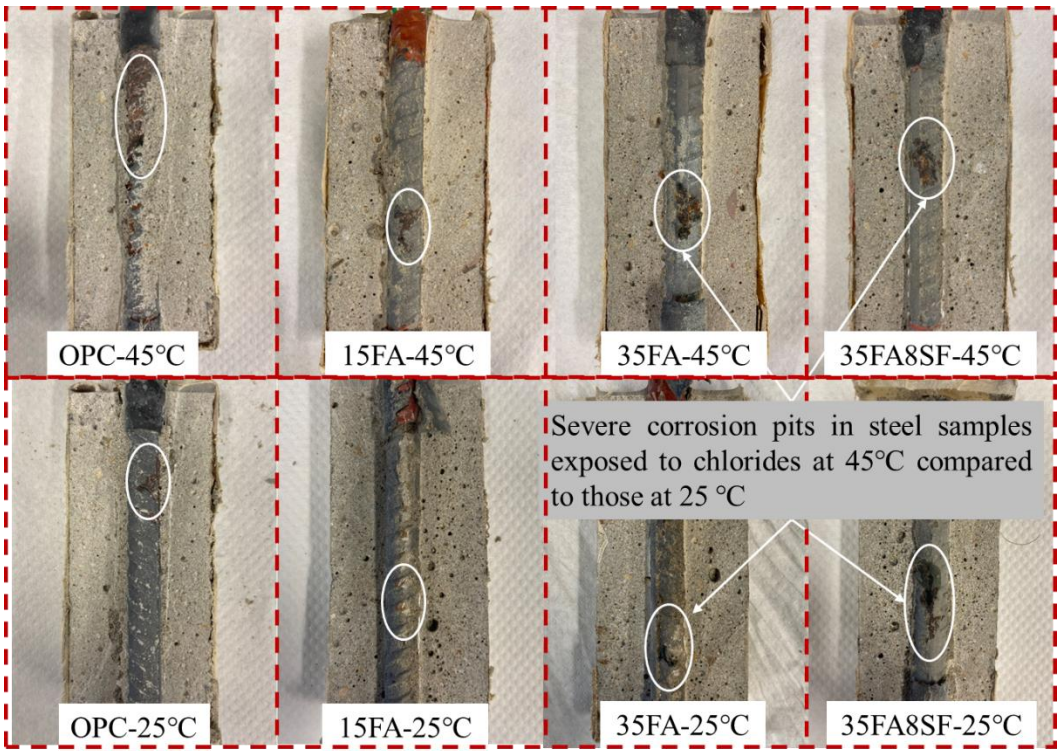

Figure 5.10. Corrosion attack on steel reinforcement embedded in different mortars.

5.3.5 Rust characterization

Figure 5.11 depicts the corroded regions of steel reinforcement and the corresponding spectral intensity distribution for key Raman peaks. One possible error in the results could be the additional oxidation of rust products during the Raman mapping of the sample, which took about 1.5 hours for the observed area. Examination of chloride-exposed steel surfaces at temperatures of 25 °C and 45 °C revealed a darker corrosion texture, with more pronounced localized variations under elevated thermal conditions. Based on prior research, specific Raman peaks can be linked to distinct iron corrosion products. Peaks observed at approximately 660 cm^{-1}, 719 cm^{-1}, and 362 cm^{-1} are commonly attributed to Maghemite (γ-Fe_2O_3), which emerged as the dominant corrosion product on steel surfaces (Mi, Wang, et al., 2023). Maghemite is generally considered a stable form of iron oxide with compact morphology (Singh & Singh,

2012). A comparison of the spectral intensities at 719 cm^{-1} for the two steel samples indicates that higher temperatures marginally enhanced the concentration of Maghemite.

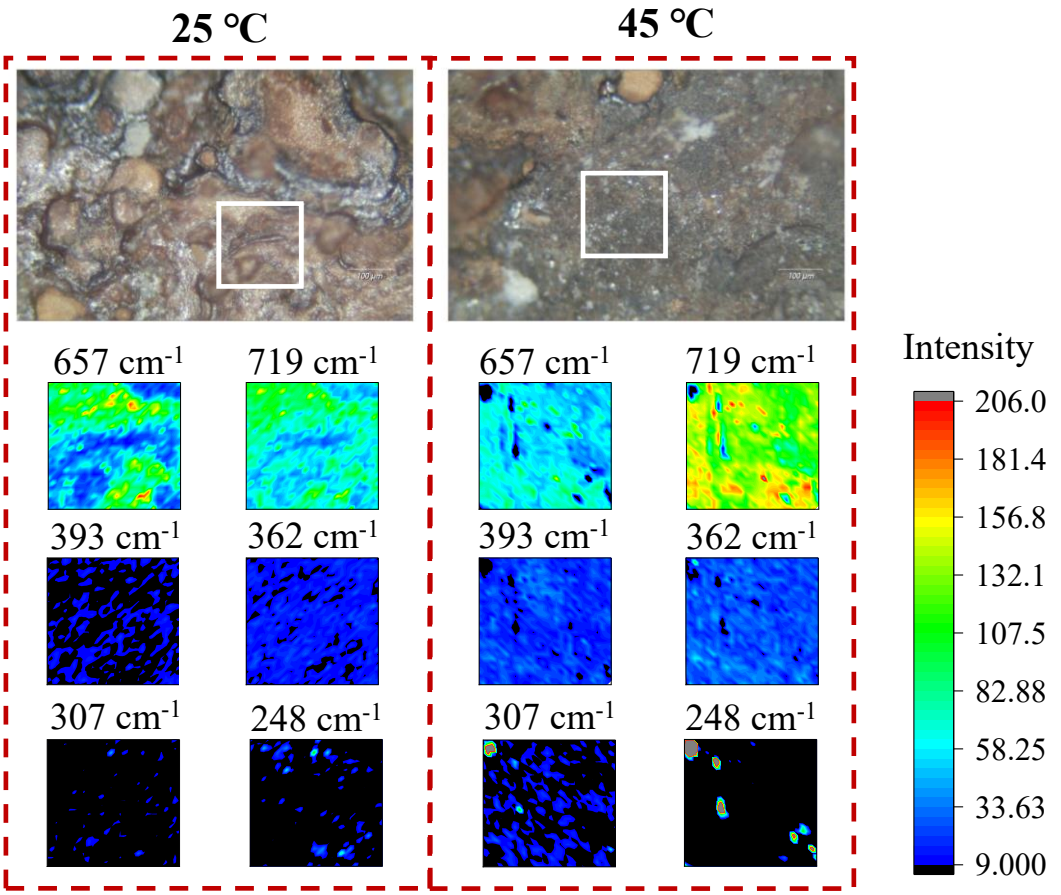

Figure 5.11. Raman mapping of corroded areas of steel embedded in 35FA mortars and exposed to chlorides at 25 °C and 45 °C.

Goethite (α-FeOOH), identified by a peak near 392 cm^{-1}, was another significant corrosion product, with its abundance also increasing at elevated temperatures. Akaganeite (β-FeOOH), characterized by a peak at 307 cm^{-1}, exhibited a slight rise in concentration under elevated temperature exposure. Due to its structural arrangement, Akaganeite typically exhibits a lower density compared to Goethite and Lepidocrocite. Lepidocrocite (γ-FeOOH), identifiable by a peak around 247 cm^{-1}, was detected but showed a decline in concentration at higher

temperatures. This reduction suggests a potential transformation of Lepidocrocite into Goethite and Akaganeite under elevated thermal conditions.

The variation in corrosion product composition may stem from differences in oxygen availability at the steel surface. Lepidocrocite formation is favoured in oxygen-rich environments through the oxidation of Fe(II) (Qin et al., 2025). For steels exposed to chlorides at elevated temperatures, the reduced oxygen solubility in the mortar's pore solution can likely impede the formation of Lepidocrocite. Akaganeite is formed by the slow oxidation of iron complexes containing chloride, and a low-oxygen and high-temperature environment is preferable for its formation (Nomura et al., 1988). A previous study on steels in simulated marine environments also observed such a trend (Pan et al., 2020). These observations highlight the influence of temperature on the formation and transformation of iron oxide and oxyhydroxide phases during chloride-induced corrosion.

5.3.6 Characterization of mortar properties

Compressive strength of mortars

The compressive strength of the mortar cubes was tested on 28 and 90 days to check the strength gain in samples over time. The average value from the test of three samples of each mix is provided in Figure 5.12. At 28 days, the control OPC sample showed marginally higher strength than fly ash-replaced samples (15FA and 35FA), possibly due to the slow pozzolanic reaction. However, by 90 days, due to continuous pozzolanic reactions, the fly ash mixed samples showed an improved strength compared to the control OPC. The strength gain from 28 days to 90 days of curing was about 11.4% for OPC, 31% for 15FA, 30.4% for 35FA and 29% for 35FA8SF. It was also observed that adding silica fume improved early strength, possibly mitigating early-age durability concerns when OPC is replaced with a high volume of low-reactive pozzolanic material like fly ash.

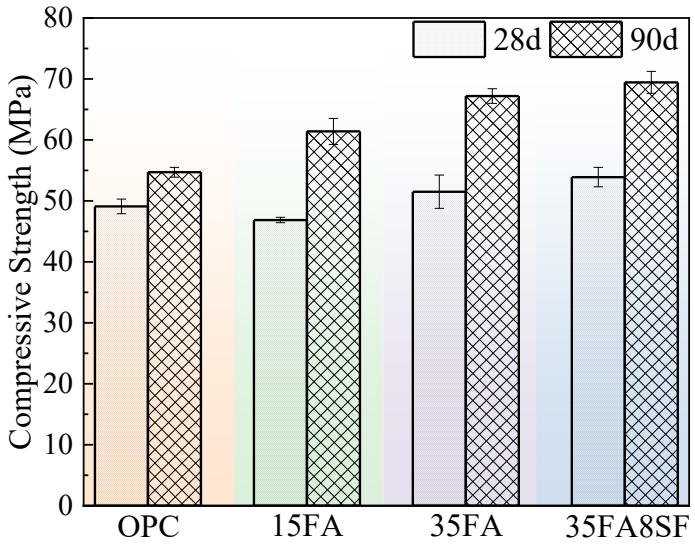

Figure 5.12. Compressive strength of mortars at 28 days and 90 days of curing.

pH of the mortars

The pH of the mortars was evaluated after 90 days of curing and is provided in Table 5.4. OPC samples demonstrated a high pH in the range of 13.42. With the addition of fly ash, which led to pozzolanic reactions, the pH dropped to 13.31 for 15FA and 13.11 for 35FA samples. The most significant pH drop was observed for 35FA8SF samples; the measured pH was 12.79, which could be attributed to the high pozzolanic reactions in the mix. One consequence of the lower pH is slow redox kinetics involving hydroxyl ions, which results in high charge transfer resistance in the passivation stage, as previously discussed from EIS analysis.

Table 5.4. pH of the mortar pore solution after 28 days

OPC	**15FA**	**35FA**	**35FA8SF**
13.42 ± 0.02	13.31± 0.01	13.11± 0.04	12.79± 0.03

Porosity of mortars

Considering the change in mortar resistance observed through electrochemical measurements during chloride exposure at different temperatures, two representative specimens (15FA and 35FA8SF) were analyzed for their pore structure characterization after corrosion initiation. The detailed pore distribution obtained through MIP is provided in Figure 5.13. Exposure to elevated temperature increased the porosity of samples, but most of those pores were of small diameter. The share of gel pores (<10 nm) of total porosity increased at the expense of capillary pore reduction. For example, in sample 15FA, high-temperature exposure to chlorides increased the gel pore share from 3.35% to 4.41% and in 35FA8SF samples from 3.67% to 4.98% of sample volume. This was also accompanied by a drop in the percentage of pores from 10 to 100,000 nm. This refinement of pore structure led to a significant increase in mortar resistance, as explained in Section 5.3.2. The increase in the addition of fly ash and silica fume had minimal impact on overall porosity. Still, if we compare the % of pores larger than 100 nm, we see a significant drop in 35FA8SF samples compared to 15FA samples. Such observations were also drawn in previous studies, where they suggested that increasing SCMs beyond certain levels shifted the median pore diameter to lower levels without much change in overall porosity (Poon et al., 1999).

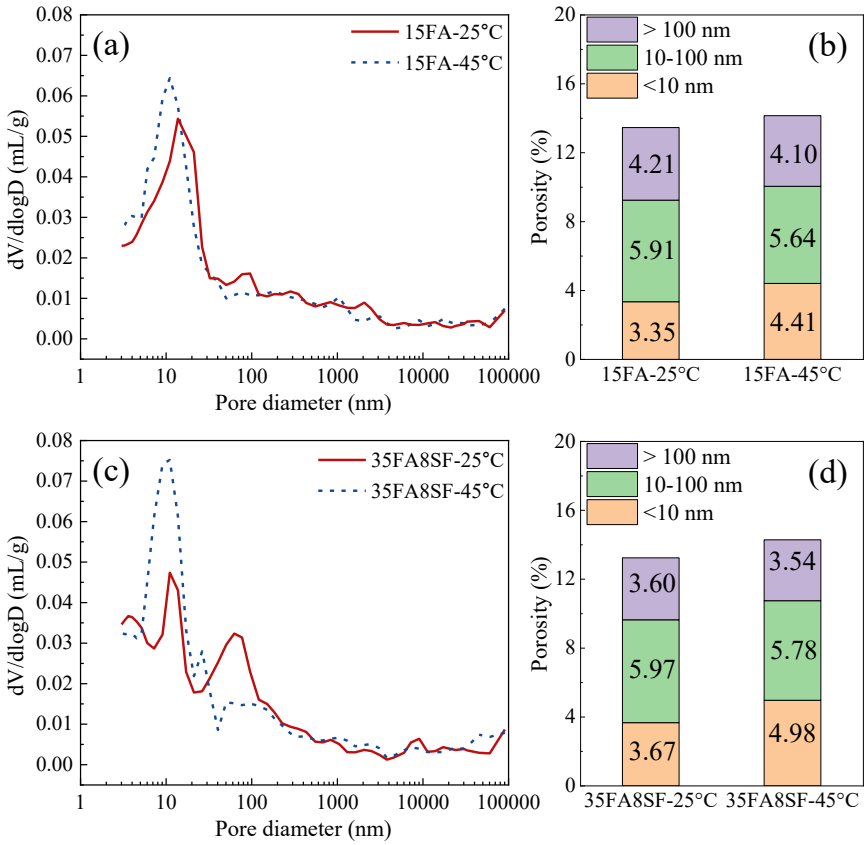

Figure 5.13. Pore structure characterization of (a) 15FA and (b) 35FA8SF samples after exposure to chloride solutions until the embedded steel started to corrode.

TG/DTG analysis of the surface layer

Figure 5.14 presents the TG/DTG curves of the outermost 3 mm of two representative mixes after mortars with embedded steel bars were removed from the chloride solution when corrosion was initiated. The mass loss at about 100℃ is related to the dehydration of C-(A)-S-H and ettringite in the mix. The mass loss between 240-390℃ corresponds to Friedel salt in the samples, which is formed due to chloride exposure (Babaahmadi et al., 2022). A slight decrease in Fridel salt content was observed in mixes 15FA and 35FA as the exposure temperature increased. The mass loss at about 420-500℃ represents the decomposition of portlandite (CH). It can be observed that the mortar samples exposed to chlorides at elevated

temperature (45 °C) showed almost negligible CH contents, even though the time for corrosion initiation was shorter. The trend in CH contents suggests that the leaching of CH was accelerated due to chloride exposure at elevated temperatures. It has been reported before that leaching of CH can lead to deeper penetration of chlorides (Chen et al., 2024; Machner et al., 2022). This could be one of the reasons for earlier corrosion initiation for steel bars exposed to chlorides at elevated temperatures. The mass loss due to carbonates was in a similar range for all the samples, likely due to the saturated condition of mortars at most times.

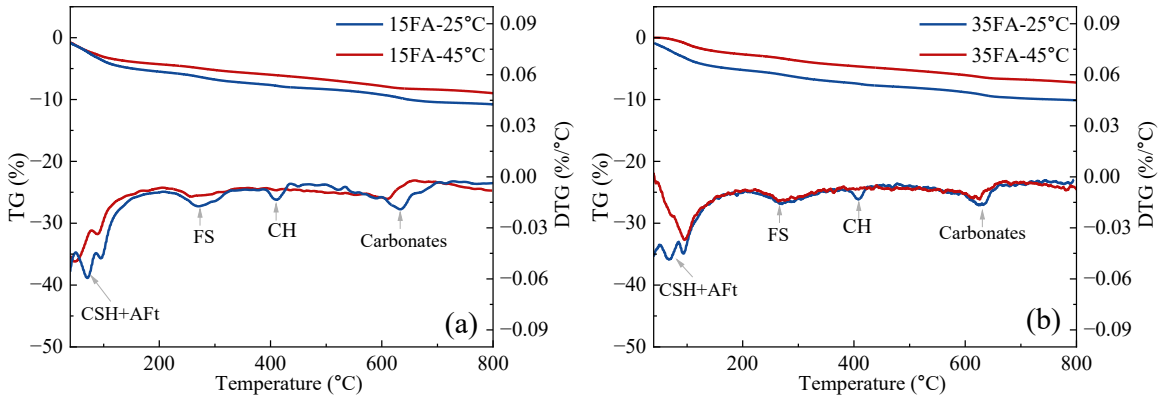

Figure 5.14. TG/DTG curves of the outermost 3 mm of the (a) 15FA and (b) 35FA samples after exposure to chloride solutions until the embedded steel started to corrode.

5.4 Overall Summary

In this study, a set of four reinforced mortar mixes was continuously monitored for nearly 600 days during their exposure to NaCl solution at two temperatures of 25 °C and 45 °C, with the main purpose of evaluating the role of temperature on the chloride threshold value and studying concrete degradation during the exposure period. Based on the results obtained, the following conclusions can be drawn:

(a) Elevated temperatures (45 °C) markedly accelerated chloride-induced corrosion initiation, reducing the time-to-corrosion by 67% in ordinary Portland cement (OPC)

mortars compared to 25 °C exposure. However, supplementary cementitious materials (SCMs), such as fly ash (35%) and silica fume (8%), mitigated this effect due to enhanced pozzolanic reactivity, as evidenced by electrochemical impedance spectroscopy (EIS) and reduced porosity. The 35FA8SF mix exhibited a 55% reduction in corrosion initiation time under the same temperature increase, underscoring the role of SCMs in slightly improving chloride resistance even at elevated temperatures.

(b) Post-corrosion visual and microstructural analysis revealed localized dark reddish-orange corrosion products on steel rebars in mortars exposed to 45 °C, which were visibly absent in samples exposed at 25 °C. Thus, corrosion possibly becomes more localized at elevated temperatures. The elevated temperatures also favoured the formation of Akaganeite and Goethite over Lepidocrocite.

(c) The chloride threshold value (CTV) decreased by 40–62% with a 20 °C temperature increase (25 °C to 45 °C). For mortars containing fly ash and silica fume (35FA8SF), the critical $[Cl^-]/[OH^-]$ molar ratio at corrosion initiation dropped to approximately one-third of its value at 25 °C, highlighting the synergistic impact of temperature and pore chemistry on depassivation.

To our knowledge, this is the first study to systematically correlate long-term chloride exposure at elevated temperatures with CTV reduction and phase-specific corrosion product evolution in reinforced mortars. This study highlights the significant risk posed by chlorides at elevated service temperatures, where a fraction of chlorides can cause depassivation of the steel reinforcement compared to that observed under laboratory conditions with standard temperatures of 20-25°C. It is also worth highlighting that many literature studies have failed to specify the experimental temperature. This inconsistency may have partly contributed to the significant variations observed in chloride threshold values.

CHAPTER 6

SERVICE LIFE MODELING AGAINST CORROSION CONSIDERING DIFFERENT CLIMATE PROJECTION SCENARIOS

6.1 Introduction

Chapter 5 revealed that while adding SCMs is beneficial in reducing the adverse impact of elevated temperature due to the enhanced pozzolanic reaction and pore refinement, they have a negligible impact on countering the negative effect of temperature on the chloride threshold value. Consequently, the drop in chloride threshold value for corrosion initiation observed in simulated pore solution due to increased temperature was of nearly similar magnitude in mortar samples. While the last three chapters provide insights into the effect of temperature on chloride-induced corrosion risk during accelerated/short-term exposure tests, corrosion in RC structures is a long-term phenomenon spanning several decades. During this timeline, they are subjected to variable environmental actions, which significantly affect their long-term safety and serviceability. The environmental conditions, as we all know, are dynamic and complex. Thus, it is necessary for the life cycle models to consider the time-dependent variations in environmental loads and their impact on the service life of RC structures.

The recent Intergovernmental Parliament on Climate Change (IPCC) report (Kikstra et al., 2022) predicts that if global CO_2 emissions are allowed to increase unabated, it could potentially cause the mean surface temperature to rise to a maximum of about 4.4℃ by 2100 compared to the average of 1850-1900, triggering a surge in mean sea level. During this period, the CO_2 concentration in the atmosphere may also peak from the current levels of 420 ppm to

over 1000 ppm in the worst-case scenario. Given the considerable uncertainty surrounding future global temperatures and CO_2 levels, it is essential from a civil engineering standpoint to understand their potential implications. This understanding is crucial to ensure that constructed structures are durable and can fulfil their intended lifespan without requiring significant interventions.

Over the years, many models have been created to evaluate isolated cases of chloride penetration into concrete cover or carbonation in concrete and their impact on corrosion initiation. However, only a few models have considered the combined deterioration caused by carbonation and chloride ingress. This is due to the highly non-linear nature of chloride binding and the complications associated with reduced chloride binding of cement hydrates that lead to the release of chlorides previously bound. The first model by Puatatsananon and V. E. Saouma (Puatatsananon & Saouma, 2005) did not account for the changes in chloride binding and only considered increased porosity and accelerated chloride diffusion coefficient. Subsequently, Geng et al. (Geng et al., 2016) established a model to account for the release of bound chlorides in chloride-contaminated concrete using a reduction function. This was further improved by Shen et al. (Shen, Jiang, et al., 2019; Shen, Liu, et al., 2019) into a semi-empirical function, which was also used later by Wang et al. (Wang et al., 2023) to obtain the changes in cement hydration products due to carbonation. However, these studies had a limited aim of evaluating the chloride redistribution inside concrete due to carbonation. Zhu et al. (Zhu, Zi, Cao, et al., 2016; Zhu, Zi, Lee, et al., 2016) developed a more comprehensive model that considered the simultaneous penetration of chlorides and carbon dioxide into concrete and obtained a reduction in service years, assuming the chloride threshold at 0.4% of binder weight. An analytical modeling methodology has also been recently proposed (Li et al., 2019), considering the carbonation front as a moving boundary condition where an extra chloride flux is imposed

due to the release of bound chlorides. However, the model simplifies the chloride transport to be driven only by diffusion, which reduces its applicability for actual exposure conditions.

The above literature review highlights a research gap in existing models, which often overlook the synergistic effect of chloride and carbonation attacks, as well as the cyclical nature of environmental conditions and future climate projections. Previous studies using climate models to understand the implications (isolated cases) under different global warming scenarios (Bastidas-Arteaga et al., 2010; Guo et al., 2020) have reported that the corrosion initiation time could be shortened by about 2-20 % for chloride-induced corrosion and 20-400% for carbonation-induced corrosion (Bastidas-Arteaga et al., 2013; Peng & Stewart, 2016; Stewart et al., 2011; Talukdar & Banthia, 2013), depending on the geographical location. When taking into account the impact of temperature on the initiation and progression of chloride-induced corrosion in conjunction with carbonation, the decrease in the service life due to climate change is expected to be more pronounced. This raises an important question: to what extent can the service life reduction be expected when considering various climate scenarios to account for the increase in atmospheric CO_2 concentrations and surface temperature?

Thus, this work aims to provide a comprehensive framework to evaluate the corrosion risk in coastal RC structures by considering:

1) Time-varying environmental model under different climate change scenarios considering temperature variations (daily, seasonal and annual), humidity variations (seasonal) and yearly rise of CO_2 concentrations;
2) Temperature dependency on chloride diffusion rate, chloride binding ability, chloride threshold for corrosion initiation and corrosion current density;
3) Interactions of CO_2 with different cement hydrates (calcium hydroxide-CH and calcium silicate hydrate-C-(A)-S-H) and release of bound chlorides due to carbonation.

6.2 Methodology

6.2.1 Evaluation of concrete properties

The reference chloride transport rate was experimentally measured for a ternary concrete mix commonly used in concrete piers in Hong Kong. The mix had a significant amount of different supplementary cementitious materials (SCMs), which followed the global trend of reducing cement usage in concrete and achieving sustainability. Details of the mix proportions per m^3 of concrete mix (hereafter named 35FA8SF) are as follows: ordinary Portland cement – 257 kg, fly ash – 157 kg, silica fume – 36 kg, aggregate – 1700 kg and water 160 kg. The casting of concrete samples was carried out in a commercial lab. The flow diameter of the mix was above 600 mm during the two hours after casting, demonstrating good flowability. The concrete samples were demolded after 1 day of casting and cured in a water tank maintained at a temperature of about 22℃ until the day of testing.

After 28 days of casting, the concrete cylinders (100 mm diameter and 200 mm height) were cut into slices of (50 ±1) mm height and 100 mm diameter for the chloride penetration test. Prior to the test, the lateral surface of the cylinders was sealed with epoxy and water-sealing tape. This was followed by saturation of the samples in saturated $Ca(OH)_2$ solution for 24 hours to ensure a diffusion-based transport mechanism. The samples were further immersed in $Ca(OH)_2$ solution maintained at different test temperatures (25 ℃, 35 ℃ and 45 ℃) for 3 hours before testing. The immersion was done to achieve a thermal equilibrium state of the overall concrete during the testing period. The chloride penetration test was carried out as per NT Build 492, with an external voltage of 30V and a testing period of 24 hours. The different temperature conditions were achieved using a thermostatic-controlled water bath. After the test, the samples were split and sprayed with $AgNO_3$. The penetration depth was then measured on at least 5 points using a vernier calliper. The places with aggregates and voids were eliminated during

chloride penetration depth measurement. This was followed for three identical concrete samples at each temperature, and the chloride diffusion coefficient of the mix was taken as the average of the three values.

6.2.2 Mass transport

Heat transport through concrete

The temperature distribution throughout concrete was based on the heat flow equation considering the external environmental temperature as a boundary condition. This is given by:

$$\rho_c q_c \frac{\partial T}{\partial t} = \nabla \cdot (\lambda \nabla \mathrm{T}) \tag{6.1}$$

where, ρ_c, q_c, λ are density, specific heat capacity and thermal conductivity of concrete.

Moisture transport in concrete

The moisture transport through concrete was based on pore relative humidity (h) gradient (Muthulingam & Rao, 2014; Xi et al., 1994):

$$\frac{\partial w_e}{\partial h}\frac{\partial h}{\partial t} - \nabla \cdot (D_h \nabla h) = 0 \tag{6.2}$$

where, w_e is the volume fraction of pore water per unit volume of concrete and $D_h$is the diffusion coefficient of humidity. The volume fraction of pore water was obtained based on the Braunauer–Skalny–Bodor (BSB) model for water absorption as:

$$w_e = \frac{CkV_m h}{(1-kh)[1+(C-1)kh]} \tag{6.3}$$

where, the model parameter V_m is the monolayer capacity, C is related to the influence of temperature and is related to the number of diffuse layers. For cement hydration period (t) of more than 5 days and w/c ratio between 0.3 and 0.7, they can be defined as:

$$V_m = \left(0.068 - \frac{0.22}{t}\right)(0.85 + 0.45w/c)V_{ct} \tag{6.4}$$

$$C = exp\left(\frac{855}{T}\right) \tag{6.5}$$

$$k = \frac{\left(1 - \frac{1}{n}\right)C - 1}{(C - 1)} \tag{6.6}$$

$$n = \left(2.5 + \frac{15}{t}\right)(0.33 + 2.2w/c)N_{ct} \tag{6.7}$$

where, T is the temperature in K, w/c is the water to binder ratio, and the values of N_{ct} and V_{ct} were taken as 1.1 and 0.9 in the model.

The diffusion coefficient of humidity, D_h, is a function of temperature, pore humidity and the age of the concrete, i.e., $D_h = D_{h,ref} f_h(h) f_h(T) f_h(t)$, where $D_{h,ref}$ is the reference diffusion coefficient of humidity and is 2.02 x 10^{-10} m^2/s during drying measured at a reference temperature, T_{ref} = 296K (Ren et al., 2024). The functions can be given as:

$$f_h(T) = exp\left(\frac{U_h}{R}\left(\frac{1}{T_{ref}} - \frac{1}{T}\right)\right) \tag{6.8}$$

where U_h is the activation energy of the moisture diffusion (kJ/mol), R is the gas constant (J/mol.K). At the drying stage, the moisture transport rate as a function of pore relative humidity can be expressed as (Xi et al., 1994):

$$f_h(h) = \alpha_0 + \frac{1 - \alpha_0}{1 + (1 - h)^n/(1 - h_c)^n} \tag{6.9}$$

where α_0 is the diffusivity ratio between the minimal and maximal values of D_h taken as 0.05. h_c is a specified humidity corresponding to the middle value of D_h (taken as 0.75) and n is a model parameter (taken as 10) based on previous literature (Ren et al., 2024). During the wetting stage, the moisture transport rate was considered 10 times the moisture transport rate

during drying as an approximation since moisture absorption is significantly faster than drying (Guo et al., 2020; Ren et al., 2024).

$$f_h(t) = 0.3 + \sqrt{\frac{13}{t}} \tag{6.10}$$

describes the influence of the hydration period on the moisture diffusion coefficient.

Carbonation in concrete

Carbonation reaction involves the transport of CO_2 partially in the form of gas through concrete pores due to the concentration gradient and the remaining part as dissolved anions in the concrete pore solution, followed by subsequent reaction with different cement hydrates. The transport process of CO_2 can be defined as (Wang et al., 2023):

$$\frac{\partial(\phi - w_e)C_{CO_2}^{(g)}}{\partial t} = \nabla \cdot \left[(\phi - w_e)D_{g,CO_2}\nabla C_{CO_2}^{(g)}\right] - r_{D,CO_2} \tag{6.11}$$

$$\frac{\partial(w_e)C_{CO_2}^{(l)}}{\partial t} = \nabla.\left(D_{l,CO2}\nabla.C_{CO_2}^{(l)}\right) + r_{D,CO2} - w_e r_c \tag{6.12}$$

where, $C_{CO_2}^{(g)}$ and $C_{CO_2}^{(l)}$ are CO_2 concentrations in gaseous and liquid form, $r_{D,CO2}$ is the dissolution rate of $CO_2^{(g)}$ in concrete pore solution and $w_e r_c$ represents the amount of consumed $CO_2^{(g)}$ due to the carbonation of CH and C-S-H and ϕ is the concrete porosity.

Using Henry's law to express the concentration of dissolved CO_2, $C_{CO_2}^{(l)}$ as $HRTC_{CO_2}^{(g)}$ and combining Eqs. (6.11) and (6.12), the concentration of $C_{CO_2}^{(g)}$ at different depths of concrete pores can be predicted as:

$$\frac{\partial(\phi - w_e + w_e HRT)C_{CO_2}^{(g)}}{\partial t} = \nabla \cdot \left[D_{CO_2}\nabla C_{CO_2}^{(g)}\right] - w_e r_c \tag{6.13}$$

where, $H$is the Henry constant (34.2 moles·m³·atm), $R$is the ideal gas constant (8.314 J/mol·K), T is the temperature (K) and r_c is the reaction rate for carbonation of CH and C-S-H and can be defined as: $r_c = r_{CH} + 1.5r_{CSH}$ with the assumption that one mole of CH and C-S-H consumes, on average, 1 and 1.5 moles of CO_2 for complete carbonation.

r_{CH} and r_{CSH} represent the reaction rate of CH and C-S-H and can be given as:

$$r_{CH} = -\frac{\partial C_{CH}}{\partial t} = K_{CH} H R T C_{CH} C_{CO_2}^{(g)} \tag{6.14}$$

$$r_{CSH} = -\frac{\partial C_{CSH}}{\partial t} = K_{CSH} H R T C_{CSH} C_{CO_2}^{(g)} \tag{6.15}$$

where, C_{CH} and C_{CSH} are the concentrations of CH and C-S-H at any time.

K_{CH} and K_{CSH} are the reaction rate constants with values of 10^{-6} and 10^{-7} m^3/mole.s, respectively (Pan et al., 2018). The diffusion coefficient of CO_2, D_{CO2} can be defined as (Papadakis et al., 1991):

$$D_{CO2} = 1.64 \times 10^{-6} \times (\phi)^{1.8} \times (1-h)^{2.2} \tag{6.16}$$

Carbonation has been known to induce change in the porosity of matrices. While carbonation of CH leads to reduced porosity, the porosity changes due to carbonation in C-S-H vary significantly with the Ca/Si ratio. Thus, the model has not considered the effect of carbonation on porosity for simplicity.

Chloride transport in concrete

The free chlorides are transported through the concrete pore solution by diffusion due to a concentration gradient, and through capillary water absorption due to cyclic wetting and evaporation of water from the concrete surface. The inward progress of the carbonation front will also lead to the release of bound chlorides. Thus, considering the effect of chloride binding, diffusion, capillary transport and carbonation, the chloride transport equation is:

$$\left(1+\frac{1}{w_e}(1-dC_d)\frac{\partial C_{bc}}{\partial C_{fc}}\right)\frac{\partial C_{fc}}{\partial t}=\nabla.\left(D_{cl}.\nabla C_{fc}\right)+\nabla.(D_h.\nabla h)+K_b\frac{\partial C_{bc}}{\partial C_d}\frac{\partial C_d}{\partial t} \quad (6.17)$$

where, C_{bc} is the bound chloride content (kg/m^3 of concrete), C_{fc} is the free chloride content (kg/m^3 of concrete pore solution), D_h is the diffusion coefficient of humidity. The chloride diffusion coefficient, D_{cl} is defined as a function of temperature, humidity and age of concrete, i.e., $D_{cl} = D_{cl,ref}\, f_{cl}(T) f_{cl}(h) f_{cl}(t)$ where, $D_{cl,ref}$ is the chloride diffusion coefficient measured at a reference temperature, T_{ref}. The functions can be defined as:

$$f_{cl}(T)=exp\left(\frac{U_{cl}}{R}\left(\frac{1}{T_{ref}}-\frac{1}{T}\right)\right) \quad (6.18)$$

where U_{cl} is the activation energy for chloride diffusion, T is the exposure temperature,

$$f_{cl}(h)=\left[1+\left(\frac{1-h}{1-h_c}\right)^4\right]^{-1} \quad (6.19)$$

where, h_c is the specified humidity corresponding to the middle value of D_{cl} taken as 0.75

$$f_{cl}(t)=\begin{cases}\left(\frac{t_{ref}}{t}\right)^m, & t\le 30\ years\\ \left(\frac{t_{ref}}{10950}\right)^m, & t>30\ years\end{cases} \quad (6.20)$$

where, t_{ref} is reference day when $D_{cl,ref}$ was measured, and m is the ageing factor.

The bound chloride content C_{bc} was calculated using the Freundlich chloride binding isotherm ($C_{bc}=\alpha C_{fc}^{\beta}$). The free chlorides and the corresponding bound chlorides at 25 ℃ and 45 ℃ were obtained from the chloride binding experiment conducted for pastes in Chapter 4 for the mix 35FA8SF, as shown in Figure 6.1.

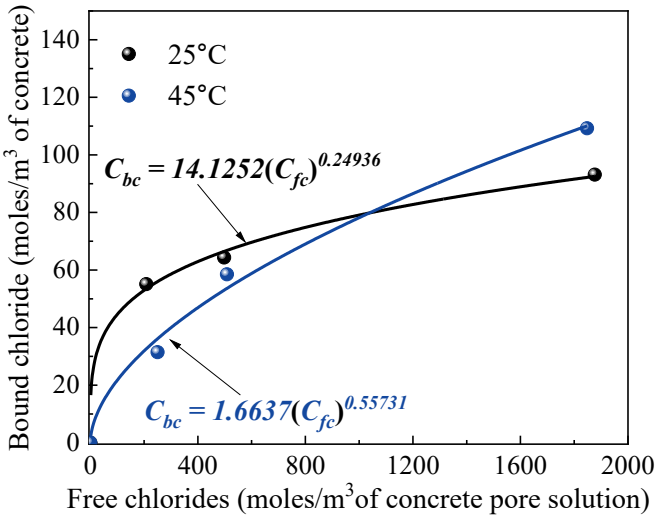

Figure 6.1. Influence of temperature on chloride binding isotherm for 35FA8SF mix after chloride exposure for 8 weeks at exposure temperatures of 25 °C and 45 °C.

It was assumed that the chloride binding coefficients α and β varied linearly with exposure temperature, as presented in equations 6.21 and 6.22.

$$\alpha = 199.8015 - 0.6231(T[K]) \tag{6.21}$$

$$\beta = -4.3402 + 0.0154(T[K]) \tag{6.22}$$

The term *d* is the reduction in binding capacity due to carbonation and C_d represents the degree of carbonation and is defined as:

$$C_d = \frac{(C_{CH}^0 - C_{CH}) + (C_{CSH}^0 - C_{CSH})}{(C_{CH}^0 + C_{CSH}^0)} \tag{6.23}$$

where, C_{CH}^0 is the initial calcium hydroxide content and C_{CSH}^0 is the initial calcium silicate hydrate content in the concrete (mole/m^3). These values were obtained using thermodynamic modeling, considering a 100% reaction degree of cement, a 15% reaction degree of fly ash and a 60% reaction degree of silica fume, aligning with a previous study (Skibsted & Snellings, 2019). For simplicity, the reaction degree of the binders was assumed to remain constant during the entire exposure duration.

6.2.3 Corrosion propagation model

Steel reinforced in concrete is covered with a protective passive film, which deteriorates when sufficient chloride ions accumulate at the steel surface, or the carbonation front reaches the steel surface, such that the degree of carbonation (C_d) approaches 1. Once there is a local breakdown of the passive film, these depassivated regions behave as anodic sites while the surrounding passive areas of steel act as cathodes. This study considered the two electrochemical processes, i.e., microcell and macrocell corrosion. The amount of free chlorides for depassivation, the chloride threshold value (C_{th}) was as 0.9% of binder weight at 25℃ based on experimental results from Chapter 5. Subsequently, the C_{th} was considered to drop linearly by 53% from 0.9% of binder weight at 25℃ to 0.42% at a temperature of 45 ℃. It must be noted that the transition from the passive to the active state of steel also accounted for seasonal and daily temperature variations.

If the carbonation front reaches the steel surface, the C_{th} is observed to reduce proportionally to the remaining CH contents in concrete. In this study, we considered $C_{th} = f(T, CH)$ to be a function of temperature based on the results of Chapter 5 and CH contents (Zhu, Zi, Cao, et al., 2016), as given by:

$$f(T,CH) = \begin{cases} 0.9\%\dfrac{C_{CH}}{C_{CH}^{0}}, T = 298K \\ 0.9\%\dfrac{C_{CH}}{C_{CH}^{0}}\left(1 - 0.053\left(T - T_{ref}\right)\right), (T - 298K) \le 20 \\ . \end{cases} \quad (6.24)$$

Potential distribution

For simulation of the electrochemical process, the concrete was treated as a conductor with a resistivity ρ (ohm-m) as a function of concrete mix proportion, age of concrete, moisture and chloride content (Q. Zhang et al., 2021).

The potential distribution throughout the concrete cover can thus be obtained as: $\nabla.\left(\frac{1}{\rho}\nabla\emptyset\right) = 0$. Thus, the electric current flux within the concrete pore solution (electrolyte) can be obtained by: $\boldsymbol{i} = -\frac{1}{\rho}\nabla\emptyset$. At the boundary of the steel-concrete interface, this current flux is equal to macrocell current (i_{mac}, A/m^2), i.e., $i_{mac} = \boldsymbol{n}.\left(\frac{1}{\rho}\nabla\emptyset\right)$ where, n is a unit vector perpendicular to the boundary. The other boundaries have a net zero current flux i.e., $\boldsymbol{n}.\left(\frac{1}{\rho}\nabla\emptyset\right) = 0$.

Corrosion current

At cathodic and anodic sites, the two major reactions are iron oxidation and oxygen reduction. At anodes, the dominating electrochemical reaction comprises iron oxidation. The iron oxidation is generally activation controlled. So, the corrosion current can be described as:

$$i_{Fe} = i_{Fe}^{0}\exp\left(2.303\frac{\emptyset - \emptyset_{Fe}^{0}}{\beta_{Fe}}\right) \tag{6.25}$$

where, i_{Fe}^{0} is the exchange current density (A/m^2), $\emptyset_{Fe}^{0}$ is the equilibrium potential (mV) and β_{Fe} (mV/dec) is the tafel slope considering iron oxidation. The influence temperature was also considered in determining both equilibrium potential and exchange current density as:

$$\emptyset_{Fe}^{0} = \emptyset_{Fe}^{0,ref} + 0.000052\left(T - T_{ref}\right) \tag{6.26}$$

$$i_{Fe}^{0} = i_{Fe}^{0,ref} exp\left[\frac{\alpha_{Fe} z_{Fe} F \emptyset_{Fe}^{0}}{R}\left(\frac{1}{T} - \frac{1}{T_{ref}}\right)\right] \tag{6.27}$$

where, α_{Fe} is the symmetry factor for anodic reaction and z_{Fe} is the anodic reaction valency, and F is the Faraday constant. For steel in a passive state, the tafel slope is considered infinity; for an active state, the tafel slope is 90 mV/decade (Cao, 2014; P. Zhang et al., 2023a).

The main chemical reaction at cathodes involves oxygen reduction. The corrosion current consists of an activation-controlled and oxygen concentration-controlled part. The dependency of corrosion current on oxygen concentration makes it highly non-linear and makes it difficult to obtain explicit solutions. Thus, an approximate solution provided by Gulikers (Gulikers, 2005) can be used:

$$i_{O2} = \frac{i_{O2}^0 exp\left(2.303 \frac{\emptyset - \emptyset_{O2}^0}{\beta_{O2}}\right)}{1 + \frac{i_{O2}^0}{i_L} exp\left(2.303 \frac{\emptyset - \emptyset_{O2}^0}{\beta_{O2}}\right)} \tag{6.28}$$

where, i_{O2} is the exchange current density (A/m^2), $\emptyset_{O2}^0$ is the equilibrium potential (mV) and β_{O2} is the cathodic tafel slope (mV/dec) considering oxygen reduction. Under the assumption oxygen concentration linearly varies inside concrete cover, the limiting current density i_L is:

$$i_L = \frac{D_{O2} z_{O2} F C_{O2}^s}{X} \tag{6.29}$$

where, D_{O2} is oxygen diffusion coefficient, X is the distance of steel bar from the external environment, $C_{O_2}^s$ is the dissolved oxygen concentration at the concrete surface. The temperature dependency on C_{O2}^s (Pour-Ghaz et al., 2009a) and D_{O2} (Liu et al., 2021) were taken as:

$$\ln C_{O_2}^s = -139.344 + \frac{1.575 \times 10^5}{T} - \frac{6.642 \times 10^7}{T^2} + \frac{1.244 \times 10^{10}}{T^3} - \frac{8.622 \times 10^{11}}{T^4} \tag{6.30}$$

$$log_{10}\left(\frac{D_{O2}}{D_{O2,ref}}\right) = \frac{1.3272[(T - 298.15) + 0.001053(T - 298.15)^2]}{(T - 168.15)} \tag{6.31}$$

where, $D_{O2,ref}$ was taken as 6×10^{-9} m^2/s (Cao, 2014).

For steel in concrete in unsaturated condition, the cathodic tafel slope is 180 mV/dec (Cao, 2014). By considering the influence of temperature on equilibrium potential and exchange current density:

$$\emptyset_{O2}^{0} = \emptyset_{O2}^{0,ref} + 0.00168(T - T_{ref}) \tag{6.32}$$

$$i_{O2}^{0} = i_{O2}^{0,ref} exp\left[\frac{\alpha_{o2} z_{O2} F \emptyset_{O2}^{0}}{R}\left(\frac{1}{T} - \frac{1}{T_{ref}}\right)\right] \tag{6.33}$$

where, α_{O2} is symmetry factor for cathodic reaction and z_{O2} is cathodic reaction valency.

Both the active and passive steel bars undergo cathodic and anodic reactions due to the formation of microcells or macrocells. Thus, the net macrocell current at the active steel bar is the sum of currents due to anodic and cathodic reactions, i.e.,

$$i_{mac}^{a} = i_{Fe}^{a} - i_{O2}^{a} = i_{Fe}^{0} exp\left(2.303\frac{\emptyset - \emptyset_{Fe}^{0}}{\beta_{Fe}}\right) - \frac{i_{O2}^{0} exp\left(2.303\frac{\emptyset - \emptyset_{O2}^{0}}{\beta_{O2}}\right)}{1 + \frac{i_{O2}^{0}}{i_L} exp\left(2.303\frac{\emptyset - \emptyset_{O2}^{0}}{\beta_{O2}}\right)} \tag{6.34}$$

Since the corrosion current due to anodic activity is significantly lower in the passive regions of the steel bar, it can be ignored. Thus, the macrocell current for passive regions is:

$$i_{mac}^{p} = i_{Fe}^{p} - i_{O2}^{p} \cong -i_{O2}^{p} = -\frac{i_{O2}^{0} exp\left(2.303\frac{\emptyset - \emptyset_{O2}^{0}}{\beta_{O2}}\right)}{1 + \frac{i_{O2}^{0}}{i_L} exp\left(2.303\frac{\emptyset - \emptyset_{O2}^{0}}{\beta_{O2}}\right)} \tag{6.35}$$

For microcell corrosion, the corrosion current is controlled by oxygen reduction, which gives

$$i_{mic}^{a} = \frac{i_{O2}^{0} exp\left(2.303\frac{\emptyset - \emptyset_{O2}^{0}}{\beta_{O2}}\right)}{1 + \frac{i_{O2}^{0}}{i_L} exp\left(2.303\frac{\emptyset - \emptyset_{O2}^{0}}{\beta_{O2}}\right)} \tag{6.36}$$

Thus, total corrosion current density,

$$i_{total}^{a} = i_{mic}^{a} + i_{mac}^{a} = i_{Fe}^{0} exp\left(2.303\frac{\emptyset - \emptyset_{Fe}^{0}}{\beta_{Fe}}\right) \tag{6.37}$$

6.2.4 Time to first crack formation

For a total corrosion current density i_{total}^{a} flowing through the corroding steel, the mass loss of steel at a time, *t* is given by:

$$M_{loss} = \frac{M_{Fe} \int_0^t i_{total}^a(\theta, t)\mathrm{d}t}{F.z_{Fe}} \tag{6.38}$$

It is generally known that the first crack around steel reinforcement due to corrosion is formed when the radial pressure (P_{cor}) exerted by the formation of expansive rusts exceeds the tensile strength of the concrete cover. The time to predict the first crack in this study was obtained based on an analytical equation proposed by Maaddawy and Soudki (2007) (El Maaddawy & Soudki, 2007) as given,

$$P_{cor} = \frac{2E_{eff}\left[\frac{M_{rust}}{\rho_{rust}} - \frac{M_{loss}}{\rho_{steel}}\right]}{\pi D(1+\upsilon+\psi)(D+2\delta_0)} - \frac{2\delta_0 E_{eff}}{(1+\upsilon+\psi)(D+2\delta_0)} = \frac{2Cf_{ct}}{D} \tag{6.39}$$

where, E_{eff} is the effective concrete elastic modulus, and is calculated $\frac{E_c}{1+\emptyset_{cr}}$ where E_c is elastic modulus and $\emptyset_{cr}$ is the creep coefficient of concrete. M_{rust} and ρ_{rust} are the mass and density of rust formed from corrosion-induced mass loss M_{loss} of steel rebar of diameter D, m and density ρ_{steel}. δ_0 is the thickness of the porous zone around the steel rebar, and υ is the Poisson's ratio of concrete. ψ is a dimensionless parameter that is defined by $\psi = \frac{D^{*2}}{2C(C+D^*)}$ where, $D^* = D + 2\delta_0$ and C is concrete cover depth.

The overall numerical model can thus be summarized as shown in Figure 6.2.

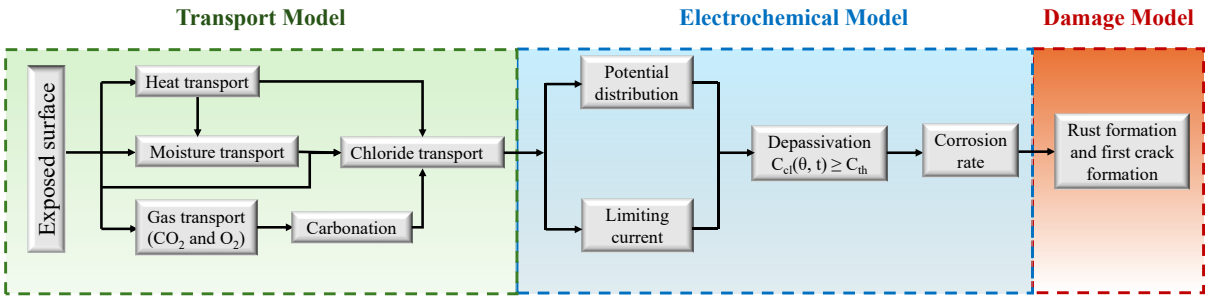

Figure 6.2. Flowchart of the proposed numerical model for service life analysis.

6.3 Model Verification

6.3.1 Chloride transport model

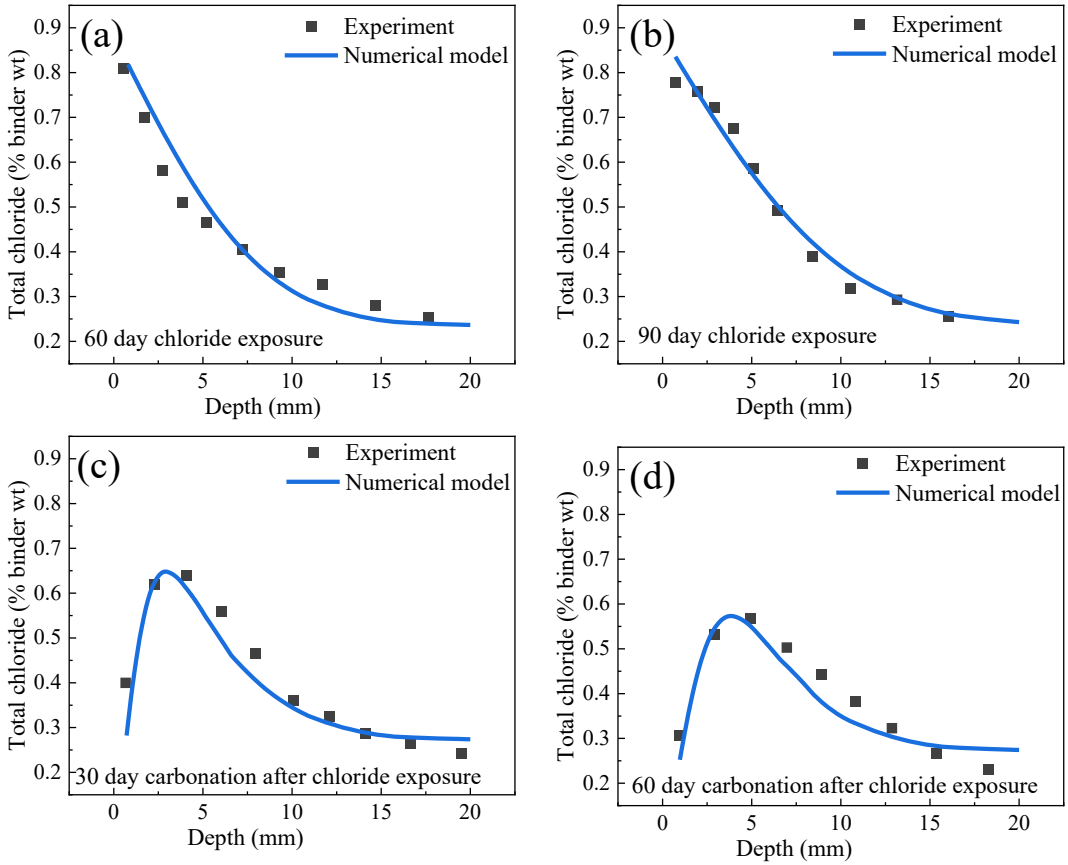

Figure 6.3. Comparison of experimental data and data from the numerical model for chloride distribution inside concrete after (a) 60 days and (b) 90 days immersion in chloride solution of concentration 165 g/l and effect of accelerated carbonation (5%) for (c) 30 days and (d) 60 days on chloride redistribution in concretes specimens post 90 days chloride exposure.

The proposed model to evaluate chloride distribution in concrete due to combined carbonation and chloride ingress was validated by an experiment conducted by Wang et al. (Wang et al., 2017), where they exposed concretes to chloride exposure followed by carbonation. The concrete samples of diameter 75 mm and 80 mm in height made with a 0.55 water-to-cement ratio were saturated in an alkaline solution before being immersed inside a 165g/l concentration of NaCl solution for 90 days. The total chloride contents were then measured at different depths of concrete following the standard NT Build 443 at every 1 mm distance at the surface and 2 mm at deeper depths. Figure 6.3 (a, b) shows the chloride contents inside concrete determined

by experiment and compared with predictions from the numerical model. After immersion in chloride solution, the samples were conditioned at 65% RH and exposed to accelerated carbonation with a CO_2 concentration of 5%. The numerical model reasonably captured the redistribution of chlorides and the shifting of peak chloride into deeper layers of concrete, as shown in Figure 6.3 (c, d). The shifting of chloride peak into deeper layers upon carbon dioxide exposure can be attributed to the additional release of chlorides, which were earlier bound to cement hydration products.

6.3.2 Corrosion model considering varying climate conditions

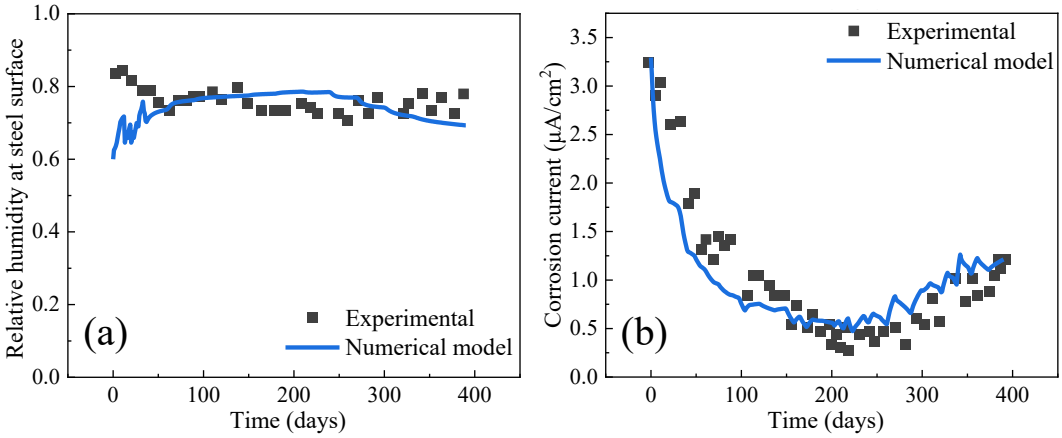

Figure 6.4. Comparison of experimental data and data from the numerical model for (a) internal relative humidity at the steel surface and (b) corrosion current density for 2-D reinforced beam considering time-varying temperature and humidity exposure conditions.

The model was also evaluated for its accuracy in determining the corrosion rate in samples exposed to natural climate (e.g., changing RH and temperature) as shown in Figure 6.4. The experimental data were obtained from a study by Jiang and Yuan (Jiang & Yuan, 2013) where concrete samples of dimensions (250 mm × 150 mm × 100 mm) were cast with 5% binder weight of admixed chlorides and exposed to natural climate. A 2D simulation of the experiment and the periodic variations of temperature and humidity on moisture transport and corrosion

current were considered. The initial parameters used to simulate the corrosion process at 298K are anode tafel slope of 150 mV/decade, cathodic tafel slope of 180 mV/decade, anodic exchange current of 3 x 10^{-4} A/m^2 and cathodic exchange current density of 1 x 10^{-5} A/m^2. It can be observed that the predicted internal humidity at the steel surface and corrosion current show a reasonable agreement with the experimental data.

6.4 Results and Discussions

6.4.1 Influence of temperature on chloride transport rate through concrete

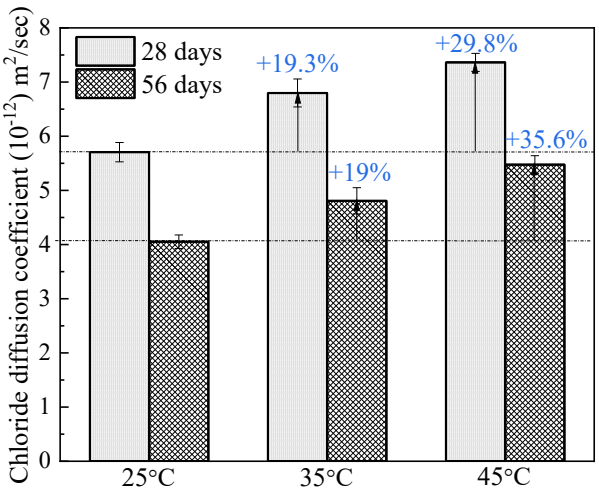

Figure 6.5. Influence of temperature on chloride diffusion coefficients mix obtained through NT Build 392 method at 28 and 56 days of curing of 35FA8SF concrete mix

The chloride diffusion coefficient of mixes obtained after 28 and 56 days of curing are provided in Figure 6.5. The measured chloride diffusion coefficients decreased with curing age due to increased hydration and pore refinement regardless of exposure temperature aligning with previous studies. It was also observed that temperature significantly impacted the chloride diffusion coefficients. For example, compared to the diffusion coefficient at 25 °C, the chloride diffusion coefficient increased by about 20% for a 10 °C temperature rise and about 29-35% for a 20 °C temperature rise. Previous researchers have attributed this increase in diffusion

coefficients to enhanced chloride ion mobility (Al-Sodani et al., 2021; Yuan et al., 2008). The chloride diffusion coefficients at different temperatures can thus be predicted based on the activation energy of a concrete mix, which was 10.05 kJ/mol at 28 days and 11.9 kJ/mol at 28 days and 56 days of curing. The activation energy for the modeling was taken as the average of these two values. The chloride transport rate from the rapid chloride migration test (NT Build 492) was then used to obtain the apparent chloride diffusion coefficient using a factor suggested by Elfmarkova et al. (Elfmarkova et al., 2015).

6.4.2 Corrosion initiation prediction of 35FA8SF mortars from Chapter 5

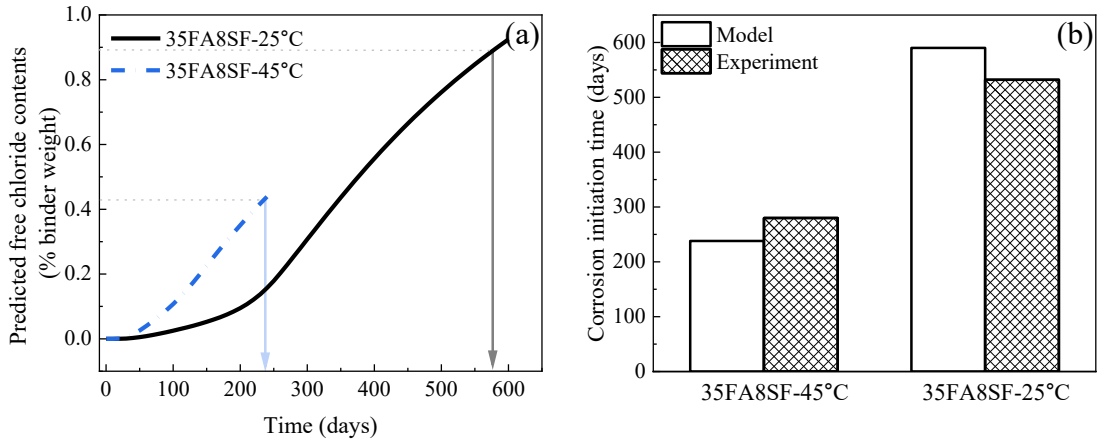

Figure 6.6. (a) Calculated chloride contents at the surface of steel bar for 35FA8SF samples exposed to chlorides at 25 ℃ and 45 ℃ through numerical modeling and (b) comparison of time for corrosion initiation between modeling and experiment.

Finally, the model was checked for its ability to predict the time for corrosion initiation of reinforced mortar samples containing 35% fly ash and 8% silica fume (35FA8SF mix) from Chapter 5. Once corrosion had initiated in the samples, 1 gram of powder from the surface of the mortar samples was tested for total surface chloride content. Considering the short exposure time after which the reinforced mortars exposed to chlorides at an elevated temperature of 45 ℃ started corrosion, the surface chloride content for 35FA8SF-45 was 1.565% and

significantly lower than 35FA8SF-25 (2.462%). For the numerical model, surface chloride content was considered to be the constant value as determined above, and the relation between bound and free chloride was based on results from Chapter 4. The apparent chloride diffusion coefficient was taken to be 6E-12 m^2/s, and the activation energy was 10.975 kJ/mol, measured experimentally (details provided in Section 6.4.1). Thus, the chloride distribution in the mortar samples can be numerically predicted, as shown in Figure 6.6 (a). Subsequently, the measured and calculated time (in days) for corrosion initiation, assuming the chloride threshold values mentioned in Section 5.3.4, are provided in Figure 6.6 (b). It can be observed that the time for corrosion initiation could be calculated with reasonable accuracy with a maximum error of 20%. The lower corrosion initiation time obtained through the numerical model for samples exposed to chlorides at elevated temperatures might be related to the assumed activation energy, which was measured for concretes using NT Build 492 as described in Section 6.4.1 and the constant surface chloride values from an early age.

6.4.3 Geometry of the structural model

The service life modeling was conducted on a 2D-RC beam of dimensions (500 mm height and 325 mm width, as shown in Figure 6.7 (a)). Three rebars of 25 mm diameter were cast as tensile reinforcement at the bottom of the beam with a spacing of 75 mm. Considering the severe risk of corrosion, for a tidal zone scenario with periodic wetting and drying, a case of 75 mm cover thickness was also measured (refer to Figure 6.7 (b)). The chloride ingress was from three sides of the beam, with the upper surface insulated for chloride, carbon dioxide and moisture transport.

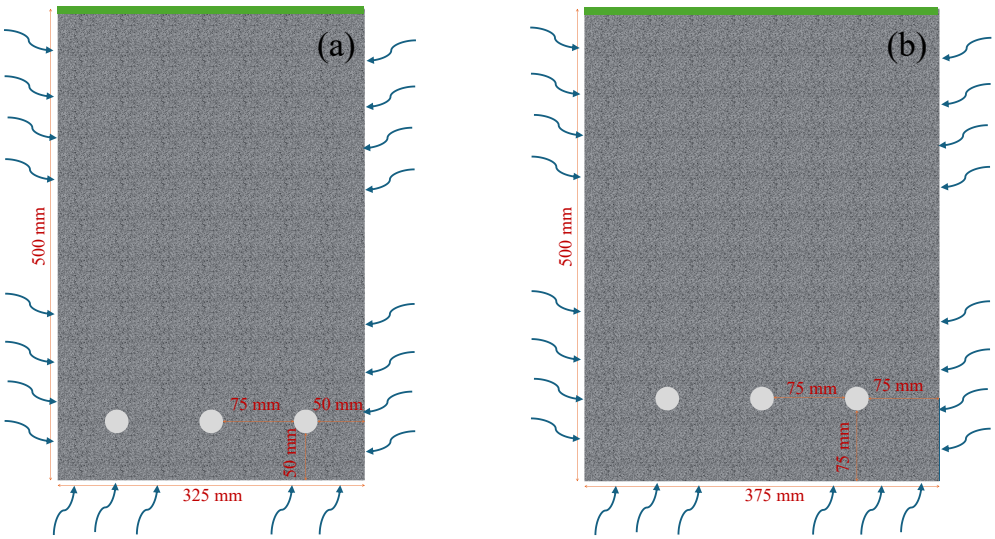

Figure 6.7. Geometries of the RC beams exposed to combined chloride ingress and carbonation from three sides for a cover depth of (a) 50 mm and (b) 75 mm.

6.4.4 Sensitivity of the model to temperature rise

The developed model was used to evaluate the sensitivity of the corrosion process to fixed environmental temperature when temperature-dependent chloride binding ability (denoted by the TCB model) was considered in the simulation and when both temperature-dependent chloride binding isotherm and chloride threshold for corrosion initiation (denoted by TCTH) were considered. This was compared to the existing models, which only consider the temperature to accelerate the chloride transport based on the Arrhenius equation. A summary of transport and electrochemical parameters used for modeling is provided in Table 6.1.

Table 6.1. Mass transport and electrochemical parameters used for modeling (Bastidas-Arteaga et al., 2010; Ren et al., 2024; Wang et al., 2023).

Mass transport model parameters	Value
Density of concrete, ρ_c	2500 kg/m^3
Specific heat capacity, q_c	1000 kg°C
Thermal conductivity, λ	2.5 W/(m °C)

Reference moisture diffusion coefficient $D_{h,drying}^{ref}$	2.02 x 10^{-10} m^2/s
Reference moisture diffusion coefficient $D_{h,wetting}^{ref}$	20.2 x 10^{-10} m^2/s
Moisture diffusion activation energy U_h	20.3 kJ/mol
Gas constant R	8.314 J/mol
Specified relatively humidity h_c	0.75
Moisture diffusivity ratio α_0	0.05
Model parameter for humidity n	10
Hydration period t_e	28 days
Water/cement ratio w/c	0.39
Paste volume relative to concrete	0.37
Initial calcium hydroxide content, C_{CH}^0	112.5 $moles/m^3$
Initial calcium silicate hydrate content, C_{CSH}^0	1885 $moles/m^3$
Carbonation reaction rate constant, K_{CH}	1E-6 $m^3/mol.s$
Carbonation reaction rate constant, K_{CSH}	1 x 10^{-7} $m^3/mol.s$
Henry constant, H	34.2 $moles.m^3.atm$
Reduction factor in chloride binding after carbonation, d	0.88
Porosity, ϕ	0.085
Chloride binding rate, K_b	3.13 x10^{-7}
Reference chloride diffusion coefficient D_{cl}^{ref}	4 x 10^{-12} m^2/s
Chloride diffusion activation energy U_{cl}	10.98 KJ/mol
Surface chloride content, Tidal zone	0.59% of concrete weight
Surface chloride content, Atmospheric zone	0.135% of concrete weight
Reference time t_{ref}	28 days
Ageing factor m	0.2

Electrochemical parameters	Value
Anodic exchange current i_{Fe}^{0}	3 x 10^{-4} A/m^2
Cathodic exchange current $i_{O_2}^{0}$	1 x 10^{-5} A/m^2
Anodic equilibrium potential ϕ_{Fe}^{0}	-0.78 V
Cathodic equilibrium potential $\phi_{O_2}^{0}$	0.16 V
Anodic Tafel slope (Passive) β_{Fe}	10 V/dec
Anodic Tafel slope (Active) β_{Fe}	0.09 V/dec
Cathodic Tafel slope β_{O_2}	0.2 V/dec
Faraday's constant F	96500 s·A·mol^{-1}
Molar mass of rust/molar mass of steel (M_{rust}/M_{steel})	0.622
Density of rust/density of steel	0.5
Molar mass of iron M_{Fe}	56 g/mol
Density of rebar ρ_{Fe}	7.85 g/cc

The variations in chloride ion concentration at the surface of corner and centre bars for different orientations are provided in Figure 6.8 (a-c). The chloride concentrations increased with temperature, irrespective of the various models employed in the study. It can be observed that the corner bar is more susceptible to corrosion than the central bar, and the highest chloride contents inside concrete are observed in the case when the framework of the existing model was considered in the 5°C temperature rise case. It is worth mentioning that the effect of environmental temperature on chloride binding counteracts the increase in chloride diffusion coefficient such that an increase in a temperature up to 5 °C seems to reduce the corrosion initiation time marginally (refer to Figure 6.8 (d)). As a result, for a 5 °C temperature increase, the difference in corrosion initiation time between the TCTH model and the existing model is

only 0.25 years (2%). This suggests that even though the existing models do not consider the temperature effect on chloride threshold and binding, they can still predict the chloride distribution in concrete with reasonable accuracy.

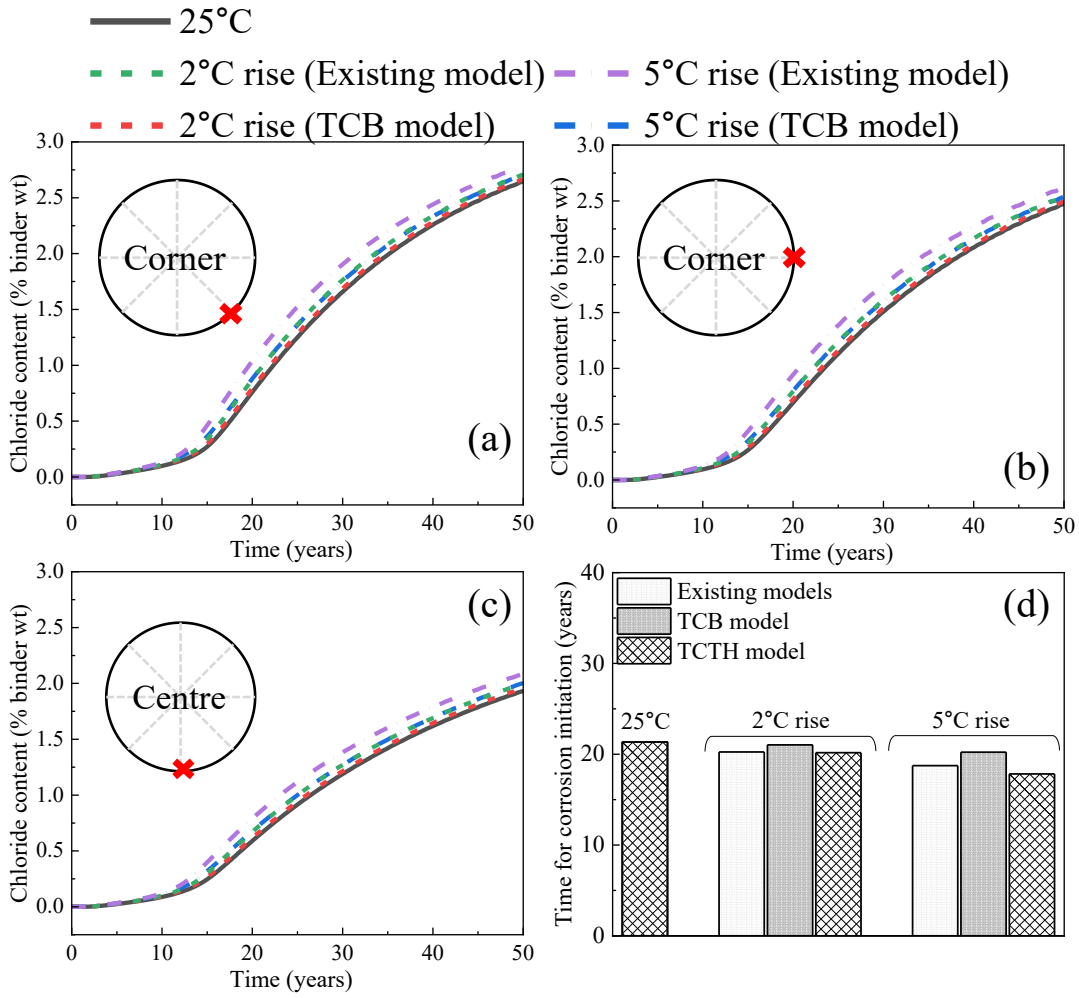

Figure 6.8. Prediction of free chloride distribution at the surface of (a, b) corner rebar, (c) central rebar for different orientations and (d) corrosion initiation time using the three different corrosion models for three different constant temperatures (i.e., 25°C, 27°C and 30°C).

6.4.5 Service life modeling considering different climate projections

Environmental exposure conditions

The environmental exposure model considered variations in temperature, humidity and CO_2 concentrations for two exposure classes: tidal and atmospheric zone. The atmospheric zone had seasonal humidity variations as the boundary condition for moisture transport. A monthly drying-to-wetting period of 2:1 was used as the exposure condition to simulate the tidal zone. During the drying period, the boundary condition of humidity was the atmospheric relative humidity, while for the wetting period, the relative humidity was fixed at 1. Based on the IPCC reports, the carbon emissions and corresponding temperature change for the three shared socio-economic pathways (SSP1.9, SSP 4.5 and SSP 8.5) until the year 2100 were used in the study. Thus, 6 cases were considered in this study. The framework for CO_2 concentration and temperature during the service years was based on the methodology adopted by Guo et al. (Guo et al., 2020). The daily and seasonal variations in temperature and seasonal variations for relative humidity were based on Hong Kong Observatory data. It must be noted that the seasonal and daily variations in temperature and humidity were assumed to remain unchanged for different climate projections. The equations for temperature, humidity and CO_2 variations during the service period are listed in equations 6.40-6.45, and the fitting of these curves is provided in Figure 6.9.

The temperature on any day, T(t), during the year 2020-2100 can be given by

$$T(t) = T_{Seas}(m) + T_{Daily}(d) + T_{Rise} + T_{Ref} \tag{6.40}$$

$$T_{Seas}(m) = a11 + a12sin(w1.m + b1) + a13sin(w2.m + b2) - a14sin(w3.m + b3) \tag{6.41}$$

$$T_{Daily}(d) = a21sin(w4.d) - a22sin(w5.d) - a23cos(w6.d) + a24sin(w7.d) + a25cos(w8.d) \tag{6.42}$$

$$T_{Rise}(y) = Ay^p \tag{6.43}$$

$T_{Ref} = 22.1$℃, average annual temperature between 1885-1904 (preindustrial period) (6.44)

where, A and p are model parameters for the three projected scenarios.

Similarly, the rise of CO_2 every year is given by:

$$CO_{2,Rise}(y) = By^q \tag{6.45}$$

where, B and q are model parameters for three projected scenarios.

The seasonal variations of relative humidity can be written as:

$$RH_{Seas}(m) = a31 + a32sin(w9.m + b4) + a33cos(w10.m + b5) \tag{46}$$

The environmental exposure parameters are presented in Table 6.2.

Table 6.2. Environmental exposure parameters

Fixed parameters for different future climate projections										
$T_{Seasonal}$	***a11***	***a12***	***w1***	***b1***	***a13***	***w2***	***b2***	***a14***	***w3***	***b3***
Value	-0.33	6.61	0.52	4.06	3.08	0.59	4.16	-3.57	0.59	4.06
T_{Daily}	***a21***	***w4***	***a22***	***w5***	***a23***	***w6***	***a24***	***w7***	***a25***	***w8***
Value	1.54	0.61	-0.42	1.35	-0.43	2.61	1.20	0.95	1.28	1.04
$RH_{Seasonal}$	***a31***	***a32***	***w9***	***b4***	***a33***	***w10***	***b5***	-	-	-
Value	74.75	2.44	0.87	0.94	7.24	6.73	-64.85	-	-	-

Variables for different future climate projections			
	SSP 1.9	**SSP 4.5**	**SSP 8.5**
Temp rise by 2100	1.4°C	2.7°C	4.4°C
CO_2 conc at 2100	400 ppm	600 ppm	1100 ppm
A	0.0223	0.0056	0.0006
p	0.938	1.41	2.012
B	-0.0002	0.0017	0.004
q	0.33	0.362	0.447

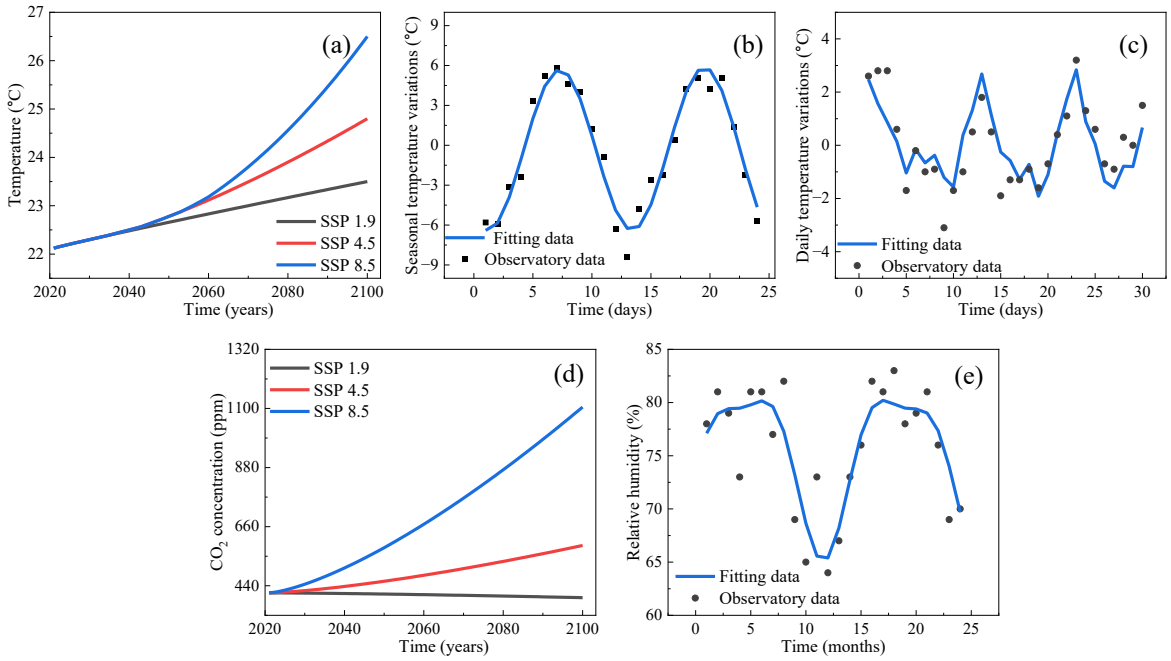

Figure 6.9. Prediction of (a) annual temperature variations considering different climate projections, (b) seasonal temperature variations, (c) daily temperature variations, (d) annual CO_2 concentrations for different projections and (e) seasonal variations in atmospheric relative humidity.

Condition of RC beams in the tidal zone

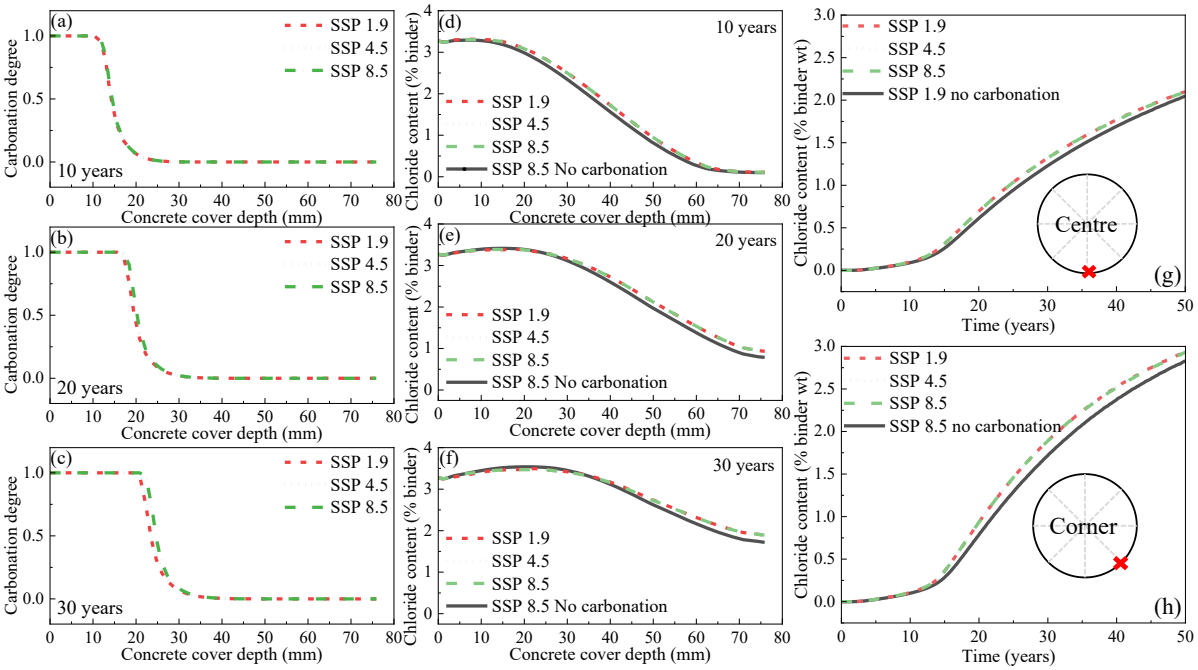

Figure 6.10. Prediction of (a-c) carbonation degrees and (d-f) chloride profiles at different concrete depths for 10, 20 and 30 years of service period, maximum free chloride contents at the surface of (g) central rebar and (h) corner rebar in tidal exposure zone.

The RC beams were evaluated for the carbonation depths and chloride distribution after different years of service. The carbonation depths at 10, 20 and 30 years of service are provided in Figure 6.10 (a-c) when considering different climate change trajectories. It can be observed that the carbonation depths showed a noticeable increase with the service period, but the overall carbonation front only reached the shallow depths of the concrete. During 30 years of exposure, 20 mm of the surface layer was fully carbonated, while about 10 mm was partially carbonated. When comparing the different climate projections, it was observed that they had a minimal impact on carbonation depths, increasing by about 1 mm when the most severe scenario (SSP 8.5) was considered instead of SSP 1.9. Overall, the carbonation alone did not pose a risk to the steel rebars during the service period due to the high saturation conditions (pore relative humidity around 0.8 or higher at most times).

During the service period, chloride profiles were also predicted for different climate projections, as shown in Figure 6.10 (d-f) during the 10, 20 and 30 years of service. Since there are currently limited models incorporating the combined degradation, the profiles were also compared with a simulation that only considered temperature rise (following SSP 8.5) but with no carbonation. Without considering the combined impact of carbonation, it can be observed that the chloride contents at deeper levels were underestimated. However, the effect was lower due to the limited carbonation depths in concrete. At the surface of corner rebars, the chloride contents increased by a maximum of 10% when considering carbonation. When comparing the effects of climate change scenarios, there was virtually no change in chloride profiles for either of the rebars until 30 years. However, the chloride contents at the steel surface exceeded the chloride threshold (0.9% binder content without considering temperature effect) by 21.04 years without considering carbonation and 19.7 years when considering carbonation (reduction of 6.3%). Thus, even though the carbonation had a limited impact on the tidal zone, the corrosion started at an early period of about 21 years due to the high chloride content at the concrete surface and drying and wetting action, which led to faster chloride ingress. It is evident that a 50 mm concrete cover leads to corrosion initiation at a very early service period, and thus, the effect of using 75 mm concrete on the corrosion risk was evaluated subsequently. It is worth noting that the effect of convection in shifting chloride peak to concrete interiors could be captured in the model. The peak chloride value increased with exposure time but showed a marginal decrease when considering the carbonation effect.

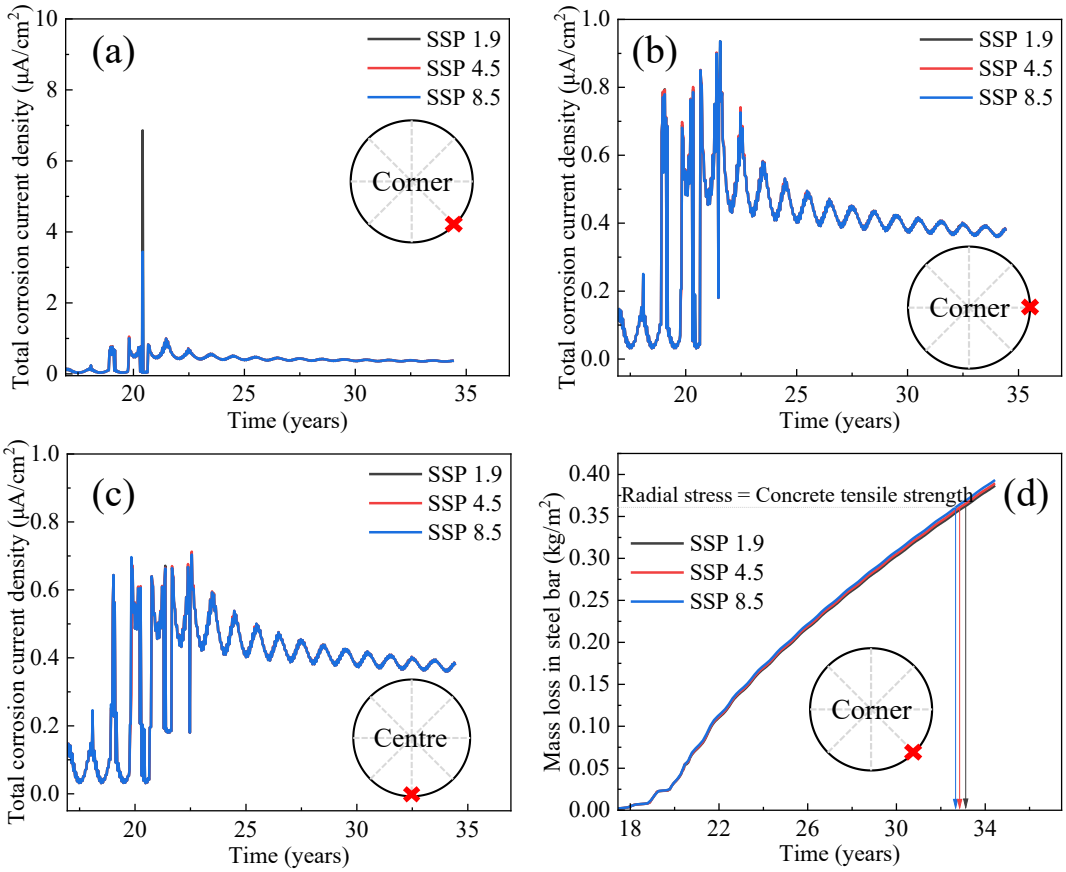

Figure 6.11. Total corrosion current for (a, b) corner rebar and (c) central rebar with different orientations, (d) mass loss in steel for corner rebar in most severe orientation and time for cracking for tidal exposure.

The time for corrosion initiation and propagation period until the time for cracking was subsequently evaluated. The corrosion initiation time was assumed based on the spike of corrosion current density for either of the rebars. When comparing the different climate projections, the time for corrosion initiation was reduced by a maximum of 4 months for SSP 8.5 (18.8 years) relative to SSP 1.9 (19.1 years). The corrosion time was 18.9 years for SSP 4.5. Among the two bars, the corner rebar corroded earlier than the central rebar, aligning with the trend for chloride distribution inside the concrete. The total corrosion current density at the surface of rebars and the trend of mass loss of steel with time are provided in Figure 6.11. Irrespective of the different climate projections, the corrosion current followed a similar trend,

with its intensity varying due to seasonal and daily temperature fluctuations. The total corrosion current initially peaked at about 7 μA/cm^2 for the corner rebar right after the transition from passive to active condition due to the localized aspect of corrosion, which led to a higher cathode/anode ratio. After that, the corrosion current density showed a sharp drop due to the reduction of the cathode/anode ratio, which significantly influences macro-cell current. The drastic change in the cathode/anode ratio could be attributed to the faster chloride transport rate in tidal zone concrete, which increases the active corrosion area. Subsequently, the time for cracking was calculated based on equation 6.37. It was found that the time from corrosion initiation to cracking was about 13 years for the three different climate projections, with a minor reduction in corrosion initiation time for different projection scenarios.

Effect of extended cover depth

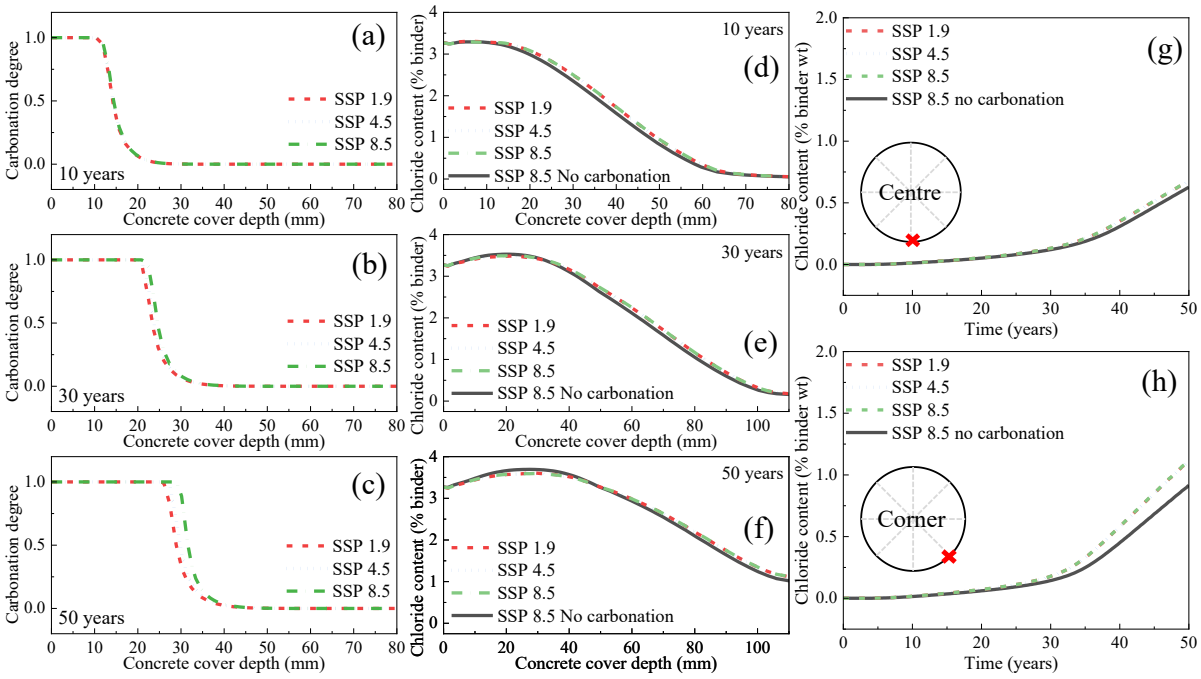

Figure 6.12. Prediction of (a-c) carbonation degrees and (d-f) free chloride profiles at different concrete depths for 10, 30 and 50 years of service period, maximum free chloride contents at the surface of (g) central rebar and (h) corner rebar in tidal exposure zone with 75 mm cover.

Considering the severity of steel corrosion risk in the tidal zone, the RC beams were also analyzed for a cover thickness of 75 mm. The carbonation depths and free chloride contents inside the concrete cover after different years of service are presented in Figure 6.12 (a-h). The effect of future climate projections on carbonation depth was more prominent in this case than in lower cover depth due to increased exposure time. For example, at 50 years of service, the carbonation depth was about 30 mm, considering the worst-case scenario (SSP 8.5) and 25 mm when considering the best-case scenario (SSP 1.9). Thus, there was no risk of corrosion initiation by carbonation in all situations due to the high moisture content in concretes. When comparing the chloride contents for different future climate projections, the observed trend was similar to that observed in beams with a 50 mm cover. The chloride distribution only changed marginally based on different projected scenarios. Comparing the chloride distribution in concretes without carbonation, a drop in the peak chloride content and a slight increase in chloride contents at deeper layers of concrete were observed when considering the effect of combined chloride ingress and carbonation. The maximum chloride content at the corner steel surface for the combined case was about 20% higher than that of the non-carbonated case at about 40 years of service. The time for corrosion initiation without considering the temperature-dependent chloride threshold was about 45-46 years (depending on projected scenarios) for the combined deterioration case and 50 years for the non-carbonated case.

Condition of RC beams in atmospheric zone

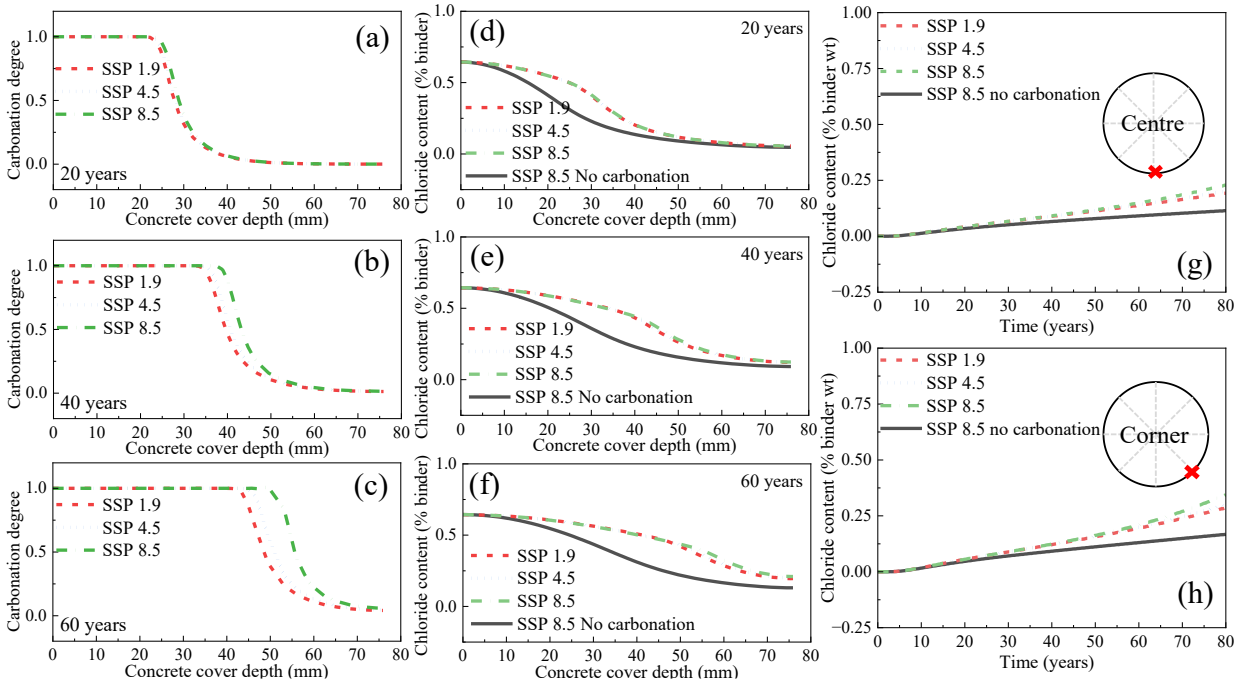

Figure 6.13. Prediction of (a-c) carbonation degrees and (d-f) free chloride profiles at different concrete depths for 20, 40 and 60 years of service period, maximum free chloride contents at the surface of (g) central rebar and (h) corner rebar in atmospheric exposure zone.

For the RC beam in the atmospheric exposure zone, the carbonation degree and chloride contents at different depths of concrete are presented in Figure 6.13. When evaluating the carbonation front for different climate projections during 60 years of service, the top 50 mm of the concrete cover were fully carbonated for SSP 8.5, 44 mm for SSP 4.5 and 41 mm for the SSP 1.9 scenario, as shown in Figure 6.13 (a-c). This suggests that the carbonation front would reach the steel surface during 60 years of service. This can significantly reduce the chloride content required for corrosion initiation in steel rebars. Contrary to the tidal exposures, the deeper penetration of the carbonation front was due to the lower pore degree saturation for such concretes (between 0.6 and 0.8). This subsequently affected chloride profiles with higher free chloride contents at deeper areas of concrete cover. Compared to the case when carbonation was not considered, the chloride contents at the steel surface of corner rebar were about 44% higher when considering SSP 1.9 climate projections, 80% higher when considering SSP 4.5

and 103% higher when considering the most severe SSP 8.5 scenario. It is worth noting that compared to the variations in the carbonation front, the variations in chloride distribution were less pronounced between different climate projections. This is because severe climate projections led to a greater rise in temperature and carbon dioxide concentrations. While the greater carbon dioxide concentrations increased the corrosion risk, it was countered by the increased chloride binding ability in the uncarbonated layers of concrete at greater temperature rise, whose effect had been previously shown in Section 6.4.3. When comparing the corrosion risk of rebars based on their location, the central rebar had lower chloride contents at its surface and reduced corrosion risk. For example, when considering climate projections as per SSP 8.5, the maximum free chloride contents for the rebar at the centre was 0.227% of binder weight % while it was about 0.350% for the corner bar, which presents an increase of about 54.2% in corrosion risk.

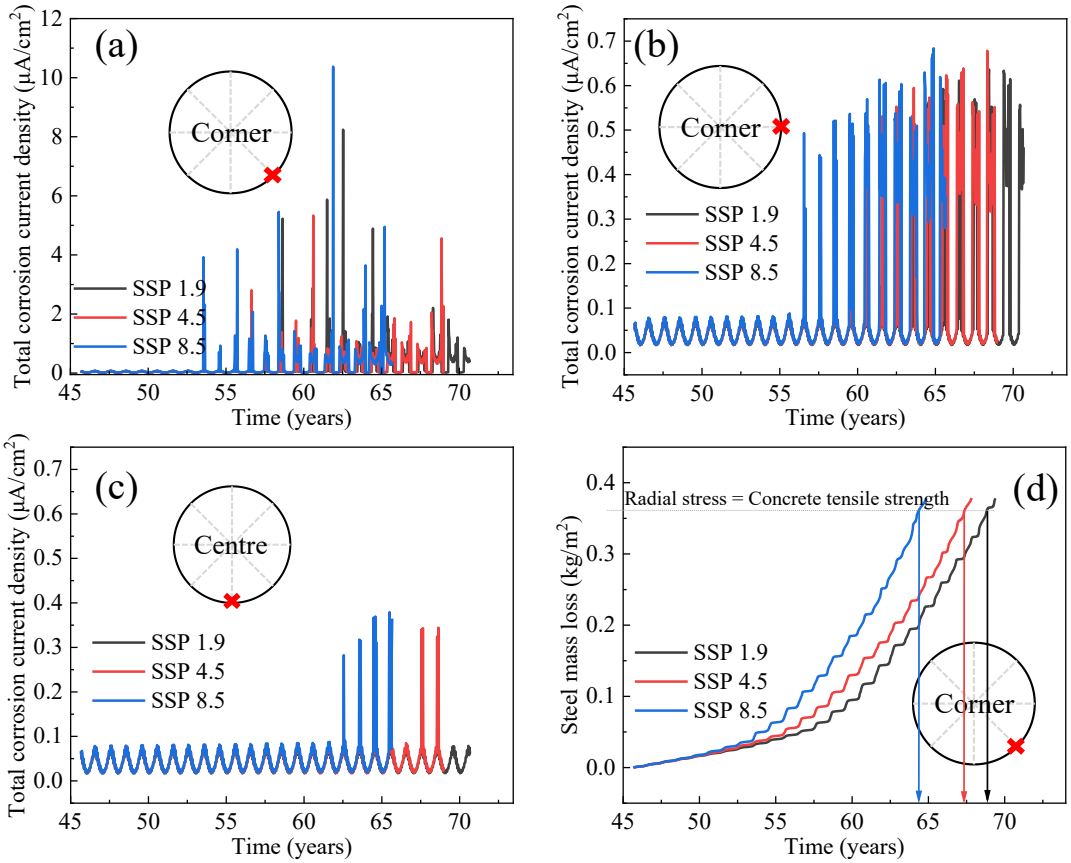

Figure 6.14. Total corrosion current for (a, b) corner rebar and (c) central rebar with different orientations, (d) mass loss in steel for corner rebar in the most severe orientation and time for cracking.

The time for corrosion initiation was calculated based on the variation of corrosion current density in steel rebars, which showed a spike in magnitude after the rebar's transition from passive to active steel. The evolution of total corrosion current density and steel mass loss with time, which leads to crack initiation, is provided in Figure 6.14. The corner rebar corroded earlier than the central rebar, aligning with the chloride penetration and previous exposure. Based on the spike of corrosion current, the corrosion initiation time for corner rebar was 53.5 years for SSP 8.5, 55.6 years for SSP 4.5 and 57.6 years for SSP 1.9. This presents a reduction in corrosion initiation time of more than 100% compared to isolated cases of chloride ingress. A comparison of the chloride contents and carbonation degree at the same time suggests that the cause of corrosion initiation in the atmospheric zone was a reduced chloride threshold by partial carbonation of concrete in the vicinity of the steel rebar. Similar to the trend of corrosion current density in the tidal zone, the corrosion initiation in the corner rebar was marked by a high current density magnitude. However, instead of a sudden drop in magnitude as observed for the tidal zone, the higher corrosion current density was observed for a longer duration in the atmospheric zone. One possible reason for this phenomenon is a sustained high cathode/anode ratio in the beam due to the slower chloride penetration in the atmospheric zone. This can be observed in the difference between the corner and central rebar corrosion initiation period. For example, following the SSP 8.5 projected scenario, the corrosion initiation time for the central rebar was 60.8 years compared to 53.5 years for the corner rebar. On the contrary, the corrosion initiation time between the corner and central rebar was just about 8 months. As a result, the time from corrosion initiation to first crack formation was shortened to 10.8 years for SSP 8.5, 10.9 years for SSP 4.5 and 11.4 years for SSP 1.9.

6.5 Overall Summary

This paper presented a comprehensive approach for service life estimation of coastal RC structures against corrosion by considering temperature-dependent chloride transport rate, chloride binding ability in the cement matrix, and chloride threshold value required for corrosion initiation through combined experiment and numerical modeling. This framework was first used to evaluate the sensitivity of temperature on chloride-induced corrosion risk. Subsequently, it was expanded to predict the time until corrosion initiation and the formation of the first crack, considering three future climate projections (SSP 1.9, SSP 4.5, and SSP 8.5) for typical structures in Hong Kong, which experiences a sub-tropical climate and is located near the sea. Based on the findings of the study, the following conclusions can be drawn:

(a) Most of the current service life analysis models have considered isolated scenarios of chloride transport or carbonation. The current model can accurately predict both the chloride distribution and electrochemical processes, accounting for time-varying exposure conditions, considering future climate projections.

(b) The influence of temperature on chloride binding counteracts the effect on chloride transport and the threshold value, causing the corrosion initiation time to decrease marginally (2%) when a temperature increase up to 5 °C is considered.

(c) For the tidal zone, the high chloride contents pose the primary risk of corrosion. The different projection scenarios had a limited impact on corrosion risk. For the most severe SSP 8.5 years, the corrosion initiation time was 18.8 years compared to 19.1 years in SSP 1.9. Increasing the cover thickness by about 25 mm can extend the corrosion initiation time to 46 years.

(d) For the marine atmospheric zone, the partially carbonated concrete at the steel surface reduces the chloride threshold required for corrosion initiation. This leads to a reduced

corrosion initiation time of 53.5 years for SSP 8.5, 55.6 years for SSP 4.5 and 57.6 years for SSP 1.9.

(e) Different projection scenarios had a marginal impact on the time from corrosion initiation to first crack formation. Considering the slow chloride transport in the coastal atmospheric zone, prolonged periods of high cathode/anode ratio led to higher corrosion current and lower time for first crack formation compared to the tidal zone.

(f) The synergistic effect of carbonation and chloride ingress must be considered during service life estimation. Otherwise, service life can be overestimated by more than 100% in the marine atmospheric zone and 8-10% in tidal exposures.

CHAPTER 7

CONCLUSIONS AND RECOMMENDATIONS

7.1 Conclusions

Corrosion of steel reinforcement poses the maximum threat to degradation for coastal RC structures. This causes a great deal of economic and social cost. The most promising and economical way of extending the structure's service life and preventing any catastrophic failure is taking appropriate preventive maintenance measures at optimum frequency to balance the cost and benefits. The first step in this regard is to develop an accurate service modeling framework that can consider coupled degradation mechanisms in the different service environments.

As evident in previous literature, the current service life modeling for RC structures against corrosion takes a simplified approach and does not accurately consider the effect of micro-climate due to a lack of understanding of the underlying interaction mechanisms. Thus, in this dissertation, comprehensive work has been carried out to evaluate the corrosion-induced degradation of RC structures under the coupled influences of chlorides and environmental temperature marked by daily, seasonal and annual changes, considering future climate change projections. The dissertation comprises the effect of coupled interactions on passivation and depassivation of steel in simulated pore solution (Chapter 3), cement hydration products (Chapter 4), the chloride threshold value in reinforced mortars during accelerated chloride exposure tests (Chapter 5) and implications on the long-term service life of RC structures (Chapter 6). The main conclusions from the different chapters are as follows:

(a) Compared to the standard temperature condition of 25 ℃, increased exposure temperatures of 35 ℃ and 45 ℃ promoted rapid oxidation of Fe(metal) to Fe(II) oxides, such that the oxide film reached a steady thickness at a significantly lower immersion

(12 hours in the case of 45 ℃) in alkaline solution. Extended immersion only facilitated structural transformation from Fe(II) oxides to Fe(III) oxides. Thus, oxide films at elevated temperatures had lower Fe(II)/Fe(III) ratios along with reduced net oxide contents, probably linked to lower oxygen solubility in alkaline solution. The elevated temperatures also resulted in a greater concentration of defects in the passive film, which caused the passive film resistance of samples at 25 ℃ to be seven times the passive film resistance at 35 ℃ and 20 times that at 45 ℃. When chlorides were introduced, the passivity breakdown occurred at 1.2M chloride concentration for 45 ℃, compared to 1.8M at 35℃ and 3.4M chloride concentration at 25 ℃.

(b) The chloride binding in samples exposed to chlorides at room temperature increased with increasing fly ash content. Increasing exposure temperature from 25 ℃ to 45 ℃ increased both physical and chemical chloride binding in samples without silica fume for a high chloride exposure of 3M. At a low chloride exposure of 0.5M, the chemically bound chloride increased at elevated exposure temperature for samples without silica fume. However, there was a drop in physically bound chlorides in C-(A)-S-H. Higher Friedel salt at an elevated temperature of 45 ℃ could be linked to the faster transformation of ettringite (AFm) and other AFm phases to Friedel salt and additional AFm formed by the reaction between C_3A and portlandite. For samples with fly ash and silica fume, the pH dropped below 12 at 45 ℃, destabilizing the Friedel salt and reducing chemically bound chlorides. The physical binding of chlorides was strongly linked to the Ca/Si and had a weak correlation with aluminium contents, i.e., Al/(Al+Si) in C-(A)-S-H.

(c) Exposure of reinforced mortars to chloride solution at elevated temperatures of 45 ℃ reduced the corrosion initiation time significantly. This was due to accelerated chloride ingress and a reduction of the chloride threshold value for corrosion initiation. Adding

supplementary cementitious materials (SCMs) like fly ash and silica fume can partially mitigate the negative impact of temperature due to their enhanced pozzolanic effect, which refines the pore structure. Consequently, the mortar resistance for those with high SCM content (more than 35%) at 45 ℃ was 2-3 times that at 25℃. Detailed observation of corroded areas revealed that corrosion became more localised, with severe pitting, at higher temperatures and favoured the formation of Akaganeite and Goethite over Lepidocrocite. A 20 ℃ rise in temperature also led to a drop in chloride threshold value in the 40-62% range, with no apparent benefits of SCMs in mitigating this adverse impact due to temperature. The critical ratio of [Cl-]/[OH-] was reduced to nearly 1/3rd of its value at 25 ℃ for samples containing fly ash and silica fume.

(d) The influence of temperature on chloride binding counteracted the effect on chloride transport and the threshold value, causing the corrosion initiation time to decrease marginally (2%) when a temperature increase up to 5 °C is considered. For the tidal zone, the high chloride contents pose the primary risk of corrosion. Increasing the cover thickness by 25 mm could more than double the corrosion initiation time. For the marine atmospheric zone, the partially carbonated concrete at the steel surface reduced the chloride threshold required for corrosion initiation. Different projection scenarios had a marginal impact on the time from corrosion initiation to first crack formation, to a maximum of 4-5 years. The synergistic effect of carbonation and chloride ingress must be considered during service life estimation. Otherwise, service life can be overestimated by more than 100% in the marine atmospheric zone and 8-10% in the tidal exposure zone.

7.2 Recommendations

While this dissertation has made significant progress in understanding how environmental temperature impacts the mechanism and rate of chloride-induced corrosion in RC structures, further research is needed to apply these findings toward developing a comprehensive maintenance plan for coastal RC structures, balancing cost and benefits. Key areas for future study include:

(a) With the recent increase in the use of high-strength and composite reinforcing steel for structural applications, it is imperative to understand how steel reinforcements made with different alloys show susceptibility to chloride-linked corrosion in different service environments.

(b) Given the crucial role of chloride binding in extending the service life of RC structures, more focus should be placed on how this binding is affected by the addition of different SCMs or in low-carbon concrete systems across a range of service conditions. This will help identify the most suitable cementitious systems for specific applications.

(c) The service model in Chapter 6 treats concrete as a uniform material and uses a finite element model for ingress and corrosion. However, concrete is a highly heterogeneous and multi-phased material. Future modeling should, therefore, consider multi-ionic transport and cracking phenomena in concrete through meso-scale characterization.

(d) Due to significant uncertainties related to both the service environment and localized concrete properties like voids and cracks, future work could adopt stochastic service life modeling. The finite element model can also be replaced with robust analytical models that can be integrated with Monte Carlo analysis.

(e) For RC structures in coastal atmospheric zones, combined carbonation and chloride ingress are the primary risks for deterioration. However, there is limited understanding

of how the porosity of different cementitious systems changes with carbonation. Including these variations in service life modeling will enhance its accuracy.

(f) Once service life modeling is robust and accurate, the focus should shift to understanding the impact of various maintenance strategies on the overall cost and life cycle assessment of infrastructures during service conditions. This can help optimize the repair and maintenance framework for coastal RC structures.

REFERENCES

Abd El Haleem, S., Abd El Aal, E., Abd El Wanees, S., & Diab, A. (2010). Environmental factors affecting the corrosion behaviour of reinforcing steel: I. The early stage of passive film formation in Ca (OH) 2 solutions. *Corrosion Science*, *52*(12), 3875-3882.

Abd El Haleem, S., Abd El Wanees, S., & Bahgat, A. (2013). Environmental factors affecting the corrosion behaviour of reinforcing steel. V. Role of chloride and sulphate ions in the corrosion of reinforcing steel in saturated Ca (OH) 2 solutions. *Corrosion Science*, *75*, 1-15.

Al-Sodani, K. A. A. (2022). Effect of exposure temperatures on chloride penetration resistance of concrete incorporating polypropylene Fibers, silica fume and metakaolin. *Construction and Building Materials*, *346*, 128445.

Al-Sodani, K. A. A., Al-Zahrani, M. M., Maslehuddin, M., Al-Amoudi, O. S. B., & Al-Dulaijan, S. U. (2021). Chloride diffusion models for Type I and fly ash cement concrete exposed to field and laboratory conditions. *Marine Structures*, *76*, 102900.

Alhozaimy, A., Hussain, R. R., & Al-Negheimish, A. (2016). Significance of oxygen concentration on the quality of passive film formation for steel reinforced concrete structures during the initial curing of concrete. *Cement and Concrete Composites*, *65*, 171-176.

Alhozaimy, A., Hussain, R. R., Al-Zaid, R., & Al-Negheimish, A. (2012). Coupled effect of ambient high relative humidity and varying temperature marine environment on corrosion of reinforced concrete. *Construction and Building Materials*, *28*(1), 670-679.

Alonso, C., Andrade, C., Nóvoa, X., Izquierdo, M., & Pérez, M. C. (1998). Effect of protective oxide scales in the macrogalvanic behaviour of concrete reinforcements. *Corrosion Science*, *40*(8), 1379-1389.

Ambler, H., & Bain, A. (1955). Corrosion of metals in the tropics. *Journal of Applied Chemistry*, *5*(9), 437-467.

Andrade, C., Alonso, C., & Garcia, A. (1990). Oxygen availability in the corrosion of reinforcements. *Advances in cement research*, *3*(11), 127-132.

Andrade, C., Alonso, C., & Sarría, J. (2002). Corrosion rate evolution in concrete structures exposed to the atmosphere. *Cement and Concrete Composites*, *24*(1), 55-64.

Andrade, C., Keddam, M., Nóvoa, X. R., Pérez, M., Rangel, C., & Takenouti, H. (2001). Electrochemical behaviour of steel rebars in concrete: influence of environmental factors and cement chemistry. *Electrochimica Acta*, *46*(24-25), 3905-3912.

Andrade, C., Sarría, J., & Alonso, C. (1999). Relative humidity in the interior of concrete exposed to natural and artificial weathering. *Cement and Concrete Research*, *29*(8), 1249-1259.

Angst, U., Elsener, B., Larsen, C. K., & Vennesland, Ø. (2009). Critical chloride content in reinforced concrete—A review. *Cement and Concrete Research*, *39*(12), 1122-1138.

Angst, U. M., Elsener, B., Larsen, C. K., & Vennesland, Ø. (2011). Chloride induced reinforcement corrosion: Electrochemical monitoring of initiation stage and chloride threshold values. *Corrosion Science*, *53*(4), 1451-1464.

Angst, U. M., Geiker, M. R., Alonso, M. C., Polder, R., Isgor, O. B., Elsener, B., Wong, H., Michel, A., Hornbostel, K., & Gehlen, C. (2019). The effect of the steel–concrete interface on chloride-induced corrosion initiation in concrete: a critical review by RILEM TC 262-SCI. *Materials and Structures*, *52*(4), 1-25.

Ann, K. Y., & Song, H.-W. (2007). Chloride threshold level for corrosion of steel in concrete. *Corrosion Science*, *49*(11), 4113-4133.

Arya, C., Bioubakhsh, S., & Vassie, P. (2014). Chloride penetration in concrete subject to wet/dry cycling: influence of moisture content. *Proceedings of the Institution of Civil Engineers-Structures and Buildings*, *167*(2), 94-107.

Arya, C., Buenfeld, N., & Newman, J. (1990). Factors influencing chloride-binding in concrete. *Cement and Concrete Research*, *20*(2), 291-300.

Avadh, K., Jiradilok, P., Bolander, J. E., & Nagai, K. (2021). Mesoscale simulation of pull-out performance for corroded reinforcement with stirrup confinement in concrete by 3D RBSM. *Cement and Concrete Composites*, *116*, 103895.

Azarsa, P., & Gupta, R. (2017). Electrical resistivity of concrete for durability evaluation: a review. *Advances in Materials Science and Engineering*, *2017*(1), 8453095.

Babaahmadi, A., Machner, A., Kunther, W., Figueira, J., Hemstad, P., & De Weerdt, K. (2022). Chloride binding in Portland composite cements containing metakaolin and silica fume. *Cement and Concrete Research*, *161*, 106924.

Bai, L., Xie, J., Liu, J., & Xie, Y. (2021). Effect of salt on hygroscopic properties of cement mortar. *Construction and Building Materials*, *305*, 124746.

Balonis, M., Lothenbach, B., Le Saout, G., & Glasser, F. P. (2010). Impact of chloride on the mineralogy of hydrated Portland cement systems. *Cement and Concrete Research*, *40*(7), 1009-1022.

Barzgar, S., Tarik, M., Ludwig, C., & Lothenbach, B. (2021). The effect of equilibration time on Al uptake in CSH. *Cement and Concrete Research*, *144*, 106438.

Bastidas-Arteaga, E., Chateauneuf, A., Sánchez-Silva, M., Bressolette, P., & Schoefs, F. (2010). Influence of weather and global warming in chloride ingress into concrete: A stochastic approach. *Structural Safety*, *32*(4), 238-249.

Bastidas-Arteaga, E., Schoefs, F., Stewart, M. G., & Wang, X. (2013). Influence of global warming on durability of corroding RC structures: A probabilistic approach. *Engineering Structures*, *51*, 259-266.

Behera, P. K., Moon, A. P. K., Mondal, K., & Misra, S. (2016). Estimating critical corrosion for initiation of longitudinal cracks in RC structures considering phases and composition of corrosion products. *Journal of materials in civil engineering*, *28*(12), 04016158.

Birnin-Yauri, U., & Glasser, F. (1998). Friedel's salt, Ca2Al (OH) 6 (Cl, OH)· 2H2O: its solid solutions and their role in chloride binding. *Cement and Concrete Research*, *28*(12), 1713-1723.

Cai, R., Hu, Y., Yu, M., Liao, W., Yang, L., Kumar, A., & Ma, H. (2020). Skin effect of chloride ingress in marine concrete: A review on the convection zone. *Construction and Building Materials*, *262*, 120566.

Cai, Y., Zheng, H., Hu, X., Lu, J., Poon, C. S., & Li, W. (2021). Comparative studies on passivation and corrosion behaviors of two types of steel bars in simulated concrete pore solution. *Construction and Building Materials*, *266*, 120971.

Cao, C. (2014). 3D simulation of localized steel corrosion in chloride contaminated reinforced concrete. *Construction and Building Materials*, *72*, 434-443.

Cao, J., Jin, Z., Ding, Q., Xiong, C., & Zhang, G. (2022). Influence of the dry/wet ratio on the chloride convection zone of concrete in a marine environment. *Construction and Building Materials*, *316*, 125794.

Cao, Y., Gehlen, C., Angst, U., Wang, L., Wang, Z., & Yao, Y. (2019). Critical chloride content in reinforced concrete—An updated review considering Chinese experience. *Cement and Concrete Research*, *117*, 58-68.

Care, S. (2008). Effect of temperature on porosity and on chloride diffusion in cement pastes. *Construction and Building Materials*, *22*(7), 1560-1573.

Carsana, M., Gastaldi, M., & Redaelli, E. (2022). A case study on corrosion conditions and guidelines for repair of a reinforced concrete chimney in industrial environment. *Structure and Infrastructure Engineering*, *19*(3), 366-377.

Chalhoub, C., Francois, R., & Carcasses, M. (2020). Effect of cathode–anode distance and electrical resistivity on macrocell corrosion currents and cathodic response in cases of chloride induced corrosion in reinforced concrete structures. *Construction and Building Materials*, *245*, 118337.

Chang, H. (2017). Chloride binding capacity of pastes influenced by carbonation under three conditions. *Cement and Concrete Composites*, *84*, 1-9.

Chang, H., Mu, S., & Feng, P. (2018). Influence of carbonation on "maximum phenomenon" in surface layer of specimens subjected to cyclic drying-wetting condition. *Cement and Concrete Research*, *103*, 95-109.

Chang, H., Mu, S., Xie, D., & Wang, P. (2017). Influence of pore structure and moisture distribution on chloride "maximum phenomenon" in surface layer of specimens exposed to cyclic drying-wetting condition. *Construction and Building Materials*, *131*, 16-30.

Chauhan, A., & Sharma, U. K. (2019). Influence of temperature and relative humidity variations on non-uniform corrosion of reinforced concrete. Structures,

Cheewaket, T., Jaturapitakkul, C., & Chalee, W. (2010). Long term performance of chloride binding capacity in fly ash concrete in a marine environment. *Construction and Building Materials*, *24*(8), 1352-1357.

Chen, C., Wang, L., Liu, R., Zhu, P., Liu, H., Wang, X., Yu, J., & Chen, Y. (2023). Chloride penetration of concrete exposed to dry-wet cycle with various dry-wet ratios and temperature. *Construction and Building Materials*, *400*, 132883.

Chen, J.-j., Liu, Q.-f., Jin, W.-l., & Xia, J. (2024). Experiment and Simulation on the Coupled Effects of Calcium Leaching and Chloride Transport in Concrete under Hydraulic Pressure. *Cement and Concrete Composites*, 105834.

Chen, J. J., Thomas, J. J., & Jennings, H. M. (2006). Decalcification shrinkage of cement paste. *Cement and Concrete Research*, *36*(5), 801-809.

Chen, L., & Su, R. K. L. (2020). Effect of high rebar temperature during casting on corrosion in carbonated concrete. *Construction and Building Materials*, *249*, 118718.

Chen, L., & Su, R. K. L. (2023). Experimental and numerical investigations on macrocell corrosion of partially carbonated reinforced concrete with supplementary cementitious materials. *Cement and Concrete Composites*, *135*, 104827.

Choudhary, H. K., Anupama, A., Kumar, R., Panzi, M., Matteppanavar, S., Sherikar, B. N., & Sahoo, B. (2015). Observation of phase transformations in cement during hydration. *Construction and Building Materials*, *101*, 122-129.

Costa, A., & Appleton, J. (1999). Chloride penetration into concrete in marine environment—Part I: Main parameters affecting chloride penetration. *Materials and Structures*, *32*, 252-259.

Criado, M., & Provis, J. L. (2018). Alkali activated slag mortars provide high resistance to chloride-induced corrosion of steel. *Frontiers in Materials*, *5*, 34.

Das, C. S., Ahmad, M. R., Zhao, X.-L., & Dai, J.-G. (2025). Influences of temperatures on the physical and chemical chloride binding of calcium silicate hydrate and Friedel salt at different chloride concentrations. *Construction and Building Materials*, *476*, 141303.

Das, C. S., Zheng, H., & Dai, J.-G. (2025). A review of chloride-induced steel corrosion in coastal reinforced concrete structures: Influence of micro-climate. *Ocean Engineering*, *325*, 120794.

Das, C. S., Zheng, H., Zhao, X.-L., & Dai, J.-G. (2023). Corrosion inhibition of steel reinforcements in seawater sea sand concrete by alkali-activated slag based coatings. *Construction and Building Materials*, *394*, 132210.

de Medeiros-Junior, R. A., de Lima, M. G., de Brito, P. C., & de Medeiros, M. H. F. (2015). Chloride penetration into concrete in an offshore platform-analysis of exposure conditions. *Ocean Engineering*, *103*, 78-87.

De Weerdt, K., Colombo, A., Coppola, L., Justnes, H., & Geiker, M. R. (2015). Impact of the associated cation on chloride binding of Portland cement paste. *Cement and Concrete Research*, *68*, 196-202.

De Weerdt, K., Plusquellec, G., Revert, A. B., Geiker, M., & Lothenbach, B. (2019). Effect of carbonation on the pore solution of mortar. *Cement and Concrete Research*, *118*, 38-56.

Dehwah, H., Maslehuddin, M., & Austin, S. (2003). Effect of sulfate ions and associated cation type on the pore solution chemistry in chloride-contaminated plain and blended cements. *Cement and Concrete Composites*, *25*(4-5), 513-525.

Delagrave, A., Marchand, J., Ollivier, J.-P., Julien, S., & Hazrati, K. (1997). Chloride binding capacity of various hydrated cement paste systems. *Advanced Cement based materials*, *6*(1), 28-35.

Deus, J., Díaz, B., Freire, L., & Nóvoa, X. (2014). The electrochemical behaviour of steel rebars in concrete: an Electrochemical Impedance Spectroscopy study of the effect of temperature. *Electrochimica Acta*, *131*, 106-115.

Deus, J., Freire, L., Montemor, M., & Nóvoa, X. (2012). The corrosion potential of stainless steel rebars in concrete: Temperature effect. *Corrosion Science*, *65*, 556-560.

Dhir, R., Jones, M., & Elghaly, A. (1993). PFA concrete: Exposure temperature effects on chloride diffusion. *Cement and Concrete Research*, *23*(5), 1105-1114.

Díaz, B., Guitián, B., Nóvoa, X., & Pérez, M. (2018). The effect of long-term atmospheric aging and temperature on the electrochemical behaviour of steel rebars in mortar. *Corrosion Science*, *140*, 143-150.

Dousti, A., & Khaksar, H. (2023). Impact of Simultaneous Carbonation and Chloride Attack on Chloride Diffusion in Portland Cement Concrete Mixtures Blended with Natural Zeolite and Silica Fume. *Journal of materials in civil engineering*, *35*(12), 04023478.

Dousti, A., Rashetnia, R., Ahmadi, B., & Shekarchi, M. (2013). Influence of exposure temperature on chloride diffusion in concretes incorporating silica fume or natural zeolite. *Construction and Building Materials*, *49*, 393-399.

Dousti, A., & Shekarchi, M. (2015). Effect of exposure temperature on chloride-binding capacity of cementing materials. *Magazine of Concrete Research*, *67*(15), 821-832.

Ekolu, S., Thomas, M., & Hooton, R. (2006). Pessimum effect of externally applied chlorides on expansion due to delayed ettringite formation: Proposed mechanism. *Cement and Concrete Research*, *36*(4), 688-696.

El Hassan, J., Bressolette, P., Chateauneuf, A., & El Tawil, K. (2010). Reliability-based assessment of the effect of climatic conditions on the corrosion of RC structures subject to chloride ingress. *Engineering Structures*, *32*(10), 3279-3287.

El Maaddawy, T., & Soudki, K. (2007). A model for prediction of time from corrosion initiation to corrosion cracking. *Cement and Concrete Composites*, *29*(3), 168-175.

Elakneswaran, Y., Nawa, T., & Kurumisawa, K. (2009). Electrokinetic potential of hydrated cement in relation to adsorption of chlorides. *Cement and Concrete Research*, *39*(4), 340-344.

Elfmarkova, V., Spiesz, P., & Brouwers, H. (2015). Determination of the chloride diffusion coefficient in blended cement mortars. *Cement and Concrete Research*, *78*, 190-199.

Fan, L., Zhong, W., & Zhang, X. (2021). Chloride-induced corrosion of reinforcement in simulated pore solution of geopolymer. *Construction and Building Materials*, *291*, 123385.

Feliu, S., Morcillo, M., & Chico, B. (1999). Effect of distance from sea on atmospheric corrosion rate. *Corrosion*, *55*(9), 883-891.

Feng, X., Wu, T., Luo, J.-l., & Lu, X. (2020). Degradation of passive film on 304 stainless steel in a simulated concrete pore solution under alternating temperature condition. *Cement and Concrete Composites*, *112*, 103651.

Figueira, R. B., Sadovski, A., Melo, A. P., & Pereira, E. V. (2017). Chloride threshold value to initiate reinforcement corrosion in simulated concrete pore solutions: The influence of surface finishing and pH. *Construction and Building Materials*, *141*, 183-200.

Florea, M., & Brouwers, H. (2012). Chloride binding related to hydration products: Part I: Ordinary Portland Cement. *Cement and Concrete Research*, *42*(2), 282-290.

Gadala, I. M., & Alfantazi, A. (2015). A study of X100 pipeline steel passivation in mildly alkaline bicarbonate solutions using electrochemical impedance spectroscopy under potentiodynamic conditions and Mott–Schottky. *Applied Surface Science*, *357*, 356-368.

Galan, I., & Glasser, F. P. (2015). Chloride in cement. *Advances in cement research*, *27*(2), 63-97.

Gang, X., Yun-pan, L., Yi-biao, S., & Ke, X. (2015). Chloride ion transport mechanism in concrete due to wetting and drying cycles. *Structural Concrete*, *16*(2), 289-296.

Gastaldi, M., & Bertolini, L. (2014). Effect of temperature on the corrosion behaviour of low-nickel duplex stainless steel bars in concrete. *Cement and Concrete Research*, *56*, 52-60.

Geng, J., Easterbrook, D., Liu, Q.-F., & Li, L.-Y. (2016). Effect of carbonation on release of bound chlorides in chloride-contaminated concrete. *Magazine of Concrete Research*, *68*(7), 353-363.

Ghods, P., Isgor, O., Brown, J., Bensebaa, F., & Kingston, D. (2011). XPS depth profiling study on the passive oxide film of carbon steel in saturated calcium hydroxide solution and the effect of chloride on the film properties. *Applied Surface Science*, *257*(10), 4669-4677.

Ghods, P., Isgor, O. B., Carpenter, G., Li, J., McRae, G., & Gu, G. (2013). Nano-scale study of passive films and chloride-induced depassivation of carbon steel rebar in simulated concrete pore solutions using FIB/TEM. *Cement and Concrete Research*, *47*, 55-68.

Glasser, F., Pedersen, J., Goldthorpe, K., & Atkins, M. (2005). Solubility reactions of cement components with NaCl solutions: I. Ca (OH) 2 and CSH. *Advances in cement research*, *17*(2), 57-64.

Gulikers, J. (2005). Numerical modelling of reinforcement corrosion in concrete. *Corrosion in reinforced concrete structures*, *57*(8), 71-90.

Guo, H., Dong, Y., & Gu, X. (2020). Durability assessment of reinforced concrete structures considering global warming: A performance-based engineering and experimental approach. *Construction and Building Materials*, *233*, 117251.

Guzman, R. S., Vilche, J. R., & Arvia, A. J. (1979). The potentiodynamic behaviour of iron in alkaline solutions. *Electrochimica Acta*, *24*(4), 395-403.

Hausmann, D. A. (1967). Steel corrosion in concrete--How does it occur? *Materials protection*.

Hay, R., & Celik, K. (2024). Comparative performance of OPC and LC3-based composites under combined action of carbonation and chloride exposure. *Construction and Building Materials*, *429*, 136428.

Hayat, U., Kai, M.-F., Hu-Bao, A., Liew, J.-X., & Dai, J.-G. (2024). Atomic-level investigation into the transport of NaCl solution in porous cement paste: The effects of pore size and temperature. *Journal of Building Engineering*, 108976.

He, H., Qiao, H., Sun, T., Yang, H., & He, C. (2024). Research progress in mechanisms, influence factors and improvement routes of chloride binding for cement composites. *Journal of Building Engineering*, 108978.

Hemstad, P., Machner, A., & De Weerdt, K. (2020). The effect of artificial leaching with HCl on chloride binding in ordinary Portland cement paste. *Cement and Concrete Research*, *130*, 105976.

Holthuizen, P. E., Çopuroğlu, O., & Polder, R. B. (2018). Chloride ingress of carbonated blast furnace slag cement mortars. In *High Tech Concrete: Where Technology and Engineering Meet* (pp. 73-82). Springer.

Hong, K., & Hooton, R. (1999). Effects of cyclic chloride exposure on penetration of concrete cover. *Cement and Concrete Research*, *29*(9), 1379-1386.

Hooton, R. D. (2019). Future directions for design, specification, testing, and construction of durable concrete structures. *Cement and Concrete Research*, *124*, 105827.

Huet, B., L'Hostis, V., Miserque, F., & Idrissi, H. (2005). Electrochemical behavior of mild steel in concrete: Influence of pH and carbonate content of concrete pore solution. *Electrochimica Acta*, *51*(1), 172-180.

Hussain, R. R., & Ishida, T. (2010). Influence of connectivity of concrete pores and associated diffusion of oxygen on corrosion of steel under high humidity. *Construction and Building Materials*, *24*(6), 1014-1019.

Hussain, S. E. (1993). Effect of temperature on pore solution composition in plain cements. *Cement and Concrete Research*, *23*(6), 1357-1368.

International, A. (2015). ASTM C876-15 Standard Test Method for Corrosion Potentials of Uncoated Reinforcing Steel in Concrete. In: ASTM International West Conshohocken, PA.

Isteita, M., & Xi, Y. (2017). The effect of temperature variation on chloride penetration in concrete. *Construction and Building Materials*, *156*, 73-82.

Jain, A., Gencturk, B., Pirbazari, M., Dawood, M., Belarbi, A., Sohail, M., & Kahraman, R. (2021). Influence of pH on chloride binding isotherms for cement paste and its components. *Cement and Concrete Research*, *143*, 106378.

Jaśniok, T., & Jaśniok, M. (2015). Influence of rapid changes of moisture content in concrete and temperature on corrosion rate of reinforcing steel. *Procedia Engineering*, *108*, 316-323.

Jiang, J.-h., & Yuan, Y.-s. (2013). Development and prediction strategy of steel corrosion rate in concrete under natural climate. *Construction and Building Materials*, *44*, 287-292.

Jin, H., Fan, X., Li, Z., Zhang, W., Liu, J., Zhong, D., & Tang, L. (2022). An experimental study on the influence of continuous ambient humidity conditions on relative humidity changes, chloride diffusion and microstructure in concrete. *Journal of Building Engineering*, *59*, 105112.

Jin, H., Liu, J., Jiang, Z., Zhou, H., & Liu, J. (2021). Influence of the rainfall intensity on the chloride ion distribution in concrete with different levels of initial water saturation. *Construction and Building Materials*, *281*, 122561.

Jin, H., Liu, J., Zhong, D., & Tang, L. (2023). Experimental study on chloride ion diffusion behavior and microstructure in concrete under alternating ambient humidity conditions. *Construction and Building Materials*, *401*, 132886.

Jin, M., Gao, S., Jiang, L., Chu, H., Lu, M., & Zhi, F. F. (2018). Degradation of concrete with addition of mineral admixture due to free chloride ion penetration under the effect of carbonation. *Corrosion Science*, *138*, 42-53.

Jin, Z., Xiong, C., Zhao, T., Du, Y., Zhang, X., Li, N., Yu, Y., & Wang, P. (2022). Passivation and depassivation properties of Cr–Mo alloyed corrosion-resistant steel in simulated concrete pore solution. *Cement and Concrete Composites*, *126*, 104375.

Joiret, S., Keddam, M., Nóvoa, X. R., Pérez, M., Rangel, C., & Takenouti, H. (2002). Use of EIS, ring-disk electrode, EQCM and Raman spectroscopy to study the film of oxides formed on iron in 1 M NaOH. *Cement and Concrete Composites*, *24*(1), 7-15.

Ju, X., Wu, L., Lin, C., Yang, X., & Yang, C. (2021). Prediction of chloride concentration with elevation in concrete exposed to cyclic drying-wetting conditions in marine environments. *Construction and Building Materials*, *278*, 122370.

Justnes, H., Skocek, J., Østnor, T. A., Engelsen, C. J., & Skjølsvold, O. (2020). Microstructural changes of hydrated cement blended with fly ash upon carbonation. *Cement and Concrete Research*, *137*, 106192.

Kamde, D. K., & Pillai, R. G. (2020). Effect of surface preparation on corrosion of steel rebars coated with cement-polymer-composites (CPC) and embedded in concrete. *Construction and Building Materials*, *237*, 117616.

Kapeluszna, E., Kotwica, Ł., Różycka, A., & Gołek, Ł. (2017). Incorporation of Al in CASH gels with various Ca/Si and Al/Si ratio: Microstructural and structural characteristics with DTA/TG, XRD, FTIR and TEM analysis. *Construction and Building Materials*, *155*, 643-653.

Kikstra, J. S., Nicholls, Z. R., Smith, C. J., Lewis, J., Lamboll, R. D., Byers, E., Sandstad, M., Meinshausen, M., Gidden, M. J., & Rogelj, J. (2022). The IPCC Sixth Assessment Report WGIII climate assessment of mitigation pathways: from emissions to global temperatures. *Geoscientific Model Development*, *15*(24), 9075-9109.

Kuosa, H., Ferreira, R., Holt, E., Leivo, M., & Vesikari, E. (2014). Effect of coupled deterioration by freeze–thaw, carbonation and chlorides on concrete service life. *Cement and Concrete Composites*, *47*, 32-40.

Li, B., Giordano, R., Tulliani, J.-M., & Meng, Q. (2024). Effect of sea salt on carbonation and CO2 uptake in cement mortar. *Construction and Building Materials*, *438*, 137212.

Li, B., Huan, Y., & Zhang, W. (2017). Passivation and corrosion behavior of P355 carbon steel in simulated concrete pore solution at pH 12.5 to 14. *Int. J. Electrochem. Sci*, *12*, 10402-10420.

Li, C.-z., & Song, X.-b. (2022). Mesoscale modeling of chloride transport in unsaturated concrete based on Voronoi tessellation. *Cement and Concrete Research*, *161*, 106932.

Li, C., Jiang, L., & Li, S. (2020). Effect of limestone powder addition on threshold chloride concentration for steel corrosion in reinforced concrete. *Cement and Concrete Research*, *131*, 106018.

Li, H., Farzadnia, N., Zhao, Y., Hu, X., & Shi, C. (2024). Effects of SCMs on chloride binding capacity of ultra-low water-to-binder ratio cement paste with internally introduced chloride. *Construction and Building Materials*, *413*, 134725.

Li, J., & Shao, W. (2014). The effect of chloride binding on the predicted service life of RC pipe piles exposed to marine environments. *Ocean Engineering*, *88*, 55-62.

Li, J., Xiong, J., Fan, Z., Chen, M., Sun, L., Zhu, C., Liu, W., Zheng, H., & Li, W. (2023). Mechanistic study of macrocell effect on corrosion initiation and propagation of

reinforcement in submarine immersed tunnel. *Cement and Concrete Composites*, *136*, 104890.

Li, J., Xiong, J., Fan, Z., Gu, Z., Chen, M., Sun, L., Zheng, H., & Li, W. (2023). Macrocell Effect on Chloride Threshold Value and Corrosion Rate of Steel Bar in Simulated Concrete Pore Solution. *Journal of materials in civil engineering*, *35*(12), 04023436.

Li, K., Zhang, Y., Wang, S., & Zeng, J. (2018). Impact of carbonation on the chloride diffusivity in concrete: experiment, analysis and application. *Materials and Structures*, *51*(6), 1-15.

Li, K., Zhao, F., & Zhang, Y. (2019). Influence of carbonation on the chloride ingress into concrete: Theoretical analysis and application to durability design. *Cement and Concrete Research*, *123*, 105788.

Li, K., Zheng, H., Lu, J.-X., Li, W., & Poon, C. S. (2024). Role of encapsulated corrosion inhibitor on the anti-corrosion performance of reinforcing steel in lightweight concrete. *Cement and Concrete Composites*, *146*, 105388.

Liang, C., Cai, Z., Wu, H., Xiao, J., Zhang, Y., & Ma, Z. (2021). Chloride transport and induced steel corrosion in recycled aggregate concrete: A review. *Construction and Building Materials*, *282*, 122547.

Lin, L., Chao, C., & Macdonald, D. (1981). A point defect model for anodic passive films: II. Chemical breakdown and pit initiation. *Journal of The Electrochemical Society*, *128*(6), 1194.

Lindvall, A. (2007). Chloride ingress data from field and laboratory exposure–Influence of salinity and temperature. *Cement and Concrete Composites*, *29*(2), 88-93.

Liu, G., Zhang, Y., Wu, M., & Huang, R. (2017). Study of depassivation of carbon steel in simulated concrete pore solution using different equivalent circuits. *Construction and Building Materials*, *157*, 357-362.

Liu, J.-z., Ba, M.-f., Du, Y.-g., He, Z.-m., & Chen, J.-b. (2016). Effects of chloride ions on carbonation rate of hardened cement paste by X-ray CT techniques. *Construction and Building Materials*, *122*, 619-627.

Liu, J., Ou, G., Qiu, Q., Xing, F., Tang, K., & Zeng, J. (2018). Atmospheric chloride deposition in field concrete at coastal region. *Construction and Building Materials*, *190*, 1015-1022.

Liu, J., Qiu, Q., Chen, X., Wang, X., Xing, F., Han, N., & He, Y. (2016). Degradation of fly ash concrete under the coupled effect of carbonation and chloride aerosol ingress. *Corrosion Science*, *112*, 364-372.

Liu, J., Qiu, Q., Chen, X., Xing, F., Han, N., He, Y., & Ma, Y. (2017). Understanding the interacted mechanism between carbonation and chloride aerosol attack in ordinary Portland cement concrete. *Cement and Concrete Research*, *95*, 217-225.

Liu, M., Cheng, X., Li, X., Zhou, C., & Tan, H. (2017). Effect of carbonation on the electrochemical behavior of corrosion resistance low alloy steel rebars in cement extract solution. *Construction and Building Materials*, *130*, 193-201.

Liu, P., Yu, Z., Lu, Z., Chen, Y., & Liu, X. (2016). Predictive convection zone depth of chloride in concrete under chloride environment. *Cement and Concrete Composites*, *72*, 257-267.

Liu, R., Jiang, L., Huang, G., Zhu, Y., Liu, X., Chu, H., & Xiong, C. (2016). The effect of carbonate and sulfate ions on chloride threshold level of reinforcement corrosion in mortar with/without fly ash. *Construction and Building Materials*, *113*, 90-95.

Liu, R., Jiang, L., Xu, J., Xiong, C., & Song, Z. (2014). Influence of carbonation on chloride-induced reinforcement corrosion in simulated concrete pore solutions. *Construction and Building Materials*, *56*, 16-20.

Liu, T., & Weyers, R. (1998). Modeling the dynamic corrosion process in chloride contaminated concrete structures. *Cement and Concrete Research*, *28*(3), 365-379.

Liu, X., Feng, P., Chen, J., Liu, Q., Yu, X., Cai, Y., Zhu, H., Qing, L., & Hong, J. (2024). A critical review on the interaction between calcium silicate hydrate (CSH) and different ions. *Construction and Building Materials*, *413*, 134931.

Liu, X., MacDonald, D. D., Wang, M., & Xu, Y. (2021). Effect of dissolved oxygen, temperature, and pH on polarization behavior of carbon steel in simulated concrete pore solution. *Electrochimica Acta*, *366*, 137437.

Liu, Y., & Shi, J. (2022). Corrosion resistance of carbon steel in alkaline concrete pore solutions containing phytate and chloride ions. *Corrosion Science*, *205*, 110451.

Lothenbach, B., Scrivener, K., & Hooton, R. (2011). Supplementary cementitious materials. *Cement and Concrete Research*, *41*(12), 1244-1256.

Lothenbach, B., Winnefeld, F., Alder, C., Wieland, E., & Lunk, P. (2007). Effect of temperature on the pore solution, microstructure and hydration products of Portland cement pastes. *Cement and Concrete Research*, *37*(4), 483-491.

Lu, C.-f., Wang, W., Jiang, J.-h., & Hao, M. (2017). Micro-environment temperature and relative humidity response of fly ash concrete under natural climatic conditions. *Advances in cement research*, *29*(6), 236-245.

Lu, C., Gao, Y., Cui, Z., & Liu, R. (2015). Experimental analysis of chloride penetration into concrete subjected to drying–wetting cycles. *Journal of materials in civil engineering*, *27*(12), 04015036.

Machner, A., Bjørndal, M., Šajna, A., Mikanovic, N., & De Weerdt, K. (2022). Impact of leaching on chloride ingress profiles in concrete. *Materials and Structures*, *55*(1), 1-18.

Machner, A., Zajac, M., Haha, M. B., Kjellsen, K. O., Geiker, M. R., & De Weerdt, K. (2018). Chloride-binding capacity of hydrotalcite in cement pastes containing dolomite and metakaolin. *Cement and Concrete Research*, *107*, 163-181.

Malheiro, R., Camões, A., Meira, G., & Amorim, M. T. (2021). Influence of chloride contamination on carbonation of cement-based materials. *Construction and Building Materials*, *296*, 123756.

Malheiro, R., Camões, A., Meira, G., Amorim, M. T., & Castro-Gomes, J. (2020). Effect of coupled deterioration by chloride and carbonation on chloride ions transport in concrete. *RILEM Technical Letters*, *5*, 56-62.

Maradani, L. S. R., & Pradhan, B. (2024). Effect of chloride and sulphate on ionic concentration of aqueous pore solution and microstructural properties of fly ash-GBFS geopolymer concrete. *Construction and Building Materials*, *440*, 137422.

Martın-Pérez, B., Zibara, H., Hooton, R., & Thomas, M. (2000). A study of the effect of chloride binding on service life predictions. *Cement and Concrete Research*, *30*(8), 1215-1223.

Maslehuddin, M., Paget, C., & Rasheeduzzafar. (1997). Temperature effect on the pore solution chemistry in contaminated cements. *Magazine of Concrete Research*, *49*(178), 5-14.

Masson-Delmotte, V., Zhai, P., Pörtner, H.-O., Roberts, D., Skea, J., Shukla, P. R., Pirani, A., Moufouma-Okia, W., Péan, C., & Pidcock, R. (2018). Global warming of 1.5 C. *An IPCC Special Report on the impacts of global warming of*, *1*(5).

Medeiros-Junior, R. A. (2018). Impact of climate change on the service life of concrete structures. In *Eco-efficient repair and rehabilitation of concrete infrastructures* (pp. 43-68). Elsevier.

Medeiros, M., Gobbi, A., Réus, G., & Helene, P. (2013). Reinforced concrete in marine environment: Effect of wetting and drying cycles, height and positioning in relation to the sea shore. *Construction and Building Materials*, *44*, 452-457.

Meira, G. R., Andrade, C., Alonso, C., Borba Jr, J., & Padilha Jr, M. (2010). Durability of concrete structures in marine atmosphere zones–The use of chloride deposition rate on the wet candle as an environmental indicator. *Cement and Concrete Composites*, *32*(6), 427-435.

Meira, G. R., Andrade, C., Alonso, C., Padaratz, I., & Borba Jr, J. (2007). Salinity of marine aerosols in a Brazilian coastal area—Influence of wind regime. *Atmospheric environment*, *41*(38), 8431-8441.

Meira, G. R., Andrade, C., Alonso, C., Padaratz, I., & Borba, z. J. (2008). Modelling sea-salt transport and deposition in marine atmosphere zone–A tool for corrosion studies. *Corrosion Science*, *50*(9), 2724-2731.

Meira, G. R., Andrade, C., Padaratz, I., Alonso, C., & Borba Jr, J. (2007). Chloride penetration into concrete structures in the marine atmosphere zone–Relationship between deposition of chlorides on the wet candle and chlorides accumulated into concrete. *Cement and Concrete Composites*, *29*(9), 667-676.

Meira, G. R., Andrade, M., Padaratz, I., Alonso, M. C., & Borba Jr, J. (2006). Measurements and modelling of marine salt transportation and deposition in a tropical region in Brazil. *Atmospheric environment*, *40*(29), 5596-5607.

Melchers, R. E. (2020). Long-term durability of marine reinforced concrete structures. *Journal of Marine Science and Engineering*, *8*(4), 290.

Melchers, R. E., & Chaves, I. A. (2020). Reinforcement corrosion in marine concretes-2. long-term effects. *ACI materials journal*, *117*(2), 217-228.

Melchers, R. E., Pape, T. M., Chaves, I. A., & Heywood, R. J. (2017). Long-term durability of reinforced concrete piles from the Hornibrook Highway bridge. *Australian journal of structural engineering*, *18*(1), 41-57.

Mi, T., Wang, J. J., Mccague, C., & Bai, Y. (2023). Application of Raman Spectroscopy in the study of the corrosion of steel reinforcement in concrete: A critical review. *Cement and Concrete Composites*, *143*, 105231.

Mi, T., Yang, E.-H., & Unluer, C. (2023). Passivation of reinforcing steel in reactive MgO cement blended with Portland cement. *Cement and Concrete Composites*, *143*, 105269.

Michel, A., Nygaard, P., & Geiker, M. (2013). Experimental investigation on the short-term impact of temperature and moisture on reinforcement corrosion. *Corrosion Science*, *72*, 26-34.

Mohammed, T. U., & Hamada, H. (2006). Corrosion of steel bars in concrete with various steel surface conditions. *ACI materials journal*, *103*(4), 233.

Montemor, M., Simoes, A., & Ferreira, M. (2003). Chloride-induced corrosion on reinforcing steel: from the fundamentals to the monitoring techniques. *Cement and Concrete Composites*, *25*(4-5), 491-502.

Moradllo, M. K., Sadati, S., & Shekarchi, M. (2018). Quantifying maximum phenomenon in chloride ion profiles and its influence on service-life prediction of concrete structures exposed to seawater tidal zone–A field oriented study. *Construction and Building Materials*, *180*, 109-116.

Morcillo, M., Chico, B., Mariaca, L., & Otero, E. (2000). Salinity in marine atmospheric corrosion: its dependence on the wind regime existing in the site. *Corrosion Science*, *42*(1), 91-104.

Mundra, S., Criado, M., Bernal, S. A., & Provis, J. L. (2017). Chloride-induced corrosion of steel rebars in simulated pore solutions of alkali-activated concretes. *Cement and Concrete Research*, *100*, 385-397.

Mundra, S., & Provis, J. L. (2021). Mechanisms of passivation and chloride-induced corrosion of mild steel in sulfide-containing alkaline solutions. *Journal of Materials Science*, 1-20.

Muthulingam, S., & Rao, B. (2014). Non-uniform time-to-corrosion initiation in steel reinforced concrete under chloride environment. *Corrosion Science*, *82*, 304-315.

Nazari, M. H., Allahkaram, S., & Kermani, M. (2010). The effects of temperature and pH on the characteristics of corrosion product in CO2 corrosion of grade X70 steel. *Materials & Design*, *31*(7), 3559-3563.

Ngala, V., & Page, C. (1997). Effects of carbonation on pore structure and diffusional properties of hydrated cement pastes. *Cement and Concrete Research*, *27*(7), 995-1007.

Nguyen, T., Lorente, S., & Carcasses, M. (2009). Effect of the environment temperature on the chloride diffusion through CEM-I and CEM-V mortars: An experimental study. *Construction and Building Materials*, *23*(2), 795-803.

Nomura, K., Tasaka, M., & Ujihira, Y. (1988). Conversion electron Mossbauer spectrometric study of corrosion products of iron immersed in sodium chloride solution. *Corrosion*, *44*(3), 131-135.

Ogirigbo, O. R., & Black, L. (2017). Chloride binding and diffusion in slag blends: Influence of slag composition and temperature. *Construction and Building Materials*, *149*, 816-825.

Ortolan, V., Mancio, M., & Tutikian, B. (2016). Evaluation of the influence of the pH of concrete pore solution on the corrosion resistance of steel reinforcement. *Journal of building pathology and rehabilitation*, *1*(1), 10.

Otieno, M., Golden, G., Alexander, M., & Beushausen, H. (2019). Acceleration of steel corrosion in concrete by cyclic wetting and drying: Effect of drying duration and concrete quality. *Materials and Structures*, *52*(2), 50.

Otsuki, N., Madlangbayan, M. S., Nishida, T., Saito, T., & Baccay, M. A. (2009). Temperature dependency of chloride induced corrosion in concrete. *Journal of advanced concrete technology*, *7*(1), 41-50.

Page, C. (1975). Mechanism of corrosion protection in reinforced concrete marine structures. *nature*, *258*(5535), 514-515.

Page, C., Short, N., & El Tarras, A. (1981). Diffusion of chloride ions in hardened cement pastes. *Cement and Concrete Research*, *11*(3), 395-406.

Pan, C., Cui, Y., Liu, L., Guo, M., & Wang, Z. (2020). Effect of temperature on corrosion behavior of low-alloy steel exposed to a simulated marine atmospheric environment. *Journal of materials engineering and performance*, *29*, 1400-1409.

Pan, Z., Chen, A., Ma, R., Wang, D., & Tian, H. (2018). Three-dimensional lattice modeling of concrete carbonation at meso-scale based on reconstructed coarse aggregates. *Construction and Building Materials*, *192*, 253-271.

Panesar, D., & Chidiac, S. (2011). Effect of cold temperature on the chloride-binding capacity of cement. *Journal of Cold Regions Engineering*, *25*(4), 133-144.

Papadakis, V., Vayenas, C., & Fardis, M. (1991). Physical and chemical characteristics affecting the durability of concrete. *ACI materials journal*, *88*(2), 186-196.

Pati, A. R. (2010). *Effects of rebar temperature and water to cement ratio on rebar-concrete bond strength of concrete containing fly ash*. University of North Texas.

Peng, L., & Stewart, M. G. (2016). Climate change and corrosion damage risks for reinforced concrete infrastructure in China. *Structure and Infrastructure Engineering*, *12*(4), 499-516.

Pergola, A. D., Lollini, F., Redaelli, E., & Bertolini, L. (2013). Numerical modeling of initiation and propagation of corrosion in hollow submerged marine concrete structures. *Corrosion*, *69*(12), 1158-1170.

Poon, C. S., Lam, L., & Wong, Y. L. (1999). Effects of fly ash and silica fume on interfacial porosity of concrete. *Journal of materials in civil engineering*, *11*(3), 197-205.

Popova, A. (2007). Temperature effect on mild steel corrosion in acid media in presence of azoles. *Corrosion Science*, *49*(5), 2144-2158.

Pour-Ghaz, M., Isgor, O. B., & Ghods, P. (2009a). The effect of temperature on the corrosion of steel in concrete. Part 1: Simulated polarization resistance tests and model development. *Corrosion Science*, *51*(2), 415-425.

Pour-Ghaz, M., Isgor, O. B., & Ghods, P. (2009b). The effect of temperature on the corrosion of steel in concrete. Part 2: Model verification and parametric study. *Corrosion Science*, *51*(2), 426-433.

Poursaee, A. (2016). Temperature dependence of the formation of the passivation layer on carbon steel in high alkaline environment of concrete pore solution. *Electrochemistry Communications*, *73*, 24-28.

Poursaee, A., & Hansson, C. (2007). Reinforcing steel passivation in mortar and pore solution. *Cement and Concrete Research*, *37*(7), 1127-1133.

Puatatsananon, W., & Saouma, V. (2005). Nonlinear coupling of carbonation and chloride diffusion in concrete. *Journal of materials in civil engineering*, *17*(3), 264-275.

Qiao, C., Suraneni, P., Ying, T. N. W., Choudhary, A., & Weiss, J. (2019). Chloride binding of cement pastes with fly ash exposed to CaCl2 solutions at 5 and 23° C. *Cement and Concrete Composites*, *97*, 43-53.

Qin, L., Zhao, H., Gao, J., Wu, H., Zhang, C., Huang, Y., Wang, S., & Mao, X. (2025). Revisiting Raman spectroscopy findings: The contested presence of γ-FeOOH in inner rust layers of weathering steel. *Materials Characterization*, *220*, 114707.

Qiu, Q. (2020). A state-of-the-art review on the carbonation process in cementitious materials: Fundamentals and characterization techniques. *Construction and Building Materials*, *247*, 118503.

Qu, F., Li, W., Guo, Y., Zhang, S., Zhou, J. L., & Wang, K. (2022). Chloride-binding capacity of cement-GGBFS-nanosilica composites under seawater chloride-rich environment. *Construction and Building Materials*, *342*, 127890.

Ranger, M., Hasholt, M. T., & Barbosa, R. A. (2023). Pore solution alkalinity of cement paste as determined by Cold Water Extraction. *Cement*, *11*, 100055.

Raupach, M. (1996a). Chloride-induced macrocell corrosion of steel in concrete—theoretical background and practical consequences. *Construction and Building Materials*, *10*(5), 329-338.

Raupach, M. (1996b). Investigations on the influence of oxygen on corrosion of steel in concrete—Part 2. *Materials and Structures*, *29*, 226-232.

Raupach, M. (1996c). Investigations on the influence of oxygen on corrosion of steel in concrete—Part I. *Materials and Structures*, *29*, 174-184.

Ren, D., Jiradilok, P., Waghmare, D., & Nagai, K. (2024). Meso-scale simulation of moisture transport in concrete during wet-dry cycles using 3D RBSM conduit model with variable diffusion model. *Cement and Concrete Composites*, *149*, 105497.

Renaudin, G., Kubel, F., Rivera, J.-P., & Francois, M. (1999). Structural phase transition and high temperature phase structure of Friedels salt, 3CaO· Al2O3· CaCl2· 10H2O. *Cement and Concrete Research*, *29*(12), 1937-1942.

Revert, A. B., Hornbostel, K., De Weerdt, K., & Geiker, M. R. (2019). Macrocell corrosion in carbonated Portland and Portland-fly ash concrete-Contribution and mechanism. *Cement and Concrete Research*, *116*, 273-283.

Ruan, T., Spandley, N., Johnson, C., & Poursaee, A. (2015). The impact of fire and fire extinguishing method on the corrosion behavior of the steel bars in concrete pore solution. *Fire Safety Journal*, *78*, 196-201.

Saillio, M., Baroghel-Bouny, V., & Barberon, F. (2014). Chloride binding in sound and carbonated cementitious materials with various types of binder. *Construction and Building Materials*, *68*, 82-91.

Saillio, M., Baroghel-Bouny, V., Bertin, M., Pradelle, S., & Vincent, J. (2019). Phase assemblage of cement pastes with SCM at different ages. *Construction and Building Materials*, *224*, 144-157.

Saillio, M., Baroghel-Bouny, V., Pradelle, S., Bertin, M., Vincent, J., & de Lacaillerie, J.-B. d. E. (2021). Effect of supplementary cementitious materials on carbonation of cement pastes. *Cement and Concrete Research*, *142*, 106358.

Samson, E., & Marchand, J. (2007). Modeling the effect of temperature on ionic transport in cementitious materials. *Cement and Concrete Research*, *37*(3), 455-468.

Sánchez-Moreno, M., Takenouti, H., García-Jareño, J., Vicente, F., & Alonso, C. (2009). A theoretical approach of impedance spectroscopy during the passivation of steel in alkaline media. *Electrochimica Acta*, *54*(28), 7222-7226.

Sánchez, M., Gregori, J., Alonso, C., García-Jareño, J., Takenouti, H., & Vicente, F. (2007). Electrochemical impedance spectroscopy for studying passive layers on steel rebars immersed in alkaline solutions simulating concrete pores. *Electrochimica Acta*, *52*(27), 7634-7641.

Sánchez, M., Gregori, J., Alonso, M., García-Jareño, J., & Vicente, F. (2006). Anodic growth of passive layers on steel rebars in an alkaline medium simulating the concrete pores. *Electrochimica Acta*, *52*(1), 47-53.

Santhanam, M., & Otieno, M. (2016). Deterioration of concrete in the marine environment. *Marine concrete structures*, 137-149.

Scott, A., & Alexander, M. (2016). Effect of supplementary cementitious materials (binder type) on the pore solution chemistry and the corrosion of steel in alkaline environments. *Cement and Concrete Research*, *89*, 45-55.

Scrivener, K., Snellings, R., Lothenbach, B., & Press, C. (2016). *A practical guide to microstructural analysis of cementitious materials* (Vol. 540). Crc Press Boca Raton, FL, USA:.

Segura, I., Cavalaro, S., Fuente, A. d. l., Aguado, A., & Alegre, V. (2016). Service-life assessment of existing precast concrete structure exposed to severe marine conditions. *Journal of Performance of Constructed Facilities*, *30*(3), 04015036.

Shafikhani, M., & Chidiac, S. (2019). Quantification of concrete chloride diffusion coefficient–A critical review. *Cement and Concrete Composites*, *99*, 225-250.

Sharifi-Asl, S., Mao, F., Lu, P., Kursten, B., & Macdonald, D. D. (2015). Exploration of the effect of chloride ion concentration and temperature on pitting corrosion of carbon steel in saturated Ca (OH) 2 solution. *Corrosion Science*, *98*, 708-715.

Shen, X.-h., Jiang, W.-q., Hou, D., Hu, Z., Yang, J., & Liu, Q.-f. (2019). Numerical study of carbonation and its effect on chloride binding in concrete. *Cement and Concrete Composites*, *104*, 103402.

Shen, X.-h., Liu, Q.-f., Hu, Z., Jiang, W.-q., Lin, X., Hou, D., & Hao, P. (2019). Combine ingress of chloride and carbonation in marine-exposed concrete under unsaturated environment: A numerical study. *Ocean Engineering*, *189*, 106350.

Shi, J., Wu, M., & Ming, J. (2020). Degradation effect of carbonation on electrochemical behavior of 2304 duplex stainless steel in simulated concrete pore solutions. *Corrosion Science*, *177*, 109006.

Shi, X., Xie, N., Fortune, K., & Gong, J. (2012). Durability of steel reinforced concrete in chloride environments: An overview. *Construction and Building Materials*, *30*, 125-138.

Shi, Z., Geiker, M. R., De Weerdt, K., Østnor, T. A., Lothenbach, B., Winnefeld, F., & Skibsted, J. (2017). Role of calcium on chloride binding in hydrated Portland cement–metakaolin–limestone blends. *Cement and Concrete Research*, *95*, 205-216.

Simões, M., Koga, G., & Ferreira, F. (2024). Steel rebar passivation in cementitious blend solutions–Silica fume vs. glass powder. *Materials Letters*, 136709.

Singh, J., & Singh, D. (2012). The nature of rusts and corrosion characteristics of low alloy and plain carbon steels in three kinds of concrete pore solution with salinity and different pH. *Corrosion Science*, *56*, 129-142.

Skibsted, J., & Snellings, R. (2019). Reactivity of supplementary cementitious materials (SCMs) in cement blends. *Cement and Concrete Research*, *124*, 105799.

Song, H.-W., Lee, C.-H., & Ann, K. Y. (2008). Factors influencing chloride transport in concrete structures exposed to marine environments. *Cement and Concrete Composites*, *30*(2), 113-121.

Spragg, R. P., Castro, J., Li, W., Pour-Ghaz, M., Huang, P.-T., & Weiss, J. (2011). Wetting and drying of concrete using aqueous solutions containing deicing salts. *Cement and Concrete Composites*, *33*(5), 535-542.

Stefanoni, M., Angst, U., & Elsener, B. (2020). The mechanism controlling corrosion of steel in carbonated cementitious materials in wetting and drying exposure. *Cement and Concrete Composites*, *113*, 103717.

Stewart, M. G., Wang, X., & Nguyen, M. N. (2011). Climate change impact and risks of concrete infrastructure deterioration. *Engineering Structures*, *33*(4), 1326-1337.

Sun, M., Sun, C., Zhang, P., Liu, N., Li, Y., Duan, J., & Hou, B. (2021). Influence of carbonation on chloride binding of mortars made with simulated marine sand. *Construction and Building Materials*, *303*, 124455.

Suryavanshi, A., Scantlebury, J., & Lyon, S. (1996). Mechanism of Friedel's salt formation in cements rich in tri-calcium aluminate. *Cement and Concrete Research*, *26*(5), 717-727.

Talukdar, S., & Banthia, N. (2013). Carbonation in concrete infrastructure in the context of global climate change: Development of a service lifespan model. *Construction and Building Materials*, *40*, 775-782.

Thomas, M., Hooton, R., Scott, A., & Zibara, H. (2012). The effect of supplementary cementitious materials on chloride binding in hardened cement paste. *Cement and Concrete Research*, *42*(1), 1-7.

Tong, L.-y., Šavija, B., Zhang, M., Xiong, Q. X., & Liu, Q.-f. (2025). Chloride penetration in concrete under varying humidity and temperature changes: A numerical study. *Construction and Building Materials*, *458*, 138380.

Tongning, C., Lijuan, Z., Guowen, S., Caihui, W., Ying, Z., Pengshuo, W., & Aoxue, X. (2020). Simulation of chloride ion transport in concrete under the coupled effects of a bending load and drying–wetting cycles. *Construction and Building Materials*, *241*, 118045.

Tran, V. Q., Nguyen, H.-L., Dao, D. V., Hilloulin, B., Nguyen, L. K., Nguyen, Q. H., Le, T.-T., & Ly, H.-B. (2021). Effect of temperature on the chloride binding capacity of cementitious materials. *Magazine of Concrete Research*, *73*(15), 771-784.

Ukpata, J. O., Basheer, P., & Black, L. (2019). Slag hydration and chloride binding in slag cements exposed to a combined chloride-sulphate solution. *Construction and Building Materials*, *195*, 238-248.

Uusitalo, M., Vuoristo, P., & Mäntylä, T. (2003). High temperature corrosion of coatings and boiler steels in oxidizing chlorine-containing atmosphere. *Materials Science and Engineering: A*, *346*(1-2), 168-177.

Vollpracht, A., Lothenbach, B., Snellings, R., & Haufe, J. (2016). The pore solution of blended cements: a review. *Materials and Structures*, *49*, 3341-3367.

Volpi, E., Olietti, A., Stefanoni, M., & Trasatti, S. P. (2015). Electrochemical characterization of mild steel in alkaline solutions simulating concrete environment. *Journal of Electroanalytical Chemistry*, *736*, 38-46.

von Greve-Dierfeld, S., Lothenbach, B., Vollpracht, A., Wu, B., Huet, B., Andrade, C., Medina, C., Thiel, C., Gruyaert, E., & Vanoutrive, H. (2020). Understanding the carbonation of concrete with supplementary cementitious materials: a critical review by RILEM TC 281-CCC. *Materials and Structures*, *53*(6), 1-34.

Wang, D., Wu, J., Wang, Q., Wan, L., Emori, W., Zhang, S., & Wang, J. (2021). Temperature-dependent corrosion behaviour of the amorphous steel in simulated wet storage environment of spent nuclear fuels. *Corrosion Science*, *188*, 109529.

Wang, S., Liu, D., Du, N., Zhao, Q., & Xiao, J. (2016). Cathodic reactions involved in the corrosion of X80 steel in acidic soil simulated solution. *Int. J. Electrochem. Sci*, *11*, 8797-8809.

Wang, X., Zhang, Z., Xu, Z., Wang, Y., Zhan, B., & Xing, F. (2023). Modelling of carbonation of hardened cement pastes with premixed Cl− and resulting Cl− redistribution. *Construction and Building Materials*, *384*, 131470.

Wang, Y., Nanukuttan, S., Bai, Y., & Basheer, P. (2017). Influence of combined carbonation and chloride ingress regimes on rate of ingress and redistribution of chlorides in concretes. *Construction and Building Materials*, *140*, 173-183.

Wang, Y., Shui, Z., Gao, X., Huang, Y., Yu, R., & Song, Q. (2020). Chloride binding capacity and phase modification of alumina compound blended cement paste under chloride attack. *Cement and Concrete Composites*, *108*, 103537.

Wang, Z., Jin, J., Zhang, G.-H., Fan, X.-H., & Zhang, L. (2022). Effect of temperature on the passive film structure and corrosion performance of CoCrFeMoNi high-entropy alloy. *Corrosion Science*, 110661.

Wilson, W., Gonthier, J. N., Georget, F., & Scrivener, K. L. (2022). Insights on chemical and physical chloride binding in blended cement pastes. *Cement and Concrete Research*, *156*, 106747.

Wu, B., & Ye, G. (2017). Development of porosity of cement paste blended with supplementary cementitious materials after carbonation. *Construction and Building Materials*, *145*, 52-61.

Wu, L., Wang, W., & Jiang, C. (2023). Study on the similarity of chloride penetration in concrete exposed to field and laboratory conditions. *Materials and Structures*, *56*(5), 95.

Xi, Y., Bažant, Z. P., & Jennings, H. M. (1994). Moisture diffusion in cementitious materials adsorption isotherms. *Advanced Cement based materials*, *1*(6), 248-257.

Xiang-peng, F., Li-ping, G., Jian-dong, W., Bang-cheng, L., Ying-jie, C., & Xu-yan, S. (2023). Impact of temperature, pH value and multiple ions on the physisorption of chloride ion on CSH gel surface. *Construction and Building Materials*, *392*, 131967.

Xie, X., Feng, Q., Chen, Z., Jiang, L., & Lu, W. (2019). Diffusion and distribution of chloride ions in carbonated concrete with fly ash. *Construction and Building Materials*, *218*, 119-125.

Xie, Y., Xie, J., Bai, L., & Liu, J. (2023). Experimental study on the effect of salt on the water absorption characteristic of cement mortar. *Journal of Building Engineering*, *73*, 106693.

Xu, J., Song, Y., Jiang, L., Feng, W., Cao, Y., & Ji, W. (2016). Influence of elevated temperature on release of bound chlorides from chloride-admixed plain and blended cement pastes. *Construction and Building Materials*, *104*, 9-15.

Yang, N., Das, C. S., Xue, X., Li, W., & Dai, J.-G. (2022). Geopolymer coating modified with reduced graphene oxide for improving steel corrosion resistance. *Construction and Building Materials*, *342*, 127942.

Yang, Z., Gao, Y., Mu, S., Chang, H., Sun, W., & Jiang, J. (2019). Improving the chloride binding capacity of cement paste by adding nano-Al2O3. *Construction and Building Materials*, *195*, 415-422.

Yang, Z., Sui, S., Wang, L., Feng, T., Gao, Y., Mu, S., Tang, L., & Jiang, J. (2020). Improving the chloride binding capacity of cement paste by adding nano-Al2O3: The cases of blended cement pastes. *Construction and Building Materials*, *232*, 117219.

Yao, N., Zhou, X., Liu, Y., & Shi, J. (2022). Synergistic effect of red mud and fly ash on passivation and corrosion resistance of 304 stainless steel in alkaline concrete pore solutions. *Cement and Concrete Composites*, *132*, 104637.

Ye, H., Jin, X., Fu, C., Jin, N., Xu, Y., & Huang, T. (2016). Chloride penetration in concrete exposed to cyclic drying-wetting and carbonation. *Construction and Building Materials*, *112*, 457-463.

Yi, Y., Zhu, D., Guo, S., Zhang, Z., & Shi, C. (2020). A review on the deterioration and approaches to enhance the durability of concrete in the marine environment. *Cement and Concrete Composites*, *113*, 103695.

Ylmén, R., Jäglid, U., Steenari, B.-M., & Panas, I. (2009). Early hydration and setting of Portland cement monitored by IR, SEM and Vicat techniques. *Cement and Concrete Research*, *39*(5), 433-439.

Yoon, I. S. (2007). Deterioration of concrete due to combined reaction of carbonation and chloride penetration: experimental study. *Key Engineering Materials*, *348*, 729-732.

Yoshida, S., Elakneswaran, Y., & Nawa, T. (2021). Electrostatic properties of C–S–H and CASH for predicting calcium and chloride adsorption. *Cement and Concrete Composites*, *121*, 104109.

Yu, P., Kirkpatrick, R. J., Poe, B., McMillan, P. F., & Cong, X. (1999). Structure of calcium silicate hydrate (C-S-H): Near-, Mid-, and Far-infrared spectroscopy. *Journal of the American Ceramic Society*, *82*(3), 742-748.

Yuan, Q., Shi, C., De Schutter, G., & Audenaert, K. (2008). Effect of temperature on transport of chloride ions in concrete. In *Concrete repair, rehabilitation and retrofitting II* (pp. 177-178). CRC Press.

Yuan, Q., Shi, C., De Schutter, G., Audenaert, K., & Deng, D. (2009). Chloride binding of cement-based materials subjected to external chloride environment–a review. *Construction and Building Materials*, *23*(1), 1-13.

Zha, J., Jiang, L., Xu, P., Jin, M., & Jiang, P. (2022). Influence of Temperature and Carbonation on Chloride Induced Corrosion of Carbon Steel in Concrete Pore Solutions. *Int. J. Electrochem. Sci*, *17*(220130), 2.

Zhang, G., Zhu, Y., Lin, X., Tian, Y., Ye, H., Jin, X., Jin, N., Yan, D., Xiao, F., & Yao, K. (2021). Numerical simulation of electrochemical mechanism of steel rebar corrosion in

concrete under natural climate with time-varying temperature and humidity. *Construction and Building Materials*, *306*, 124873.

Zhang, P., Dai, J.-G., Das, C. S., & Zheng, J.-J. (2023a). A fully coupled meso-scale electro-chemo-mechanical phase field method for corrosion-induced fracture in concrete. *International Journal of Solids and Structures*, *267*, 112165.

Zhang, P., Dai, J.-G., Das, C. S., & Zheng, J.-J. (2023b). A fully coupled meso-scale electro-chemo-mechanical phase field method for corrosion-induced fracture in concrete. *International Journal of Solids and Structures*, 112165.

Zhang, Q., Lun, P.-Y., & Li, X. (2021). A simplified approach for prediction of concrete resistivity: experimental study and mathematic model. *Materials and Structures*, *54*(4). https://doi.org/10.1617/s11527-021-01688-9

Zhang, Y., Sun, C., Zhang, P., Sun, M., Geng, Y., Zhao, M., Fan, L., Liu, N., & Duan, J. (2023). Chloride absorption capacity of calcium silicate hydrate (CSH) and its effect on steel corrosion in simulated concrete pore solution. *Journal of Sustainable Cement-Based Materials*, *12*(12), 1548-1563.

Zhang, Y., Wu, S., Zhang, Y., Zhou, C., & Fu, C. (2023). Similarities and probability distributions of chloride convection zone depth in concrete exposed to cyclic drying-wetting environments. *Cement and Concrete Composites*, *139*, 105040.

Zhang, Y., & Zhang, M. (2014). Transport properties in unsaturated cement-based materials–A review. *Construction and Building Materials*, *72*, 367-379.

Zhao, Y., Ren, H., Dai, H., & Jin, W. (2011). Composition and expansion coefficient of rust based on X-ray diffraction and thermal analysis. *Corrosion Science*, *53*(5), 1646-1658.

Zheng, H., Dai, J.-G., Hou, L., Meng, G., Poon, C. S., & Li, W. (2020a). Enhanced passivation of galvanized steel bars in nano-silica modified cement mortars. *Cement and Concrete Composites*, *111*, 103626.

Zheng, H., Dai, J.-G., Hou, L., Meng, G., Poon, C. S., & Li, W. (2020b). Enhanced passivation of galvanized steel bars in nano-silica modified cement mortars. *Cement and Concrete Composites*, 103626.

Zheng, H., Dai, J.-G., Li, W., & Poon, C. S. (2018). Influence of chloride ion on depassivation of passive film on galvanized steel bars in concrete pore solution. *Construction and Building Materials*, *166*, 572-580.

Zheng, H., Dai, J.-G., Poon, C. S., & Li, W. (2018). Influence of calcium ion in concrete pore solution on the passivation of galvanized steel bars. *Cement and Concrete Research*, *108*, 46-58.

Zheng, H., Lu, J., Shen, P., Sun, L., Poon, C. S., & Li, W. (2022). Corrosion behavior of carbon steel in chloride-contaminated ultra-high-performance cement pastes. *Cement and Concrete Composites*, *128*, 104443.

Zheng, H., Poon, C. S., & Li, W. (2020). Mechanistic study on initial passivation and surface chemistry of steel bars in nano-silica cement pastes. *Cement and Concrete Composites*, *112*, 103661.

Zheng, Y., Russell, M., Davis, G., McPolin, D., Yang, K., Basheer, P., & Nanukuttan, S. (2021). Influence of carbonation on the bound chloride concentration in different cementitious systems. *Construction and Building Materials*, *302*, 124171.

Zhou, X., Yao, N., & Shi, J. (2022). Unraveling electrochemical performance of a 10CrMo steel in alkaline concrete pore solutions with red mud and ground granulated blast-furnace slag. *Corrosion Science*, *207*, 110568.

Zhou, Y., Hou, D., Jiang, J., Liu, L., She, W., & Yu, J. (2018). Experimental and molecular dynamics studies on the transport and adsorption of chloride ions in the nano-pores of calcium silicate phase: the influence of calcium to silicate ratios. *Microporous and Mesoporous Materials*, *255*, 23-35.

Zhu, Q., Jiang, L., Chen, Y., Xu, J., & Mo, L. (2012). Effect of chloride salt type on chloride binding behavior of concrete. *Construction and Building Materials*, *37*, 512-517.

Zhu, W., Dai, J.-G., & Poon, C.-S. (2018). Prediction of the bond strength between non-uniformly corroded steel reinforcement and deteriorated concrete. *Construction and Building Materials*, *187*, 1267-1276.

Zhu, W., François, R., Poon, C. S., & Dai, J.-G. (2017). Influences of corrosion degree and corrosion morphology on the ductility of steel reinforcement. *Construction and Building Materials*, *148*, 297-306.

Zhu, X., Zi, G., Cao, Z., & Cheng, X. (2016). Combined effect of carbonation and chloride ingress in concrete. *Construction and Building Materials*, *110*, 369-380.

Zhu, X., Zi, G., Lee, W., Kim, S., & Kong, J. (2016). Probabilistic analysis of reinforcement corrosion due to the combined action of carbonation and chloride ingress in concrete. *Construction and Building Materials*, *124*, 667-680.

Zibara, H. (2001). *Binding of external chlorides by cement pastes*

Zibara, H., Hooton, R., Thomas, M., & Stanish, K. (2008). Influence of the C/S and C/A ratios of hydration products on the chloride ion binding capacity of lime-SF and lime-MK mixtures. *Cement and Concrete Research*, *38*(3), 422-426.

Zuo, X.-B., Li, X.-N., Liu, Z.-Y., Huang, W.-Y., & Sun, X.-h. (2019). Electrochemical and microstructural study on depassivation of ductile iron surface in chloride-contained simulated cement-mortar pore solution. *Construction and Building Materials*, *229*, 116907.

Zuquan, J., Xia, Z., Tiejun, Z., & Jianqing, L. (2018). Chloride ions transportation behavior and binding capacity of concrete exposed to different marine corrosion zones. *Construction and Building Materials*, *177*, 170-183.

Appendix 1

Table 1. Mix composition and testing condition for evaluating the nature of chloride transport in drying and wetting zones

Mix	Cement type	Supplementary cementitious materials (% wt replacement of cement)			W/b	Exposure scheme	Exposure period (d)	Ref
		FA	GGBS	SF				
#1	OPC	-	-	-	0.35	Field exposure in a marine tidal zone in Qingdao Wheat Island, China, for 12-hour cycles with three drying-to-wetting ratios of (i) 11:1, (ii) 1:1 and (iii) 1:11	30, 60, 90	(Cao et al., 2022)
#2	OPC	17	32	-	0.35			
#3	OPC	-	-	-	0.43	Drying and wetting cycles in a lab with 5% by weight NaCl solution for (i) 2-week cycle with 7 days wetting and 7 days drying (ii) 3-week cycle with 7 days wetting and 14 days drying	420	(Lu et al., 2015)
#4	OPC	-	-	-	0.385			
#5	OPC	15	-	-	0.385			
#6	OPC	30	-	-	0.385			

FA: Fly ash, GGBS: Ground granulated blast furnace slag, Sf: Silica fume

Table 2. Concrete mix and testing condition for evaluating the effect of temperature on chloride binding ability of cement paste

Mix	Cement type	Supplementary cementitious materials (% wt replacement of cement)				W/b	Exposure condition	Exposure temperature (°C)	Ref
		MK	GGBS	NZ	SF				
#1	OPC	-	-		-	0.4	25 g of powder samples cured for two months were exposed to 100 ml NaCl solutions of concentrations 0.1M, 0.5M, 1M, 2M, and 3M for eight weeks	-4, 3, 22, 35, 50, 70	(Dousti & Shekarchi, 2015)
#2	OPC	-	-	-	8	0.4			
#3	OPC	8	-	-	-	0.4			
#4	OPC	-	-	10	-	0.4			
#5	OPC	-	-	-	-	0.31	2.5-gram samples of size 10 X 10 X 2.5 mm thickness cured for 28 days were stored in 5 ml NaCl solutions of concentrations 0.1M, 0.5M, 0.75M, 1M, and 3M for 55 days	-3, 5, 13, 22	(Panesar & Chidiac, 2011)
#6	OPC	-	25	-	-	0.31			
#7	OPC	-	50	-	-	0.31			
#8	OPC	-	75	-	-	0.31			
#9	OPC	-	-	-	-	0.3, 0.5	25 gram of disc specimens of 50 mm diameter and 3 mm thickness cured for 9 months were placed in 125 ml NaCl solutions of concentrations 0.1M, 1M and 3M for 6 months	7, 23 and 38	(Zibara, 2001)
#10	OPC	-	-	-	8	0.3, 0.5			
#11	OPC	8	-	-	-	0.3, 0.5			

MK: Metakaolin, NZ: Natural pozzolona

Table 3. Concrete mix proportion and testing condition for evaluating the effect of temperature on chloride diffusion coefficient and activation energy

Mix	Cement type	Supplementary cementitious materials (% wt replacement of cement)				W/b	Exposure condition	Exposure temperature (°C)	Ref
		SF	FA	MK	NZ				
#1	OPC	-	-	-	-	0.35	Diffusion tests following NT Build 443 (165 g/l NaCl solution) were conducted on samples cured for 56 days for a period of 42 days	5, 25, 40	(Yuan et al., 2008)
#2	OPC	-	-	-	-	0.48			
#3	OPC	-	-	-	-	0.6			
#4	OPC	-	-	-	-	0.40	Concrete cylindrical samples of diameter 150 mm, which were cured for 5 months, were immersed in 32 g/l NaCl solution for a period of 450 days	22, 35, 50	(Dousti et al., 2013)
#5	OPC	5	-	-	-	0.40			
#6	OPC	10	-	-	-	0.40			
#7	OPC	12.5	-	-	-	0.40			
#8	OPC	-	-	-	10	0.40			
#9	OPC	-	-	-	15	0.40			

#10	OPC	-	-	-	20	0.40			
#11	OPC	-	-	-	-	0.4	75 mm diameter and 150 mm height samples, which were cured for 21 days before being immersed in 26 g/L of Cl solution for 365 days	22, 35, 50, 60	(Al-Sodani et al., 2021)
#12	OPC	-	20	-	-	0.4			
#13	CEMI	-	-	-		0.39	11 cm diameter and 5 cm thick cylinders were cured for 28 days after immersing in 33 g/L NaCl solution for 180 days		
#14	CEMV	-	-	-	-	0.43			
#15	OPC	-	-	-	-	0.38	75 mm diameter and 150 mm height samples, which were cured for 28 days before being immersed in 45 g/L of NaCl solution for 390 days	23, 38, 53, 68	(Al-Sodani, 2022)
#16	OPC	-	-	-	-	0.38			
#17	OPC	5	-	-	-	0.38			
#18	OPC	10	-	-	-	0.38			
#19	OPC	15	-	-	-	0.38			
#20	OPC	-	-	5	-	0.38			
#21	OPC	-	-	10	-	0.38			
#22	OPC	-	-	15	-	0.38			

Table 4. Mixing composition and testing parameters of studies involving effect of carbonation on chloride transport rate.

Mix	Cement type	Supplementary cementitious materials (% wt replacement of cement)			CO_2 conc	CO_2 exposure period (d)	W/b	Chloride transport testing method	Chloride ingress testing starting age (d)	Ref
		FA	GGBS	SF						
#1	OPC	-	-	-	5%	90	0.55	Immersion for 3 months as per NT Build 443	150	(Wang et al., 2017)
#2	OPC	30	-	-	5%	90	0.55		150	
#3	OPC	10	-	5	5%	90	0.55		150	
#4	OPC	-	-	-	20%	28	0.38	10h aerosol chloride spray and 14h drying for 28 days	56	(J. Liu et al., 2017)
#5	OPC	-	-	-	20%	28	0.47		56	
#6	OPC	-	-	-	20%	28	0.53		56	
#7	OPC	-	-	-	20%	28	0.47		56	

#8	OPC	15	-	-	20%	28	0.47	10h aerosol chloride spray and 14h drying for 28 days	56	(J. Liu et al., 2016)
#9	OPC	30	-	-	20%	28	0.47		56	
#10	OPC	-	-	-	20%	62	0.51	Use of empirical equation to obtain chloride diffusion coefficient from ASTM C1202	90	(Xie et al., 2019)
#11	OPC	15	-	-	20%	62	0.57		90	
#12	OPC	30	-	-	20%	62	0.53		90	
#13	OPC	-	-	-	20%	62	0.35		90	
#14	OPC	15	-	-	20%	62	0.33		90	
#15	OPC	30	-	-	20%	62	0.26		90	
#16	CEM I 42.5R	-	-	-	4%	30	0.60	Non steady migration test as per LNEC	150	(Malheiro et al., 2020)
#17	CEM I 42.5R	-	-	-	4%	210	0.60		330	
#18	OPC PO42.5	-	-	-	20%	90	0.5		180	
#19	OPC PO42.5	-	-	-	20%	90	0.6		180	

#20	OPC PO42.5	8.6	7.6	-	20%	90	0.5	Immersion for 35 days as per NT Build 443	180	(Li et al., 2018)
#21	OPC PO42.5	14.7	12.9	-	20%	90	0.6		180	
#22	OPC PII 42.5	-	-	-	20%	28	0.35	Immersion in 1M/litre NaCl solution for 6 weeks (diffusion coefficient of free chlorides only)	56	(Jin et al., 2018)
#23	OPC PII 42.5			-	20%	28	0.45		56	
#24	OPC PII 42.5	-	-	-	20%	28	0.55		56	
#25	OPC PII 42.5	34.9	-	-	20%	28	0.55		56	
#26	OPC PII 42.5	-	34.9	-	20%	28	0.55		56	
#27	CEM I	-	-	-	3%	180	0.5		208	
#28	CEM I	-	20	-	3%	180	0.5		208	
#29	CEM I	-	25	-	3%	180	0.5		208	
#30	CEM I	-	30	-	3%	180	0.5		208	
#31	CEM I	-	35	-	3%	180	0.5		208	
#32	CEM I	-	40	-	3%	180	0.5		208	

#33	CEM I	-	45	-	3%	180	0.5	NT Build 492	208	(Holthuizen et al., 2018)
#34	CEM I	-	50	-	3%	180	0.5		208	
#35	CEM I	-	55	-	3%	180	0.5		208	
#36	CEM I	-	60	-	3%	180	0.5		208	
#37	CEM I	-	65	-	3%	180	0.5		208	
#38	CEM I	-	70	-	3%	180	0.5		208	

Appendix 2

Derivative thermogravimetric (DTG) plots

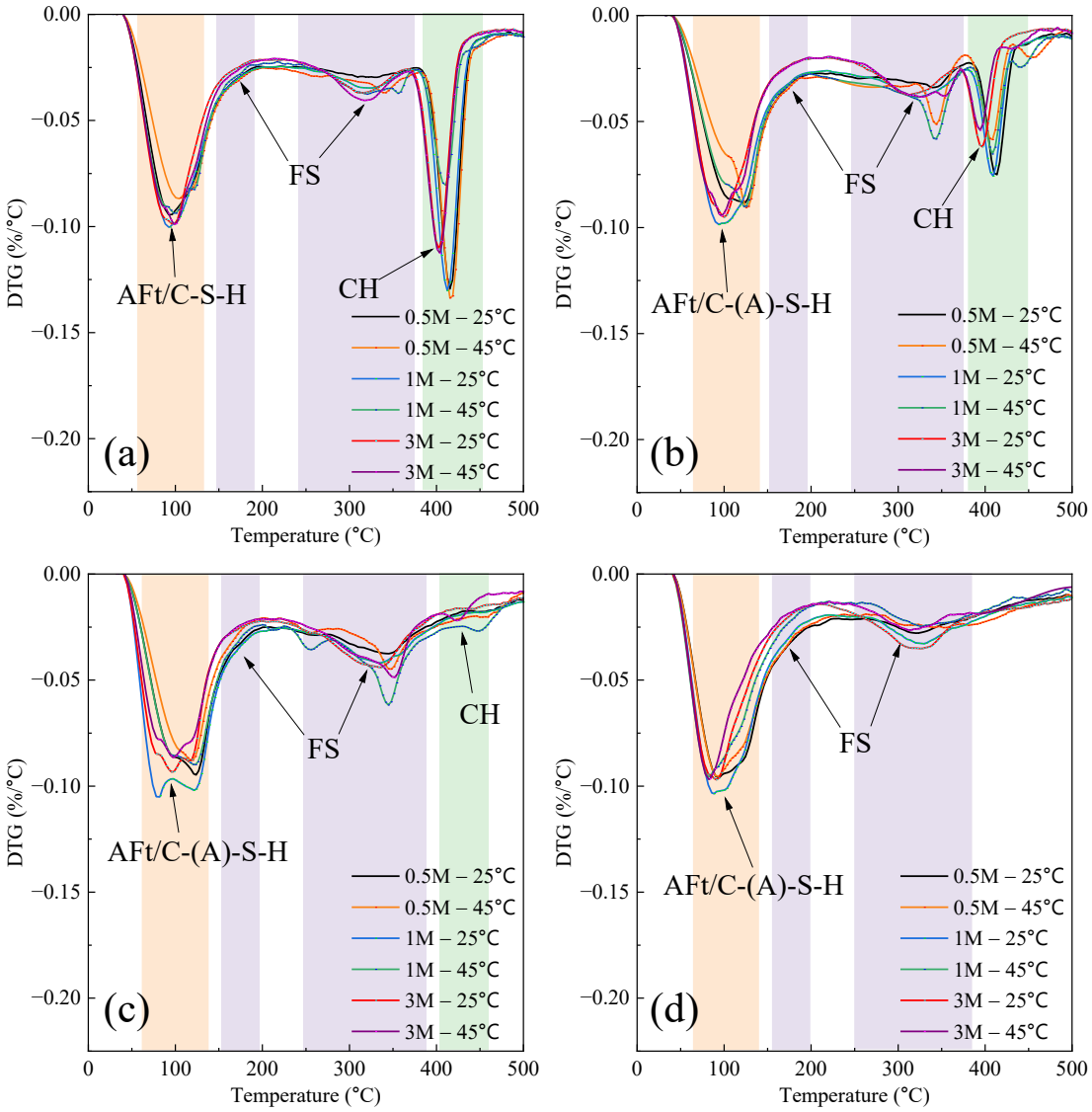

Figure 1. DTG curves of (a) OPC, (b) 15FA, (c) 35FA, and (d) 35FA8SF powder samples exposed to different chloride concentrations at exposure temperatures of 25℃ and 45℃

Energy-dispersive X-ray Spectroscopy (EDS) statistical plot

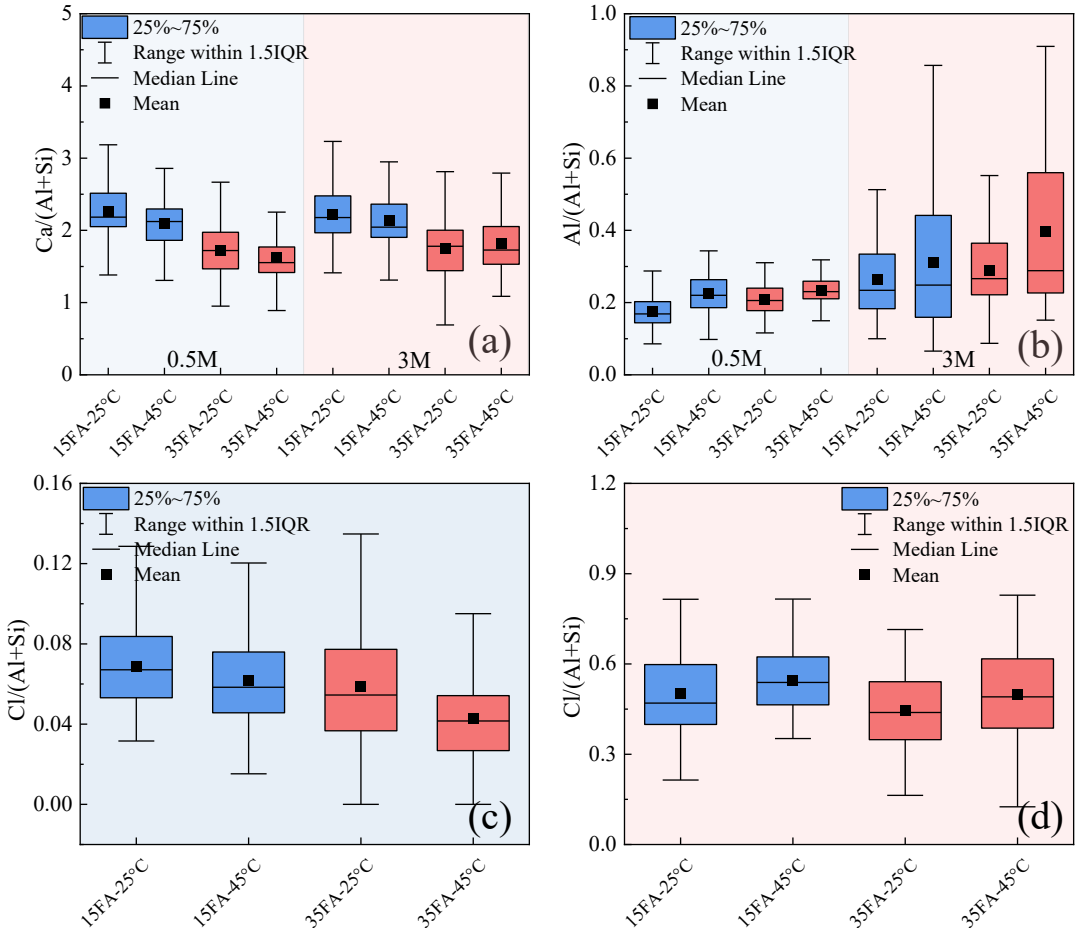

Figure 2. EDS point scatter of powder samples (15FA and 35FA) to find (a) Ca/(Si+Al), (b) Al/(Si+Al), (c) Cl/(Al+Si) for reference chloride concentration of 0.5M and (d) Cl/(Al+Si) for reference chloride concentration of 3M.